Steady and Unsteady Dynamics of an Azimuthing Podded Propulsor Related to Vehicle Maneuvering

By

Jeffrey W. Stettler

B.S., Chemical Engineering, Lehigh University, 1983
S.M., Mechanical Engineering, Massachusetts Institute of Technology, 1995
Naval Engineer, Massachusetts Institute of Technology, 1995

Submitted to the
Department of Ocean Engineering
in partial fulfillment of the requirements for the degree of

DOCTOR OF PHILOSOPHY
in
NAVAL ARCHITECTURE AND MARINE ENGINEERING
at the
MASSACHUSETTS INSTITUTE OF TECHNOLOGY

June 2004

Author *Signature on file*
Department of Ocean Engineering, MIT
May 10, 2004

Certified by *Signature on file*
Michael S. Triantafyllou
Professor of Ocean Engineering, MIT
Thesis Supervisor

Accepted by *Signature on file*
Michael S. Triantafyllou
Professor of Ocean Engineering, MIT
Chair, Departmental Committee on Graduate Studies

This page left blank

Steady and Unsteady Dynamics of an Azimuthing Podded Propulsor Related to Vehicle Maneuvering

By

Jeffrey W. Stettler

Submitted to the Department of Ocean Engineering
on May 10, 2004, in partial fulfillment of the
requirements for the degree of

DOCTOR OF PHILOSOPHY
in
NAVAL ARCHITECTURE AND MARINE ENGINEERING

Abstract

While the implementation of azimuthing propulsors powered by internal electric motors (often called "podded propulsors") into the commercial ship market has been swift, the understanding of their hydrodynamics through research, particularly in the area of maneuvering performance, has been very limited.

This thesis research investigates the steady and unsteady dynamic maneuvering forces associated with an azimuthing podded propulsor, and provides supporting theoretical insight toward understanding their mechanisms and prediction. Because of the wide range of potential applications of azimuthing podded propulsion in the marine field, dynamic force phenomena applicable to maneuverability of both large and small scale vehicles are investigated. These include quasi-steady vectored maneuvering forces, of importance to all maneuvering vehicles or ships, as well as unsteady or transient maneuvering forces, which have more significance to the maneuverability of smaller vehicles, particularly for precision control applications. The ultimate goal of the research is to provide a comprehensive understanding of the maneuvering forces associated with an azimuthing podded propulsor, such that future maneuvering and control applications, and computational fluid dynamics studies in the field, can be appropriately focused.

The research efforts are focused in four main areas. First, a number of relevant dynamic models for the maneuvering of a surface vehicle with an azimuthing propulsor are developed. Second, an extensive test program measures and characterizes the nature of quasi-steady vectored maneuvering forces associated with a podded propulsor in azimuth to ±180° for the entire range of forward propeller speeds, as well as unsteady or transient maneuvering forces due to rapid changes in azimuth angle or propeller rate. This test program is aimed at quantifying the steady and unsteady parameters associated with the developed dynamic models. Third, two flow visualization techniques are utilized to visualize, document, and correlate the helical wake characteristics, velocities and forces for both quasi-steady and unsteady propulsor states. A new fluorescent paint flow visualization technique is developed and applied for small, moderate and

large propulsor azimuth angles, and a laser particle image velocimetry (PIV) technique is adapted for small and moderate propulsor azimuth angles. Finally, a set of comprehensive physics-based models are developed to foster the understanding of the mechanisms associated with the steady and unsteady force dynamics. The quasi-steady models are based upon a combination of momentum-based, blade-element, and vortex wake propeller theories, as applied to an azimuthing podded propulsor. The unsteady force models are based upon unsteady wake or "dynamic inflow" methods. Additionally, an interesting phenomenon associated with the formation of a vortex ring during rapid propeller rate increase is presented and discussed.

The steady and unsteady test results, flow visualizations, and theoretical models, are shown to be consistent in terms of the magnitudes and character of the azimuthing maneuvering forces. Limited comparisons of quasi-steady propulsor forces at small, moderate and large azimuth angles are also made with forces predicted by a modified combined blade-element-momentum (BEM) method, as well as the unsteady vortex-lattice propeller code MPUF-3A, with and without modified inflows to account for propulsor pod wake. The results illustrate inherent complexities related to use of existing computational fluid dynamics tools with azimuthing podded propulsors.

Thesis Supervisor: Michael S. Triantafyllou
Title: Professor of Ocean Engineering, Massachusetts Institute of Technology

Acknowledgements

While most “acknowledgements” sections of theses normally end with the acknowledgement of family, I think it is more appropriate to put them at the front, where they belong. I must say that without the constant support, encouragement, distraction, and amusement provided by my family, this time at MIT as a returning (OK, I’m old) graduate student would have been far more difficult, if not impossible. In particular, over the past year, most of which has been spent apart, my wife Lisa has remained focused and committed to the family, the relationship, and our goals. Her love and support have meant the world to me, and I truly and sincerely owe her the greatest debt of my life for sharing this dream and opportunity with me, and not to “put up with it.” Additionally, despite my absence, my son Ricky and daughter Carlie have kept a positive and healthy attitude and have made me very, very proud.

Now, I would like to thank my Thesis Supervisor, Prof. Michael Triantafyllou, for giving me the opportunity to pursue this research. I would also like to thank the other members of my Thesis Committee: Prof. Paul Sclavounos, Prof. Alexandra Techet, Dr. Franz Hover, and Dr. Richard Kimball. The entire committee has provided outstanding guidance and suggestions along the way. Their leadership and mentorship have been very much appreciated.

Like all MIT graduate students, I have found conversing and commiserating with fellow graduate students to be both helpful and vital to the breadth and value of the experiences of the past 3 years. I would like to thank specifically the fellow graduate students of the MIT Towing Tank, particularly David Beal, Victor Polidoro, and Stephen Licht. Along the same lines, I would like to thank Jim Morash and Rob Damus of the MIT Sea Grant Autonomous Underwater Vehicle Lab for their excellent early guidance regarding electronics and instrumentation.

One man who deserves special note and thanks is Mr. Fred Cote, who supervises the Edgerton Center Student Machine Shop at MIT. Without Fred, I most certainly would have floundered through all of my experiments. Fred’s most patient and skillful instruction and guidance in the finer points of machining and fabrication have truly added a great deal to the value of my education.

Special thanks to Dr. Stuart Jessup and Mr. Thad Michael of the Naval Surface Warfare Center for graciously donating their time and skill, and providing accurate propeller blade measurement. Special thanks also to Prof. Jake Kerwin of MIT and Prof. Spyros Kinnas of the University of Texas for granting permission and guidance for the use of the MPUF-3A computer code.

I would also like to thank John Hill, Stephen Enzinger, Don Bunker, John Zseleczky, Nancy Harris, Bill Beaver, and Pam Majors of the U.S. Naval Academy's Hydromechanics Laboratory, where I was fortunate enough to have had the opportunity to conduct experiments over two summers. Their expertise and support were invaluable for the thesis experiments, have made me a better experimentalist, and have greatly added to the value of the overall experience. Similarly, I would like to thank the following faculty members of the Department of Naval Architecture and Ocean Engineering at the Naval Academy, for their regular mentorship, encouragement, and support: Prof. Bruce Johnson, Prof. Bruce Nehrling, Prof. Greg White, Prof. David Kriebel, and Prof. Mike Schultz.

Finally, I would like to thank the Naval Academy's Academic Dean and Provost, Dean William Miller, and Associate Dean for the Faculty, Dean Michael Halbig, for providing to me the funding and the opportunity to pursue a doctorate at MIT. Funding for materiel and other research-related costs is also gratefully acknowledged from the MIT Sea Grant Program and the Office of Naval Research.

Table of Contents

List of Figures

List of Tables

This page left blank

Chapter 1

Introduction

1.1 Background and motivation

While azimuthing propulsion in the form of low-power electric, hydraulic, or right-angle gear-driven steerable thrusters has been around for nearly half a century, it has been only in the last decade that electric motor technology has advanced to the point where implementation of high-power azimuthing electric-drive propulsors has become practical for primary propulsion (and steering). The advantages of azimuthing electric-drive primary propulsion (often called podded or modular propulsion) are numerous, including design flexibility leading to improved arrangement efficiency, power management, maneuverability, and even reduced hull resistance.

While the implementation of podded propulsors into the commercial ship market has been swift, the complete understanding of their hydrodynamics through research, particularly in the area of maneuvering performance, has been limited. Van Terwisga et al. [75] provide a general overview of the history of mechanical and electrical steerable propulsion units, and address general hydrodynamic issues associated with their design and use. Toxopeus and Loeff [72] discuss recent applications of podded propulsion from a maneuvering perspective, comparing maneuverability between specific ship designs with conventional propulsion and podded propulsion, and highlighting the general benefits and points of attention. Additional comparative maneuvering testing has been conducted under the auspices of the OPTIPOD and FASTPOD research programs funded by the European Union, with some results just recently published in the First International Conference on Technological Advances in Podded Propulsion (T-POD), held in the UK in April 2004. Two papers deal specifically with the issues of vessel maneuverability with podded propulsors [4], [46].

Although limited free-running and captive model maneuverability testing on ships with pods has been conducted as mentioned above, there has been little basic research done specifically in the area of prediction and simulation of dynamic maneuvering forces and capabilities associated with podded propulsors. Research of this type conducted in the past has focused mainly on the design and optimization of low-power thrusters and dynamic positioning systems for deep water applications at slow speeds or in currents [57], [61], [60], [79]. A few new investigations of this

type for podded propulsors have just recently been presented at the T-POD conference [35], [30], [71].

This thesis research investigates the steady and unsteady dynamic maneuvering forces associated with an azimuthing podded propulsor, and provides supporting theoretical insight toward understanding their maneuvering attributes and performance. Because of the wide range of potential applications of azimuthing podded propulsion, dynamic force effects applicable to maneuverability of both large and small vehicles are investigated. These include quasi-steady force effects applicable to any maneuvering vehicle or ship, as well as unsteady or transient force effects which might have more significant application to the maneuverability of smaller vehicles, particularly for precision control applications. The ultimate aim of this thesis research is to provide a technical understanding and quantify the dynamic effects associated with azimuthing propulsion, particularly relating to vehicle maneuvering dynamics.

1.2 Literature review

There is very little in the literature regarding maneuvering with podded propulsion. Prior to April 2004, there have been only general literature notes regarding the effectiveness of podded propulsion in terms of maneuvering, and slow speed maneuverability with low-power thrusters. These literature sources that are relevant to the current research have been noted in the previous section.

Just recently, in April of 2004, the First International Conference on Technological Advances in Podded Propulsion (T-POD) was held in Newcastle upon Tyne in the UK. Although providing an excellent forum for exchange of information on the current status and focus of research in the area of podded propulsion, its direct applicability to the forces that effect maneuvering can be boiled down to a small handful of presented papers. These have been referenced in the previous section.

For this reason, a formal literature review will not be presented within this introductory chapter. Rather, specific references pertaining to maneuvering, propellers and propulsion, lifting theory, system dynamics, etc. will be presented as they are needed, within the relevant chapters and sections.

1.3 Chapter preview

This thesis documents an overall effort to characterize and understand maneuvering forces associated with an azimuthing podded propulsor through a focused experimental effort, and provides a theoretical basis for the behavior of the maneuvering forces based upon steady and unsteady propeller theories and calculations.

Chapter 2 provides a brief overview of the relevant dynamics associated with maneuvering with an azimuthing propulsor. First, a short presentation is provided regarding the basic force effects associated with propellers operating in oblique inflow. Then a combined dynamic maneuvering model is presented which incorporates the fully coupled dynamics of the vehicle, propeller and propulsor motor, and provides for necessary kinematics required to fully couple the various dynamics.

Since the overall goal of the research is to investigate the maneuvering dynamics associated with an azimuthing podded propulsor, a first step in the research was to design, model and construct an autonomous surface test vehicle with a dynamically-azimuthing propulsor system, which could be utilized for carrying out the investigation. Chapter 3 provides a basic overview of the design and construction of the autonomous surface test vehicle, and the dynamically-azimuthing propulsor system, which have been utilized for this research. This chapter also includes details of the propulsor and propeller geometries, and a brief discussion of the experimental identification of the vehicle maneuvering coefficients for the combined dynamic maneuvering model.

Chapter 4 provides an in-depth presentation of the test program conducted in investigating maneuvering forces associated with the azimuthing propulsor, including quasi-steady effects of importance to all vehicles, as well as the transient or unsteady effects of potential importance to smaller vehicles. The experimental setups and techniques are detailed, results presented in graphical and tabular form, and the significance of the test results to vehicle maneuvering are discussed.

Chapter 5 presents and discusses results of several efforts to visualize and document the steady and unsteady wake of the azimuthing propulsor. A novel technique using fluorescent paint and ultraviolet black light has been developed for the visualization of the vortex wake for a range of quasi-steady and unsteady/transient operating conditions. A technique using laser Particle Image Velocimetry (PIV) has also been adapted to provide more precise visualization and velocity documentation of the wake for a number of quasi-steady and unsteady/transient operating conditions. Documentation and demonstration of several important steady and

unsteady wake effects are provided, including quasi-steady wake pitch and wake angle for moderate and large angles, distortion of the wake for moderate and large angles, and the interesting development and interaction of vortex rings during rapid propeller rate increase.

Chapter 6 provides a detailed discussion of a theoretical basis for the quasi-steady maneuvering force dynamics of an azimuthing propulsor over the entire range of forward operating conditions (i.e. for propulsor azimuth to ± 90 degrees relative to the inflow). This theoretical basis begins with a discussion of "simple" momentum-based models for a propeller in axial and oblique inflows, and expands to include a modified blade-element theory, using combined blade-element and momentum, including important wake considerations from vortex theory. Finally, a discussion of the use of computational fluid dynamics for the prediction of maneuvering forces is presented. Results of calculations made are provided in comparison with experimental results, with the relevance of consistencies and inconsistencies discussed in detail.

Chapter 7 provides a detailed discussion of a theoretical basis for the unsteady maneuvering force dynamics of an azimuthing propulsor. A "dynamic inflow" model is developed which provides an expression for an approximate dynamic inflow or wake time constant. This dynamic inflow time constant represents the lag in induced velocity at the propeller disk, and the "lead" in propeller forces for rapid changes in propeller operating states, particularly propeller rate n. Additionally, asymmetry seen in the unsteady propeller rate experimental force results is addressed by discussing the formation of vortex rings during rapid propeller rate increase. Estimates for the vortex ring formation time are developed using combined vortex ring and propeller theories and results of flow visualization experiments.

Finally, Chapter 8 provides a summary of the research and the significant results, provides a summary of the unique contributions of the thesis to the field of naval architecture and marine engineering, and provides some recommendations for future research in the area.

For reference throughout the thesis, table 1-1 provides a summary of much of the nomenclature used.

Table 1-1: Nomenclature.

α	Blade element angle of attack, vehicle effective inflow angle into propulsor
α_D	Angle of rotor/disk relative to incoming flow
β	Blade element pitch angle, vehicle drift angle
χ	Wake skew angle
δ	Propulsor azimuth angle in vehicle coordinate frame
ϕ	Blade element inflow angle, propeller pitch angle, wake helix pitch angle
η_o	Propeller efficiency ($JK_T/2\pi K_Q$)
λ	Tip speed ratio
λ_i	Non-dimensional induced velocity based on propeller rate (V_i/nD)
θ	Propeller azimuthal/circumferential blade angle/location
ρ	Water density
τ	Time constant, dynamic inflow time constant
τ_R	Formation time for vortex ring from rapid increase in propeller rate
τ_T	Total system time constant (overall time constant)
ω	Angular velocity
ψ	Vehicle yaw angle in inertial (earth-fixed) frame
Γ, Γ_P, Γ_R	Circulation, circulation produced by propeller, circulation of vortex ring
b	Wing span
c	Propeller blade chord
f	Frequency (hz)
i_m, k_t	Motor current, motor torque constant
i_{m0}, i_A	Motor current zero-crossing and amplitude for motor current sinusoidal test
k_1, k_2	Empirical factors for propeller blade lift/drag coefficients
$\dot{m}$	Mass flux through disk annulus
m_a	Apparent added mass of water influenced by propeller disk (dynamic inflow)
n	Propeller rotation rate (rev/sec)
$\hat{n}$	Perturbation of propeller rotation rate for current input step or ramp test
$\hat{n}_{ss}$	Steady state perturbation of propeller rate for current input step or ramp test
P_a, P_u, P_d	Ambient pressure, pressure far upstream, far downstream propeller disk
r	Radial coordinate position
s	Span of propeller blade
u, v, r	Vehicle surge, sway, yaw velocities in vehicle coordinate frame
w	x-component of velocity far downstream propeller disk, wake fraction
x_o, y_o	Vehicle x, y location in inertial (earth-fixed) frame
x_p	Distance from center of vehicle coordinate frame to center of propulsor
A_a, A_w	Area of streamtube far upstream, far downstream propeller disk
A_p	Area of propeller disk
A_0^A, A_m^A, B_m^A, etc.	Harmonic coefficients for effective propeller inflow velocity decomposition
B_m, k_{f0}, k_{f1},k_{f2}	Mechanical “dry” stick-slip friction, friction coefficients
C_{Fa}, C_{Fn}, C_{Mz}	Non-dimensional axial force, normal force, moment on pod-only

C_L, C_D	Propeller blade lift, drag coefficients
D	Propeller diameter
D_0	Diameter of piston feeding vortex ring
F(r)	Prantdl tip loss factor
F_a, F_n, M_z	Axial force, normal force, moment on pod-only
F_x, F_y	Propulsor surge and sway forces
I	Impulse related to vortex ring formation
I_m	Mechanical "dry" rotational inertia (motor, shaft, seal, propeller)
I_a	Hydrodynamic (added) rotational inertia (unsteady hydrodynamic torque)
J	Advance coefficient (V_a/nD)
K_T, K_N	Propulsor thrust force, normal force coefficients ($T/\rho n^2D^4$, $N/\rho n^2D^4$)
K_Q, K_M	Propeller torque, propulsor steering moment coefficients ($Q/\rho n^2D^5$, $M/\rho n^2D^5$)
K_{Fx}, K_{Fy}	Propulsor surge force, sway force coefficients ($F_x/\rho n^2D^4$, $F_y/\rho n^2D^4$)
L, D	Lift force, drag force
L*, D*, etc.	* ≡ property at blade element (e.g. elemental/incremental lift, drag, etc.)
M, M_p	Propulsor steering moment (total, quasi-steady)
N, N_p	Propeller/propulsor normal force (total, quasi-steady)
P	Propeller pitch
Q, Q_p	Propeller/propulsor torque (total hydrodynamic, quasi-steady)
$\hat{Q}_s$	Motor input torque perturbation for current input step test
$\hat{Q}_R$	Motor input torque perturbation for current input ramp test
R, R_h	Propeller radius, propeller hub radius
R_e	Effective radius (Prandtl tip loss)
T, T_p	Propeller/propulsor thrust force (total, quasi-steady)
$\tilde{T}, \tilde{Q}$, etc.	Annulus-averaged thrust, torque, etc.
T_0	Nominal formation time for vortex ring
U	Velocities related to vortex ring formation
U_R	Characteristic velocity of axial flow feeding a vortex ring
V_a, V_∞	Advance velocity, towing tank carriage velocity, free-steam velocity
V_A, V_θ	Axial velocity, tangential velocity
V_{Ai}, $V_{\theta i}$	Axial induced velocity, tangential induced velocity
V_e	Effective inflow velocity at propulsor
V_i	Induced velocity
V_p, V_w	Velocity at propeller disk, velocity far downstream propeller disk (slipstream)
$\overline{V}$	Disk-averaged velocities
V_T, V_{Ti}	Transverse (in-plane) component of velocity, induced velocity
Z	Number of propeller blades, logarithmic variable for current input step test

Chapter 2

Maneuvering dynamics: an overview

For typical marine propulsion and maneuvering simulation and control applications (i.e. conventional ships with shafted propellers or ROV/AUV marine thrusters), equations for the maneuvering dynamics of the vehicle or ship are typically coupled to the dynamics of the main engine or propulsion motor through quasi-steady mappings relating ambient or advance velocity and propeller rotation rate to propeller thrust and torque. However, some recent studies have also considered coupling of propeller thrust and torque to the *unsteady* fluid velocities in the vicinity of the propeller blades for considering *very* fast thrust and torque dynamics for precision control applications [34], [77], [5], [10]. In either case, the additional complexities of propeller/propulsor azimuth lead to a necessity to expand the dynamic maneuvering equations to include additional vectored propulsion and steering force components, and expand the propeller/propulsor mappings to include *normal force* and *steering moment*, in addition to the *vectored* (altered) thrust and torque. It is mainly in the character of the *vectored* thrust force, torque, normal force, and steering moment that maneuvering with azimuthing propulsors differs so significantly from maneuvering with conventional shafted propellers and rudders, or marine thrusters.

2.1 Propellers in oblique flow and maneuvering forces

The fundamental importance of understanding vectored propulsion can be illustrated by considering the forces that result from a propeller that is operating in an oblique inflow (figure 2-1). First, the hydrodynamic thrust force (T) and torque (Q) vectors along the axis of the propeller shaft are affected by a reduction in *effective* axial inflow velocity as the propeller is azimuthed relative to the inflow. Intuitively, this reduction in effective axial inflow velocity (i.e. with the cosine of the angle) *reduces* the effective advance coefficient in terms of the inflow velocity to the propeller, and thus *increases* thrust and torque in accordance with "typical" propeller thrust-torque-speed characterization (figure 2-2). Second, a *normal* force (or side force) N is created due to unequal angles of incidence on the blades as they rotate through the oblique inflow [15], and for larger inflow angles at higher advance velocities, the transverse roll-up of the wake along its top and bottom edges, essentially forming two dominant vortex bundles (see for example [51],

[52]). Regardless of the direction of rotation of the propeller, the net normal force is in the *same* direction, away from the inflow [15].

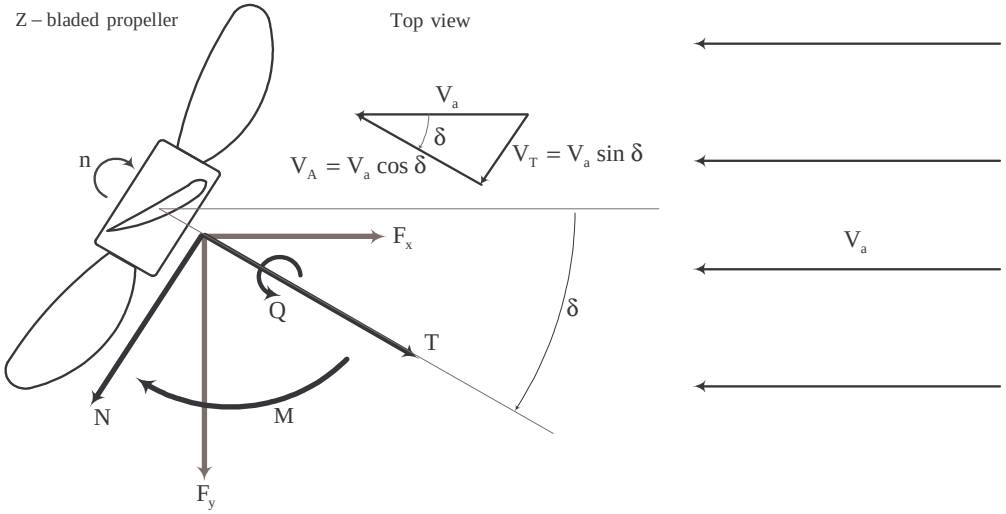

Figure 2-1: Propeller in oblique inflow. Hydrodynamic torque Q, thrust force T, normal force N, and steering moment M, resulting from a propeller in oblique inflow. F_x and F_y are the equivalent surge force and sway force in the vehicle or tunnel coordinate system.

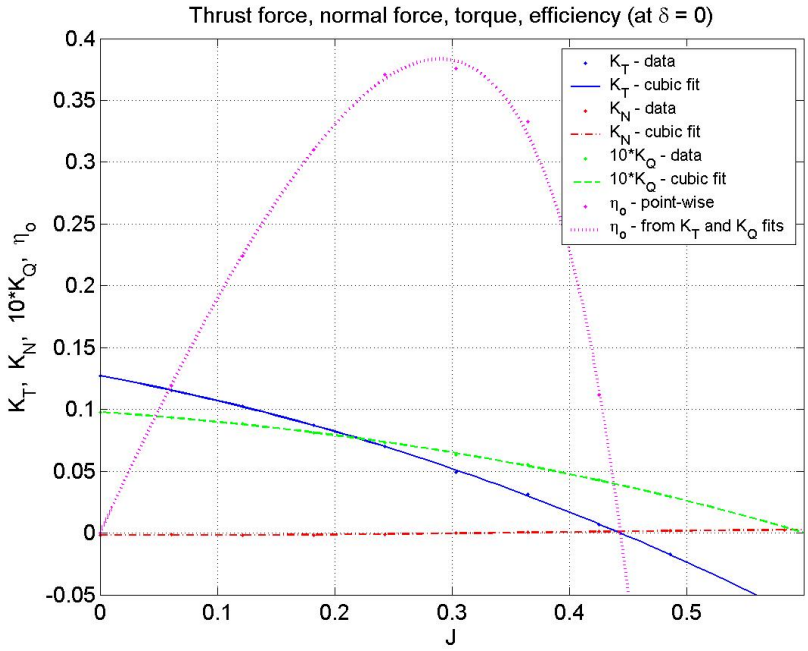

Figure 2-2: "Typical" propeller thrust-torque-speed characterization. Non-dimensional thrust force and torque coefficients (K_T and K_Q) vs. advance coefficient (non-dimensional advance velocity $J = V_a/nD$). Thrust and torque are maximum at zero advance coefficient and reduce with increasing advance coefficient.

Thus one main effect of azimuthing propulsion, in terms of maneuvering forces, is to produce propeller forces which vary in a nonlinear manner with inflow angle, propeller speed and advance

velocity (or non-dimensional advance coefficient $J = V_a/nD$). This would suggest a nonlinear 3-dimensional mapping of quasi-steady propeller thrust, torque, and normal force with azimuth angle and advance coefficient. It should be noted that, for an azimuthing podded propulsor, this also implies a coincidental mapping of the hydrodynamic moment on the propulsor about its steering shaft (i.e. the *steering moment* M). It is also noted that in addition to the vectored propeller forces, the propulsor pod itself also induces force contributions resulting from its own effective hydrodynamic characteristic drag and lift forces (or axial force along its axis and normal force perpendicular to its axis), as well as a hydrodynamic moment. This will be discussed in greater detail in Chapters 4 and 6.

In addition to the nonlinear mappings of quasi-steady propeller thrust, torque, normal force and steering moment, there are also *unsteady* hydrodynamic force components associated with accelerating and decelerating flows. In terms of maneuvering forces, the term *unsteady* is used here to denote those force components which arise due to time rate-of-change of the main state variables associated with the azimuthing propulsor (i.e. $\dot{n}, \dot{V}$, and potentially $\dot{\delta}$ and $\ddot{\delta}$). For maneuvering simulation and control of large ships or vehicles, these unsteady hydrodynamic force components are typically neglected, as the time constants are usually at least an order of magnitude faster than the dominant time constants for the maneuvering ship or vehicle. For smaller vehicles, this is not necessarily the case, and consideration of unsteady forces may be necessary, particularly for control applications such as maneuvering of precision underwater work vehicles. Therefore, this thesis research considers both the quasi-steady force components as well as the unsteady or transient force components.

2.2 Models for maneuvering dynamics

In order to tie together and motivate the test program and provide a basis for quantification of the effects of the azimuthing propulsor on vehicle maneuvering, a combined dynamic maneuvering model for a vehicle with azimuthing propulsion is briefly discussed. A combined maneuvering model can be developed based upon fundamental principles of dynamics, and parameters determined through a suitable test program for the various force components and interactions. The dynamics of an azimuthing propulsor can be incorporated into an overall vehicle dynamic maneuvering model by coupling the equations for the vehicle dynamics to those of the propulsor, through quasi-steady or dynamic equations relating velocity and propeller rotation rate to propeller thrust, torque, normal force and steering moment. This relationship, for

a surface vehicle with a single azimuthing propulsor driven by a DC motor, can be simply illustrated as in figure 2-3. In order to carry out system identification and combined system simulation or control of the maneuvering dynamics of the vehicle, the various dynamic and kinematic relations in the model must be put into suitable forms, whose parameters can be determined (identified) through a reasonable experimental test program.

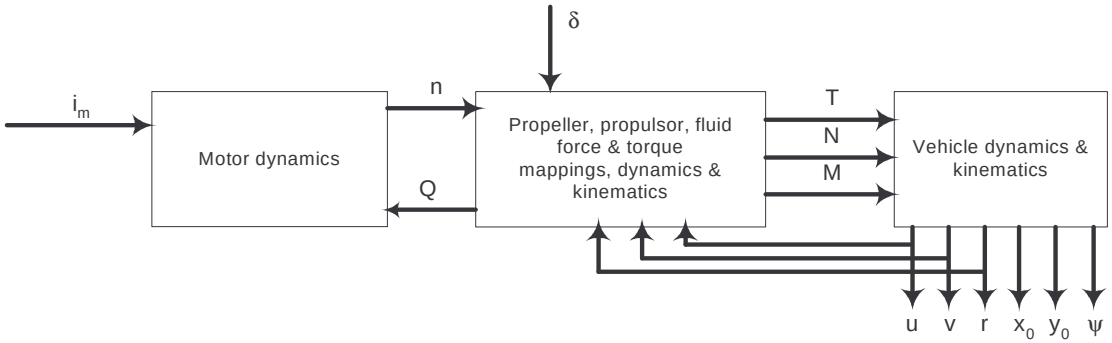

Figure 2-3: Combined dynamic maneuvering model for a surface vehicle with a DC motor-driven azimuthing propulsor.

2.2.1 A model for vehicle maneuvering in the horizontal plane

In order to motivate the direction of testing on the azimuthing propulsor and highlight the significance of the results in terms of maneuvering forces, simulation or control applications, it is necessary to define a "form" for the equations of motion, or simulation model, which is capable of capturing the relevant dynamics for the maneuvering of the vehicle (and whose parameters can be successfully identified through a suitable experimental test program).

The form of the vehicle dynamic and kinematic relations can be written based upon "standard" nonlinear equations for maneuvering of a ship or vehicle, modified to account for the *vectored* forces associated with the azimuthing propulsor, plus appropriate interaction terms. Figure 2-4 defines relevant earth-fixed (inertial) and vehicle-fixed coordinate frames, as well as forces, velocities and displacements for a surface vehicle maneuvering in the horizontal plane. Combined maneuvering equations of motion can be written based upon any of a number of ship maneuvering models, for example the "Abkowitz" maneuvering models [1], [2], [15], [21] with modifications to account for the vectored propulsor forces. With the dynamic state variables delineated in figure 2-4 relating to vehicle velocities (u, v, r) and displacements (x_o, y_o, ψ) as specified by the selected vehicle maneuvering model, a simple yet comprehensive nonlinear

maneuvering model for a vehicle maneuvering in the horizontal plane can be developed and written as three coupled equations of the form

$$m\left(\dot{u} - rv - x_{cg}r^2\right) = X_0 + X_{\dot{u}}\dot{u} + X_u\Delta u + X_{uu}\Delta u^2 + X_{uuu}\Delta u^3 + X_{vv}v^2 + X_{rr}r^2 + X_{vvu}v^2\Delta u + X_{rru}r^2\Delta u + X_{vr}vr + X_{vru}vr\Delta u + F_{xp} + (\text{inter. terms})$$

$$m\left(\dot{v} + ru + x_{cg}\dot{r}\right) = Y_0 + Y_{0u}\Delta u + Y_{0uu}\Delta u^2 + Y_{\dot{v}}\dot{v} + Y_v v + Y_{vvv}v^3 + Y_{\dot{r}}\dot{r} + Y_r r + Y_{rrr}r^3 + Y_{vrr}vr^2 + Y_{vu}v\Delta u + Y_{vuu}v\Delta u^2 + Y_{rvv}rv^2 + Y_{ru}r\Delta u + Y_{ruu}r\Delta u^2 + F_y + (\text{inter. terms}) \quad (2.1)$$

$$I_z\dot{r} + mx_{cg}\left(\dot{v} + ru\right) = N_0 + N_{0u}\Delta u + N_{0uu}\Delta u^2 + N_{\dot{v}}\dot{v} + N_v v + N_{\dot{r}}\dot{r} + N_r r + N_{vvv}v^3 + N_{vrr}vr^2 + N_{vu}v\Delta u + N_{vuu}v\Delta u^2 + N_{rrr}r^3 + N_{rvv}rv^2 + N_{ru}r\Delta u + N_{ruu}r\Delta u^2 + x_p F_y + M + (\text{inter. terms})$$

$$\left(\Delta u \equiv u - u_0\right)$$

where the first equation is for surge, the second for sway, and the third for yaw. The maneuvering coefficients (or derivatives) are defined in the standard way from Taylor series expansions of the hydrodynamic forces around prescribed operating points ($u = u_0$, $v = 0$, $r = 0$). Here, a 3rd order (nonlinear) expansion has been used (i.e. the "Abkowitz" form), although 2nd order nonlinear expansions have also commonly been used and found to be acceptable for many maneuvering simulation studies [27], [6], [38]. Note that many of the derivative terms which result from the Taylor series expansion are neglected in the model due to considerations of symmetry or homogeneity. Also note that the hydrodynamic coefficients as written here are for the "bare hull", with the terms specifically associated with the azimuthing propulsor accounting for vectored forces, in addition to interaction effects.

To complete the maneuvering model, along with the equations of motion, two sets of kinematic relations are required. Referring again to figure 2-4, one set of equations transforms from earth-fixed to vehicle-fixed coordinate frames, and can be referenced in a number of sources ([1] or [21] for example). This set of kinematic equations can be written in the form

$$\begin{aligned} \dot{x} &= u\cos(\psi) - v\sin(\psi) \\ \dot{y} &= u\sin(\psi) + v\cos(\psi) \\ \dot{\psi} &= r \end{aligned} \quad (2.2)$$

where u, v, and r are vehicle surge, sway and yaw velocities (respectively) in the vehicle-fixed frame, and x, y, and ψ are x and y position and yaw angle (respectively) in the earth-fixed frame. Another set of kinematic equations transforms the forces from the propulsor-fixed coordinate

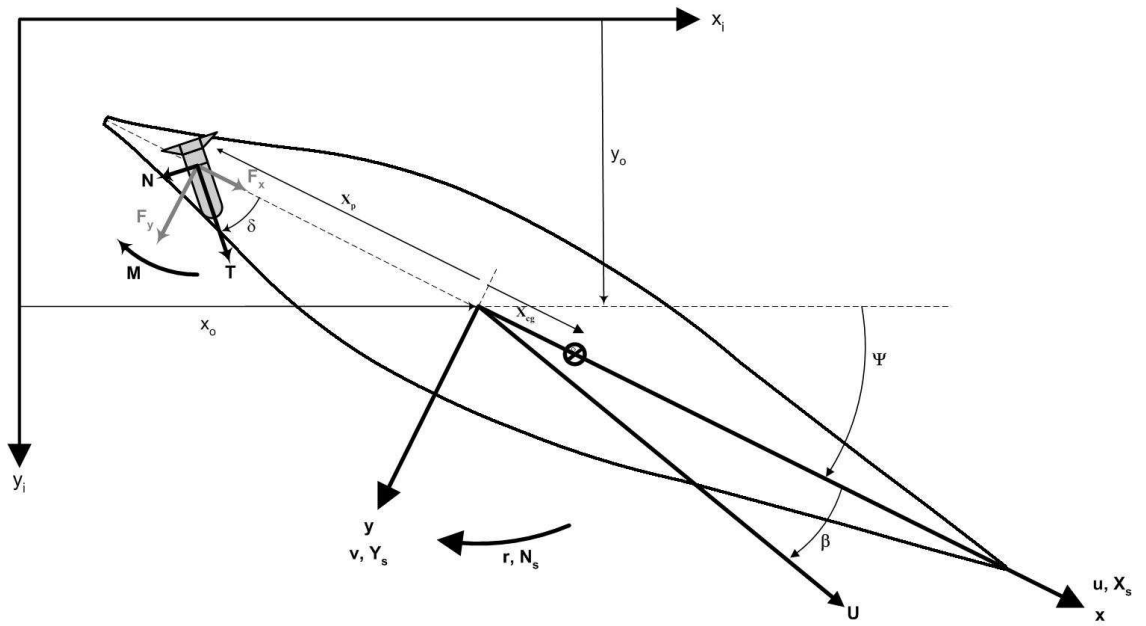

Figure 2-4: Maneuvering coordinate frames. Earth-fixed (inertial) and vehicle-fixed coordinate frames, forces, velocities and displacements for a surface vehicle with an azimuthing podded propulsor maneuvering in the horizontal plane.

frame to the vehicle-fixed coordinate frame, and can be written as

$$\begin{aligned} F_x &= T(n, V_e, \alpha)\cos\delta - N(n, V_e, \alpha)\sin\delta \\ F_y &= T(n, V_e, \alpha)\sin\delta + N(n, V_e, \alpha)\cos\delta \\ M &= M \end{aligned} \tag{2.3}$$

where the effective inflow velocity at the propulsor, V_e (in lieu of advance velocity V_a) can be written:

$$V_e = \left[u^2 + \left(v + x_p r\right)^2\right]^{1/2} \tag{2.4}$$

where x_p is the distance from the center of the vehicle reference frame to the center of the propulsor. The effective angle of inflow to the propulsor, α (in lieu of propulsor azimuth angle δ) can be written:

$$\alpha = \delta - \beta = \delta - \tan^{-1}\left(\frac{v + x_p r}{u}\right) \tag{2.5}$$

where β is the drift angle of the vehicle in the vehicle-fixed frame.

2.2.2 A model for the dynamics of an azimuthing propulsor driven by a DC motor

Referring to figure 2-3, the form of a simple equation relating motor dynamics to propeller torque (referred to as the motor torque equation) can be derived based upon fundamental principles of the torque dynamics of an electric motor. For a direct current permanent magnet motor, this can be written in a "standard" nonlinear form (see for example [17])

$$k_t i_m = I_m \dot{n} + B_m(n) + Q \tag{2.6}$$

where $k_t i_m$ (torque constant times motor current) is the motor torque, I_m is the mechanical "dry" rotary moment of inertia of the motor, shaft and propeller, and $B_m(n)$ is a general mechanical "dry" stick-slip friction associated with the motor, shaft and seal, and propeller. The latter can be written in a general quadratic form

$$B_m(n) = k_{f0}\,\mathrm{sign}(n) + k_{f1} n + k_{f2} n|n| \tag{2.7}$$

where the first term is a Coulomb friction, and the latter are dynamic friction terms.

The total propeller hydrodynamic torque Q in general includes both drag (quasi-steady) components and inertial (unsteady) components. One simple way to write this would be by analogy to the mechanical torque as

$$Q = I_a \dot{n} + Q_p \tag{2.8}$$

where the latter term, $Q_{p,}$ is the quasi-steady hydrodynamic torque which is mapped to the quasi-steady propeller states (propeller rate n, advance velocity V_a, and azimuth angle δ). The former term is an unsteady inertial term in analogy to the mechanical inertia, with I_a being a hydrodynamic (added) rotational inertia. However, since the hydrodynamic (added) inertia is related in general to fluid velocities (vice propeller rate), this term is not easily identifiable in terms of propeller rate n, and in fact can depend upon the additional propulsor state variables ($\dot{n}, \dot{V}, \dot{\delta}$, and $\ddot{\delta}$). In fact, the hydrodynamic added inertia coefficient as written here has no physical modeling basis, other than to equate it to some empirical mass of fluid that is accelerated with the propeller, which might be based upon a simplified momentum model.

As will be discussed in detail in Chapter 7, a physically-based model to represent the unsteady dynamics of hydrodynamic torque Q, as well as hydrodynamic thrust force T, normal force N, and steering moment M (i.e. the dynamics of Q(t), T(t), N(t), and M(t)), is via a dynamic inflow or wake time constant τ. The dynamic inflow time constant τ can be thought of fundamentally as representing the *lag* in the change in induced velocity at the propeller disk due to a change in the propeller operating state (n, V_a, δ), where the change in operating state translates to a change in the local blade angle of attack. This change in blade angle of attack in

turn translates to a change in blade forces, and therefore overall propeller forces. Thus, the dynamic inflow time constant τ could also be thought of as representing the time constant of the decay (or rise) in propeller blade forces from a sudden change in a propeller state. In either case, the basis for the use of a dynamic inflow time constant lies in the physical inertia of the vortex wake, and its corresponding effect on induced velocities at the propeller disk (see Chapter 7). Using the concept of a dynamic inflow time constant τ, the time-dependent propeller torque, thrust force, normal force and steering moment can be represented using the first order differential equations

$$\begin{aligned} Q(t) &\approx Q_p(n, V_a, \delta) + \tau \frac{dQ_p(n, V_a, \delta)}{dt} \\ T(t) &\approx T_p(n, V_a, \delta) + \tau \frac{dT_p(n, V_a, \delta)}{dt} \\ N(t) &\approx N_p(n, V_a, \delta) + \tau \frac{dN_p(n, V_a, \delta)}{dt} \\ M(t) &\approx M_p(n, V_a, \delta) + \tau \frac{dM_p(n, V_a, \delta)}{dt} \end{aligned} \tag{2.9}$$

where $Q_p(n,V_a,\delta)$, $T_p(n,V_a,\delta)$, $N_p(n,V_a,\delta)$ and $M_p(n,V_a,\delta)$ are the quasi-steady force mappings (i.e. from quasi-steady experiments), and the time constant τ is the dynamic inflow time constant. The argument for applying the same dynamic inflow time constant τ for all the propeller forces follows from development of the dynamic inflow theory presented in Chapter 7. The equations could be written in dimensionless form, so that the dynamic inflow time constant τ would be in terms of the propeller revolutions, as will be discussed in Chapter 7. Note that these are linearized relations, in that they are linearized about the current propulsor state (n, V_a, δ), and therefore are applied at each time t. It is acknowledged that this representation of unsteady propeller forces is different than some recent studies which have also considered unsteady thrust and torque dynamics for marine thrusters [34], [77], [5], [10]. In those studies, the unsteady propeller thrust (and torque in some cases) was considered based upon an empirical added mass or inertia which was modeled using a simplified unsteady momentum approach, but required measurement (or estimation) of the fluid velocities in the vicinity of the propeller disk. Although this approach using a dynamic inflow time constant and differential equations could also be approached from an empirical perspective (see Chapter 4), it is also based upon a fundamental model of the vortex wake and its interaction with the unsteady propeller states through induced velocity at the propeller disk (Chapter 7).

To recapitulate: referring again to figures 2-1, 2-3, and 2-4, the motor torque dynamic equation (2.6) is coupled to the full nonlinear vehicle dynamic equations (2.1) through the

propeller hydrodynamic forces and torques (Q(t), T(t), N(t), and M(t)). This coupling can be written in terms of a dynamic inflow time constant τ and the quasi-steady mappings using the first order dynamic representation equations (2.9).

The primary propulsor forces and torques investigated and discussed in this thesis are thrust force, normal force, propeller torque, and steering moment, all in the propulsor or propeller coordinate frame. These are based upon the "traditionally" reported propeller force characterizations. However, the characterizations of surge force (F_x) and sway force (F_y), as shown in figures 2-1 and 2-4, are also reported and discussed in order to provide a different perspective on maneuvering forces. All of the quasi-steady forces and torque mappings are parameterized to azimuth angle δ, as well as propeller rate n, and ambient or advance velocity V_a (or nondimensional advance coefficient $J = V_a/nD$).

Finally, note also that, although one simple dynamic equation (2.6) has been written here for the DC motor torque, more complex equations of the same basic form could be written for electric motors (or other prime-movers) with more complex dynamics, so long as the motor or engine dynamics remain coupled to the vehicle dynamics through the hydrodynamic forces and torques.

2.3 Summary

This chapter has provided a brief overview of the relevant dynamics associated with maneuvering with an azimuthing propulsor, and has provided some intuitive understanding for their application. Basic force effects associated with propellers operating in oblique inflow have been introduced, including the important concepts of vectored propeller forces leading to increased thrust and torque with propulsor azimuth. A combined dynamic maneuvering model for incorporating the fully coupled dynamics of a surface vehicle, propeller, and azimuthing propulsion motor has been introduced, also providing the relevant kinematics required to fully couple the dynamics. A new model for the dynamics of an azimuthing propulsor driven by a DC motor has been introduced, with nonlinear equations for the torque dynamics including important inertia and stick-slip dynamic friction effects. Finally, a new concept for unsteady propeller hydrodynamics has been introduced, using a "dynamic inflow" time constant (a wake time constant) for modeling the unsteady hydrodynamic thrust, torque, normal force, and steering moment of importance to the maneuvering of smaller vehicles. All of the dynamic models are used subsequently in the further analysis of the dynamics of the azimuthing podded propulsor.

This page left blank

Chapter 3

An autonomous surface test vehicle and dynamically-azimuthed propulsor system

In order to investigate the combined maneuvering dynamics of a vehicle propelled by a dynamically-azimuthed podded propulsor, as in the dynamic models presented in Chapter 2, a 12 foot autonomous surface vehicle propelled with a single dynamically-azimuthed podded propulsor was designed and constructed. The autonomous surface vehicle is of a modular design, so that the various components could be separated and tested as subsystems. Figure 3-1 provides several photographic views of the vehicle and components.

3.1 Vehicle and azimuthing propulsor system

The test vehicle was designed and built on a modified 12'2" fiberglass kayak hull (the Chesapeake Pro® model by Wilderness Systems®). The kayak hull was modified by laminating a 2.5" x 2.5" fiberglass T-hat keelson (with 2" x 2" solid oak wood core), 2 full ¾" watertight laminated fiberglass/wood bulkheads, ballast bins, and a removable ¾" wood deck plate for installation of electrical and electronic equipment. A laminated fiberglass/wood motor foundation structure with integrated shaft bearing tube and through-hull penetration for the azimuthing propulsor was also added. The integrated shaft bearing tube is used in conjunction with an integral lower PVC bearing and a removable upper Rulon bearing.

The vehicle is controlled by an onboard computer, either autonomously or remotely-controlled using a shore-based PC. The onboard Pentium-based PC104 computer system (which includes data acquisition and control I/O and Ethernet cards) provides serial and analog data acquisition and control capability, with interface to the shore-based "host" laptop PC through a wireless Ethernet bridge (Linksys® model WET11). Data acquisition and control functions utilize the xPC Target® software package (Mathworks, Inc.).

The propulsor itself is a modified trolling motor (Motorguide® model ET54 with 3-bladed Machete II aluminum propeller). The trolling motor has been modified for accurate closed-loop speed control by adding a Hall-effect latching magnetic sensor, epoxied and attached on the aft face of the propulsor, inside the propeller well. The Hall-effect sensor is an Allegro®

Microsystems model UGN-3175U with added pull-up resistor. Eight magnets of alternating pole, evenly spaced and epoxied within the propeller hub, provide alternating magnetic flux for the Hall-effect sensor. The latching Hall-effect sensor produces a clean square wave voltage output, which is used as an input signal to the onboard computer for calculating propeller rotation rate. The overall propulsor is 13 inches in length and 3.625 inches in diameter, with the open-bladed fixed-pitch propeller being 9.875 inches in diameter. Figure 3-2 provides the geometry and dimensions of the dynamically-azimuthed podded propulsor. Table 3-1 provides the measured propeller blade geometry (non-dimensional as required for input to the propeller analysis code MPUF-3A). Note that the propeller is left-handed, but the geometry is given as right-handed, as required for input into MPUF-3A.

The propulsor is dynamically-azimuthed by a Pittman® model GM9234S031 servo gearmotor, with a mechanically-connected Vishay-Spectrol® model 601-1045 360° Smart Position Sensor, which provides an analog output voltage proportional to angle, enabling closed-loop dynamic azimuth control. Both motors are permanent magnet DC and are controlled using PWM brush servo amplifiers in the torque (current) control mode. The propulsion motor is controlled using an Advanced Motion Controls® model 50A8 brush-type PWM servo amplifier, while the gearmotor is controlled using a Copley Controls® model 413 brush-type PWM servo amplifier. An F.W. Bell® model IHA-100 Hall-effect current sensor provides accurate propulsion motor current measurement. The system is powered either by (2) gel-type 12 volt batteries (in series) for autonomous operation, or a 24 volt DC power supply for non-autonomous or semi-autonomous testing.

3.2 Planar motion mechanism testing and determination of nonlinear vehicle maneuvering coefficients

In order to investigate the combined maneuvering dynamics of a vehicle propelled by a dynamically-azimuthed podded propulsor, as in the dynamic models presented in Chapter 2, the "bare-hull" maneuvering coefficients of the vehicle were experimentally identified using a Planar Motion Mechanism (PMM) technique. The PMM used was the system installed in the large 280'x26'x16' towing tank at the U.S. Naval Academy. For documentary purposes, table 3-2 provides a summary of the results for the maneuvering coefficients of equation (2.1) for the autonomous surface test vehicle. Note that maneuvering coefficients are presented in non-dimensional form, as defined in a number of references on maneuvering dynamics [1], [2], [15], [21].

Figure 3-1: Autonomous surface test vehicle with dynamically-azimuthed podded propulsor system.

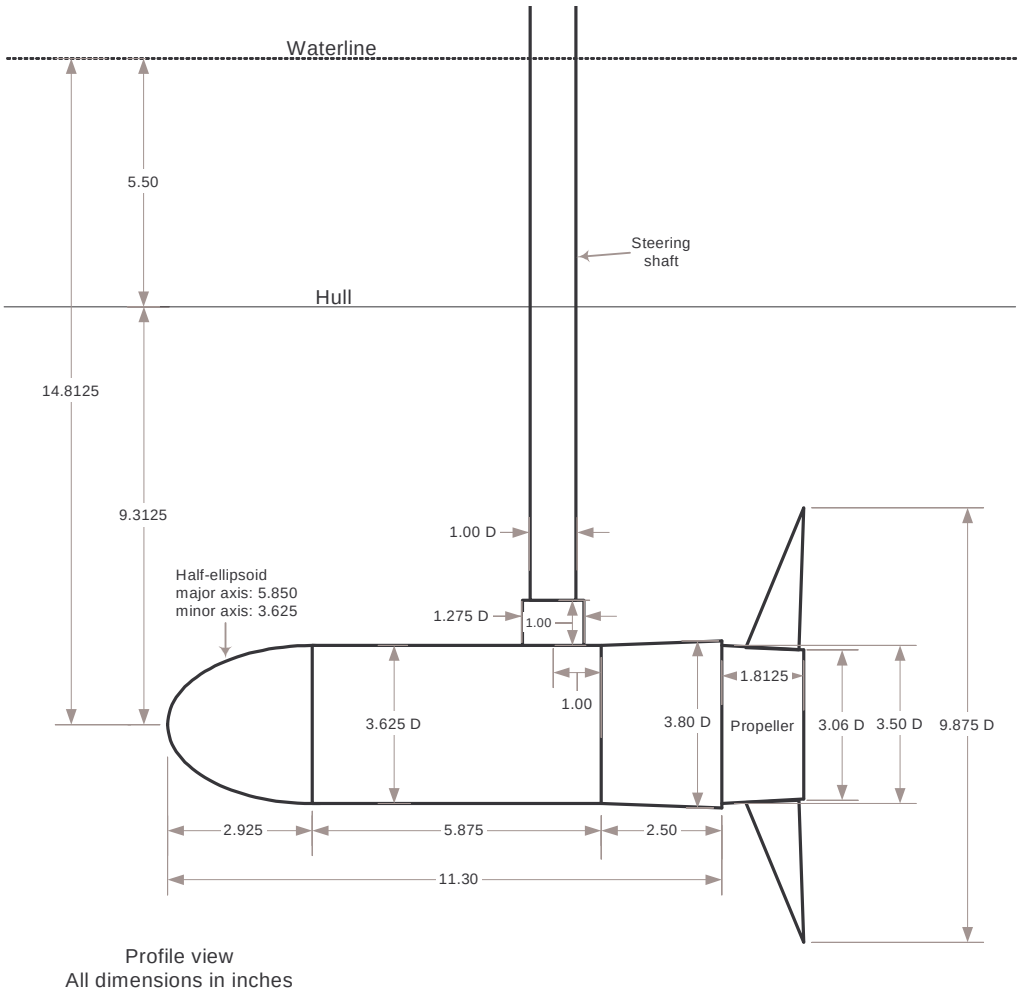

Figure 3-2: Geometry and dimensions of the dynamically-azimuthed podded propulsor.

Table 3-1: Blade geometry of Motorguide® Machete II propeller (MPUF-3A input geometry). Note that propeller is left-handed, but geometry is provided as right-handed. D is propeller diameter (9.875 inches).

Radii (r/R)	Pitch angle (β(r)) (deg)	Rake/diam. (x_m(r)/D)	Skew angle (θ_m(r)) (deg)	Chord/diam. (c(r)/D)	Max camber/chord (f_{max}(r)/c(r))	Max thickness/diam. (t_{max}(r)/D)
0.36	18.37	0.0275	-16.44	0.3386	0.0220	0.0234
0.44	17.20	0.0397	-6.19	0.3261	0.0220	0.0234
0.52	15.84	0.0515	1.31	0.3100	0.0220	0.0233
0.60	14.34	0.0629	7.20	0.2894	0.0219	0.0230
0.68	12.68	0.0740	11.90	0.2628	0.0215	0.0221
0.76	10.92	0.0846	15.91	0.2305	0.0201	0.0199
0.84	9.04	0.0949	19.45	0.1906	0.0138	0.0155
0.92	7.06	0.1047	22.96	0.1343	0.0044	0.0088
0.96	6.04	0.1094	24.93	0.0935	0.0014	0.0050
1.00	5.00	0.1140	28.00	0.0000	0.0000	0.0000

Table 3-2: Non-dimensional maneuvering coefficients for the autonomous surface test vehicle based on results of PMM testing. Results are provided for the bare hull at two test ("design") velocities.

X-equation non-dimensional coefficient	Value ($x10^{-5}$)		Y-equation non-dimensional coefficient	Value ($x10^{-5}$)		N-equation non-dimensional coefficient	Value ($x10^{-5}$)	
	U_d 2.62 ft/s	U_d 5.24 ft/s		U_d 2.62 ft/s	U_d 5.24 ft/s		U_d 2.62 ft/s	U_d 5.24 ft/s
$(X'_{\dot{u}} - m')$	-646.9		$(Y'_{\dot{v}} - m')$	-864.5	-939.0	$(N'_{\dot{r}} - I'_z)$	-62.21	-55.08
X'_0	-64.40	-65.01	Y'_0	2.787	3.216	N'_0	-3.056	-6.813
X'_u	-114.9	-167.3	Y'_{0u}	6.419	6.836	N'_{0u}	-13.63	-17.38
X'_{uu}	-42.28	-178.1	Y'_{0uu}	3.492	3.590	N'_{0uu}	-10.56	-10.57
X'_{uuu}	7.056	-80.78	$Y'_{\dot{r}}$	-12.56	-13.17	$N'_{\dot{v}}$	8.171	16.85
$(X'_{vr} + m')$	110.5 98.61	75.84 93.65	$(Y'_r - m'u')$	-434.0	-381.6	N'_v	-283.6	-308.8
X'_{vv}	-58.41	-268.7	Y'_{rrr}	-100.36	-156.8	N'_{vvv}	-1925	-3857
X'_{rr}	-41.78	-101.58	Y'_v	-97.35	-124.6	N'_r	-176.0	-219.9
X'_{vvu}	-496.4		Y'_{vvv}	-31.59	-39.94	N'_{rrr}	-229.2	-442.0
X'_{rru}	-79.74		Y'_{vvr}	-2892	-3704	N'_{vvr}	-774.2	-1666
X'_{vru}	117.2		Y'_{vrr}	-3384	-4580	N'_{vrr}	-9134	-14820
			Y'_{vu}	-1136	-2140	N'_{vu}	-524.8	-900.5
			Y'_{vuu}	-560.5	-1332	N'_{vuu}	-182.1	-697.1
			Y'_{ru}	-690.1	-543.5	N'_{ru}	-317.9	-607.0
			Y'_{ruu}	-174.0	-111.4	N'_{ruu}	-148.5	-561.8

This page left blank

Chapter 4

Experimental measurement of steady and unsteady maneuvering forces

Quasi-steady and unsteady/transient force testing of the azimuthing propulsor was conducted using two configurations. First, the modular components of the dynamically-azimuthed propulsor system were installed into a test fixture including a dynamometer and attached to the MIT towing tank (figure 4-1). Second, the entire autonomous surface test vehicle with the dynamically-azimuthed propulsor system was installed and tested on the Planar Motion Mechanism (PMM) at the U.S. Naval Academy (figure 4-2). In both configurations, quasi-steady force measurements were made over the entire desired range of quasi-steady operating conditions. In the former, a number of unsteady/transient force tests and measurements were also completed. These tests and a comprehensive presentation of results are discussed in this chapter. In addition to the integrated propulsor testing, several tests were conducted specifically to identify the necessary propulsion motor, friction, and inertia terms discussed in Section 2.2.2.

Unless otherwise noted, all time sequences in plots labeled as "filtered" are computed from the unfiltered sequence using a sharp cutoff 6^{th} order Type II Chebyshev digital filter designed for the stated cutoff frequency. The filtering is applied using a dual-direction filtering algorithm, resulting in a filtered sequence of precisely zero phase-shift and twice the filter order.

4.1 Experimental setup

Testing in the MIT towing tank was conducted utilizing a test fixture incorporating an AMTI® model MC6 six axis load cell and amplifier (figure 4-1). Both propulsor and servo gearmotor were founded within a structure attached below the load cell. The propulsor was dynamically-azimuthed in the horizontal plane with Rulon shaft bearings though a hydrodynamic strut. Because of the large moment arm, the load cell output was calibrated daily in place. Data acquisition and control utilized the modular components of the autonomous surface vehicle, with a sampling rate of 1000 Hz.

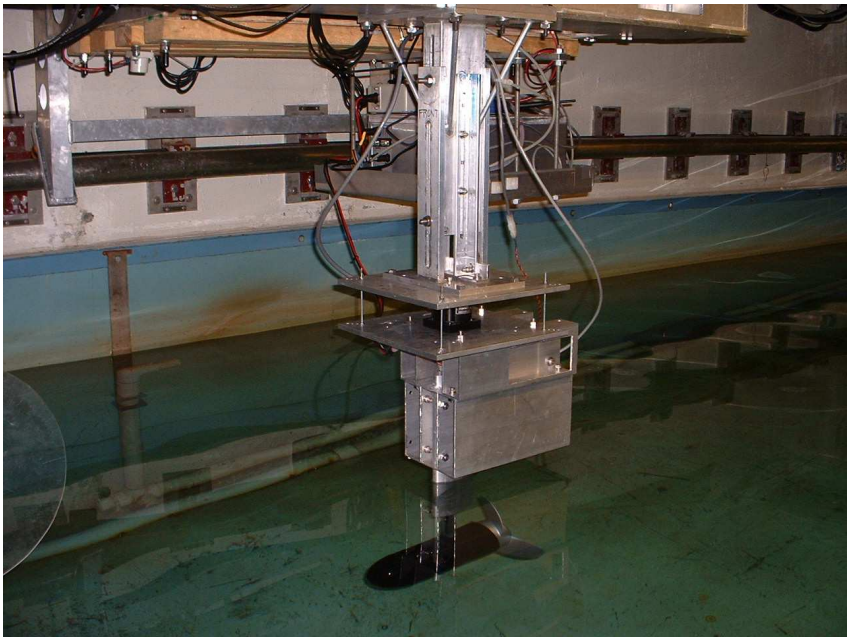

Figure 4-1: Dynamically-azimuthed propulsor system in test fixture in the MIT towing tank.

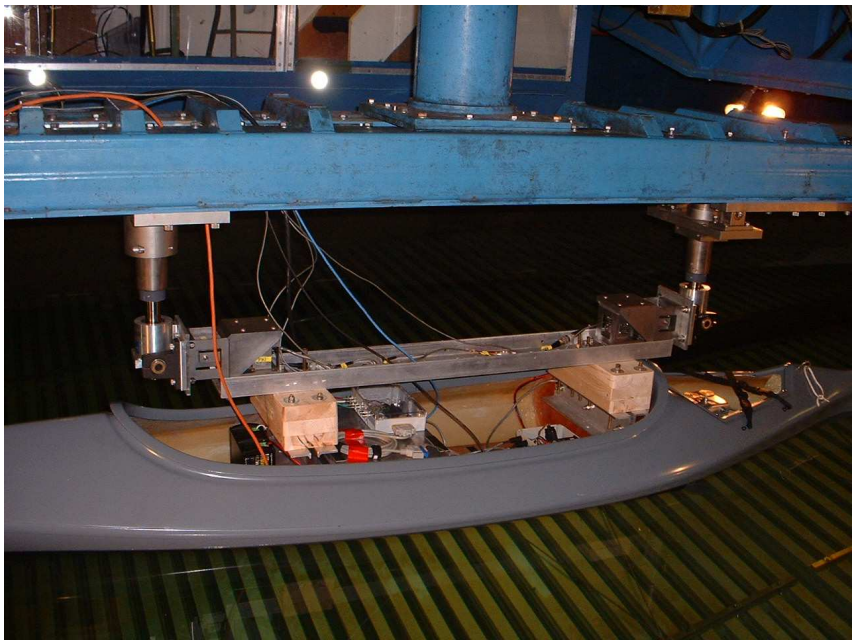

Figure 4-2: Autonomous surface test vehicle with dynamically-azimuthed propulsor on Planar Motion Mechanism (PMM) at the U.S. Naval Academy.

Testing of the quasi-steady maneuvering forces of the propulsor was also conducted on the PMM in the large towing tank at the U.S. Naval Academy using the entire autonomous surface test vehicle (figure 4-2). The vehicle was attached to the carriage via (4) 50 pound variable-reluctance modular block force gauges manufactured by Hydronautics, Inc. Force gauges were

calibrated on a special calibration stand with their corresponding amplifiers. Data acquisition and control utilized the modular components of the autonomous surface vehicle, with a sampling rate of 1000 Hz. Propulsor forces were determined from the measurements by deducting the contribution of the bare hull. Note that because of the very large separation between the hull and the propeller (by design as shown in Chapter 3), the hull wake and boundary layer are well outside the propeller slipstream and the interaction effects as discussed in Section 2.2.1 are considered minimal, and are mainly captured by this method using the bare hull deduction.

4.2 Experimental identification of propulsor motor torque and friction characteristics and mechanical "dry" rotational inertia

Since it was impractical to install a propeller torque load cell in the small propulsor, the propeller hydrodynamic torque was calculated from accurate motor current measurement, based upon the motor torque equation (2.6), by first experimentally identifying the motor torque constant, mechanical "dry" friction coefficients and mechanical "dry" rotational inertia discussed in Section 2.2.2.

Determination of the motor torque constant is discussed in a number of references, for example [17]. The torque constant for the propulsion motor was determined by driving the propeller with another motor, measuring rotation speed, and measuring the voltage generated across the motor terminals (the back EMF voltage). The slope of the linear curve fit of shaft speed vs. measured voltage provides the voltage (or speed) constant K_{EMF} (figure 4-3). By SI unit equivalence, K_t (in N-m/A) is equivalent to K_{EMF} (in V-s/rad). Referring to equations (2.6) and (2.7), the mechanical "dry" friction coefficients and mechanical "dry" rotational inertia were determined by performing a series of step current input tests in air, where propeller hydrodynamic torque is negligible (note: the shaft seals were maintained wet to maintain lubrication). The plot of steady-state propeller speed vs. input torque ($k_t i_m$) was fit with a quadratic to determine the coefficients of $B_m(n)$ (figure 4-4). These experiments were checked for repeatability and consistency over several months.

The mechanical "dry" rotary inertia coefficient (I_m) was determined using current input step testing (to be discussed in detail in Section 4.4), but conducted in air, where the hydrodynamic torque Q on the propeller could be considered negligible. The coefficient was determined by averaging the results of 10 current input step tests over a range of input current step magnitudes. Results provide a mechanical "dry" inertia for the motor, shaft, and propeller of

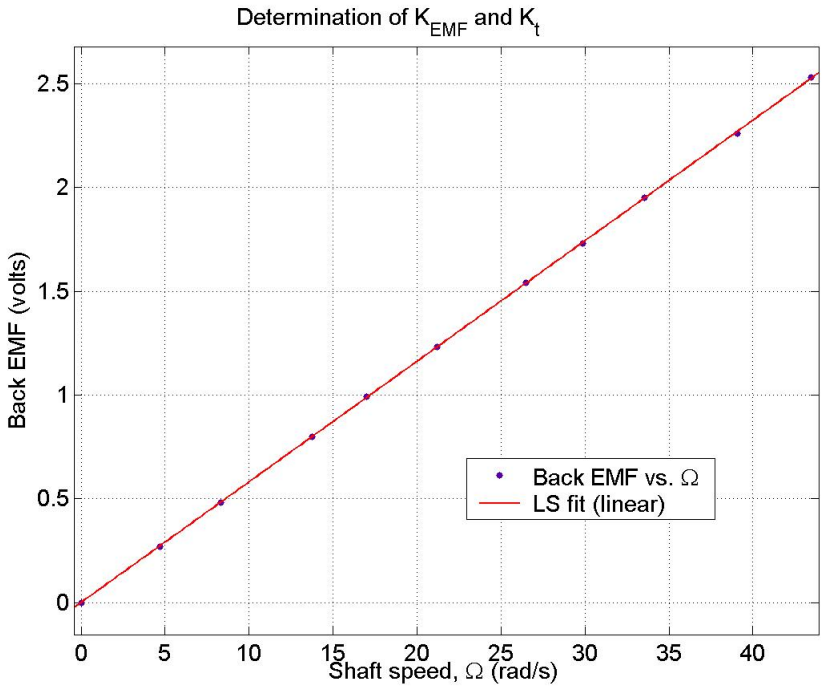

Figure 4-3: Determination of propulsion motor torque constant by linear fit and SI unit equivalence of DC motor torque and speed constants.

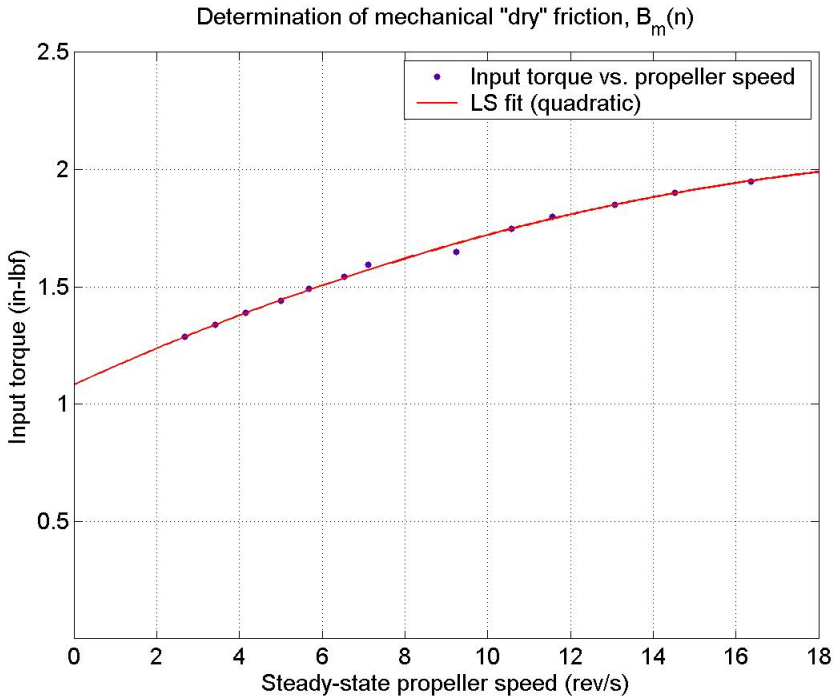

Figure 4-4: Determination of propulsor mechanical “dry” friction coefficients by quadratic fit of steady-state response to step current inputs in air.

$$I_m = 0.0184 \pm 0.0007\,(\text{in - lb}_f\text{ - s}^2\text{ / rad}) = 0.116 \pm 0.004\,(\text{in - lb}_f\text{ - s}^2\text{ / rev})$$

or non-dimensionally

$$I_m' = \frac{I_m}{\rho D^5} = 0.0252 \pm 0.0011\,(/\text{ rad}) = 0.158 \pm 0.007\,(/\text{rev})$$

where the density of *fresh water* at 68°F is used as the normalizing density (to be consistent with hydrodynamic tests), $\rho = 1.9367\ lb_f\text{-}s^2/ft^4$.

4.3 Quasi-steady propulsor force measurements and results

The quasi-steady thrust, torque, normal force, and steering moment were determined (mapped) by running the propulsor at a range of advance coefficients, $J = V_a/nD$ (by systematically varying propeller speed and carriage velocity), and the entire range of azimuth angles. The hydrodynamic torque was calculated using equations (2.6) and (2.7) from the measured current, along with the identified motor torque constant and mechanical friction terms. The thrust, normal force, and steering moment were taken from the load cell output, applying a transformation from the load cell (towing tank) coordinate system to the propulsor coordinate system (see figure 4-5):

$$\left.\begin{aligned} F_x &= (T\cos\delta - N\sin\delta) \\ F_y &= (T\sin\delta + N\cos\delta) \end{aligned}\right\} \rightarrow \begin{Bmatrix} T \\ N \end{Bmatrix} = \begin{bmatrix} \cos\delta & -\sin\delta \\ \sin\delta & \cos\delta \end{bmatrix}^{-1} \begin{Bmatrix} F_x \\ F_y \end{Bmatrix} \tag{4.1}$$

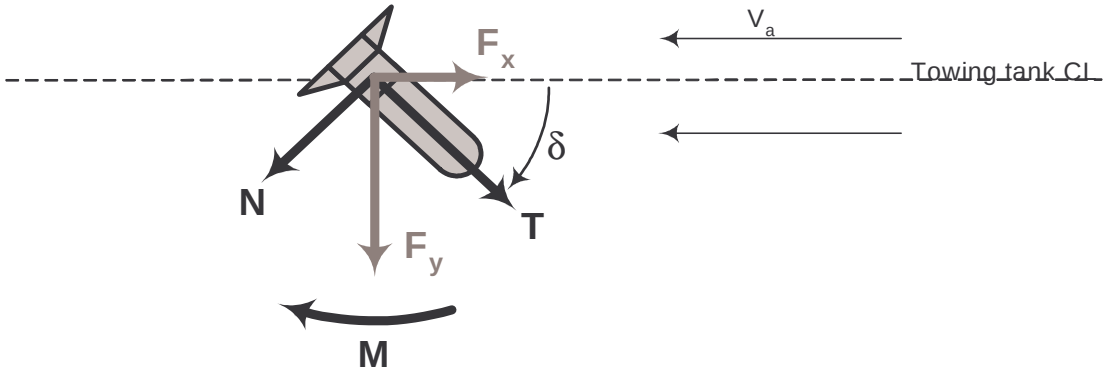

Figure 4-5: Vectored propulsor forces for towing tank and PMM testing.

The mapped forces were obtained by truncation and averaging of the force data within the steady-state portion of each run. For azimuth angles greater than 90 degrees, where an unsteady

reversing wake was encountered (due to the propulsor "driving into its own wake"), a Fourier-averaging technique was used to average the quasi-steady forces (i.e. using the 0^{th} Fourier harmonic). This will be discussed in more detail subsequently.

Figures 4-6 and 4-7 show the results for values of J up to 0.6 and azimuth angles δ to $\pm 90°$. The surface plots are mesh plots developed using bicubic interpolation of data points, which are also shown. The smooth but nonlinear nature is clearly evident. The plots show clearly the nature of vectored propulsion with regards to an azimuthing propulsor as discussed in Chapter 2 for the generic case of a propeller in oblique flow. The results for zero azimuth angle ($\delta = 0°$) are the "standard" thrust-torque-speed curves shown in figure 2-2.

Figure 4-8 shows thrust and torque for the entire range of azimuth angles (δ to $\pm 180°$). Despite the apparent "scatter" for larger angles ($\delta > \pm 90°$), there are also clearly regular nonlinear features associated with the changing wake character. Note that thrust is taken from the force load cell, while torque is calculated from the motor current (i.e. there is no sensor correlation), yet the nonlinear character of the two plots is very similar, including locations of maxima and minima. Thus, the basic features of both thrust and torque plots over most of the parameter space, as shown in figure 4-8, are real quasi-steady force effects (i.e. not load cell measurement irregularity or data scatter).

The apparent "scatter" in figure 4-8 at larger angles ($\delta > \pm 90°$) for smaller advance velocities is due to the highly unsteady nature of the reversing wake, and the resulting difficulty in calculating the 0^{th} Fourier harmonic from the *necessarily* truncated unsteady, quasi-periodic force data for each test run. Figure 4-9 shows a sample force record for a typical "crashback" condition or reversing wake, illustrating the quasi-periodic nature of the wake. It can also be seen from figure 4-8 that for larger angles, as velocity is increased, the Fourier averaging results in a much smoother plot of the quasi-steady force components. This is because, at higher advance velocities, the unsteady wake becomes even more regularly quasi-periodic, and therefore the Fourier averaging technique is more successful, since there is a more dominant period about which to truncate the data. This increase in periodicity with increase in carriage speed was visually observed during the testing. As the carriage speed was increased, stronger vortex shedding from the reversing ("crashback") unsteady wake was observed.

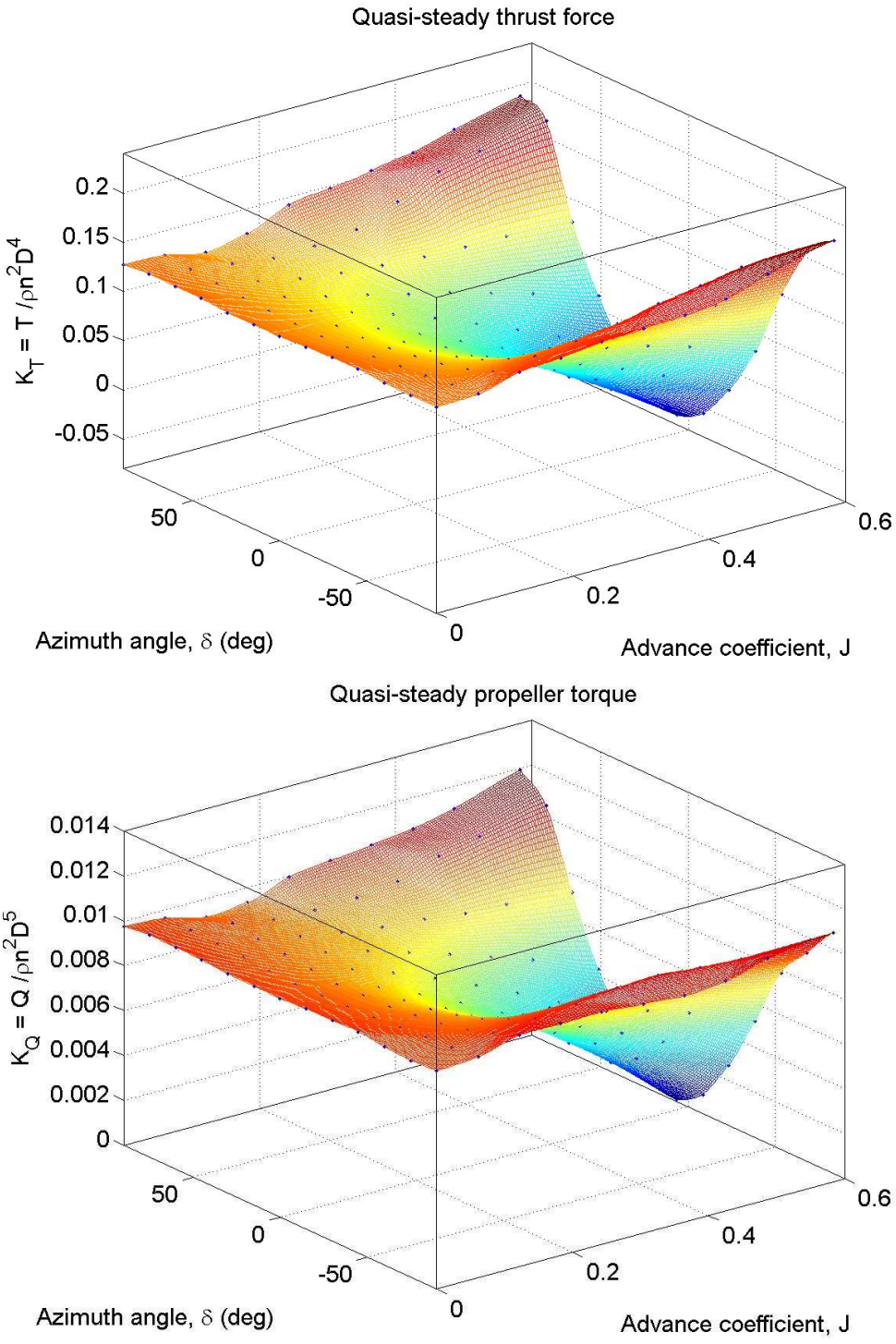

Figure 4-6: Surface plots of quasi-steady thrust force and torque (δ to $\pm$ 90°). Data points shown, surface plot is bicubic interpolation of data points.

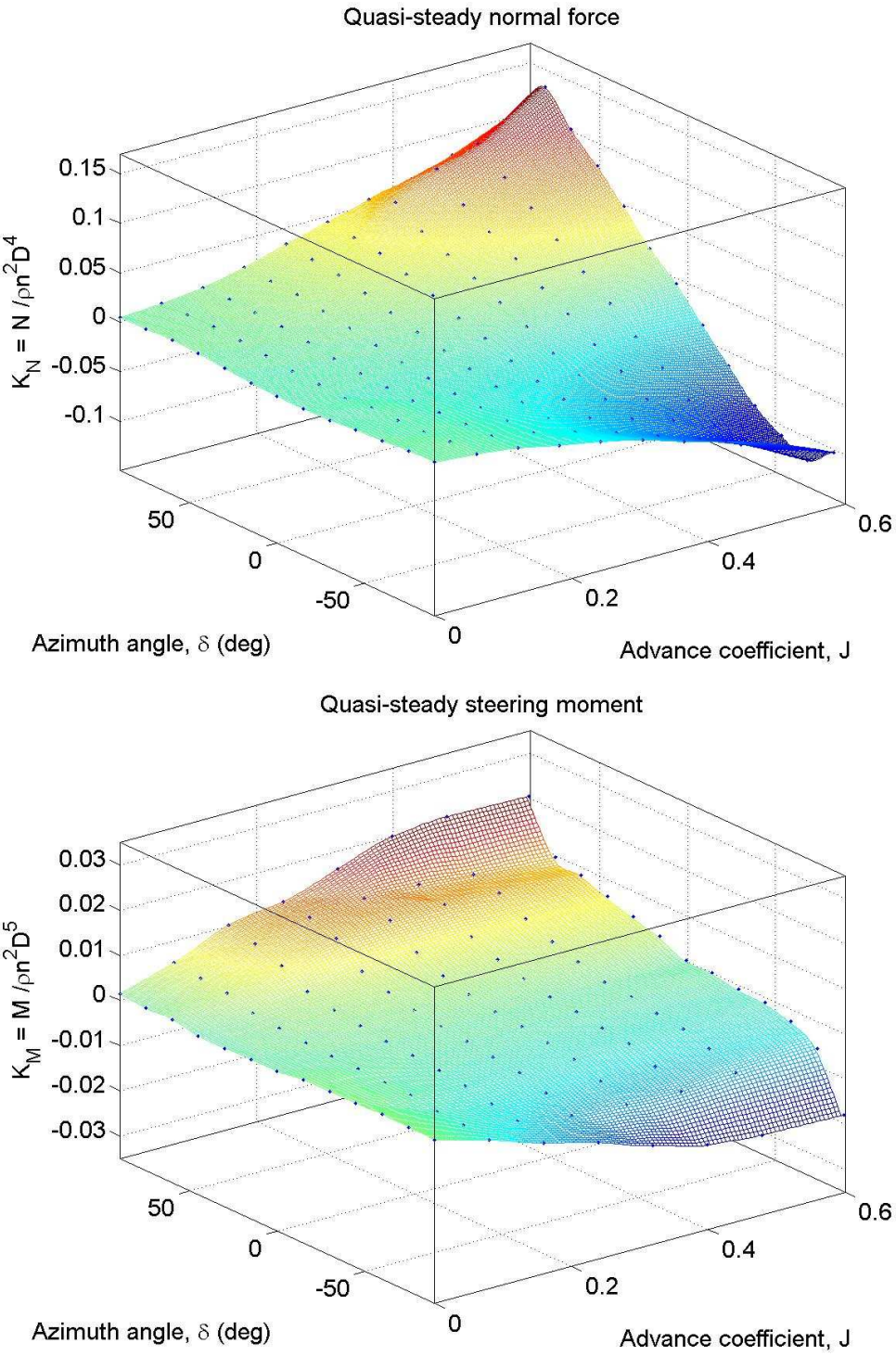

Figure 4-7: Surface plots of quasi-steady normal force and steering moment (δ to ± 90°). Data points shown, surface plot is bicubic interpolation of data points.

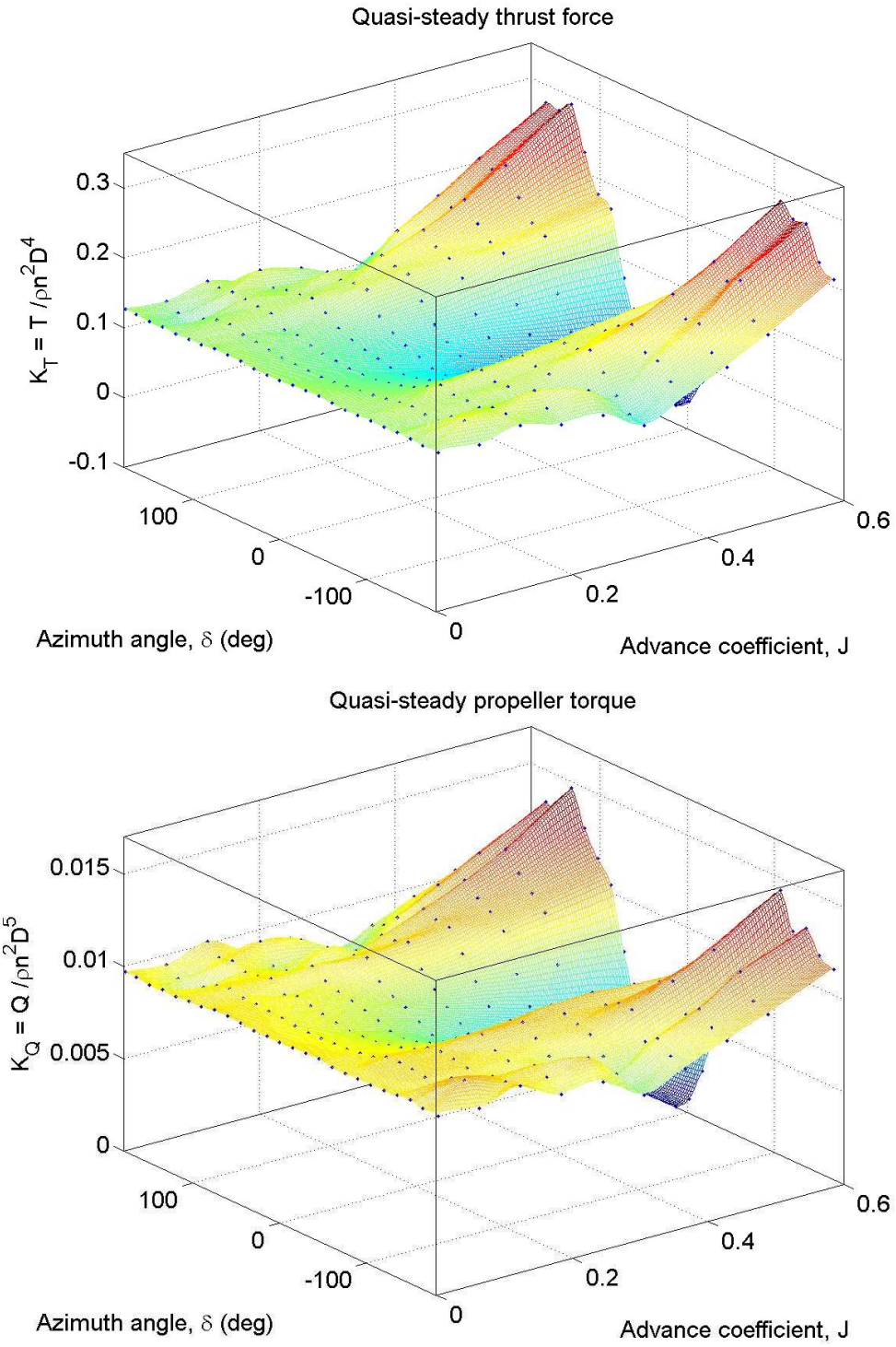

Figure 4-8: Surface plots of quasi-steady thrust and torque (δ to ± 180°). Data points shown, surface plot is bicubic interpolation of data points.

Figures 4-10 and 4-11 provide a different presentation of the quasi-steady results in the form of contour plots for each of the tested advance coefficients, providing a more detailed view of the data. Note the small asymmetry in the force data (particularly noticeable in terms of locations and magnitudes of maxima and inflection points between 0 and ±90°). These force asymmetries are due to the influence of the pod housing and strut in front of the propeller, and the effect of the direction of propeller rotation (here a left-handed propeller). Specifically, the strut or steering shaft, being in front of the propeller, causes a blockage of the flow into the propeller across the top of the pod, and results in an induced swirl around the pod housing and into the propeller, in *addition* to the swirl induced by the normal propeller rotation. This additional induced swirl causes an asymmetric swirl inflow into the propeller (i.e. for a positive propulsor rotation angle, it *increases* the normal counter-clockwise inflow swirl to the propeller, and for a negative propulsor angle, it *decreases* the normal counter-clockwise inflow swirl to the propeller). The net result is decreased angle of attack at the blades for positive propulsor rotation (decreased lift and lift-induced drag) and increased angle of attack at the blades for negative propulsor rotation (increased lift and lift-induced drag). This type of force asymmetry for "pusher" type pods and thrusters was noted in [61], and more recently in [35] and [30], but the causal effects not detailed. This asymmetry will be illustrated again in Chapter 6.

While the presentation of force data in terms of thrust and normal force (i.e. in the coordinate system of the propulsor) is more "traditional", it is perhaps more instructive in terms of maneuvering performance to present the forces in the coordinate system of the towing tank. This is similar to the forces in the coordinate system of a vehicle in which the propulsor would be installed (with the modification that the actual inflow velocity and angle of attack seen by the propulsor in the vehicle would need to be corrected for the effects of the vehicle's velocities, yaw rate, propulsor location, and wake fraction, equations (2.3) through (2.5)). Nevertheless, the forces in the coordinate system of the towing tank have been termed surge force (F_x) and sway force (F_y), to be consistent with the vehicle force terminology. Figure 4-12 shows surge force and sway force in the form of surface data mesh plots over the entire range of azimuth angles (±180°). Again, the smooth but nonlinear nature is evident. The very intuitive variation of surge force (as $\cos\delta$) and sway force (as $\sin\delta$) in the limit at $J = 0$ is obvious. As an aside, it is also interesting to note the sudden drop in surge force F_x at ±150°-180° (an increase in the negative F_x) at $J \approx 0.3$; this is the infamous "vortex ring state" [51], well known to the helicopter community for causing sudden drops in rotor thrust, with particularly dire consequences in terms of loss of flight control for the VTOL aircraft. Figure 4-13 presents F_x and F_y in the form of contour plots for each of the tested advance coefficients. It is very interesting to note the trends of both F_x and F_y in the

moderate range of azimuth angles (say up to ±45°), and in the range of a typical vehicle design advance coefficient for this propeller ($J \approx 0.36$ for the MIT vehicle). As shown in figure 4-14, in this range, F_x is nearly linear (and almost constant), and F_y is nearly linear. The implications of this in terms of vehicle maneuvering and control are significant, in that there is a strong possibility for linearization, even decoupling, in the surge-sway-yaw vehicle maneuvering control problem.

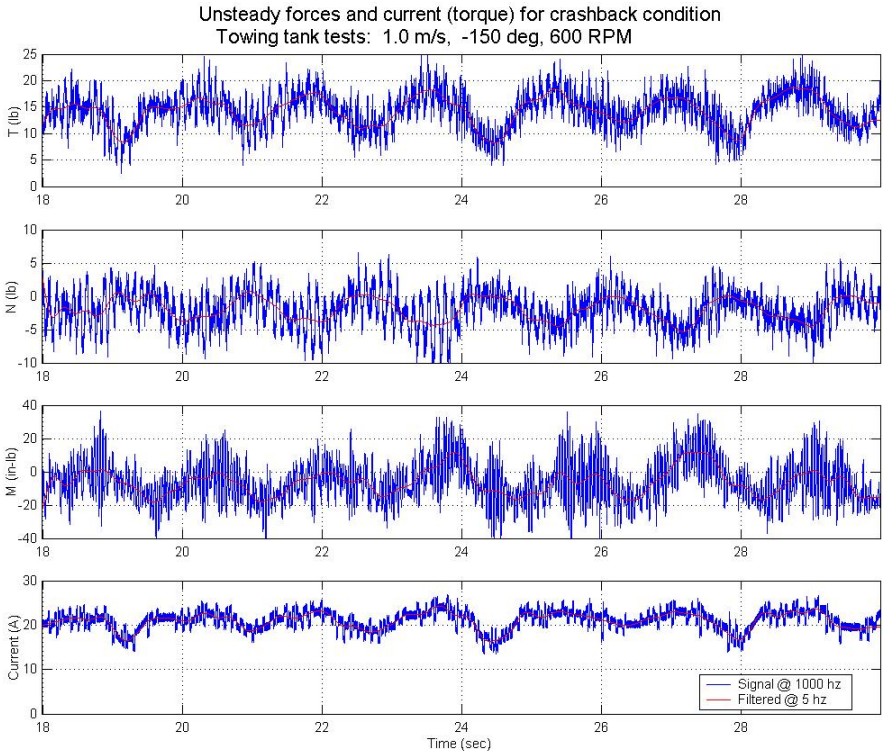

Figure 4-9: Example force and current records for a "crashback" condition (advance coefficient $J = 0.4$, azimuth angle $\delta = -150°$). Note quasi-periodic nature of force and current records. Mean value determined by truncation and Fourier averaging.

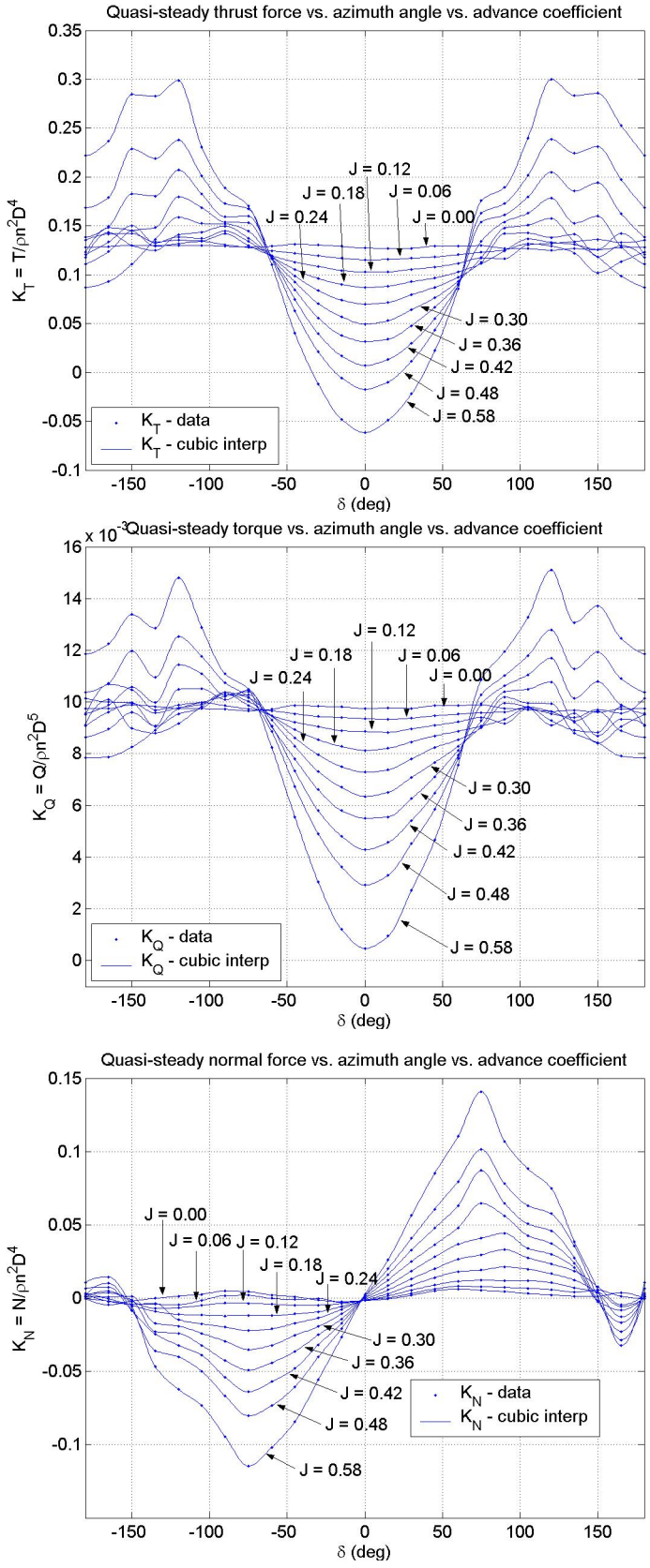

Figure 4-10: Contour plots of quasi-steady thrust force, torque, and normal force (δ to ±180°).

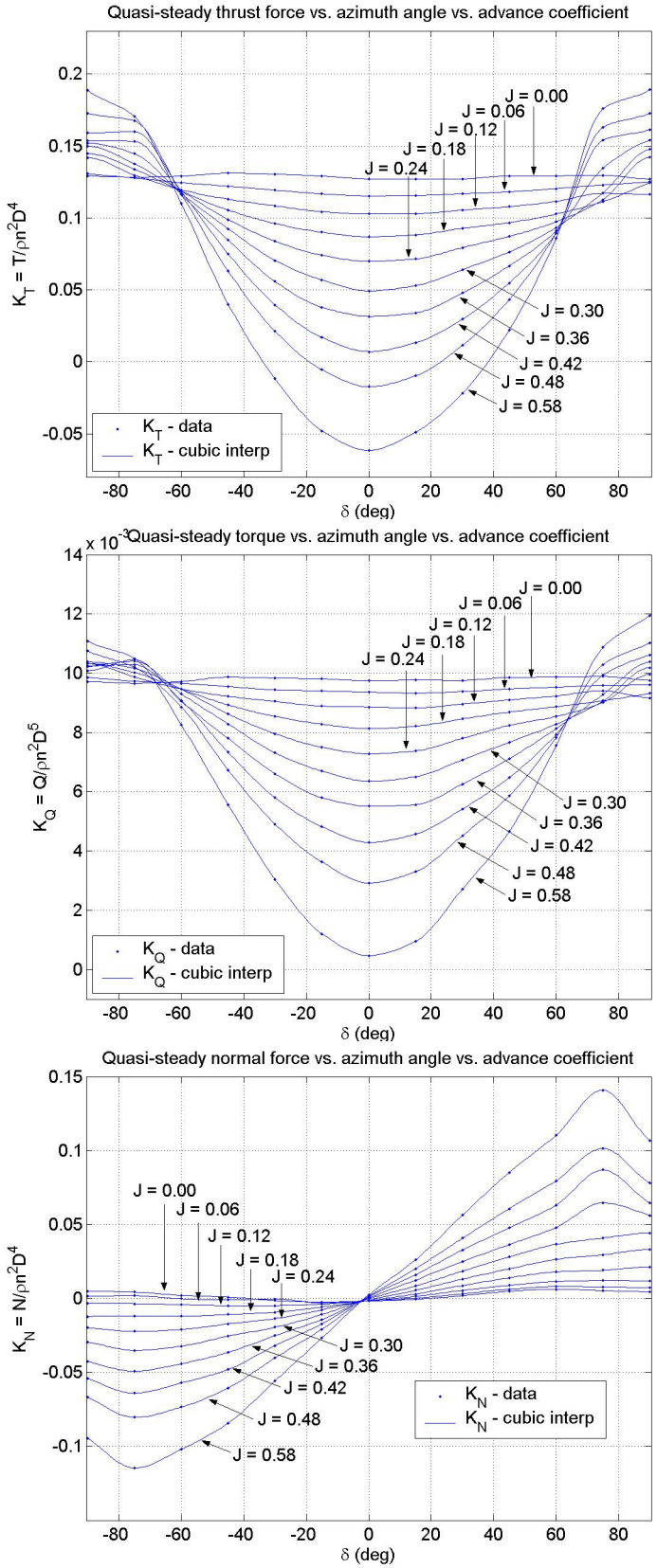

Figure 4-11: Contour plots of quasi-steady thrust force, torque, and normal force (δ to ±90°).

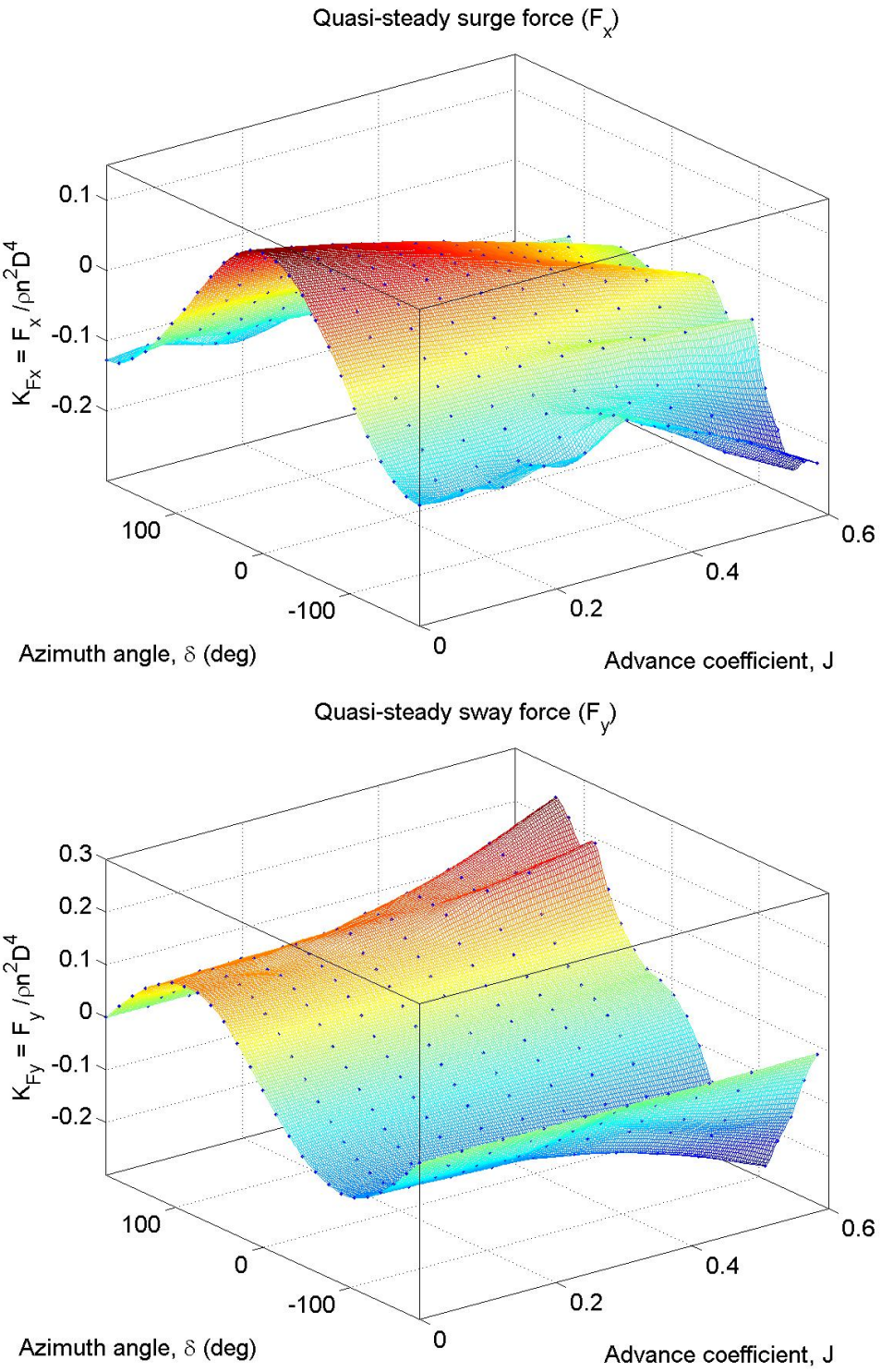

Figure 4-12: Surface plots of quasi-steady surge force (F_x), sway force (F_y) (δ to $\pm$ 180°).

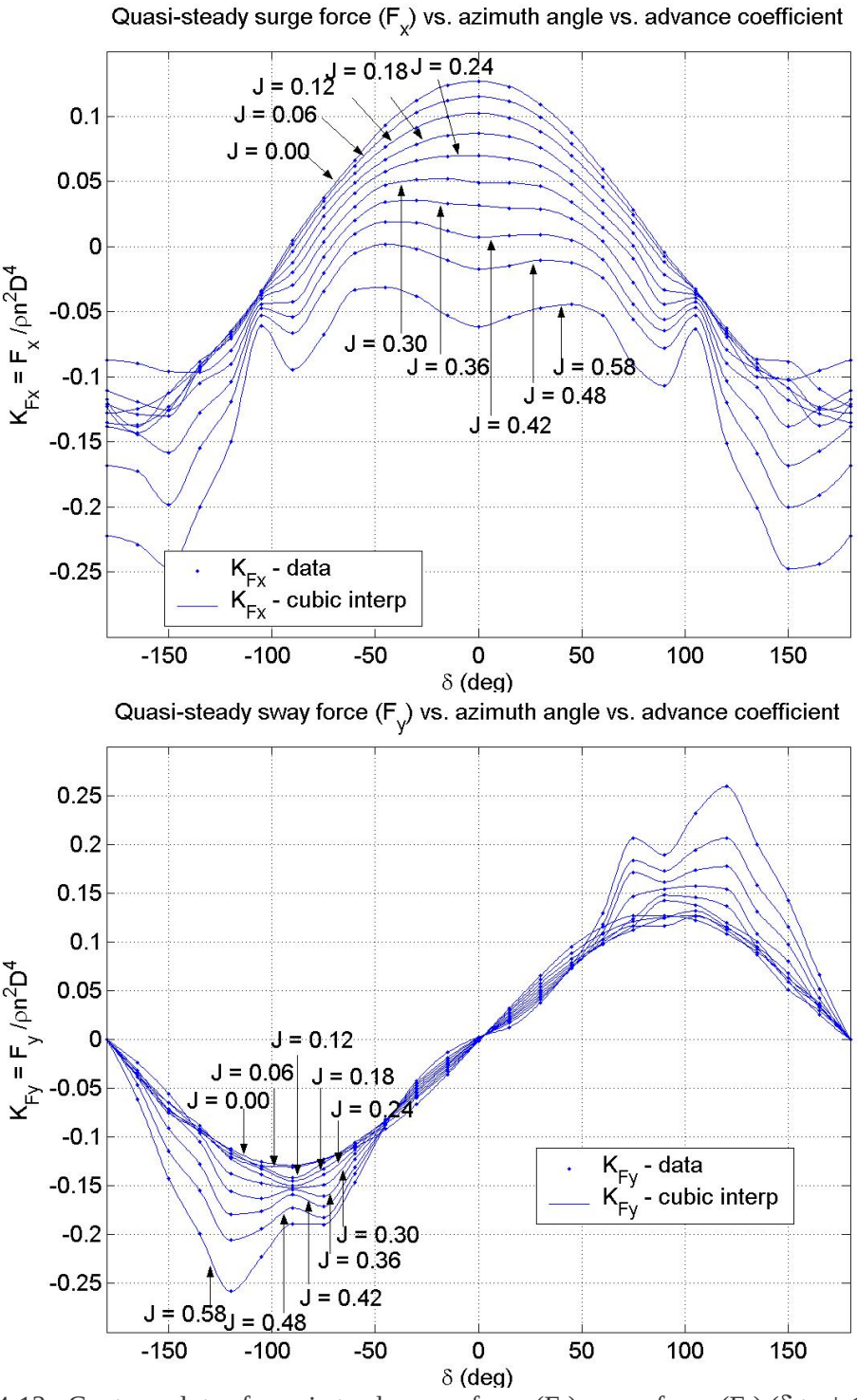

Figure 4-13: Contour plots of quasi-steady surge force (F_x), sway force (F_y) (δ to ± 180°).

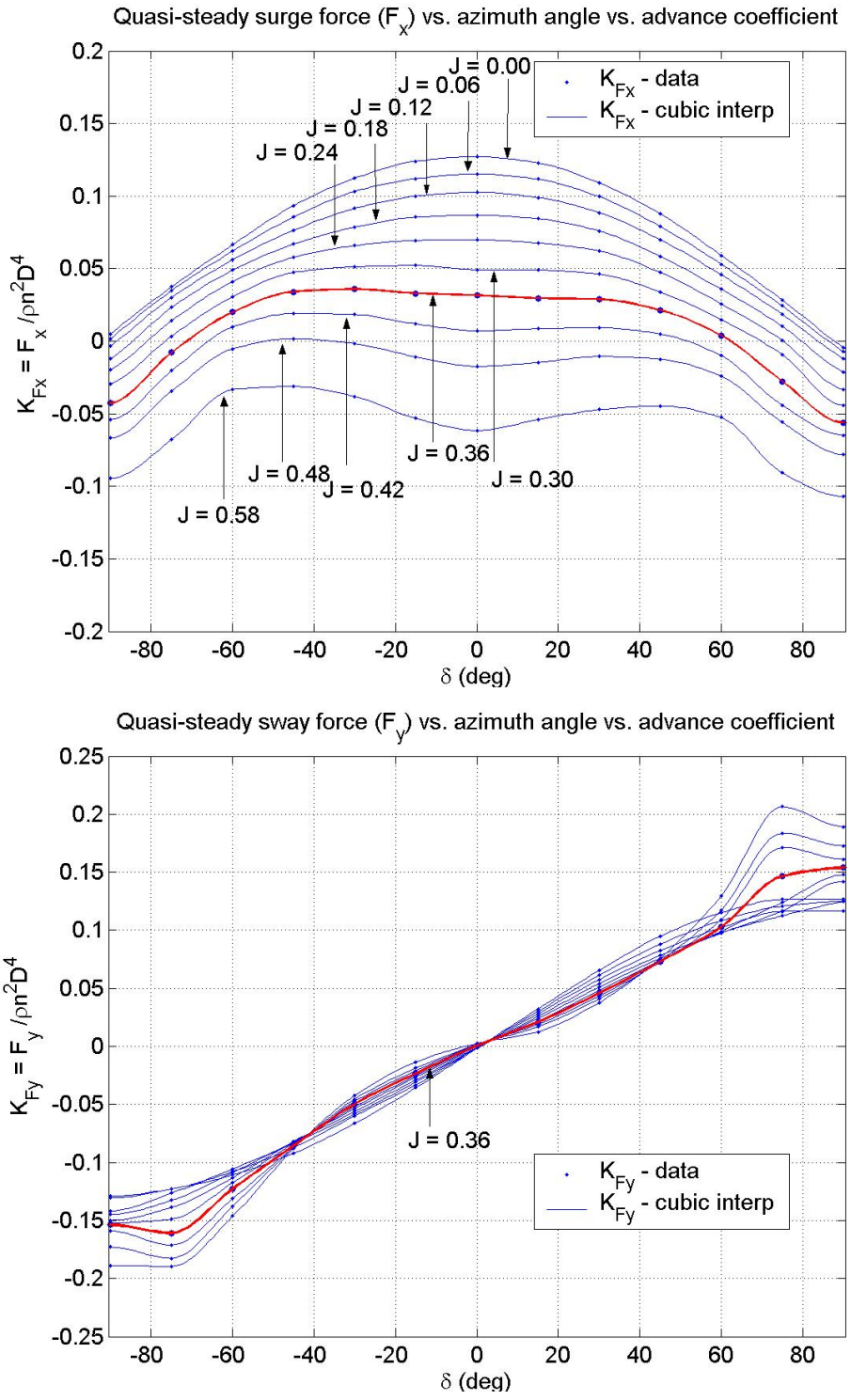

Figure 4-14: Contour plots of quasi-steady surge force (F_x), sway force (F_y). Red highlight indicates near-linear behavior for J = 0.36.

4.4 Unsteady/transient force measurements and results

Chapter 2 briefly introduced the idea of the development of unsteady propeller forces (thrust, torque, normal force, and steering moment) due to time-rate-of-change in the propeller's operating states (n, V_a, δ). The idea of modeling these unsteady propeller forces via first order differential equations using a dynamic inflow time constant was introduced as a physically-motivated representation of the dynamics of the propeller forces. A more detailed theoretical basis of this concept will be presented in Chapter 7. In this section, the empiricism of a dynamic inflow time constant representation is investigated through several experimental efforts.

In previous studies which have experimentally investigated unsteady propeller force dynamics for marine thrusters (all at zero advance velocity) [81], [34], [77], [5], parameters based upon simple momentum models used to model the steady and unsteady thrust dynamics were identified through application of a number of different input response tests. A similar approach is taken here, in that parameterization of a dynamic inflow time constant is investigated through a number of different types of input response tests. In the aforementioned marine thruster studies, high-quality marine thrusters were used which incorporated precision shaft position encoders, so that accurate propeller velocity measurements were available. However, for the experimental azimuthing propulsor used in these experiments, propeller velocity measurements were necessarily of a lower resolution, due to the method of speed measurement utilizing an external Hall-effect sensor and propeller hub-installed magnets. While, this propeller speed measurement scheme is of sufficient accuracy for quasi-steady measurements, its use for very rapid transient speed measurement is acknowledged to be of lesser accuracy. However, for purposes of the basic theoretical development and comparisons, it is believed that this system is of acceptable capability to illustrate the theoretical basis of the dynamic inflow time constant.

In order to investigate the unsteady dynamics of an azimuthing propulsor, a number of different types of dynamic tests were conducted, with the aim of measuring an approximate dynamic inflow time constant based upon measured dynamic force results. Because the dynamics of interest are those related to the maneuvering forces, the testing focused on the characterization of a first order time constant through a number of tests which target characterization of first-order system dynamics. To this end, several of the selected dynamic test methods are based upon "established" dynamic test procedures for mechanical first order dynamic systems (such as step and saturated ramp input response tests). Several others are variations of harmonic or sinusoidal test procedures, but utilized in a slightly different manner. A good overview of mechanical system dynamics and test procedures is provided in [19].

4.4.1 Current input step tests

One method utilized for investigation of an approximate first order dynamic inflow time constant was current input step testing. In these tests, a pre-determined step *change* in the motor current was provided by the control hardware (a step increase, then a subsequent step decrease after a suitable amount of time at steady-state). In all cases, the initial current was set to 5A (so that the propeller would have an initial rate) with a change to 20A, then the step was reversed at the end of each run (see figure 4-15). In order to approximate the dynamic inflow time constant from the step current input, the approximate rotational inertia of the fluid I_a (i.e. the added rotational inertia) was calculated by subtracting the known (previously identified) mechanical rotational inertia I_m, as discussed below. This amounts to a linear superposition of mechanical and hydrodynamic added inertias.

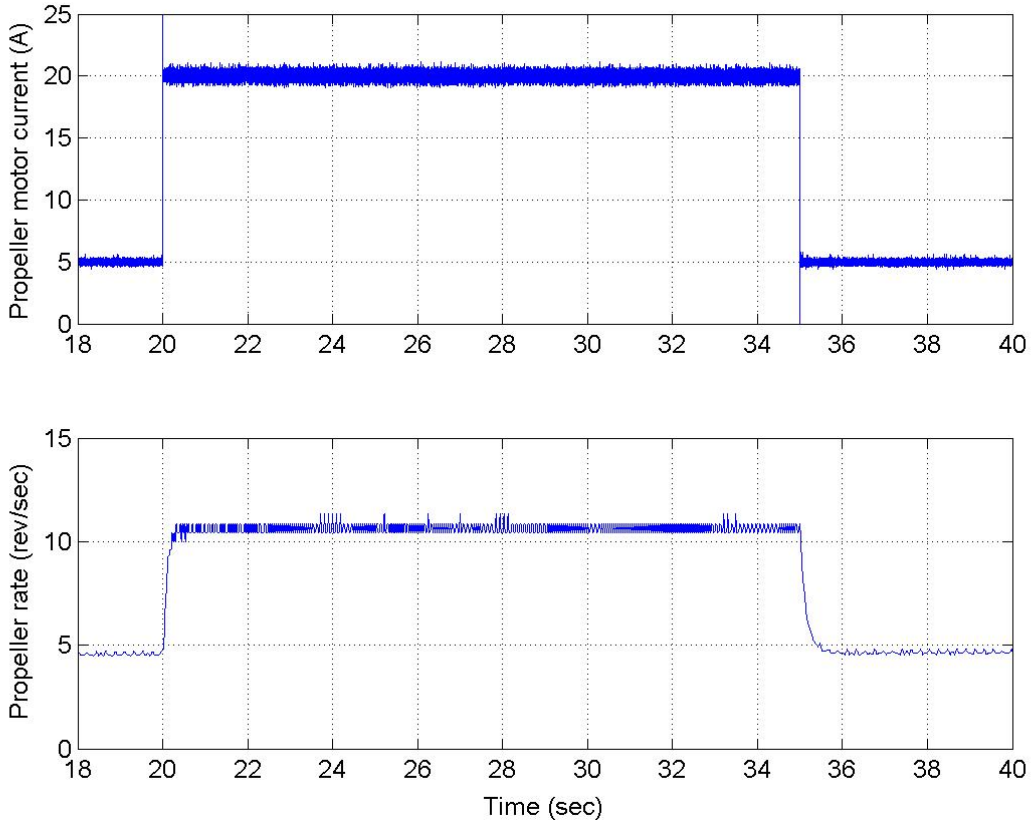

Figure 4-15: Current input step test. Unfiltered motor current (A) and propeller rate (rev/sec).

These current input step tests were carried out and results analyzed based upon the following mathematics: Referring to equations (2.6) and (2.7) for the propulsion motor torque, and applying a step change in current, where the initial propeller rate is a quasi-constant $n_0 > 0$ for $t \le t_{step}$ (and $\dot{n}_0 = 0$)

$$k_t i_{m_0} = k_{f0} + k_{f1} n_0 + k_{f2} n_0^2 + Q(n_o) \tag{4.2}$$

Note that the current step change must be started with non-zero propeller rate n_0, otherwise, there would be an unknown static friction component (which would also vary from test to test). Following the step change in current $\left(\text{i.e. for } t > t_{step}\right)$

$$k_t i_{m_f} = I_m \dot{n}(t) + k_{f0} + k_{f1} n(t) + k_{f2} n(t)^2 + I_a \dot{n}(t) + Q(n(t)) \tag{4.3}$$

Subtracting equation (4.2) from equation (4.3)

$$k_t (i_{m_f} - i_{m_0}) = I_m \dot{n}(t) + k_{f1}(n(t) - n_0) + k_{f2}(n(t)^2 - n_0^2) + I_a \dot{n}(t) + Q(n(t)) - Q(n_0) \tag{4.4}$$

Neglecting the quadratic term of the mechanical "dry" friction (which is small) and assuming that changes in propeller torque are approximately proportional to the change in propeller rate (i.e. a linear propeller torque curve at the tested azimuth angle)

$$k_t (i_{m_f} - i_{m_0}) \approx (I_m + I_a)\dot{n}(t) + k_{f1}(n(t) - n_0) + Q(n(t)) - Q(n_0) \tag{4.4}$$

Using the simplifying notation (for perturbations)

$$\hat{Q}_s \equiv k_t (i_{m_f} - i_{m_0}), \quad \hat{n}(t) \equiv n(t) - n_0, \quad b\hat{n}(t) \equiv k_{f1}\hat{n}(t) + Q(n(t)) - Q(n_0) \tag{4.5}$$

results in the first order differential equation

$$\hat{Q}_s \approx I\dot{\hat{n}}(t) + b\hat{n}(t) \tag{4.6}$$

where $I = (I_m + I_a)$ is the total system rotational inertia (mechanical plus hydrodynamic added). This is a standard linear equation for a mass-damper system. To find the step response, a Laplace transform method is applied (see for example [19]) with the resulting step response

$$\hat{n}(t) \approx \frac{\hat{Q}_s}{b}\left(1 - e^{(-b/I)t}\right) \tag{4.7}$$

For $t \to \infty$, the steady-state solution provides the steady-state gain

$$\hat{n}_{ss} = \frac{\hat{Q}_s}{b} \;\to\; \frac{1}{b} = \frac{\hat{n}_{ss}}{\hat{Q}_s} \equiv K \tag{4.8}$$

with the desired time constant and inertia terms related through

$$\tau_T = \frac{I}{b} \;\to\; I = (I_m + I_a) = b\tau_T = \frac{\tau_T}{K} \quad \to \quad I_a = \frac{\tau_T}{K} - I_m \quad \text{and} \quad \tau \approx \tau_T - K\, I_m \tag{4.9}$$

where τ_T is the overall total system time constant and τ is the time constant associated only with the *hydrodynamic* added rotational inertia I_a. Thus τ is a measure of the dynamic inflow time constant based upon development of propeller *hydrodynamic* torque Q with change in propeller rate n.

To find the total time constant τ_T, equation (4.7) is transformed by rearranging and taking the natural logarithm [19], resulting in

$$Z \equiv \ln\left(1 - \frac{\hat{n}(t)}{K\hat{Q}_s}\right) \approx -\frac{t}{\tau_T} \tag{4.10a}$$

which could also be written in the simpler form

$$Z \equiv \ln\left(1 - \frac{\hat{n}(t)}{\hat{n}_{ss}}\right) \approx -\frac{t}{\tau_T} \tag{4.10b}$$

Thus, if Z is plotted against time, the initial slope provides the time constant. Note that Z approaches negative infinity as steady-state is approached, so the slope of interest is the initial slope (roughly within the first time constant as a rule of thumb [19]). Figures 4-16 and 4-17 provide an example of the use of the current step response for estimating the dynamic inflow time constant. Figure 4-17 illustrates the fit of the exponential (Z of equations (4.10)) to obtain the total time constant τ_T. Results of the calculation of the hydrodynamic (added) rotational inertia I_a from the total inertia I, based upon the total time constant τ_T using equation (4.9), and the corresponding dynamic inflow time constant τ are also shown. It should also be noted that, although not mathematically rigorous for the step current input test, a *very* rough estimate of the dynamic inflow time constant could also be obtained by "eyeball" estimation of the *lag* of propeller rate n vs. thrust force shown in figure 4-16.

Based upon the simple dynamic inflow model to be presented in Chapter 7, it can be expected that the major influence on the unsteady dynamics of the propulsor/propeller is due to a rapid change in propeller rate n, and that changes to the unsteady magnitude of the inflow velocity V_a and azimuth angle δ would have little effect on the unsteady response (i.e. the time constant). This is illustrated by calculation of the dynamic inflow time constant from current input step test results conducted with steady-state azimuth angles varying from 0° to ±90°, and at several carriage speeds. Figure 4-18 provides a summary of results, with the calculated dynamic inflow time constant for each azimuth angle provided at each of three carriage speeds, for both step increase in current (5A to 20A) and step decrease in current (20A to 5A).

There is an obvious asymmetry in the results presented in figure 4-18. A rapid *increase* in propeller rate apparently has a *faster* dynamic inflow time constant than a corresponding rapid decrease in propeller rate. In fact, this can also be seen by careful inspection of figure 4-15.

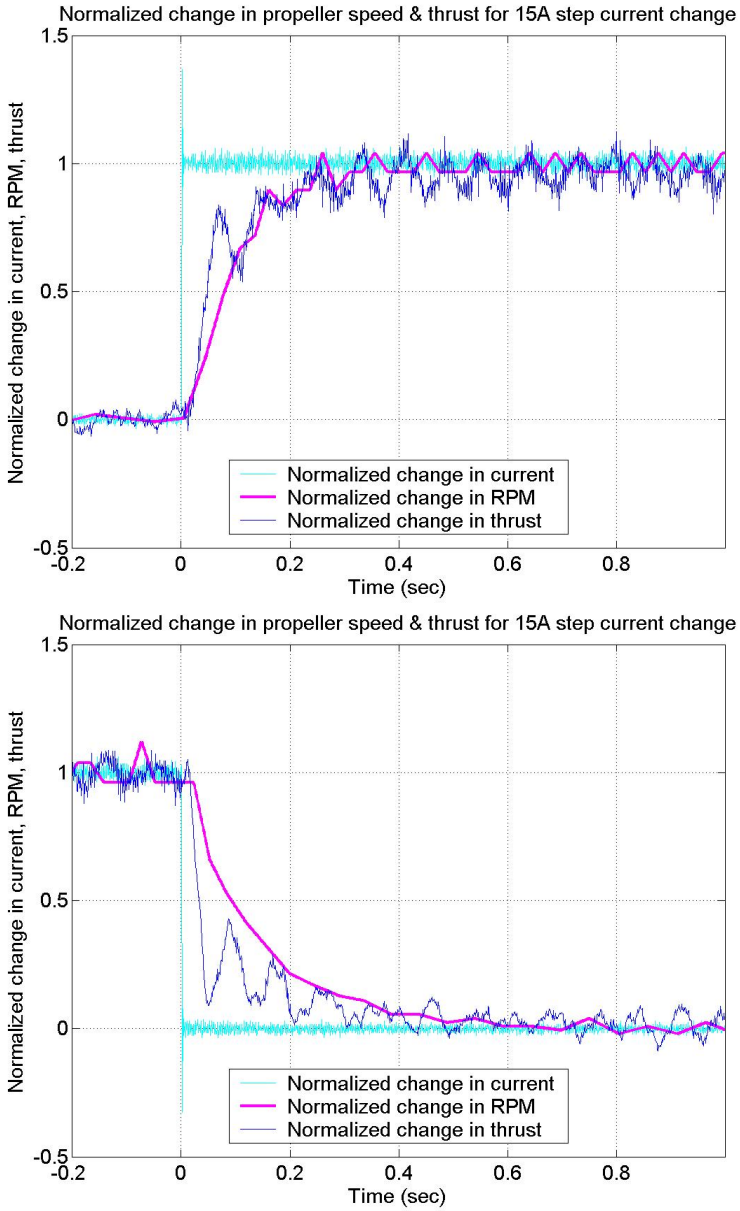

Figure 4-16: Examples of current step response. Normalized change in motor current (torque) step input, normalized change in thrust, normalized change in propeller rate. Approximate dynamic inflow time constant from propeller rate vs. thrust force. V_a = 1.31 ft/s, $\delta = 0°$. Top: initial current input i_0 = 5A, final i_f = 20A ($RPM_0 \approx 280$, $RPM_f \approx 640$), $\tau \sim 0.007$ sec ~ 0.05 rev. Bottom: i_0 = 20A, i_f = 5A ($RPM_0 \approx 640$, $RPM_f \approx 280$), $\tau \sim 0.036$ sec ~ 0.28 rev.

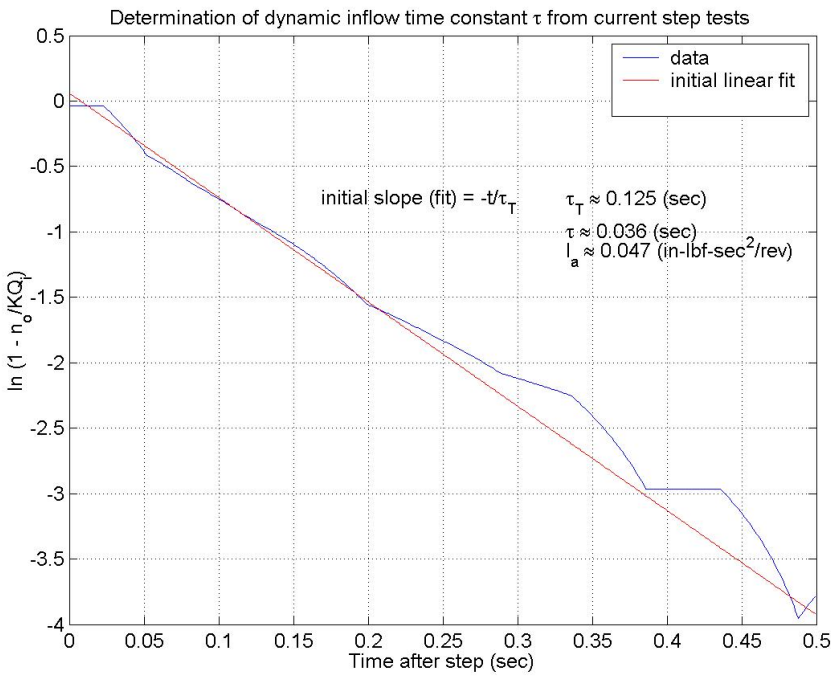

Figure 4-17: Current step response. Calculation of approximate dynamic inflow time constant from current input step tests. V_a = 1.31 ft/s, $\delta = 0°$. i_0 = 20A, i_f = 5A ($RPM_0 \approx 640$, $RPM_f \approx 280$), $\tau \approx 0.036$ sec ≈ 0.28 rev.

This asymmetry will be addressed and discussed in great detail in Chapter 7. Interestingly, in published results provided by Whitcomb and Yoerger [77] and Bachmeyer et al. [5], the plots of step current increase and step current decrease did not appear to show this obvious asymmetry. This might at first seem curious. However, it is noted that all of these tests were conducted using ROV marine thrusters designed for low speed ROV applications, and the thrusters were therefore equipped with *symmetric* constant pitch propellers with zero rake and skew (for zero vehicle speed bi-directional thrust equivalence), and were also fully ducted. This latter difference, as it turns out, may have a significant impact on this force asymmetry.

One plausible explanation for the observed force asymmetry may be described in terms of the unsteady *3-dimensional* vorticity that is shed into the wake with a rapid increase in propeller rate. For a large step current increase to the propulsion motor, and the resulting rapid increase in propeller rate, a large amount of vorticity is shed into the wake. In conjunction with this, a rapid acceleration of the fluid behind the propeller takes place in the generation or strengthening of the slipstream. This rapid slipstream acceleration is jet-like, in that it accelerates quickly relative to the fluid outside the slipstream. Owing to viscosity, the shear layer shed from the blades rolls up into a 3-dimensional vortex ring, which quickly plumes outward, then convects downstream as the slipstream convects. In consideration to the Biot-Savart law, this vortex ring induces

additional *axial* velocity at the propeller disk, in effect decreasing the (mean) angle of attack at the blades. Based on the results of flow visualizations (Chapter 5), this vortex ring could be quite large, and therefore could induce substantial axial velocity at the propeller disk. The generation of the vortex ring, and its impact on the dynamic inflow time constant will be discussed in much greater detail in Chapters 5 and 7 (for the reader who cannot wait to read Chapters 5 and 7, a quick look at figures 5-6, 5-7 and 5-8 should temporarily suffice). It is also interesting to note that the marine thrusters used in the experiments conducted by Whitcomb and Yoerger [77] and Bachmeyer et al. [5] were fully ducted. This is interesting in that then the large vortex ring would not have formed until the acceleration of the slipstream progressed beyond the end of duct. Then, by the Biot-Savart law, its ability to induce velocities at the propeller blades would be effectively removed (not to mention the fact that the ducting around the propeller would effectively shield it from seeing the effect of the ring vortex).

It should also be noted that the small negative dynamic inflow time constant τ shown for some of the data points in figure 4-18 (for the step increase in current) does *not* imply that the dynamic system has a negative time constant (i.e. infinite bandwidth). It may be recalled from equations (2.9) that the dynamic inflow time constant fundamentally represents the *lag* in the change in induced velocity at the propeller disk due to change in the propeller operating states (n, V_a, δ), where the change in operating states translates to a change in the local blade angle of attack. This change in blade angle of attack in turn translates to a change in blade forces (thrust and torque), and therefore overall propeller forces. Thus, the dynamic inflow time constant τ could also be thought of as representing the time constant of the decay (or rise) in propeller forces from a sudden change in a propeller state (here the propeller rate n). It therefore only represents the *hydrodynamic* portion of the first order system dynamics, the mechanical inertia of the system ensures a positive overall system time constant (as can be clearly seen from the composite step response record shown in figure 4-15). Further, the apparent negative time constant for some of the results with the step current increase is consistent with the overall asymmetry in results, including the existence of a vortex ring, which will be thoroughly addressed in Chapter 7.

Finally, it is also clear from figure 4-18 that the variation of dynamic inflow time constant with static propulsor azimuth angle δ and carriage speed is generally negligible (at least for the rapid step decrease). For the rapid step increase, where a vortex ring forms, the effect of the vortex ring on the induced velocities at the disk is decreased with ambient/advance velocity. This is consistent with vortex ring formation, which will be discussed in detail in Chapter 7.

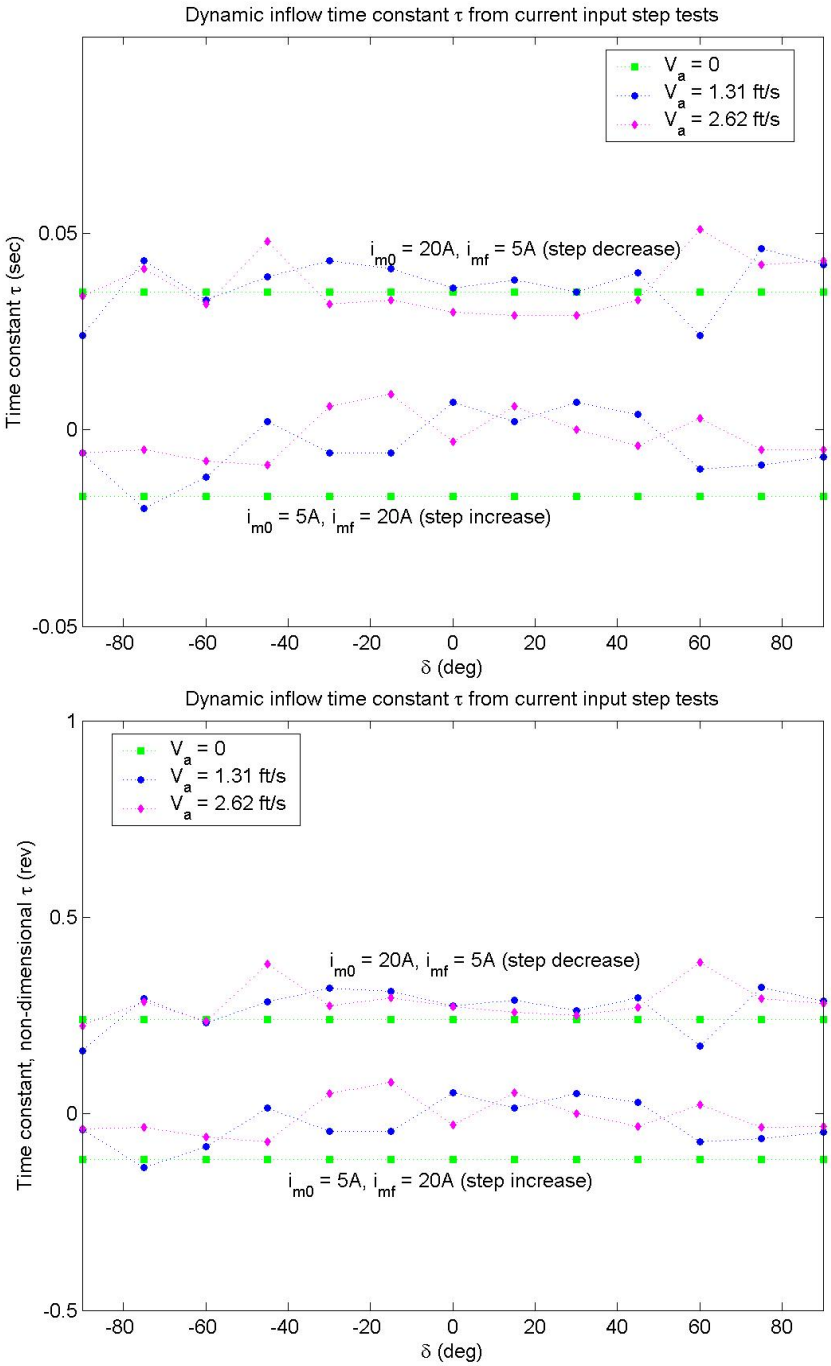

Figure 4-18: Dynamic inflow time constant calculated from current input step tests. Top: dimensional (sec). Bottom: non-dimensional (propeller revolutions). Non-dimensional calculated based upon average propeller rate.

4.4.2 Current input saturated ramp tests

Another approach to estimating the first order dynamic inflow time constant is through a saturated ramp current input response. As with the step response, a first order linear ramp response is derived using a standard Laplace transform method. Starting from the motor torque equation at time t after the beginning of the ramp

$$k_t i_m(t) = I_m \dot{n}(t) + k_{f0} + k_{f1} n(t) + k_{f2} n(t)^2 + I_a \dot{n}(t) + Q_p(n(t)) \tag{4.11}$$

and subtracting equation (4.2), using the same approximations and definitions for $\hat{n}$ and b as defined for the step response, results in the differential equation

$$k_t \left(i_m(t) - i_{m_0} \right) \approx \left(I_m + I_a \right) \dot{n}(t) + b\hat{n}(t) \tag{4.12}$$

Rearranging the left-hand side as the ramp torque input, using the notation $\hat{Q}_r(t)$, the result is the first order differential equation

$$\hat{Q}_r(t) \approx I\dot{\hat{n}}(t) + b\hat{n}(t) \tag{4.13}$$

Using the Laplace transform for a ramp input [19], the resulting ramp response is

$$\hat{n}(t) \approx K\hat{Q}_r(t)(t - \tau_T) + K\hat{Q}_r(t)\tau_T \, e^{-t/\tau_{Tr}} \tag{4.14}$$

The first term on the right-hand side is a steady-state lag between output and input (with total time constant τ_T), and the second term is the start-up transient of the ramp response. Thus, the total time constant τ_T can be measured from the ramp response curves as the horizontal distance between the ramp input ($KQ_r(t)$) and the output ($\hat{n}(t)$), once the initial transient has died.

Despite the fact that there is a notable resonance in the load cell test structure, a current ramp input also provides a means to estimate the dynamic inflow time constant τ directly using the measured thrust force in lieu of the torque as the input, with the estimation that the thrust force change during the current ramp is approximately of the form of a saturated ramp (this is much better than the "eyeball" approach suggested above for the step response). This offers the advantage of not requiring calculation of the overall time constant and hydrodynamic added inertia as an interim to calculating the hydrodynamic dynamic inflow time constant. However, both approaches are illustrated here.

Figures 4-19 and 4-20 provide examples of the application of this approach to calculating estimates of the dynamic inflow time constant τ, from both torque and thrust. These tests were conducted in the MIT recirculating water tunnel, and because of limitations in time and on azimuth angle, only angles 0°, 10° and 20° were tested in this manner. All provided approximately the same results. As can be seen in figures 4-19 and 4-20, the saturated ramp

current input response results in the same asymmetry as was seen with the current input step response. Again, this will be discussed in detail in Chapter 7.

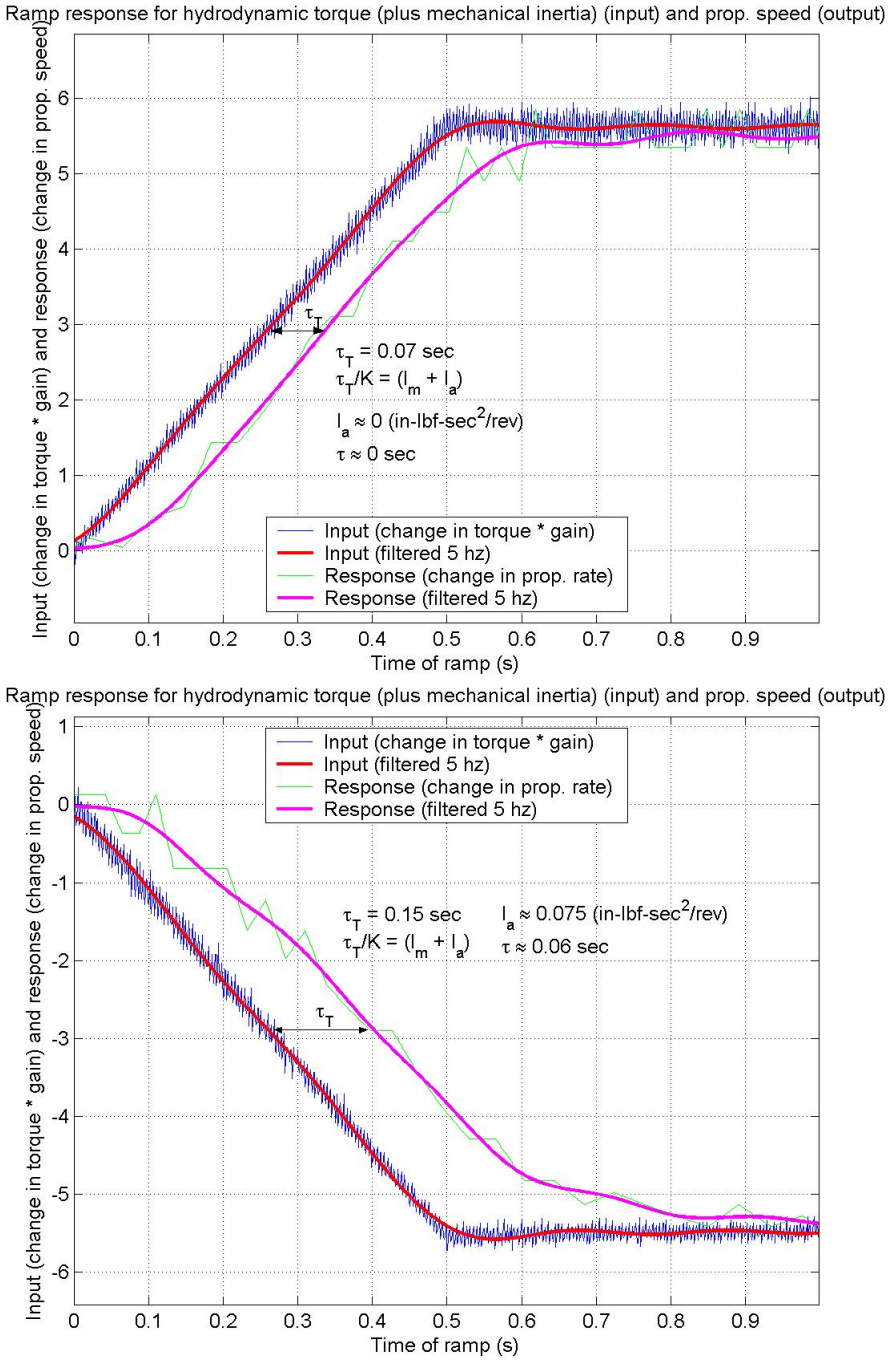

Figure 4-19: Examples of current saturated ramp response. Normalized motor torque (input) = saturated ramp. Normalized propeller rate (output). Approximate dynamic inflow time constant τ calculated from input torque using linear superposition of mechanical and hydrodynamic (added) inertias. V_a = 1.6 ft/s, δ = 10°. Top: initial current i_0 = 5A, final i_f = 20A ($RPM_0 \approx 300$, $RPM_f \approx 675$), τ ~0.0 sec ~0.0 rev. Bottom: i_0 = 20A, i_f = 5A ($RPM_0 \approx 675$, $RPM_f \approx 300$), τ ~0.06 sec ~0.48 rev.

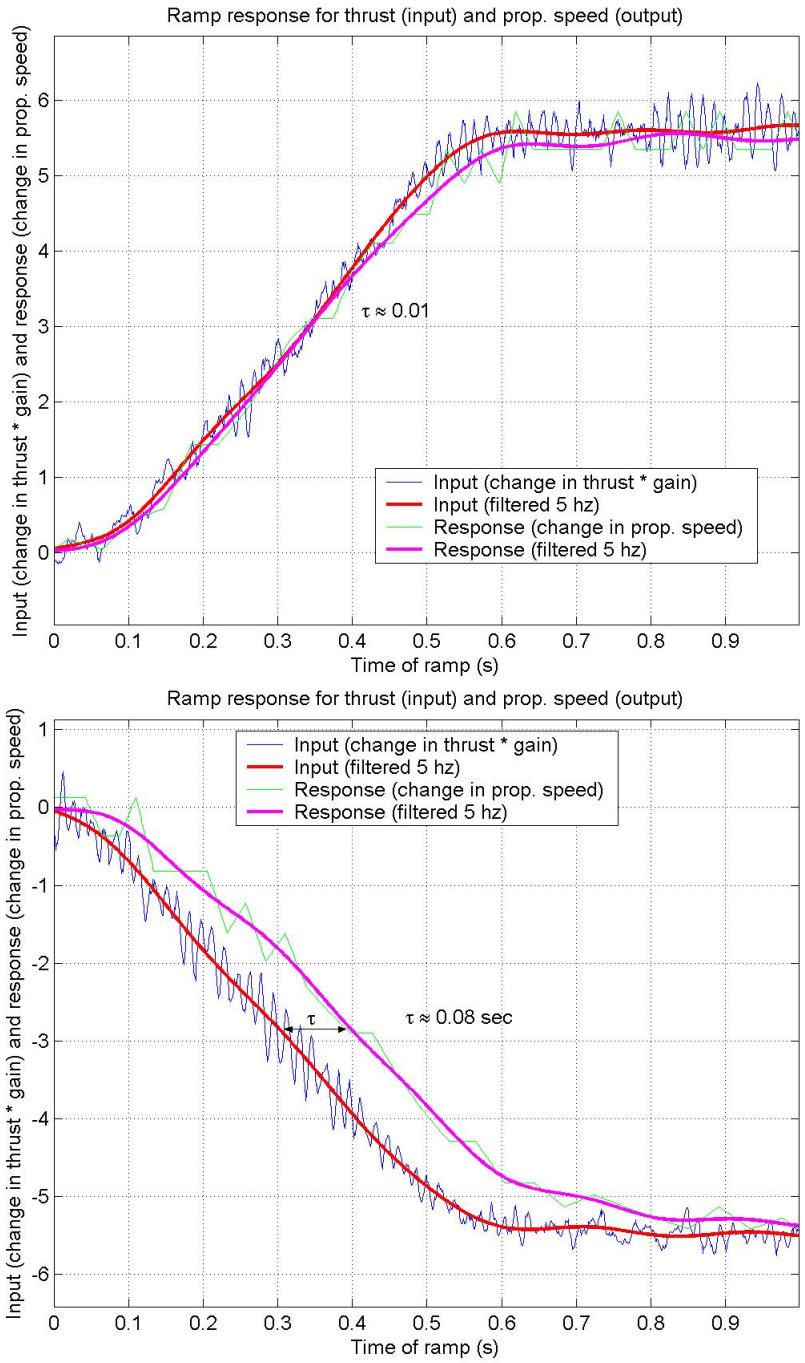

Figure 4-20: Examples of current saturated ramp response. Normalized thrust (input) ~ saturated ramp. Normalized propeller rate (output). Approximate dynamic inflow time constant τ calculated from thrust force as input and propeller rate as output. V_a = 1.6 ft/s, $\delta = 10°$.
Top: initial current i_0 = 5A, final i_f = 20A ($RPM_0 \approx 300$, $RPM_f \approx 675$), τ ~0.01 sec ~0.08 rev.
Bottom: i_0 = 20A, i_f = 5A ($RPM_0 \approx 675$, $RPM_f \approx 300$), τ ~0.08 sec ~0.65 rev.

4.4.3 Sinusoidal current input tests

In this set of tests, a series of sinusoidal current inputs was used to measure an approximate dynamic inflow time constant. An offset sinusoid was commanded for the propulsion motor current. This resulted in a steady quasi-sinusoidal response of both propeller rate n as well as measured thrust force. Figure 4-21 provides an example of the application of the sinusoidal current, showing the measured sinusoidal current (measured by the Hall-effect current sensor), as well as the quasi-sinusoidal propeller rate and thrust force. Also in figure 4-21 is shown the superposition of the normalized propeller rate and thrust force (both are normalized to their respective steady-state offsets and to their total respective steady-state amplitudes). Thus, the lag of propeller rate n behind thrust force, measured at their normalized offset crossings, provides a measure of the dynamic inflow time constant τ.

At each carriage speed and azimuth angle, a series of tests was conducted with identical sinusoidal current commands ($i_m(t) = i_{m0} + i_A \sin(2\pi ft)$), but varying the frequency. Frequencies from 0.2 Hz (5 second period) to 1.0 Hz (1 second period) were used. Figure 4-22 shows the results for frequencies of 0.2 Hz and 1.0 Hz for a carriage velocity of 1.31 ft/s and azimuth angle of 15°. Inspection of the plots and comparing results for the two frequencies implies an interesting result. The lower frequency provides a result that is similar to the current input step and ramp tests (i.e. an asymmetry in time constants for increasing and decreasing propeller rates). However, the higher frequency provides a different result: both time constants are nearly the same. Evaluating the remainder of the frequencies and for a number of carriage velocities and azimuth angles, and tabulating the results in table 4-1, it is seen that the results seem to "converge" as the frequency is increased. Time constants listed in table 4-1 are provided both in seconds (dimensional) and in propeller revolutions (non-dimensional). A discussion of these results and significance related to a theoretical basis will be provided in Chapter 7.

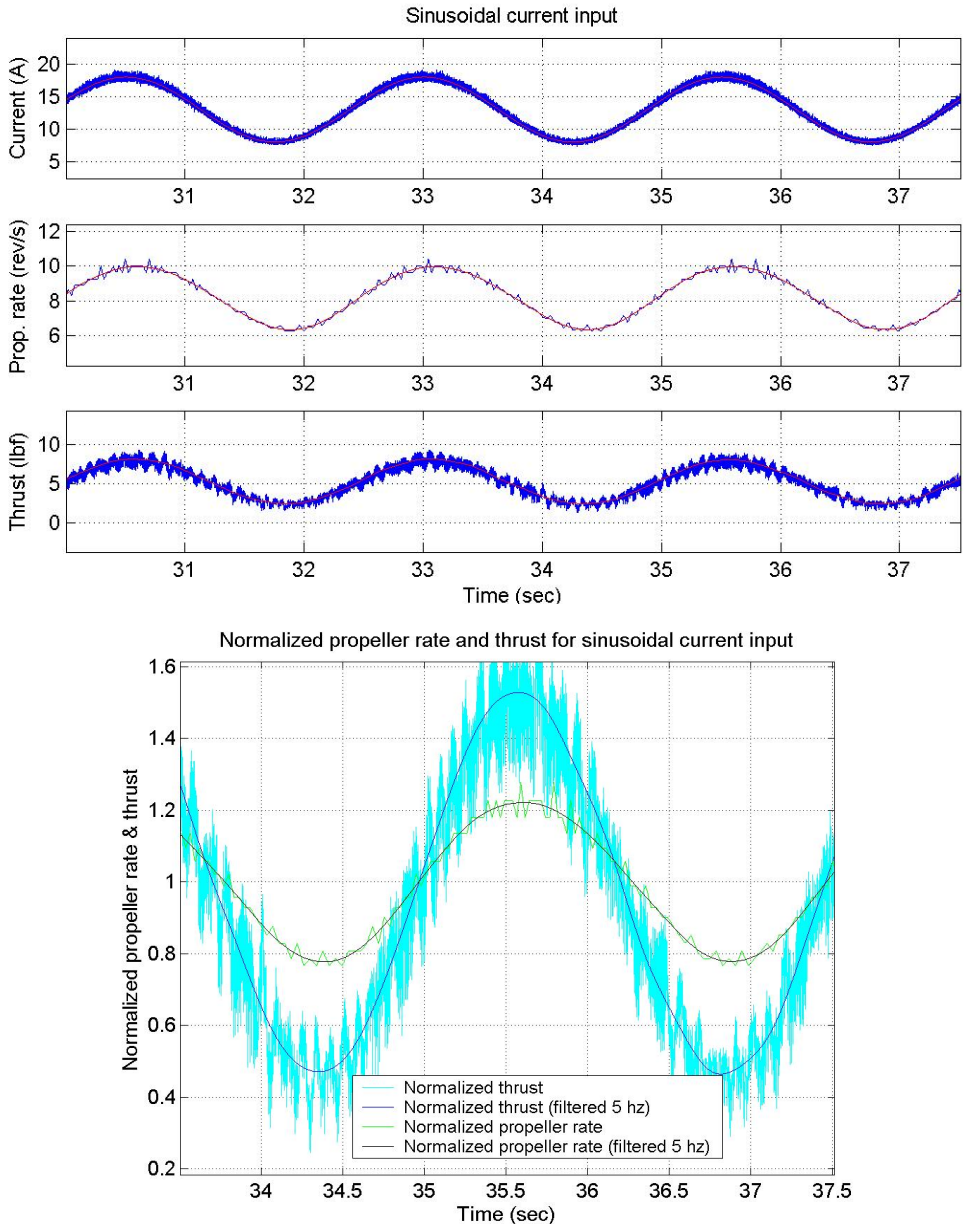

Figure 4-21: Example of sinusoidal current response. Normalized thrust ~ sinusoidal. Normalized propeller rate ~ sinusoidal. Approximate dynamic inflow time constant from lead of thrust force vs. propeller rate at normalized zero-crossing. V_a = 1.31 ft/s, $\delta = 15°$, $i_m(t) = i_{m0} + i_A \sin(2\pi ft)$, i_{m0} = 13A, i_A = 5A, f = 0.4 hz.

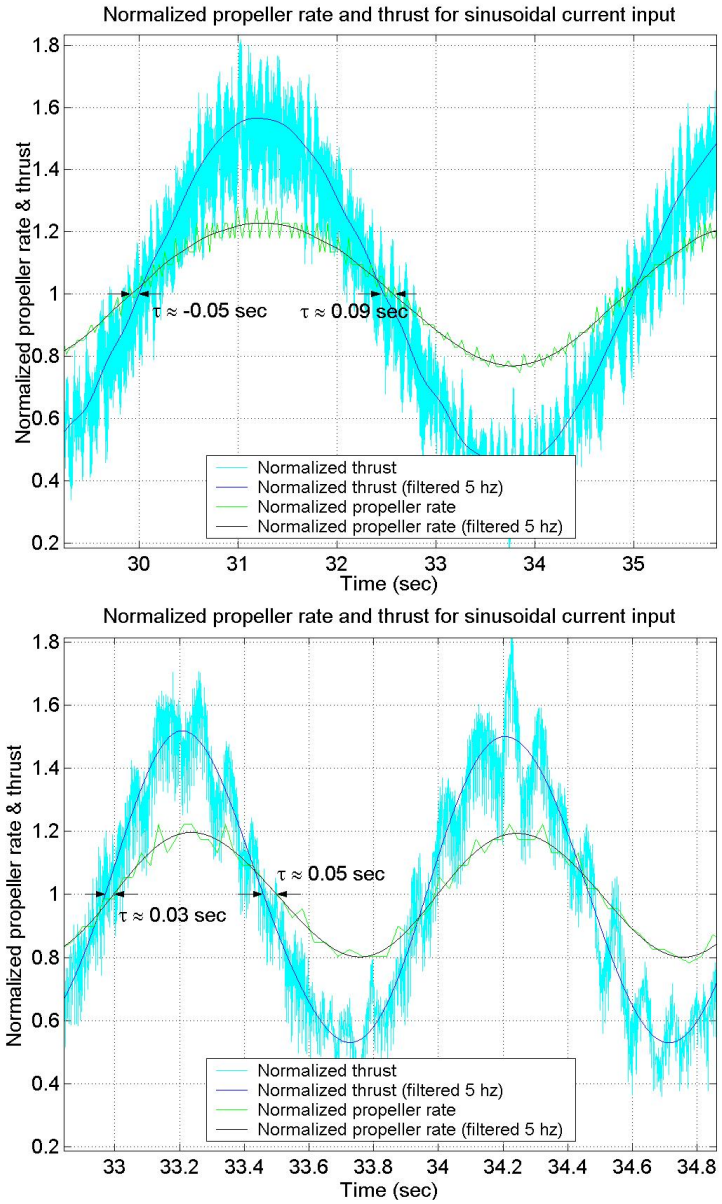

Figure 4-22: Examples of sinusoidal current response. Normalized thrust ~ sinusoidal. Normalized propeller rate ~ sinusoidal. Approximate dynamic inflow time constant from lead of thrust force vs. propeller rate at normalized zero-crossing. V_a = 1.31 ft/s, δ = 15°,
$i_m(t) = i_{m0} + i_A \sin(2\pi ft)$, i_{m0} = 13A, i_A = 5A.
Top: f = 0.2 hz, $\tau(\dot{n} > 0) \sim -0.05\,\text{sec} \sim -0.41\,\text{rev}$, $\tau(\dot{n} < 0) \sim 0.09\,\text{sec} \sim 0.73\,\text{rev}$.
Bottom: f = 1.0 hz, $\tau(\dot{n} > 0) \sim 0.03\,\text{sec} \sim 0.24\,\text{rev}$, $\tau(\dot{n} < 0) \sim 0.05\,\text{sec} \sim 0.41\,\text{rev}$.

Table 4-1: Results of sinusoidal current input tests, with variation in frequency.
$i_m(t) = i_{m0} + i_A \sin(2\pi ft)$, $i_{m0} = 13A$, $i_A = 5A$.

V (ft/s)	δ (deg)	f (hz)	0.2	0.4	0.6	0.8	1.0
0	any	$\tau(\dot{n} > 0)$ (sec, rev)	-0.09, -0.54	-0.01, -0.06	0.01, 0.06	0.03, 0.19	0.03, 0.19
		$\tau(\dot{n} < 0)$ (sec, rev)	0.15, 0.91	0.09, 0.55	0.07, 0.43	0.06, 0.37	0.05, 0.31
1.31	0	$\tau(\dot{n} > 0)$ (sec, rev)	-0.11, -0.90	0.00, 0.00	0.02, 0.16	0.03, 0.25	0.03,0.25
		$\tau(\dot{n} < 0)$ (sec, rev)	0.07, 0.57	0.07, 0.57	0.05, 0.41	0.04, 0.37	0.04,0.33
1.31	15	$\tau(\dot{n} > 0)$ (sec, rev)	-0.05, -0.41	0.00, 0.00	0.01, 0.08	0.02, 0.16	0.03, 0.24
		$\tau(\dot{n} < 0)$ (sec, rev)	0.09, 0.73	0.06, 0.49	0.05, 0.41	0.05, 0.41	0.05, 0.41
1.31	45	$\tau(\dot{n} > 0)$ (sec, rev)	-0.07, -0.55	0.00, 0.00	0.02, 0.16	0.03, 0.24	0.03, 0.24
		$\tau(\dot{n} < 0)$ (sec, rev)	0.11, 0.87	0.07, 0.56	0.06, 0.48	0.05, 0.40	0.05, 0.40
1.31	90	$\tau(\dot{n} > 0)$ (sec, rev)	-0.08, -0.59	0.00, 0.00	0.03, 0.22	0.04, 0.30	0.05, 0.38
		$\tau(\dot{n} < 0)$ (sec, rev)	0.15, 1.10	0.12, 0.89	0.09, 0.67	0.05, 0.38	0.05, 0.38

4.4.4 Sinusoidal azimuth tests

Two sinusoidal azimuth tests were also completed in order to approximate the dynamic inflow time constant, in terms of a rapid change in propulsor azimuth angle, or a propulsor azimuth maneuver. A zero offset sinusoidal azimuth was commanded by the control system, for two frequencies. The azimuth angle and sway force (F_y) were normalized in the same manner as for the current sinusoidal tests, and results plotted as shown in figure 4-23 (both are normalized to their respective steady-state total amplitudes). Thus, the lag of azimuth angle behind the sway force, measured at their normalized zero crossings, provides a measure of the dynamic inflow time constant τ (this will also be discussed in greater detail in Chapter 7). Figure 4-23 shows the approximation of the dynamic inflow time constant in this manner for frequencies of 0.25 and 0.5 hz (with maximum angular rates of 25°/sec and 49°/sec, respectively) for a velocity of 3.05 ft/s and 700 RPM (11.667 rev/s). Both frequencies yielded the same dynamic inflow time constant: $\tau \approx 0.06$ sec ≈ 0.7 rev.

Additional unsteady azimuth tests were conducted by application of an azimuth gearmotor step command input (which resulted in a fast azimuth ramp). However, because of the large amount of structural resonance in the test fixture, these tests were very difficult to effectively filter and determine a dynamic inflow time constant. These results are therefore not presented.

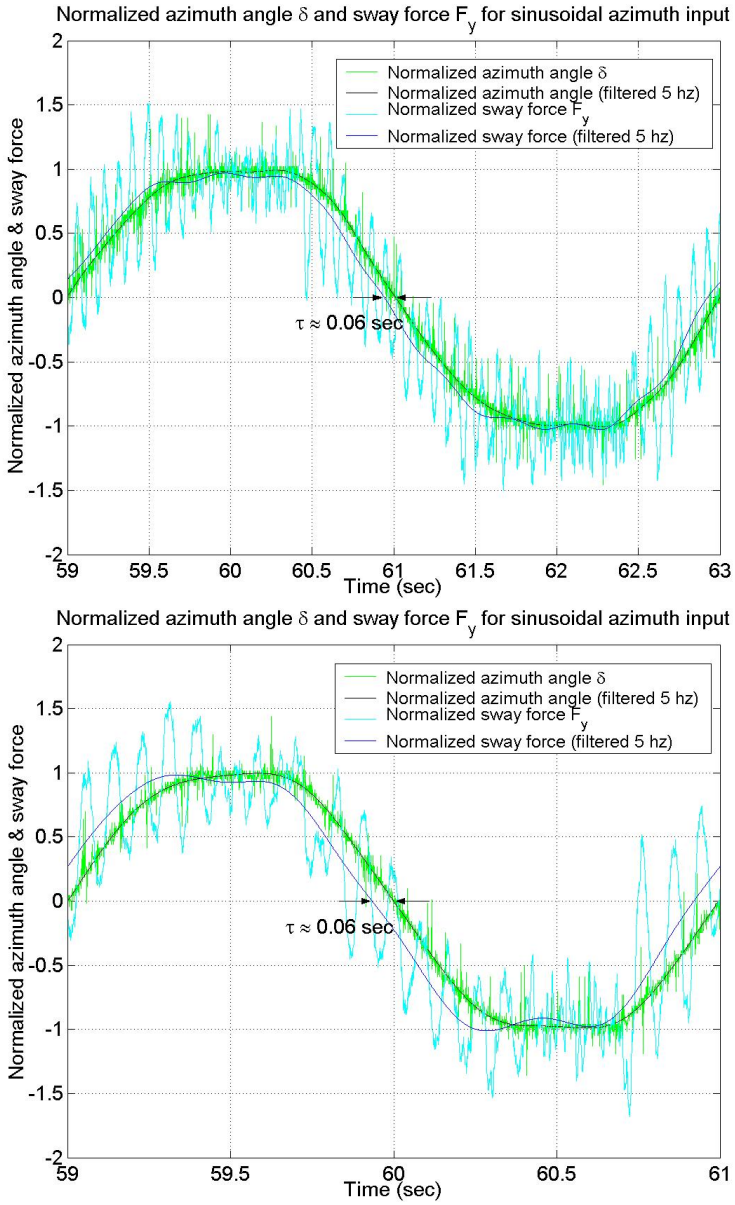

Figure 4-23: Examples of sinusoidal azimuth response. Normalized azimuth angle (input) = sinusoidal. Normalized sway force (F_y) (output). Approximate dynamic inflow time constant from lead of thrust force vs. azimuth angle at zero-crossing. V_a = 3.05 ft/s, RPM = 700, $\delta(t) = \delta_0 + \delta_A \sin(2\pi ft)$, $\delta_0 = 0°$, $\delta_A = 15°$ (note: difference in plot time scales).

Top: f = 0.25 hz, $\dot{\delta}_{max} \approx 25°/\text{sec}$, $\tau \sim 0.06$ sec ~ 0.7 rev.

Bottom: f = 0.5 hz, $\dot{\delta}_{max} \approx 49°/\text{sec}$, $\tau \sim 0.06$ sec ~ 0.7 rev.

4.5 Pod-only force tests

The data and plots presented thus far have been based upon measurements taken for the entire azimuthing propulsor unit. Since the ultimate goal of the research is to characterize the maneuvering forces associated with the azimuthing propulsor, this is in general the best way to characterize the propulsor forces. However, in considering the intuitions for a propeller in oblique flow presented in Chapter 2, it is important to realize that, in addition to the propeller forces, the pod (and the steering shaft) act to provide additional forces. There are, in addition, interaction effects due to the effects of the propeller inflow on the flow past the propulsor pod (i.e. an added resistance analogous to the drag augmentation or thrust deduction used for normal shafted propellers), and the converse (i.e. the effect of the pod wake on the propulsor inflow, analogous to the wake fraction and inflow wake field used for normal shafted propellers).

While these issues will be addressed in greater detail in Chapter 6, where propeller calculations are presented, data for force measurements taken for the bare pod (i.e. without the propeller installed) are presented here for the vehicle design operating velocity. Figure 4-24 provides plots of the pod-only (i.e. motor housing plus steering shaft – without propeller) axial force (F_a), normal force (F_n), and moment (M_z) in units of lbf and in-lbf, and the same data, non-dimensionalized as is typical for streamlined bodies (see for example [59] or [39]). These forces are analogous to propulsor thrust, normal force and steering moment defined in the propulsor coordinate system as in figure 2-1 (i.e. F_a is analogous to T, F_n is analogous to N, and M_z is analogous to M). These pod-only forces will be referred to again in Chapter 6.

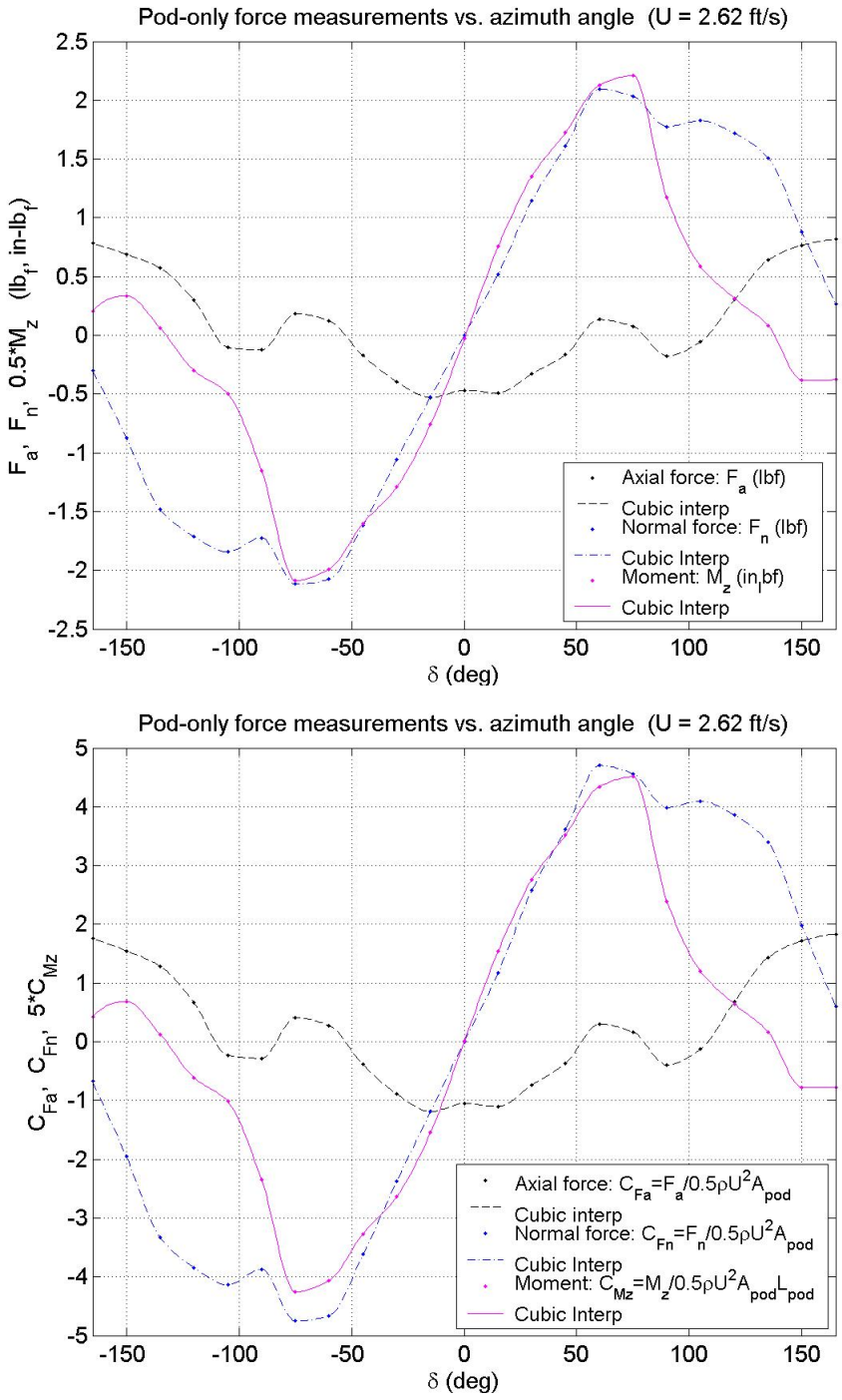

Figure 4-24: Pod-only force data (motor housing plus steering shaft – without propeller). Dimensional (top) and non-dimensional (bottom).

4.6 Summary

This chapter has provided an in-depth presentation of the test program conducted in quantitatively investigating maneuvering forces associated with the azimuthing propulsor, including quasi-steady effects, as well as the transient or unsteady effects of potential importance to smaller vehicles. The experimental setups and techniques have been detailed, for testing conducted with the propulsor installed on a special test fixture in the MIT towing tank, and with the propulsor installed in the autonomous surface test vehicle installed on the planar motion mechanism (PMM) at the U.S. Naval Academy. The results have been presented in both graphical and tabular form, with the significance of the test results to vehicle maneuvering discussed.

Specifically, parametric results clearly illustrate unique characteristics of vectored-propulsion, including generation of sizeable normal force, and significant increase in vectored thrust and torque with azimuth angle. Force data has also been presented in terms of surge force (F_x) and sway force (F_y). Contour plots of F_x and F_y for moderate azimuth angles (up to $\pm 45°$) are nearly linear in the range of the typical design advance coefficient for the tested propulsor, suggesting the strong possibility of linearization, even decoupling, of the surge-sway-yaw vehicle maneuvering control problem.

An investigation of the unsteady propulsor hydrodynamics has been reported, including identification of a characteristic "dynamic inflow" time constant, which can be used to characterize the unsteady dynamics of propeller thrust, torque, normal force and steering moment for coupled maneuvering dynamics as discussed in Chapter 2. An interesting "asymmetry" in results for rapidly changing propeller rate has been observed which indicates a hydrodynamic asymmetry in the flow through the propeller disk with propeller rate increase and decrease. Identified "asymmetric" non-dimensional dynamic inflow time constants for rapid propeller rate increase are approximately zero, while those for rapid propeller rate decrease are approximately 0.4 propeller revolutions.

Finally, the measured forces associated with only the pod (i.e. motor housing plus steering shaft – without propeller) have been presented in graphical form. The plots indicate significant lift forces associated with separation as the pod is azimuthed relative to the flow. At azimuth angles near 60 degrees, normal forces on the pod are seen to be nearly 2/3 of the total measured on the propulsor with the propeller operating.

This page left blank

Chapter 5

Flow visualization of the steady and unsteady wake

In order to more thoroughly characterize the maneuvering dynamics of the azimuthing propulsor, two methods of wake flow visualization were employed. First, a new fluorescent paint visualization technique was developed for use in the MIT towing tank to visualize the helical wake of the azimuthing propulsor for a number of quasi-steady and transient wake conditions. Second, a particle image velocimetry (PIV) technique was adapted for use in the MIT recirculating water tunnel to visualize the wake and measure and document the velocities within the wake for a number of quasi-steady and transient conditions. These two techniques provide visualization and documentation of a number of important wake parameters useful for understanding the dynamics of the wake, as well as for future validation of computational fluid dynamics studies. Wake parameters such as wake pitch/diameter ratio, wake angle, wake distortion, and velocities are documented and discussed.

5.1 Fluorescent paint flow visualization

A new fluorescent paint visualization technique was developed for the visualization and documentation of the quasi-steady and unsteady wake. In addition, it was desired to demonstrate the evolution of unsteady forces during a maneuver, and compare with this evolution the evolution of the helical wake during the maneuver. The visualization was carried out using a fluorescent paint applied to a single propeller blade, with the wake fluoresced under ultraviolet black light. The fluoresced wake was recorded using digital video for subsequent analysis.

5.1.1 Experimental setup and procedure

The visualization was carried out in the MIT towing tank using the same test fixture used for the quasi-steady and dynamic test series as discussed in Chapter 4. The wake was illuminated using several banks of ultraviolet black light attached to the carriage assembly, as shown in figure 5-1. A digital video camera was attached to the carriage assembly overhead of the propulsor,

looking down at the wake. Thus, video and still image sets were obtained from above through the free surface as the fixture was towed. This, unfortunately, did introduce some minor image distortion (which will be discussed subsequently), but was believed to allow reasonable results for basic helical wake visualization. In addition, two visualization runs were conducted with the digital video camera mounted inside a clear acrylic window fixture, looking forward at the propulsor and the wake, as shown in figure 5-1.

Figure 5-1: Experimental setup for fluorescent paint flow visualization of quasi-steady and transient wakes. Top: digital video camera mounted overhead of the propulsor, looking down at the wake. Bottom: digital video camera mounted inside a clear acrylic window fixture, looking forward at the propulsor and wake.

A clear acrylic-based (water-soluble) paint leveling gel was used as a base for the fluorescent mixture applied to the single propeller blade. To the base was added Fluorescein Sodium powder, and mixed into a thin paste, and brushed onto both sides of the single blade. The applied paste was allowed to dry for 3-4 hours.

For each visualization run, the propeller was installed onto the propulsor by hand, and the camera set to record. Within 30 seconds of propeller installation, the carriage motion was initiated and the programmed propulsor sequence (i.e. sequence trajectory of propeller speed and azimuth angle controlled by the control system) was executed. All runs were controlled to execute in entirety within 90 seconds of installation of the propeller.

The visualization was carried out for two sets of advance coefficients (combinations of carriage velocity and propeller rate) and five azimuth angles (0°, ±30°, and ±60°). Additionally, each change in azimuth angle was executed as a fast ramp (i.e. a step command change to the azimuth gearmotor) during each run, so that the transient wake effects could also be visualized and correlated with force measurements.

It should be noted that, because of the rapid diffusion of the fluorescent paint, there was a practical limitation in terms of propeller rotation rate that could be used. Here, propeller rates of 240 and 300 RPM were used (this was determined through a trial-and-error approach). Additionally, the distorting effect of the free surface at higher carriage speeds also limited practical top carriage speeds that could be used (this was also determined through a trial-and-error approach). As it turned out, the limits of both propeller rate and carriage velocity still allowed for visualization of a light propeller loading condition ($J = 0.4$), as well as a moderate propeller loading condition ($J = 0.2$), as will be discussed subsequently.

5.1.2 Visualization results

5.1.2.1 Quasi-steady visualization results

By varying propeller rate, carriage velocity, and propulsor azimuth angle, a small matrix of quasi-steady operating test conditions was completed. After each set of visualizations, from the digital video was created a set of still image sequences with frequency timed to the rotation rate of the propeller (6 image sets per propeller revolution in all cases). Ten image sets for each of the test conditions were then measured using a drawing/dimensioning software. For each image set, an approximate helical wake pitch (distance) was measured on both sides of the wake, as well as

an approximate wake angle (i.e. for the "near" and "intermediate" wake). Figure 5-2 provides a graphical definition of a blade helix, illustrated for the blade tip and root helices. The theoretical blade helix surface can be thought of as a continuous distribution of helices between tip and root. Note that the blade pitch (distance) is theoretically identical for both tip helix and root helices, and therefore there is theoretically a single blade wake pitch for the helix surface. There is however, a roll-up of the wake in the tip region (the tip vortices) which distorts the blade helix surface which is visualized in these experiments, making measurement of the "true" helix pitch more difficult. This will be discussed more subsequently. Sample images for each of the test matrix conditions are shown in figure 5-3. Because of the roll-up of the wake in the tip region, pitch measurements were made at the mid-blade region of the wake. Measurements for each of the ten image sets for each condition were averaged, and tabulated, as provided in table 5-1. The results are provided in non-dimensional form (i.e. pitch/diameter ratio (P/D) and wake angle).

The results listed in table 5-1 indicate that the P/D ratio does not appear to change with even the large change in azimuth angle, only with advance velocity or propeller rate. To understand why this might be so, consider the definition of pitch angle ϕ at a radius r (as defined in [74] for example)

$$\tan\phi(r) = \frac{P}{2\pi r} \tag{5.1}$$

where P is the pitch (distance), the distance between turns of the wake helix as shown in figure 5-2. The pitch angle at radius r can also be written as

$$\tan\phi(r) = \frac{(V_A + V_{Ai})}{2\pi r\, n} \tag{5.2}$$

where V_A is the axial component of inflow velocity at the propeller disk and V_{Ai} is the axial induced velocity at the propeller disk (together they make up the total axial velocity at the disk). Note that this representation includes account for propeller slip (i.e. it is *not* assumed that the propeller is lightly loaded). Equating equations (5.1) and (5.2) and using the dependence of axial inflow velocity on propulsor azimuth angle (see figure 2-1)

$$P = \frac{(V_A + V_{Ai})}{n} \quad \rightarrow \quad \frac{P}{D} = \frac{(V_A + V_{Ai})}{nD} = \frac{(V_a \cos\delta + V_{Ai})}{nD} = J\cos\delta + \frac{V_{Ai}}{nD} \tag{5.3}$$

Thus, the pitch/diameter ratio of the helical wake for an azimuthing propulsor is dependent on the advance ratio J and azimuth angle δ, but is also dependent upon the axial induced velocity V_{Ai}, which depends on propeller blade loading. Although the contribution of the first term on the right hand side of equation (5.3) is reduced when the propulsor is azimuthed, the second term is

increased when the propulsor is azimuthed (Chapter 4). Thus, there is an apparent cancellation-effect with propulsor azimuth in terms of pitch/diameter ratio.

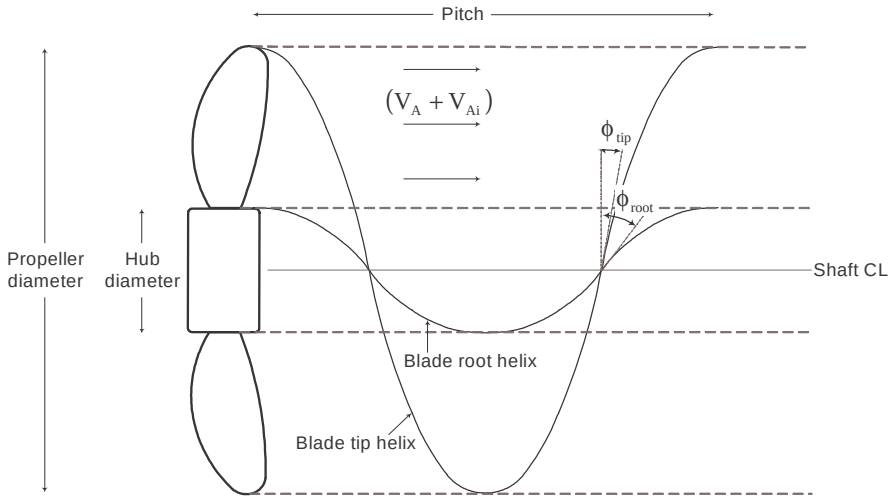

Figure 5-2: Definition of a blade helix. Illustrated are the tip and root helices. The actual theoretical blade helix surface can be thought of as a continuous distribution of helices between tip and root. Basic graphic adapted from [74].

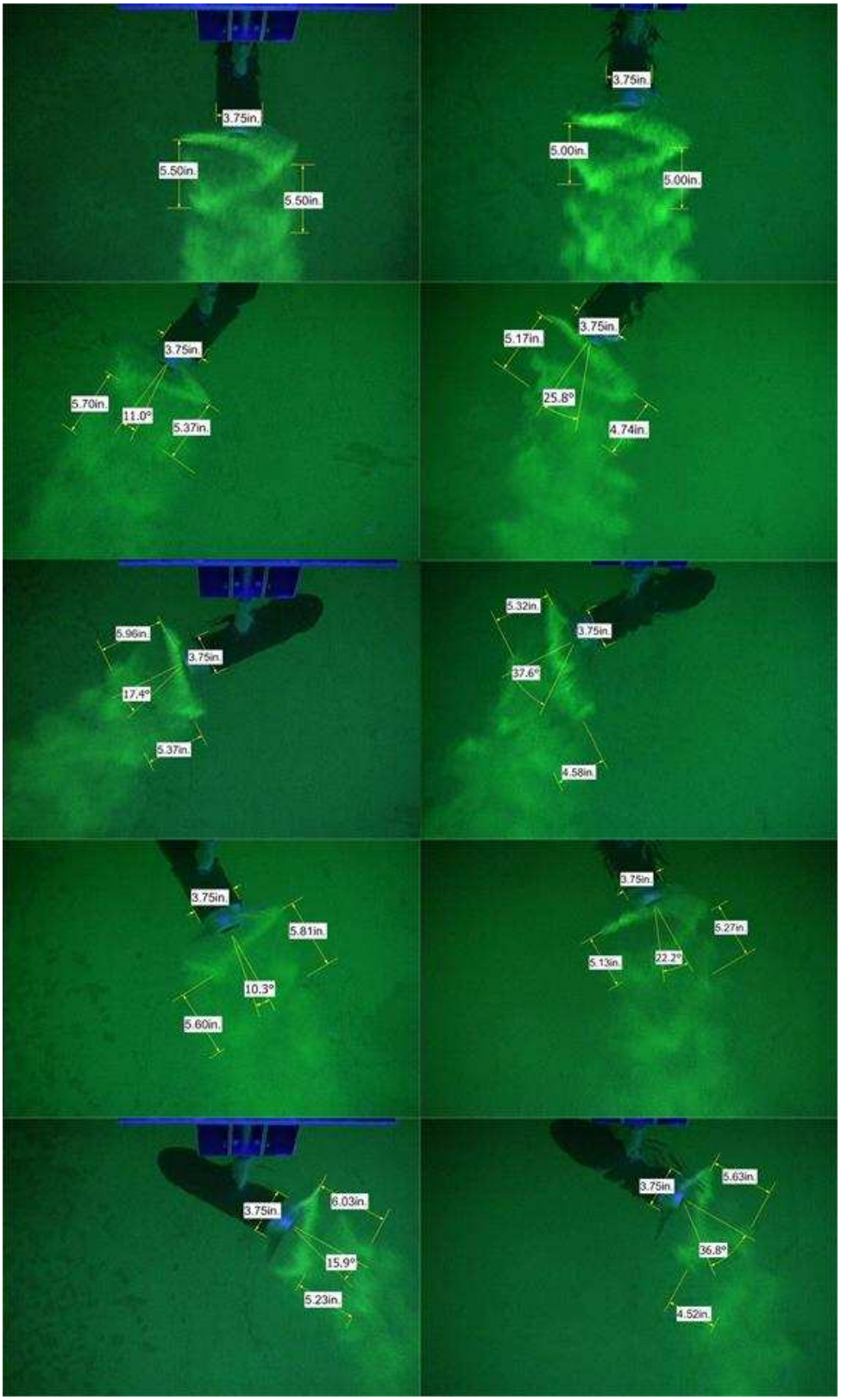

Figure 5-3: Fluorescent paint visualization. Examples of graphical measurement of helical wake parameters. Top to bottom: 0°, 30°, 60°, -30°, -60°. Left: V_a = 0.82 ft/s, RPM = 300 (J = 0.2) (moderate loading). Right: V_a = 1.31 ft/s, RPM = 240 (J = 0.4) (light loading).

Table 5-1: Fluorescent paint visualization. Summary of graphical measurement of helical wake parameters. First helix P/D and wake angle are averages take over 10 measured image sets for each operating condition. Mean axial induced velocity calculated using equation (5.3).

V_a (ft/s)	n (rev/s)	Advance coefficient $\left(J \equiv \frac{V_a}{nD}\right)$	Azimuth angle (deg) δ	First helix P/D (mid-blade wake) (average of 10)	Wake angle (deg) (average of 10)	Axial induced velocity V_{Ai}/V_a (mean, calculated)
0.82	5.0	0.2	-60	0.56	15	2.32
0.82	5.0	0.2	-30	0.56	11	1.94
0.82	5.0	0.2	0	0.56	0	1.82
0.82	5.0	0.2	30	0.56	11	1.93
0.82	5.0	0.2	60	0.56	16	2.30
1.31	4.0	0.4	-60	0.51	35	0.78
1.31	4.0	0.4	-30	0.51	24	0.41
1.31	4.0	0.4	0	0.51	0	0.27
1.31	4.0	0.4	30	0.51	25	0.41
1.31	4.0	0.4	60	0.51	37	0.77

Equation (5.3) could theoretically be used to calculate an approximate mean axial induced velocity, based upon the P/D ratio measured from the visualization. For example, for the wake at J = 0.2, n = 5 rev/s, and $\delta = 0°$, the approximate mean axial induced velocity can be calculated

$$V_{Ai} = nD\left(\frac{P}{D} - J\cos\delta\right) = (5\text{ rev/s})(0.8229\text{ ft})(0.56 - (0.2)\cos 0°) = 1.49\text{ ft/s}$$

or non-dimensional $V_{Ai}/V_a = 1.82$. Calculated approximations for the mean axial induced velocity for each condition have been added to table 5.1.

Measurement of blade pitch on both sides of the propeller wake, as shown in figure 5-3, provides an illustration of the wake distortion which occurs when the propeller is subjected to oblique inflow. The upstream side of the wake is stretched, while the downstream side of the wake is compressed. The net effect is a slight difference in wake pitch as measured on the upstream and downstream sides of the wake. The blade pitch/diameter ratios calculated and used in table 5-1 are taken from the mean of the upstream and downstream wake pitch measurements from each image.

Table 5-1 also shows that the P/D ratio is greater for the condition with the moderate propeller loading (J = 0.2) and less for the condition with the light propeller loading (J = 0.4). This is as expected. The theoretical no-slip P/D (i.e. the "no load" condition, at zero net thrust) is

approximately 0.43 (taken from figure 2-2, with accounting for the small parasitic drag associated with the propulsor pod). The P/D for the light loading condition is closer to the theoretical no-slip P/D ratio, as expected.

From observations made following the conduct of smoke wake studies of helicopter rotors in the early 1950s, R.B. Gray [28], [29] concluded that the wake from a blade consisted of a strong tip vortex and an inner vortex sheet of opposite sense. Gray observed that the outer part of the sheet moved faster than the inner part, and that the outer part of the sheet moved much faster than the tip vortex. Landgrebe conducted additional smoke tests which confirmed Gray's result and also reported that the tip vortices do not necessarily occur at the ends of the corresponding sheet [49], [20], but rather lag behind. It was reported that the blade tip vortex moved downwards relatively slowly until it passed beneath the following blade, from which point it moved down more rapidly, although always lagging behind the corresponding blade wake.

Although the blade geometry and loading distribution of a helicopter blade is clearly different than a "typical" marine propeller, it can be expected that the same basic relationship between blade and tip helices would remain. This relation was clearly observed from the paint visualization, and was the main initial source of difficulty in consistently measuring blade wake pitch as previously noted. As the blade wake is shed and convects in the wake, the region of the wake in the tip region (i.e. the tip vortex) can be clearly seen to move much more slowly than the rest of the blade wake. This is pointed out by annotation of the image sequence shown in figure 5-4. This sequence is taken at 30 Hz (6 images per revolution), thus the image sequence shows one revolution of the propeller. The separation of the blade wake from the tip vortex is annotated for blade wake sheets on both sides of the image. It is clear that the initial velocity of the tip vortex is significantly less than the rest of the blade, at least for the first diameter downstream. Beyond this, there is too much diffusion to follow the paint track. This will be illustrated again when reviewing the PIV visualization technique in the next section.

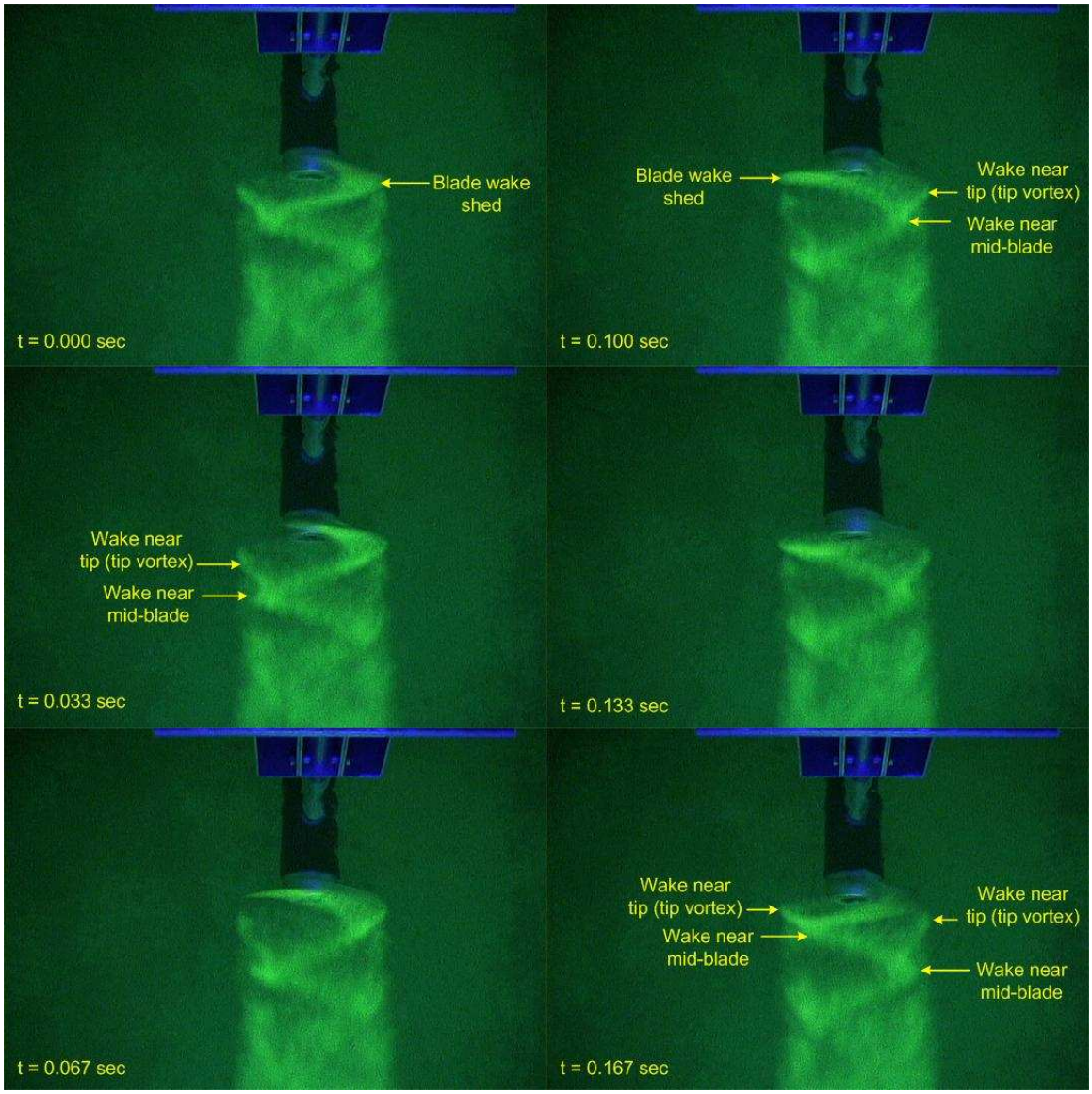

Figure 5-4: Fluorescent paint visualization. Visualizing the track of the blade wake. Note separation of wake near tip (tip vortex) from main blade wake as wake convects downstream. V_a = 0.82 ft/s, RPM = 300 (J = 0.2), δ = 0°.

5.1.2.2 Unsteady/transient visualization results

Each visualization run included 3 rapid dynamic/transient changes in azimuth angle (for example from 0° to 60°, 60° to -60°, and -60° to 0°). The rapid changes amounted to rapid saturated ramp azimuth changes (from a step command change to the azimuth gearmotor). The purpose of these rapid dynamic azimuth changes was to investigate the correlation between the change in propulsor maneuvering forces (e.g. sway force F_y) and the progression of the helical

wake during a very rapid propulsor azimuth maneuver. Figure 5-5 provides an example image sequence of the dynamic change in azimuth angle (here from 0° to 60°) and the corresponding normalized change in sway force (F_y). Despite the large amount of "noise" in the force signal due to the resonant vibration of the test fixture, the fundamental result is rather clear. As can be clearly seen from the sequence, the maximum sway force has already been reached upon the completion of the azimuth maneuver (i.e. upon the propulsor reaching 60°). Another way of looking at this is to note that for the image at t = 20.60 seconds, where the sway force has already reached its maximum, the blade wake has not progressed. In other words, the blade force *leads* the azimuth. This can be supported using a simple "dynamic inflow" model, as will be discussed in detail in Chapter 7, where it will be shown that the blade forces can be predicted to *lead* the angle during a propulsor azimuth maneuver. This is indeed consistent with the force test results presented in Chapter 4.

It will be discussed in detail in Chapter 7 that a plausible explanation for the asymmetry seen in the force tests for unsteady propeller rate (Chapter 4) may be described in terms of the unsteady *3-dimensional* vorticity that is generated and shed into the wake with a rapid increase in propeller rate. The jet-like acceleration of the slipstream, in conjunction with viscosity, results in the formation of a 3-dimensional ring vortex, which quickly plumes outward, then convects downstream with the slipstream. In consideration to the Biot-Savart law, this vortex ring induces additional velocity at the propeller disk, in effect decreasing the angle of attack at the blades. This conception is made partially based upon the visualizations of the unsteady wake with the rapid increase in propeller rate due to a step increase in motor current. Figure 5-6 provides an image sequence showing the vortex ring which forms as the vorticity is rapidly shed from the blades following a motor current step increase for zero advance velocity. Images are 0.1 seconds apart. Owing to its size and location, it is easy to see that the toroidal vortex ring would have a substantial influence on the induced velocities at the propeller disk. In particular, given the direction of the rotation of the vortex ring, it *increases* axial velocity at the disk, with the effect of *decreasing* the angle of attack at the blades, and therefore *decreasing* the blade forces (thrust, torque). This provides a potent potential explanation for the *reduced lead* dynamic inflow time constant (or *lag* in some cases) of the thrust and torque compared to the propeller rate in transient response tests discussed in Chapter 4. Figure 5-7 provides an image sequence showing the progression of the vortex ring under similar conditions, but viewed from within the clear acrylic window downstream of the propeller (see figure 5-1). Figure 5-8 provides a similar image sequence showing the progression of the wake following the motor current step increase, but here for an advance velocity of 0.82 ft/s. In this case, the forming vortex ring convects more quickly

downstream, due to the additional ambient/advance velocity. Additional background and theoretical development regarding the vortex ring formation and convection will be discussed in Chapter 7.

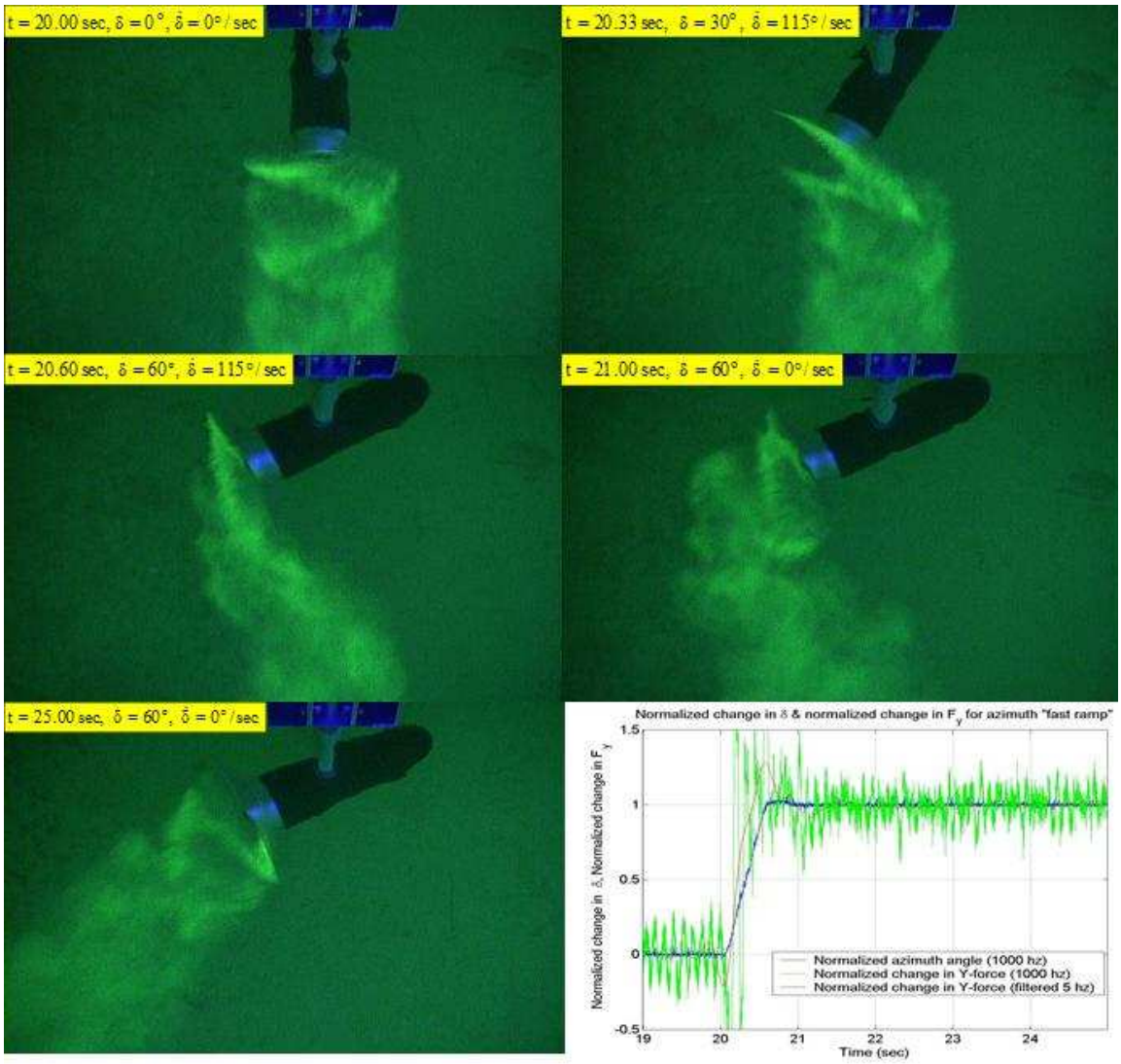

Figure 5-5: Fluorescent paint visualization. Image sequence illustrating progression of helical wake vs. sway force for a fast ramp change in azimuth angle. Plot is normalized azimuth angle (blue) and sway force (green, with filtered red). Azimuth change from 0° to 60°. V_a = 0.82 ft/s, RPM = 300 (J = 0.2).

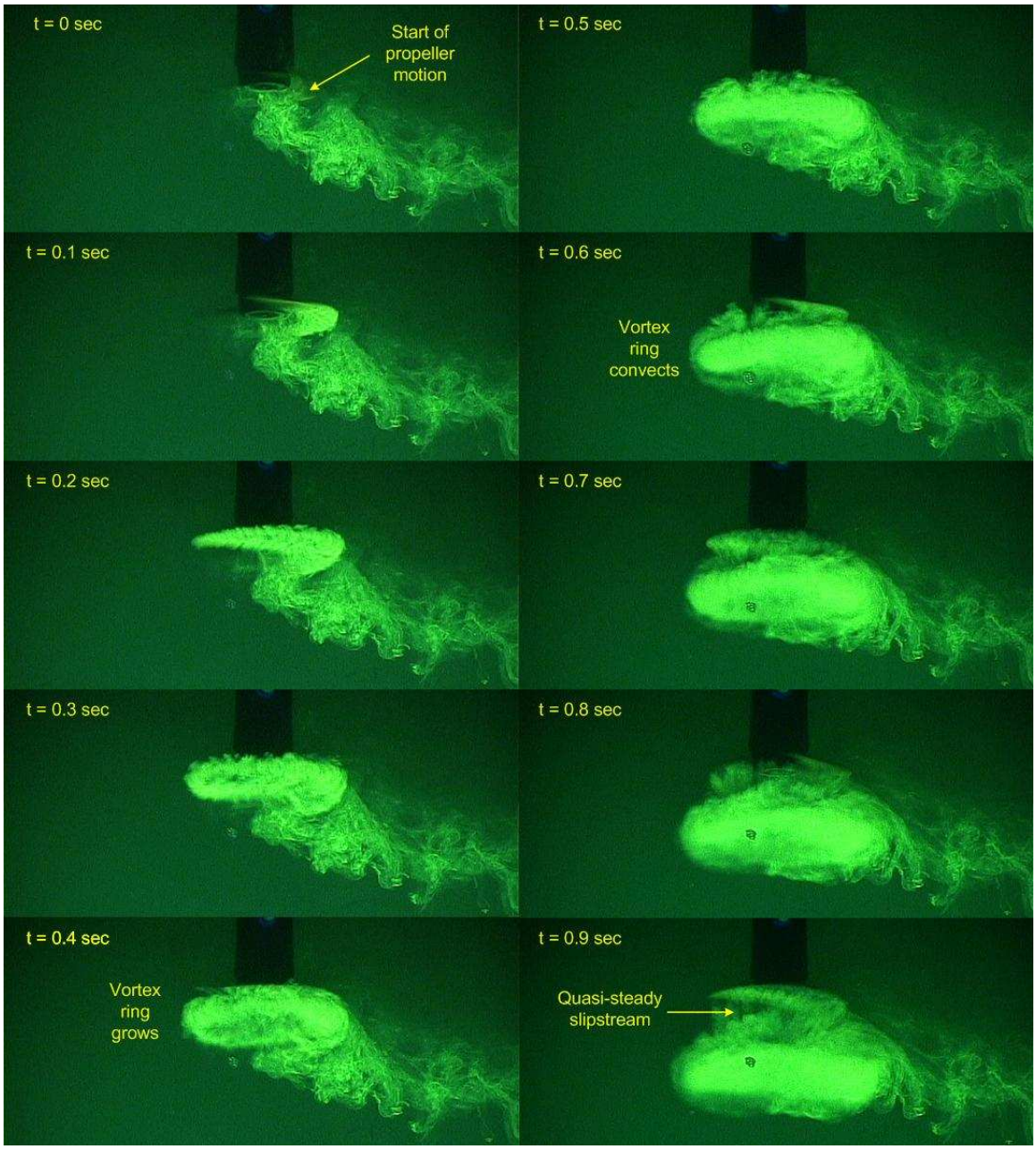

Figure 5-6: Fluorescent paint visualization. Visualization of the formation and convection of the large vortex ring associated with a rapid increase in propeller rate, here a step increase. Final propeller rate is approximately 280 RPM. V_a = 0 ft/s. Images are separated by 1/10 second (1/2 propeller revolution at final speed).

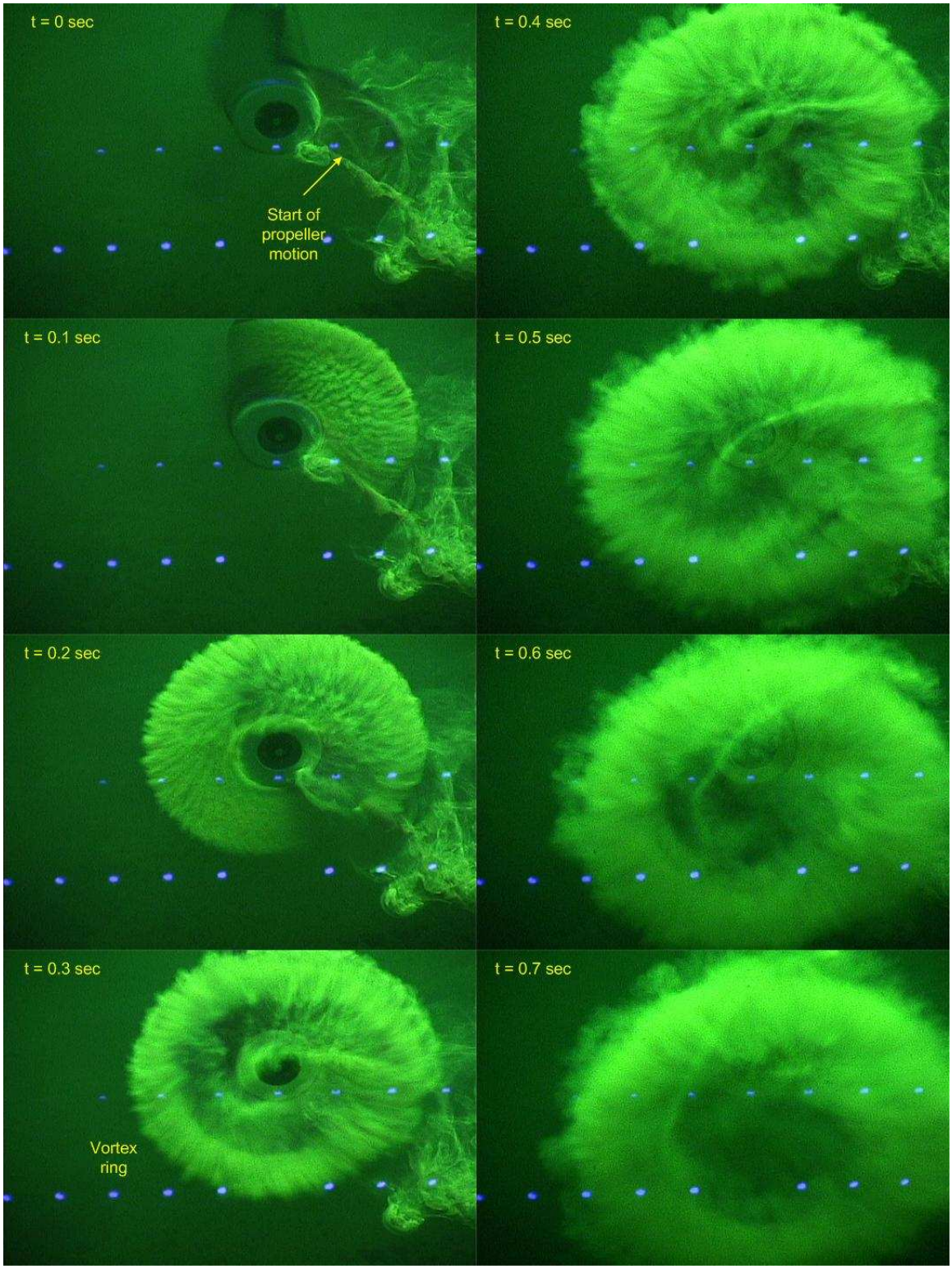

Figure 5-7: Fluorescent paint visualization. Visualization of the formation and convection of the large vortex ring associated with a rapid increase in propeller rate, here a step increase. Viewed from downstream of the propeller. Final propeller rate is approximately 300 RPM. V_a = 0 ft/s. Images are separated by 1/10 second (1/2 propeller revolution at final speed).

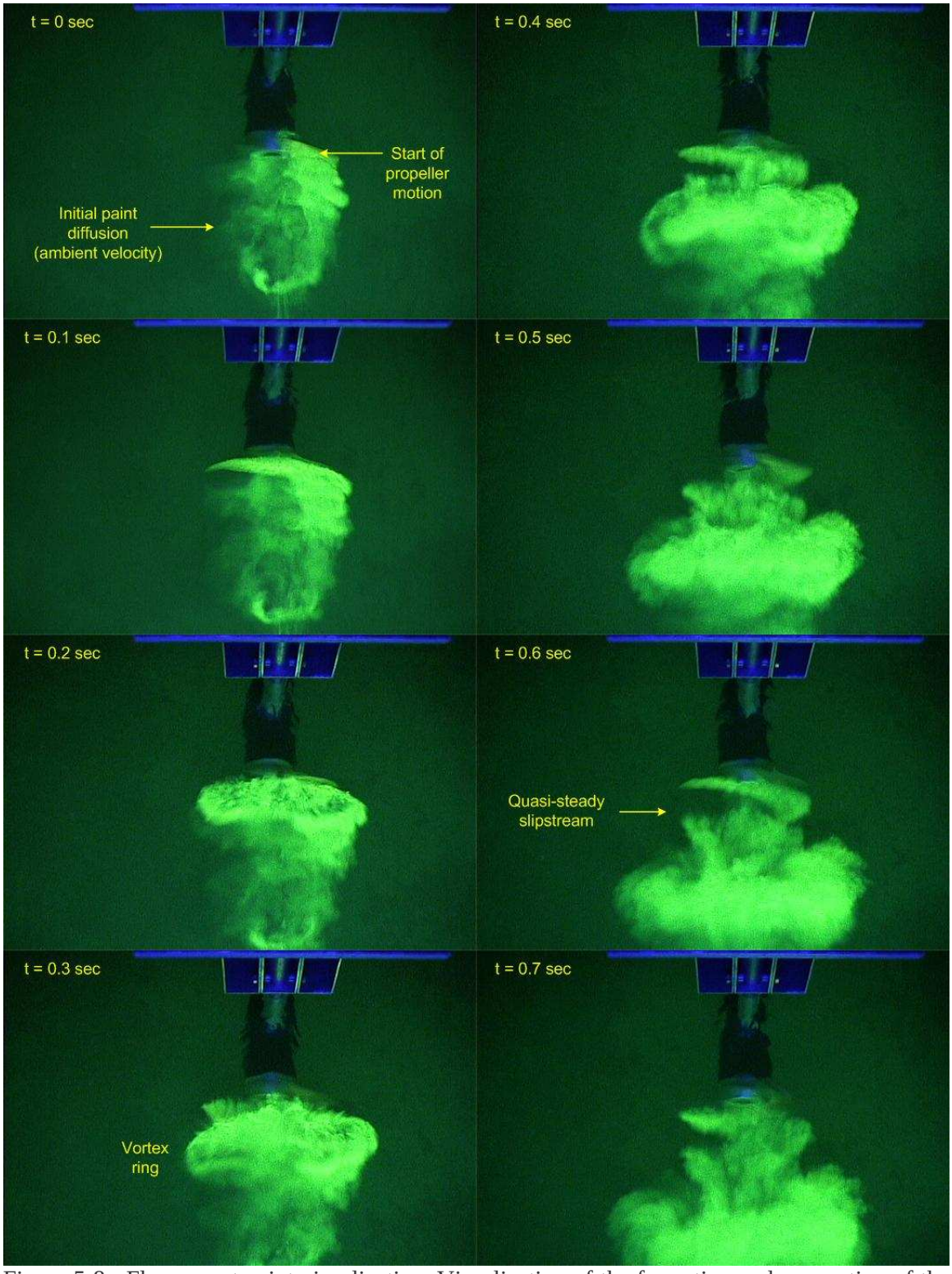

Figure 5-8: Fluorescent paint visualization. Visualization of the formation and convection of the large vortex ring associated with a rapid increase in propeller rate, here a step increase. Final propeller rate is 300 RPM. V_a = 0.82 ft/s. Images are separated by 1/10 second (1/2 propeller revolution at final speed).

5.2 Particle image velocimetry (PIV)

In addition to the wake visualization using the fluorescent paint method, a particle image velocimetry (PIV) technique was adapted for use in the MIT recirculating water tunnel to visualize the wake and measure and document the velocities within the wake for a number of quasi-steady and transient conditions. It is anticipated that the characterization of the wake in this manner provides a means for better understanding the complex flows associated with an azimuthing propulsor, as well as providing an additional tool for validation of unsteady codes and flow modeling tools.

5.2.1 Experimental setup and procedure

Quasi-steady and dynamic wake visualization, documentation, and additional dynamic testing were conducted in the MIT recirculating water tunnel utilizing an existing test fixture incorporating three coplanar axial strain-gauge load cells with amplifiers, as shown in figure 5-9. The servo gearmotor was attached to the floating collar on the fixture, and the propulsor was dynamically-azimuthed in the horizontal plane with Rulon shaft bearings through the floating collar. Data acquisition and control utilized the modular components of the autonomous surface vehicle, with a sampling rate of 1000 Hz. The main purpose of the testing in the water tunnel was to conduct dynamic wake flow visualization using particle image velocimetry (PIV) and cavitation visualization using high-speed video. The PIV utilized a New Wave Research Gemini® dual head Nd:YAG laser PIV system (120 mJ/pulse @ 532 nm), with LaVision DaVis® software for control of the laser and camera systems and initial image processing. The wake was illuminated using a horizontal laser sheet, with CCD camera (Kodak Mega plus E54.0) acquiring images of the wake from below; thus mid-plane horizontal wake cut 2D velocities were measured. In the PIV system internal triggering mode, lasers were fired at approximately 7.5 Hz. In the external triggering mode, lasers were synchronized to the propeller rotation. Internal triggering was utilized to obtain instantaneous results for dynamic wake (unsteady/transient) conditions, and external triggering was utilized to obtain phase-averaged results for quasi-steady, azimuthed conditions.

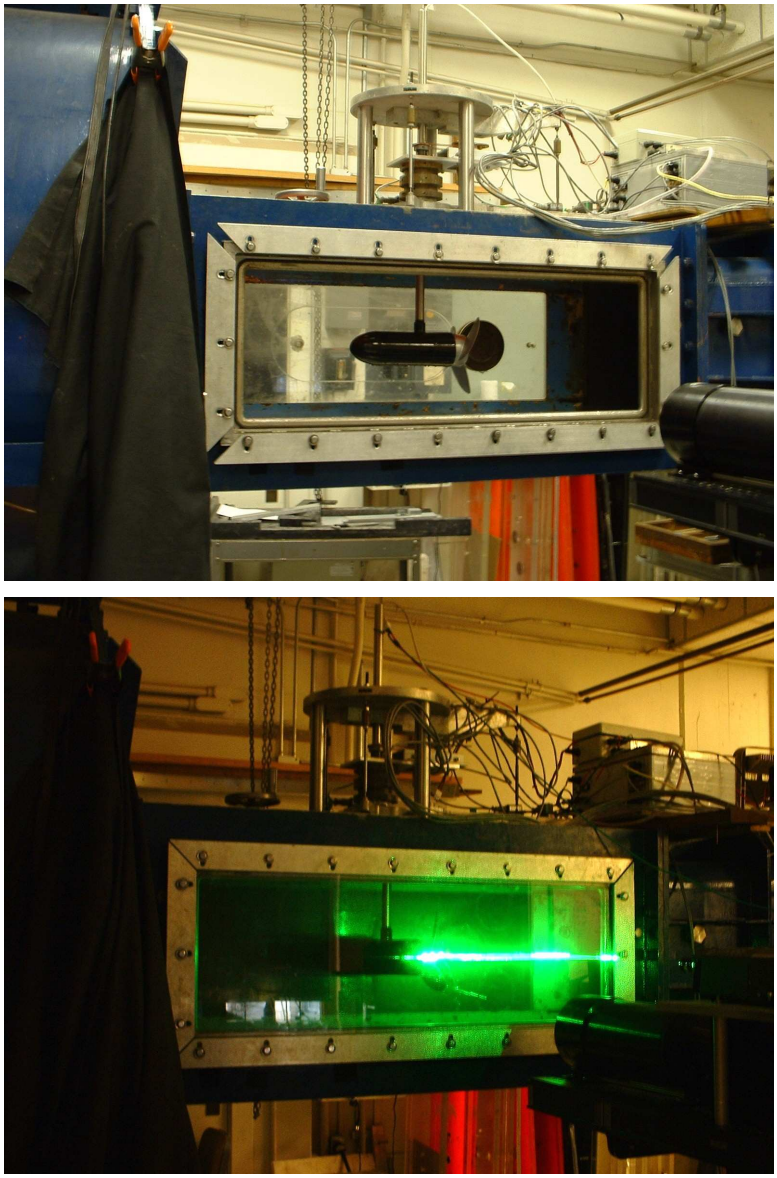

Figure 5-9: Dynamically-azimuthed propulsor in test fixture in MIT recirculating water tunnel. Wake illuminated with horizontal laser sheet.

The general approach for PIV image acquisition for the propeller wake in unsteady and oblique flow was very similar to that taken by DiFelice et al. [18] for a stationary propeller in steady axial flow, and therefore generic discussion of PIV image acquisition and processing, and application to investigation of propeller wake velocities, will not be made here; the reader is referred to DiFelice et al., and other informative papers by Willert and Gharib [80], Gui et al. [31], and Westerweel [76].

The CCD imaging camera was positioned beneath the flow, and recorded images of particle velocity fields in the horizontal mid-propulsor plane with spatial resolution of 2048 x 2048 pixels.

Image resolution was 0.01795 cm/pixel (1000 μsec between exposures providing velocity resolution 0.1795 m/s per pixel). Post-processing was conducted using a standard multi-pass window-shifting algorithm (4 pass: 64 x 64 down to 12 x 12 pixels) with 50% overlap. Produced flow fields were further post-processed in Matlab® producing maps of velocity and vorticity fields. 2-D vorticity was calculated using the curl of the 2-D velocities, and all velocities and vorticity were appropriately non-dimensionalized.

The focus in this section is on the presentation and interpretation of results of the flow visualization, and documentation of the velocities of several of the quasi-steady and dynamic wakes. Particular notice is made to the blade wake velocities, tip vortex spatial development and fluctuations, overall velocity trends, and geometries associated with the quasi-steady and unsteady/transient wakes.

5.2.2 Visualization results

5.2.2.1 Quasi-steady wake trajectories and velocities

For the quasi-steady azimuth conditions, the laser was synchronized to the rotation of the propeller, and a phase-averaging technique was utilized to calculate the quasi-steady velocities in the horizontal mid-plane of the wake. The coordinate system in all of the plots is centered on the main steering shaft of the propulsor (located 5.3125" forward of the aft face of the propeller hub, see figure 3-2). Phase-averaging in each case was made over 45 image sets, each synchronized to the same blade location.

Figures 5-10 through 5-13 provide a series of plots showing the phase-averaged velocity characteristics of the wake for quasi-steady azimuth angles 0°, 10°, 20° and 30°. Figure 5-10 provides velocity maps with the magnitude of the total in-plane velocity, normalized by the free-stream velocity (measured upstream of the propulsor). Figure 5-11 provides velocity maps with the magnitude of the perturbation (induced) velocity, also normalized by the free-steam velocity. Figure 5-12 provides the RMS velocity fluctuations, also normalized by the free-stream velocity. Figure 5-13 provides maps of the distribution of the calculated vorticity, nondimensionalized by the free-stream velocity and the propeller diameter.

These plots clearly demonstrate the character of the quasi-steady wake for small to moderate propulsor azimuth. The viscous wake due to the boundary layer on the blades is highlighted by the defect in induced velocity plots and vorticity distributions. These velocity defects transition

from the root to the tip vortex, and rapidly diffuse as the wake convects downstream. The traces of the tip vortices are obvious, particularly in the plots of induced velocity and vorticity distribution. But, tip vortices also rapidly roll-up, split, and diffuse as they convect downstream. The slower relative velocity of the tip vortices as discussed in Section 5.1.2 is also clearly seen, particularly in the plots of vorticity. Highlight should be made to the significant hub wake (due to the very large and flat-faced hub that is 1/3 the diameter of the propeller), which produces significant turbulence in its wake, creating additional unsteadiness to the wake. The strong hub wake consists of strong tangential velocity components, which are evident in all the plots.

Figure 5-14 provides a comparison between the phase-averaged vorticity distribution at 20 degrees and three of the instantaneous vorticity distributions which are among the 45 used for the phase-averaging. The hub wake is clearly the area with the greatest variability, which is also shown clearly as an area of high intensity in the plots of RMS velocity fluctuations, figure 5-12. However, despite the fact that the tip vortices in the phase-averaged plot appear to be non-uniformly distributed, their positioning and even intensity appears with little variability compared to the instantaneous plots, at least within the first propeller radius downstream (this is also shown clearly as an area of very low intensity in the plots of RMS velocity fluctuations, figure 5-12).

To further examine the character of the tip and hub vortices, several experiments were conducted of cavitation visualization using a high-speed video system and reduced pressure in the propeller tunnel. Figure 5-15 shows two images (taken at approximately the same propeller position) which illustrate the 3-dimensional nature of the tip and hub vortices. As can clearly be seen, the tip vortices within the first propeller radius downstream are generally stable and consistent. However, as the tip vortices convect downstream, they are seen to split and rapidly diffuse.

To tie the PIV results presented in figures 5-10 to 5-13 into the results for the force measurements presented in Chapter 4, it is noted that the average total and average perturbation (induced) velocities for the conditions with azimuth are noticeably greater than the 0° condition. This increase in wake velocity would be intuitively linked to an increase in thrust. For example, for the 20 degree azimuth condition (conditions noted in the figure captions), this is consistent with the 20% increase in thrust which can be estimated from figure 4-11.

One other important note should be made regarding the quasi-steady azimuth wake velocities from the PIV. It is clear from this figures 5-10 to 5-13 that the magnitude of velocity (or induced velocity) is greater for the “upstream” or “outboard” side of the wake for the azimuthed case (for the horizontal wake cut). An explanation for this wake velocity asymmetry can be understood by considering that the vortex wake undergoes distortion under the oblique inflow. Experiments for

helicopters in forward flight have confirmed vortex wake distortion effects, and progress has been made in modeling this distortion using free-vortex wake models [51], [8]. The net result is that the “upstream” side of the vortex wake is stretched (and the “downstream” side is compressed), such that the “upstream” wake velocities are higher. For these relatively small azimuth angles, the effect is minimal, but noticeable. This was also clearly illustrated in the fluorescent paint visualization discussed in the previous section.

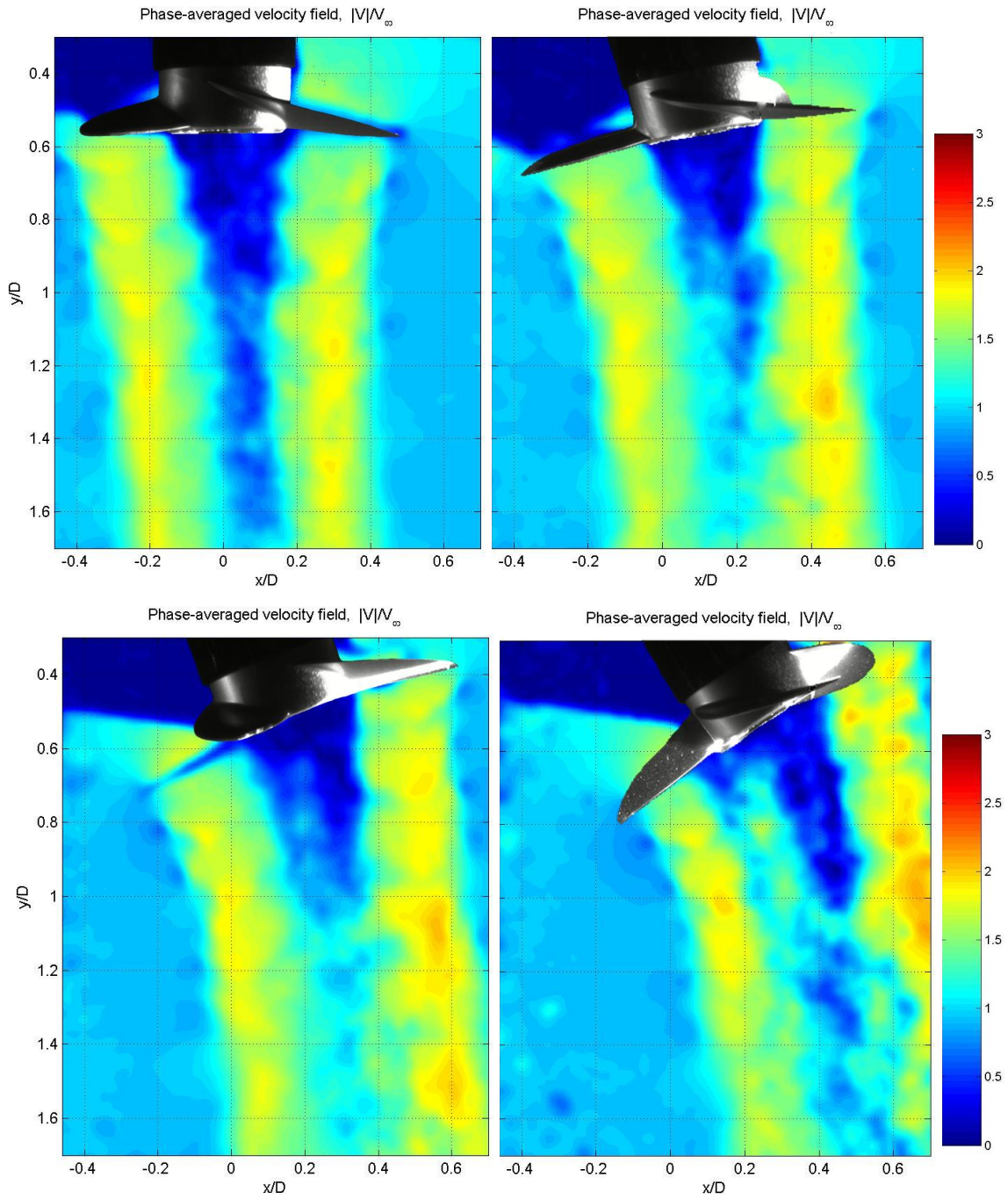

Figure 5-10: PIV. Quasi-steady phase-averaged velocity field magnitude (normalized by free-stream velocity). RPM = 700, V_∞ = 3.05 ft/s (J = 0.32), δ = 0° (top left), 10° (top right), 20° (bottom left) and 30° (bottom right).

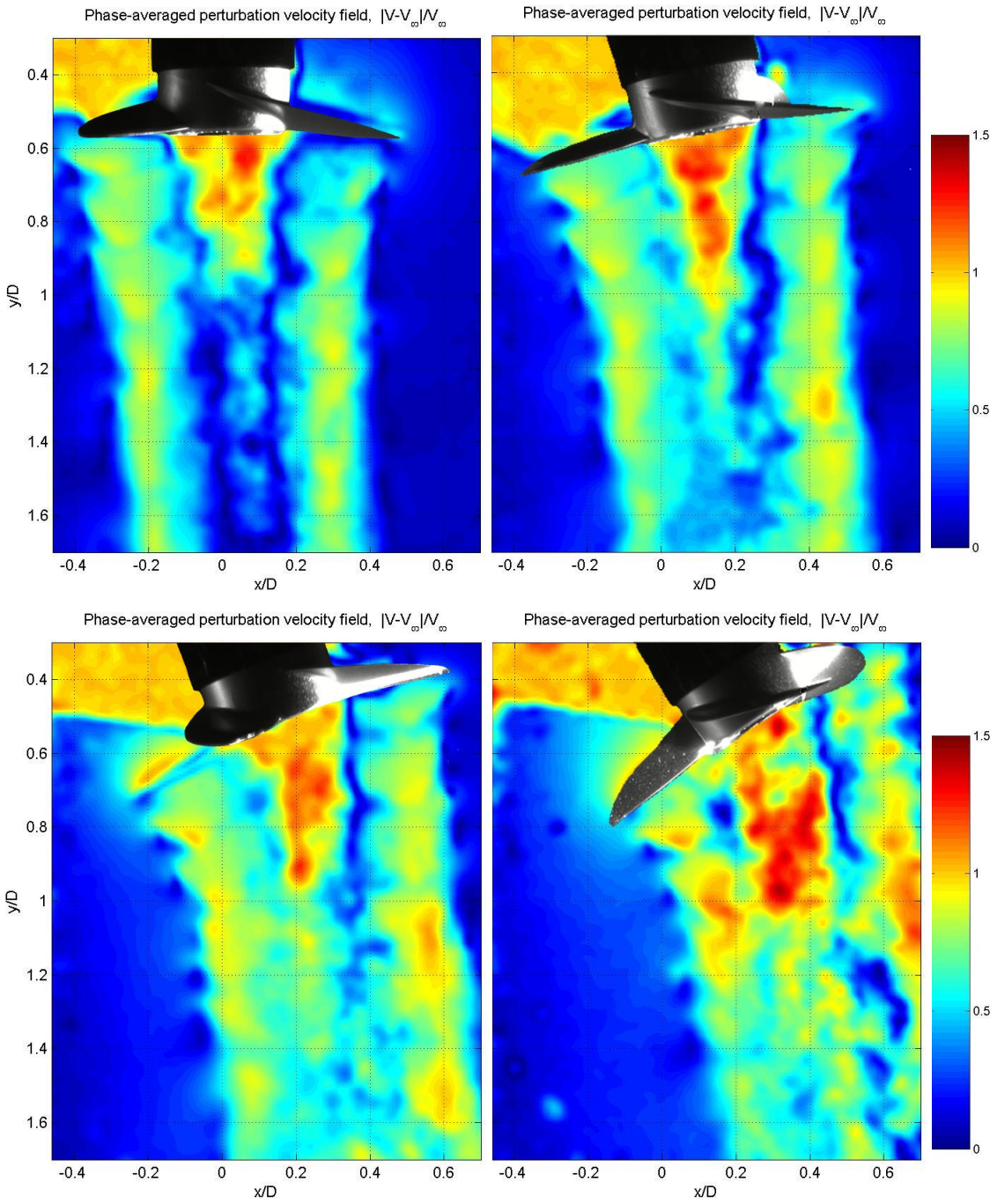

Figure 5-11: PIV. Quasi-steady phase-averaged perturbation (induced) velocity field magnitude (normalized by free-stream velocity). RPM = 700, V_∞ = 3.05 ft/s (J = 0.32), δ = 0° (top left), 10° (top right), 20° (bottom left) and 30° (bottom right).

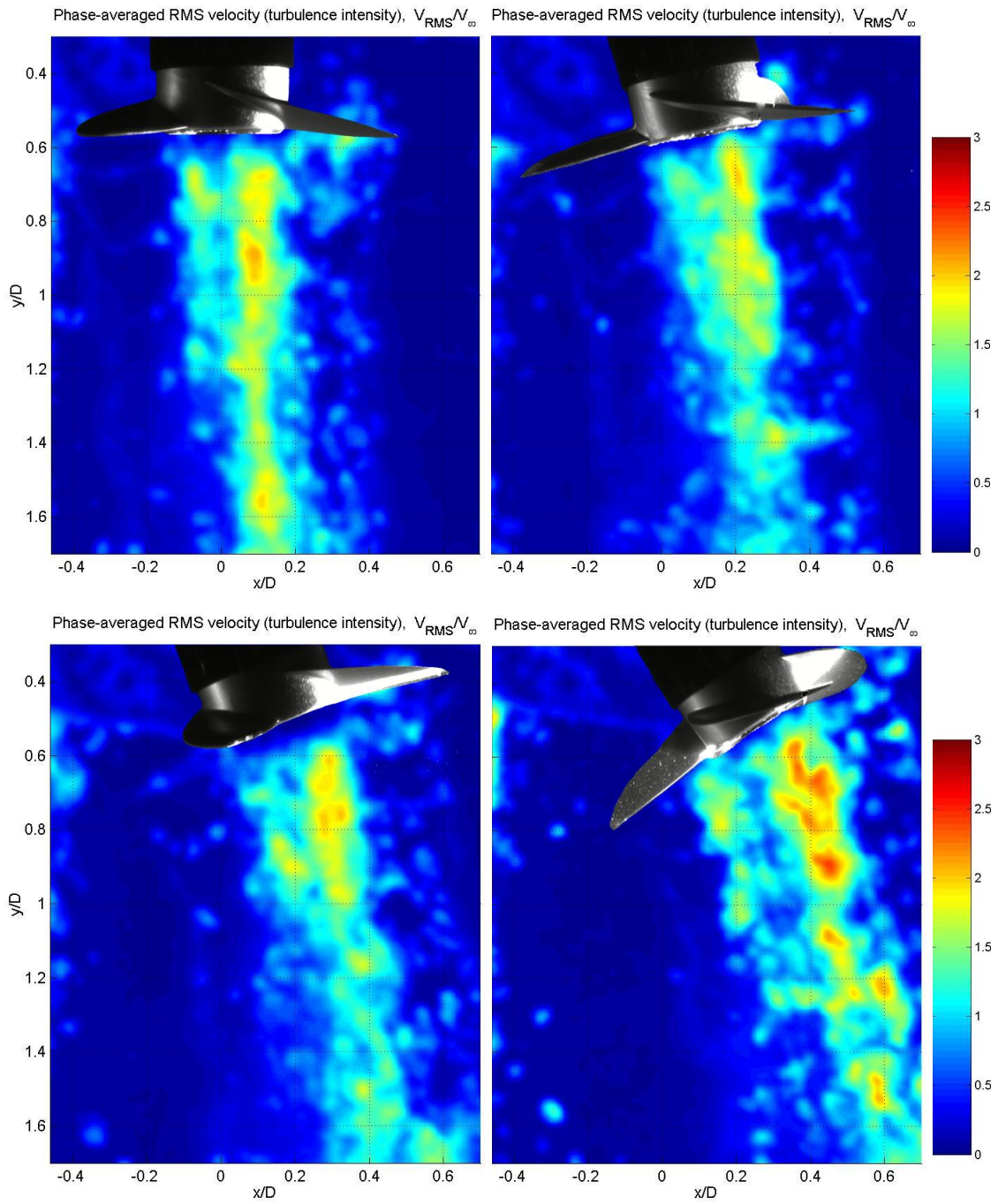

Figure 5-12: PIV. Quasi-steady phase-averaged RMS velocity fluctuation (turbulence intensity) (normalized by free-stream velocity). RPM = 700, V_∞ = 3.05 ft/s (J = 0.32), δ = 0° (top left), 10° (top right), 20° (bottom left) and 30° (bottom right).

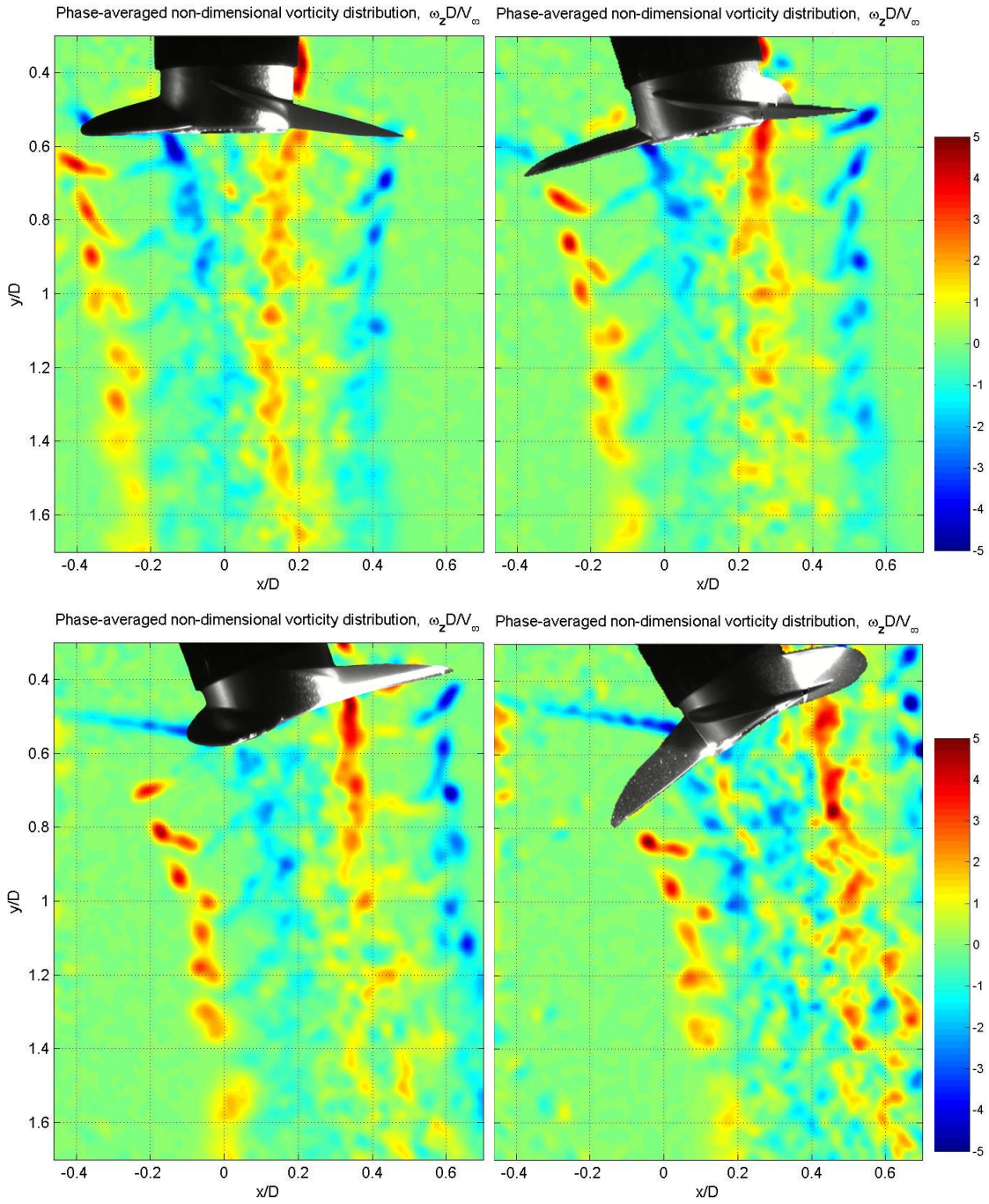

Figure 5-13: PIV. Quasi-steady phase-averaged vorticity distribution (nondimensionalized by free-stream velocity and propeller diameter). RPM = 700, V_∞ = 3.05 ft/s (J = 0.32), δ = 0° (top left), 10° (top right), 20° (bottom left) and 30° (bottom right).

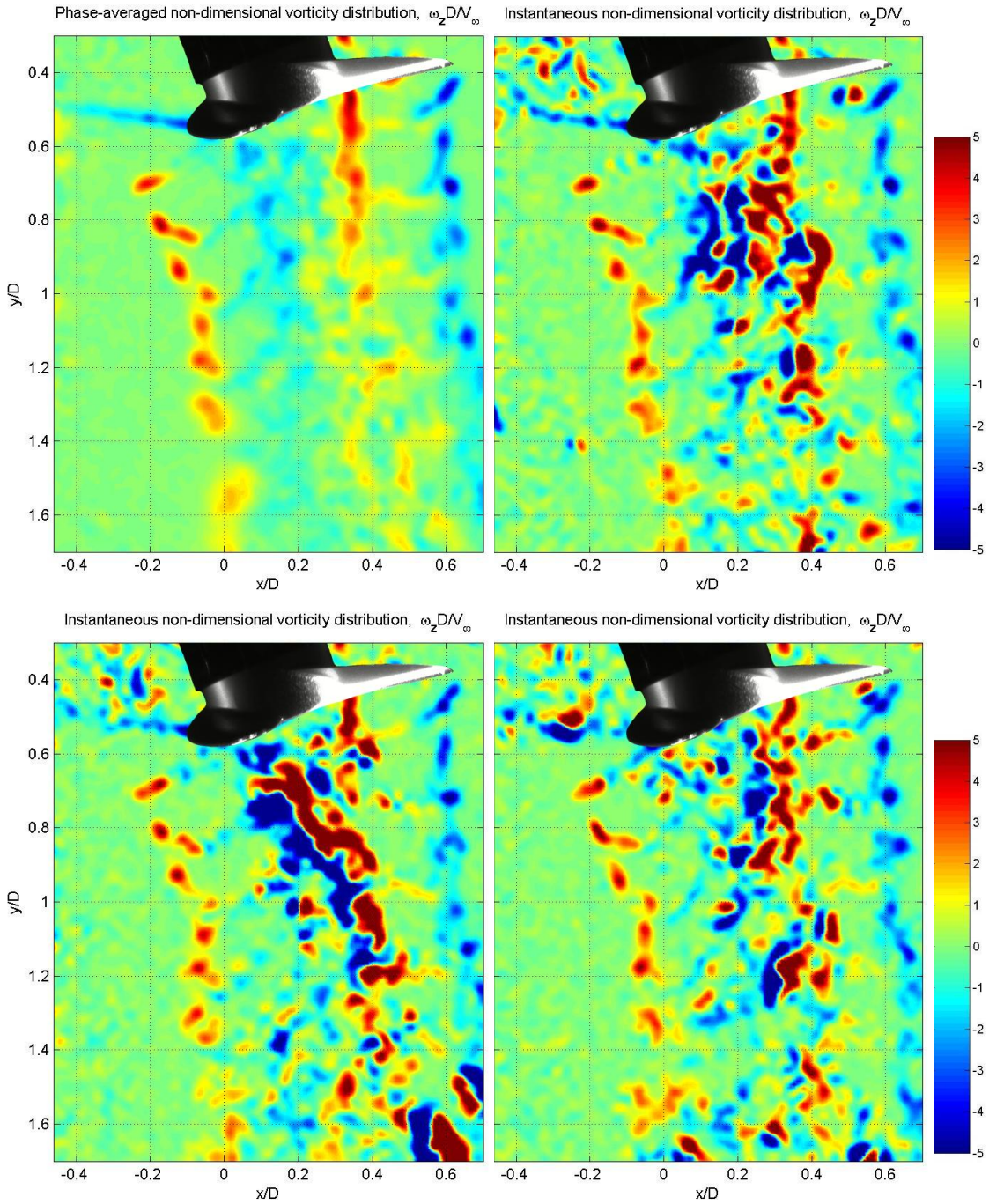

Figure 5-14: PIV. Quasi-steady vorticity distribution (nondimensionalized by free-stream velocity and propeller diameter). Phase averaged (upper left) vs. instantaneous (others). RPM = 700, V_∞ = 3.05 ft/s (J = 0.32), δ = 20°.

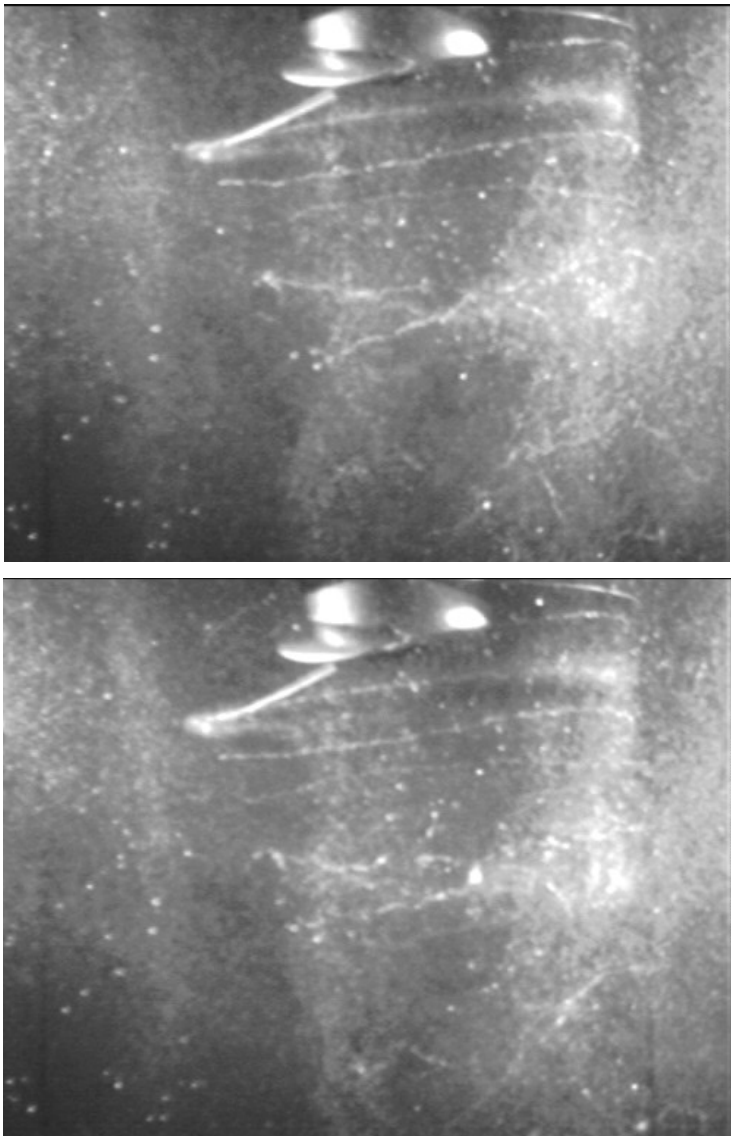

Figure 5-15: High speed video cavitation visualization. RPM = 1050, V_∞ = 1.6 ft/s (J = 0.11), δ = 15°. Uneven tip vortex rollup is clearly evident.

Figure 5-16 shows measurement of the helical wake pitch/diameter ratio and approximate helical wake skew angle. Note that plot length scales are already non-dimensionalized by diameter D, and that values measured are for 2 blades (i.e. P/D = 3/2 * value measured). A summary of these measurement results is given in table 5-2. Similar to the fluorescent paint visualization, the P/D ratio does not change with increase in azimuth angle (although there is a slight apparent "distortion" of the wake as mentioned previously). As a check, the measured P/D ratio can be used to calculate an approximate velocity (total or induced) using equation (5.3), and the results compared to the PIV total velocities from figures 5-10 or induced velocities from

figure 5-11. For example, for $\delta = 0°$, with $V_a = 3.05$ ft/s and n = 11.667 rev/s (J = 0.32), using equation (5.3)

$$V_{Ai} = nD\left(\frac{P}{D} - J\cos\delta\right) = (11.667\text{ rev/s})(0.8229\text{ ft})(0.59 - (0.32)\cos 0°) = 2.59\text{ ft/s}$$

or non-dimensional $V_{Ai} / V_\infty = 0.85$, which is close to the approximate value of 0.8 in the blade wake taken from figure 5-11.

Table 5-2: PIV. Summary of graphical measurement of helical wake parameters from PIV. First helix P/D and wake angle are taken from measurements of phase-averaged vorticity plots. Helix P/D is for mid-blade helical surface.

V_a (ft/s)	**n (rev/s)**	**Advance coefficient** $\left(J \equiv \frac{V_a}{nD}\right)$	**Azimuth angle (deg)** δ	**First helix P/D (mid-blade wake) (average)**	**Wake angle (deg) (average)**
3.05	11.667	0.32	0	0.59	0
3.05	11.667	0.32	10	0.59	4.1
3.05	11.667	0.32	20	0.59	9.6
3.05	11.667	0.32	30	0.59	15.5

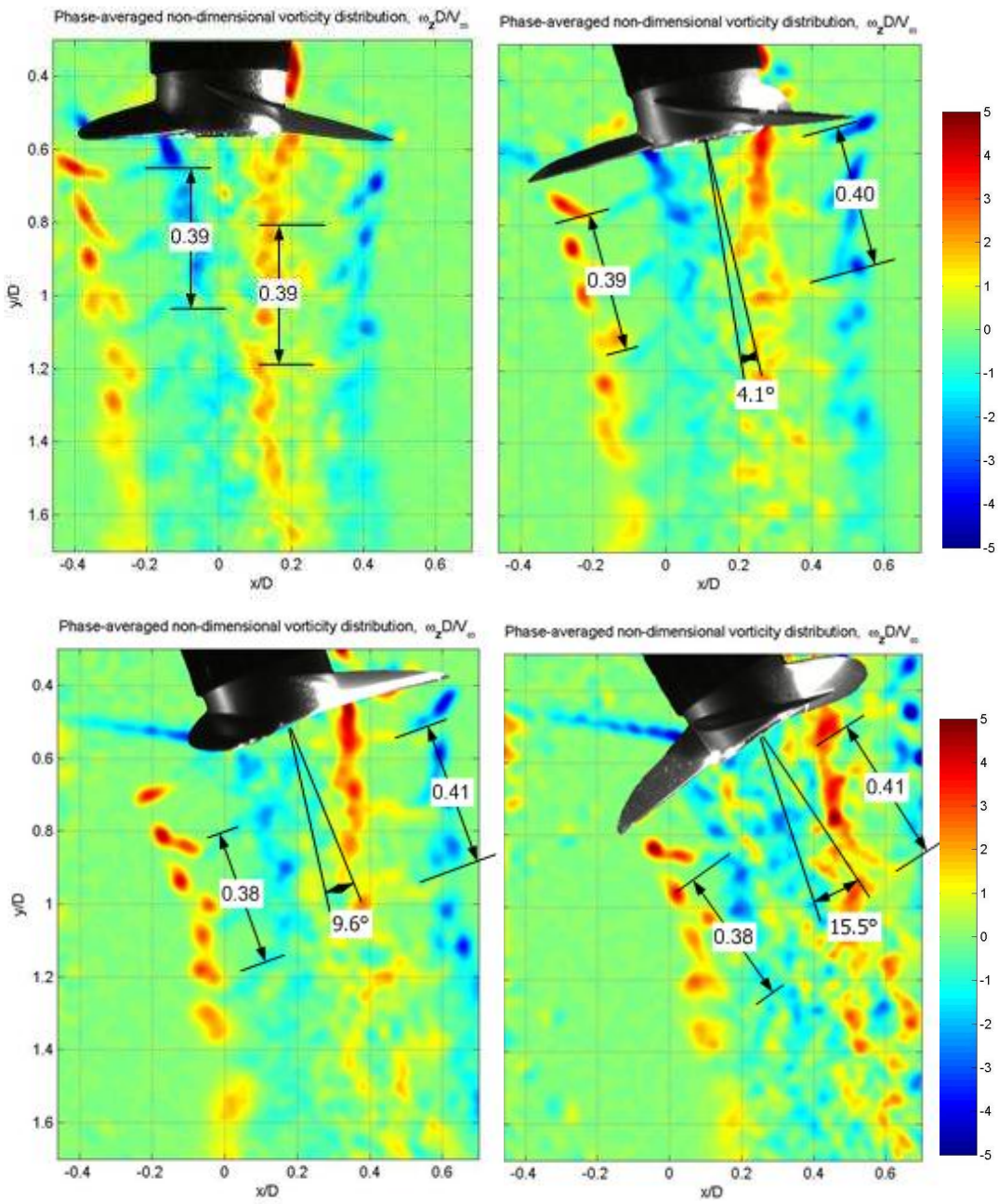

Figure 5-16: PIV. Graphical measurement of helical wake parameters. First helix P/D and wake angle are approximated from measurements of phase-averaged vorticity plots. Helix P/D is for mid-blade helical surface (note: value measured is for 2 blades: P/D = 3/2 (value measured)). V_a = 3.05 ft/s, RPM = 700 (J = 0.32).

5.2.2.2 Transient wake trajectories, velocities and force measurements

Section 5.1 provided a fluorescent paint visualization of an unsteady azimuth rate in terms of a fast ramp change in azimuth angle (from a step command change to the azimuth servo gearmotor). The results provided a visualization and rough correlation between the change in propulsor maneuvering forces (e.g. sway force F_y) and the progression of the helical wake during a very rapid propulsor azimuth maneuver, and provided confirmation of a lead in sway force vs. azimuth angle. The PIV system was also used to visualize a set of rapid propulsor azimuth maneuvers, in the form of a sinusoidal azimuth. Figure 5-17 provides two of the resulting velocity maps, taken from image sets at a point very close to the zero degree cross-over (within 2°), for frequencies of 0.5 and 0.25 Hz. The velocity maps clearly show the geometric lag of the wake behind the azimuth angle. As expected, the higher frequency azimuth (faster azimuth rate) has a larger geometric lag. Figure 5-18 provides the corresponding azimuth and sway force (F_y) records (unfiltered and filtered). As discussed in Chapter 4, an approximation to the dynamic inflow time constant is the time lead of the sway force vs. azimuth angle. Here, the resulting lead of sway force at both frequencies gives an estimate of the dynamic inflow time constant to be approximately 0.06 sec which equates to approximately 0.7 propeller revolution (at 700 RPM).

Section 5.1 also provided a fluorescent paint visualization of the results of a rapid change in propeller rate, specifically in terms of the generation of a large vortex ring, and its convection downstream with the slipstream. The PIV system was also used to visualize a rapid change in propeller rate in terms of the generation and convection of the large vortex ring. Figure 5-19 provides an image sequence showing the progression of the wake following a motor current step increase. Images here are taken from the PIV system at approximately 7.5 Hz. As with the fluorescent paint visualization, the formation and convection of the vortex ring can clearly be seen, and its impact on the induced velocities at the disk understood.

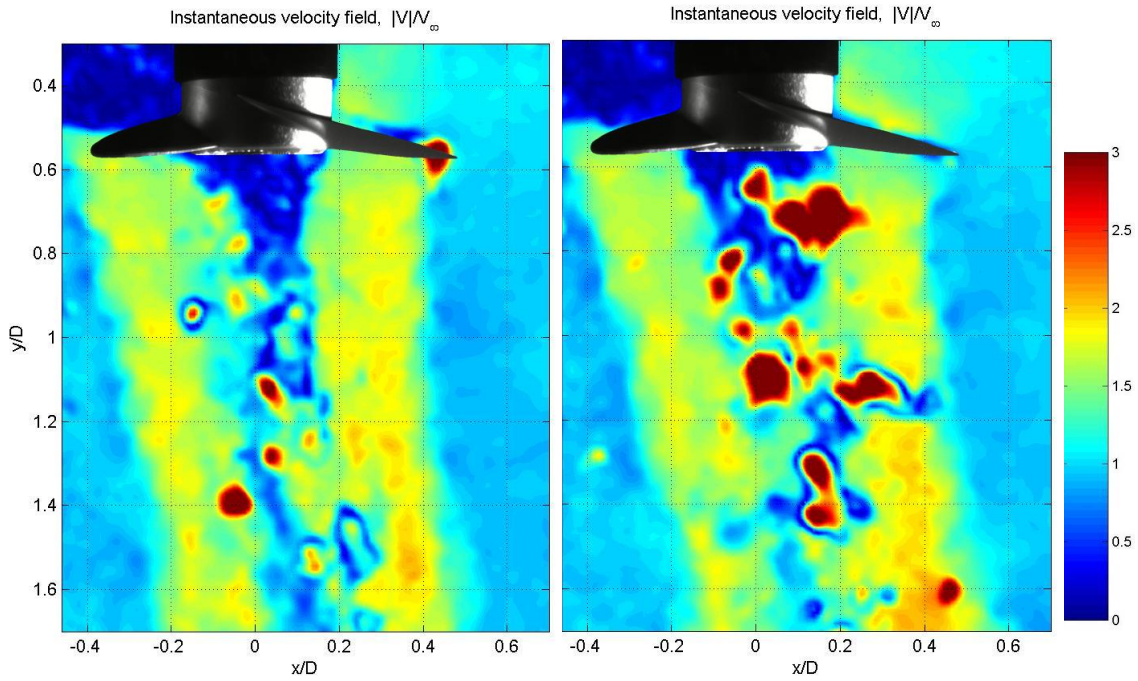

Figure 5-17: PIV. Dynamic/transient instantaneous velocities (nondimensionalized by free-stream velocity). RPM = 700, V_∞ = 3.05 ft/s (J = 0.32). Sinusoidal azimuth trajectory $\delta(t) = 15° \sin(2\pi ft)$. Left: f = 0.25 hz., $\delta \approx 0$, $\dot{\delta} \approx -25°/\sec$. Right: f = 0.5 hz., $\delta \approx 0$, $\dot{\delta} \approx -49°/\sec$.

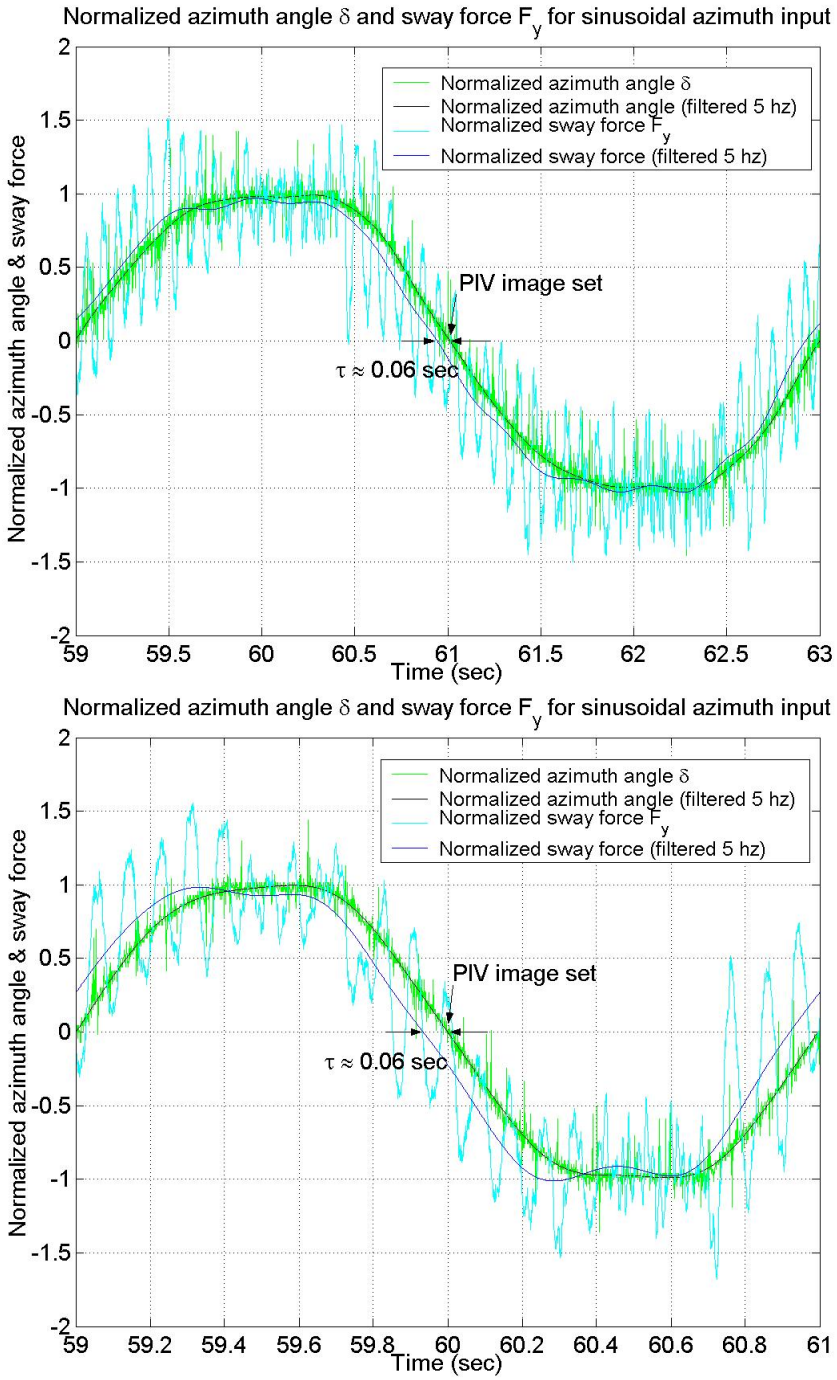

Figure 5-18: Normalized azimuth angle and normalized sway force (Fy) corresponding to PIV instantaneous velocities of figure 5-11. RPM = 700, V_∞ = 3.05 ft/s (J = 0.32). Sinusoidal azimuth trajectory $\delta(t) = 15^\circ \sin(2\pi ft)$.

Top: f = 0.25 hz., $\delta_{image} \approx 0$, $\dot{\delta}_{image} \approx -25^\circ/\text{sec}$, $\tau \sim 0.06$ sec ~ 0.7 rev.

Bottom: f = 0.5 hz., $\delta_{image} \approx 0$, $\dot{\delta}_{image} \approx -49^\circ/\text{sec}$, $\tau \sim 0.06$ sec ~ 0.7 rev.

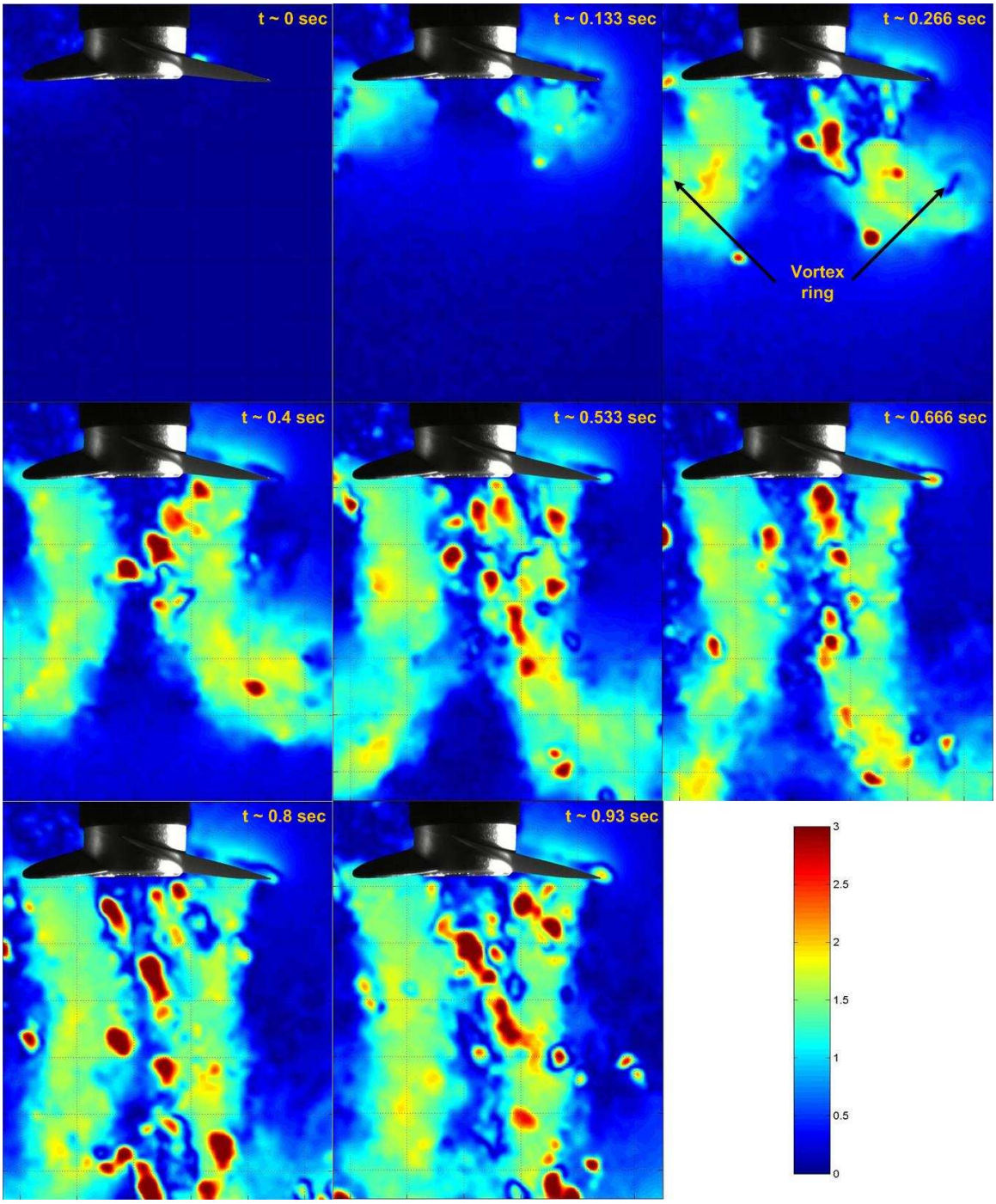

Figure 5-19: PIV. Visualization of the formation and convection of the large vortex ring associated with a rapid increase in propeller rate, here a step current increase. Initial current 0A. Final current 20A. $V_\infty = 0$. Final propeller rate approx. 600 RPM reached in approx. 0.2 sec. Instantaneous images from PIV at approx. 7.5 Hz. Colormap is absolute velocity in m/s.

5.3 Summary

This chapter has presented and discussed results of several efforts to visualize and document the steady and unsteady/transient wake of the azimuthing propulsor. A new technique using fluorescent paint and ultraviolet black light has been developed for the visualization of the vortex wake for a range of quasi-steady and unsteady/transient operating conditions. A technique using laser Particle Image Velocimetry (PIV) has also been adapted to provide more precise visualization and velocity documentation of the wake for a number of quasi-steady and unsteady/transient operating conditions.

Quasi-steady visualizations indicate that the helical wake pitch/diameter ratio for a given propeller rate does not appear to change with even large changes in azimuth angle. This is attributed to the fact that the pitch/diameter ratio for an azimuthing propeller depends not only on the advance ratio J and azimuth angle δ, but also on the axial induced velocity V_{Ai}, which depends on the propeller blade loading. Thus, there is an apparent cancellation effect with propulsor azimuth in terms of helical wake pitch/diameter ratio changes. Quasi-steady visualizations have also provided demonstration of the wake distortion effects when the propulsor is azimuthed relative to the flow. The upstream side of the wake is stretched, while the downstream side is compressed. Finally, the quasi-steady visualizations demonstrate the different convection velocities for the portion of the helical wake coming from the blade, and that portion of the wake which has rolled up into the tip vortices. The tip vortices convect downstream much slower than the corresponding blade wake.

Unsteady or transient visualizations have provided confirmation of the "dynamic inflow" effect, in terms of the leading of propeller blade forces compared to rapid propulsor azimuth. Despite the fact that the helical wake lags the azimuthal position of the propulsor, the forces lead the azimuthal position. Finally, the transient visualizations have provided powerful visual evidence of the formation and interaction of vortex rings with rapid increase in propeller rate. These vortex rings appear to induce significant velocity at the propeller disk, which would be consistent with the "asymmetric" results seen with rapid changes in propeller rate in Chapter 4.

Chapter 6

A theoretical basis for quasi-steady maneuvering dynamics

This chapter provides a detailed discussion of a theoretical basis for the quasi-steady maneuvering dynamics associated with the azimuthing propulsor over the entire range of forward operating conditions (i.e. for propulsor azimuth up to ± 90 degrees relative to the inflow). This theoretical basis begins with "simple" momentum-based models for propellers in axial and oblique inflow, and expands to include a modified combined blade-element and momentum theory, including important finite blade and wake skew considerations from vortex wake theory. Finally, a discussion of the use of computational fluid dynamics for the prediction of maneuvering forces is presented. Results of calculations made are provided in comparison with experimental results, with the relevance of consistencies and inconsistencies discussed in detail.

It is not the intent of this theoretical basis to offer a rigorous numerical method capable of accurately predicting propulsor forces, but rather to provide a physically-based intuition of the mechanisms by which the forces vary as a function of the propulsor state variables (n, V, δ) for an azimuthing propulsor. It is also noted, and will be illustrated, that in addition to propeller forces, the forces associated with the propulsor pod (i.e. motor housing plus steering shaft – without propeller), and with the interaction of pod and propeller, play an important role in the determination of propulsor maneuvering forces, especially at moderate to large azimuth angles.

The early theory of propeller action was founded in two main areas [25]. Classical momentum-based theories, which are directed mainly at the motion of the fluid and the forces necessary to impart the motion to the fluid, were initiated by W.J.M. Rankine and R.E. Froude in the mid 1800's. An extended form of the momentum theory which included the effects of slipstream rotation was developed by A. Betz in the early 1900's. The main defect of the momentum-based theories is that they give no indication of the geometry or shape of the propeller required to produce (prescribed or designed) forces (also, they give no indication of in-plane forces and moments of importance to propellers and propulsors in oblique inflow). The blade-element theories, which consider the forces experienced by the blades of the propellers in their motion through the fluid (and therefore are concerned with the geometric shape of the propeller blades and their lift characteristics) was first introduced in crude form by W. Froude in 1878, but developed mainly by S. Drzewiecki in the early 1900's. The main defect of the blade-element theories is in the uncertainty as to the characteristics which must be assumed for

generation of lift and drag forces for the blade elements (i.e. from experiment or theory of 2-dimensional foil shapes).

Modern propeller theories rest fundamentally on the conception that the lift of a foil is due to a circulation of the flow around its contour [25]. As a logical consequence of this conception, vortices must spring from the blades of the rotating propeller and pass downstream in approximately helical paths, and it is these vortices that constitute the slipstream of the propeller. These trailing vortices induce velocities which change the flow past the propeller blade elements. The vortex theory was first introduced by F.W. Lanchester in his treatise *Aerial Flight* in 1907 [74]. It is clear that, with the complex flow in the helical wake of a propeller or propulsor in oblique inflow (as could be clearly seen through the flow visualizations discussed in Chapter 5), some of the attributes embodied in the vortex theories are relevant and necessary for understanding and predicting the maneuvering forces due to a propeller or propulsor in oblique inflow.

Considering the complexity of the vortex theory of propellers in its own right, its application to a propeller (or propulsor) in oblique inflow is necessarily of even greater complexity. Even with the advent of modern computers and the development of powerful numerical methods for solving the complex 3-dimensional propeller vortex problem, most propeller design and analysis tools require some simplification and even an amount of empiricism in application to more complex flow conditions. To this end, this chapter begins with a fundamental look at the application of some of the basic momentum and blade-element theories to the performance of propellers and propulsors in oblique inflow. After the development of a basic theory for an azimuthing propulsor, some basic results from vortex theory will be applied, and a computational fluid dynamics approach will also be discussed and applied.

6.1 Steady momentum-based models for an azimuthing propulsor

6.1.1 The classical momentum propeller model

The most basic of the theories of propeller action is the so-called classical momentum theory (or actuator disk theory), which is described in detail in many references (for example [74], [25], [11], [12]). The classical momentum theory combines conservation of mass, linear momentum and Bernoulli's equation to find fluid velocity for a prescribed disk loading or thrust, or the

converse. Application of angular momentum for including effects of slipstream rotation and application of torque is also possible, and is considered in the "general" momentum model.

One method of applying the actuator disk theory is to consider a volumetric "streamtube" of flow through an idealized propeller disk (figure 6-1). The classical application of mass and momentum conservation, and Bernoulli's equation along a streamline, generally assumes the following [55]:

(a) Flow is inviscid and irrotational.

(b) Thrust loading and velocity distribution are uniform over the disk.

(c) No rotation of the slipstream is considered.

(d) A well-defined slipstream separates the flow passing through the disk from that outside the disc.

(e) Far ahead and far behind the disk, the pressure is equal to the free-stream pressure.

One important result from classical axial momentum theory is that the velocity through the propeller disk is equal to the average of the velocities in the streamtube far upstream and far downstream of the disk (V_a and V_w in figure 6-1). The increment of velocity added to the free-stream velocity is called the induced velocity V_i (note that $V_i = V_p - V_a$). The other important result is that the thrust is equal to the product of the mass flow through the propeller and the *increase* in velocity in the streamtube far upstream and downstream the propeller, or

$$T = \rho A_p V_p \left(V_w - V_a\right) \tag{6.1}$$

Combining these results gives the important result from classical momentum theory

$$T = 2\rho A_p V_p \left(V_p - V_a\right) \quad \text{or} \quad T = 2\rho A_p V_i \left(V_i + V_a\right) \tag{6.2}$$

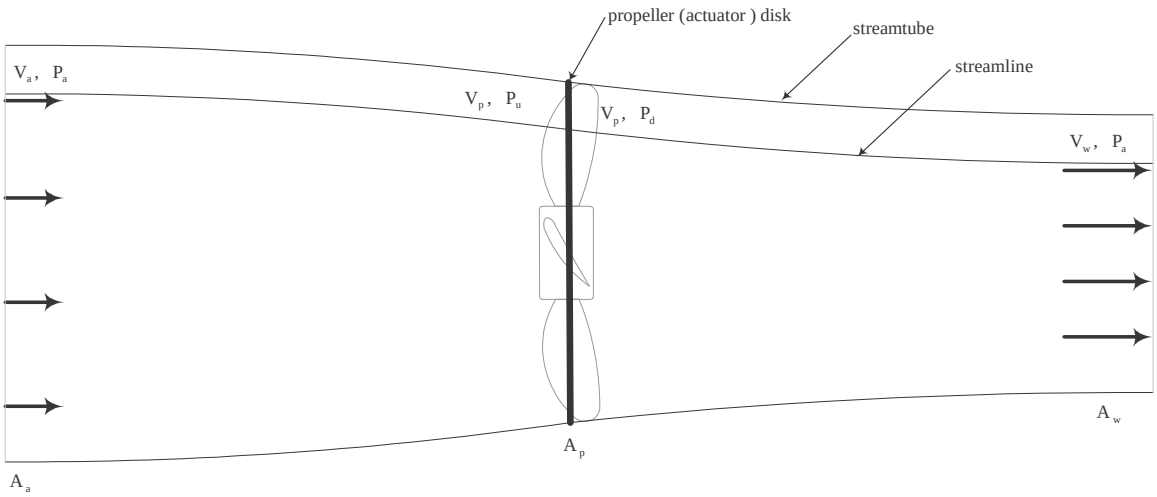

Figure 6-1: Propeller classical (axial) momentum model ("actuator disc").

6.1.2 The classical momentum propeller model modified for oblique inflow

The classical momentum theory for axial flow through a propeller can be modified for oblique inflow as shown in figure 6-2. The control volume is the streamtube with ends parallel to the propeller disk. The induced velocity perpendicular to the disk is V_i. The Bernoulli equation is applied along the streamline as shown in figure 6-2 (note that the streamline is always tangential to the flow, by definition). Conservation of momentum is applied in the x-direction (perpendicular to the disk). The component of the oblique inflow which flows perpendicular to the propeller disk is $V_a\cos\delta$, and the component parallel to the disk is $V_a\sin\delta$. Conservation of mass around the large streamtube control volume results in

$$\rho A_a V_a \cos\delta = \rho A_w \left(w + V_a \cos\delta\right) = \rho A_p \left(V_i + V_a \cos\delta\right) \tag{6.3}$$

Application of the Bernoulli equation along a streamline (including the pressure jump across the disk) results in

$$\left(p_d - p_u\right) = \frac{1}{2}\rho\overbrace{\left[\left(w + V_a\cos\delta\right)^2 + \left(V_a\sin\delta\right)^2\right]}^{V_w^2} - \frac{1}{2}\rho V_a^2 \tag{6.4}$$

Application of conservation of momentum in the x-direction in the large streamtube control volume results in

$$T = \rho A_w \left(w + V_a\cos\delta\right)\left(w + V_a\cos\delta\right) - \rho A_a \left(V_a\cos\delta\right)\left(V_a\cos\delta\right) \tag{6.5}$$

Application of conservation of momentum in the x-direction around a *negligible* control volume about the disk results in

$$T = A_p\left(p_d - p_u\right) \tag{6.6}$$

Combining equations (6.4) through (6.6)

$$\frac{1}{2}\rho A_p\left[\left(w + V_a\cos\delta\right)^2 + \left(V_a\sin\delta\right)^2\right] - \frac{1}{2}\rho A_p V_a^2 = \rho A_w\left(w + V_a\cos\delta\right)^2 - \rho A_a\left(V_a\cos\delta\right)^2 \tag{6.7}$$

Multiplying out the terms of equation (6.7) and solving for the velocity in the far wake (w) gives

$$w = 2V_i \tag{6.8}$$

This is the same result from classical momentum. Now combining the conservation of mass result, equation (6.3), with the conservation of x-momentum, equation (6.5) and using equation (6.8), results in the expression for thrust

$$\begin{aligned} T &= \rho A_w\left(2V_i + V_a\cos\delta\right)^2 - \rho A_a\left(V_a\cos\delta\right)^2 \\ &= \rho A_p\left(V_i + V_a\cos\delta\right)\left(2V_i + V_a\cos\delta\right) - \rho A_p\left(V_a\cos\delta\right)\left(V_i + V_a\cos\delta\right) \\ &= \rho A_p\left[2V_i^2 + 2V_i V_a\cos\delta\right] \\ &= 2\rho A_p V_i\left[V_i + V_a\cos\delta\right] \end{aligned} \tag{6.9}$$

Comparing the steady result from classical axial momentum theory with the result for oblique inflow:

$$\begin{aligned} T &= 2\rho A_p V_i (V_i + V_a) && \text{axial inflow} \\ T &= 2\rho A_p V_i (V_i + V_a \cos\delta) && \text{oblique inflow} \end{aligned} \tag{6.10}$$

It is clearly seen that the basic result of classical momentum is unchanged: the thrust is equal to the product of the mass flux through the propeller disk and the *increase* in velocity in the streamtube from far upstream to far downstream the propeller. The result for oblique inflow simply captures the fact that the mass flux through the propeller is the product $\rho A_p (V_i + V_a \cos\delta)$, the velocity sum in brackets being the perpendicular (normal) component of velocity through the disk.

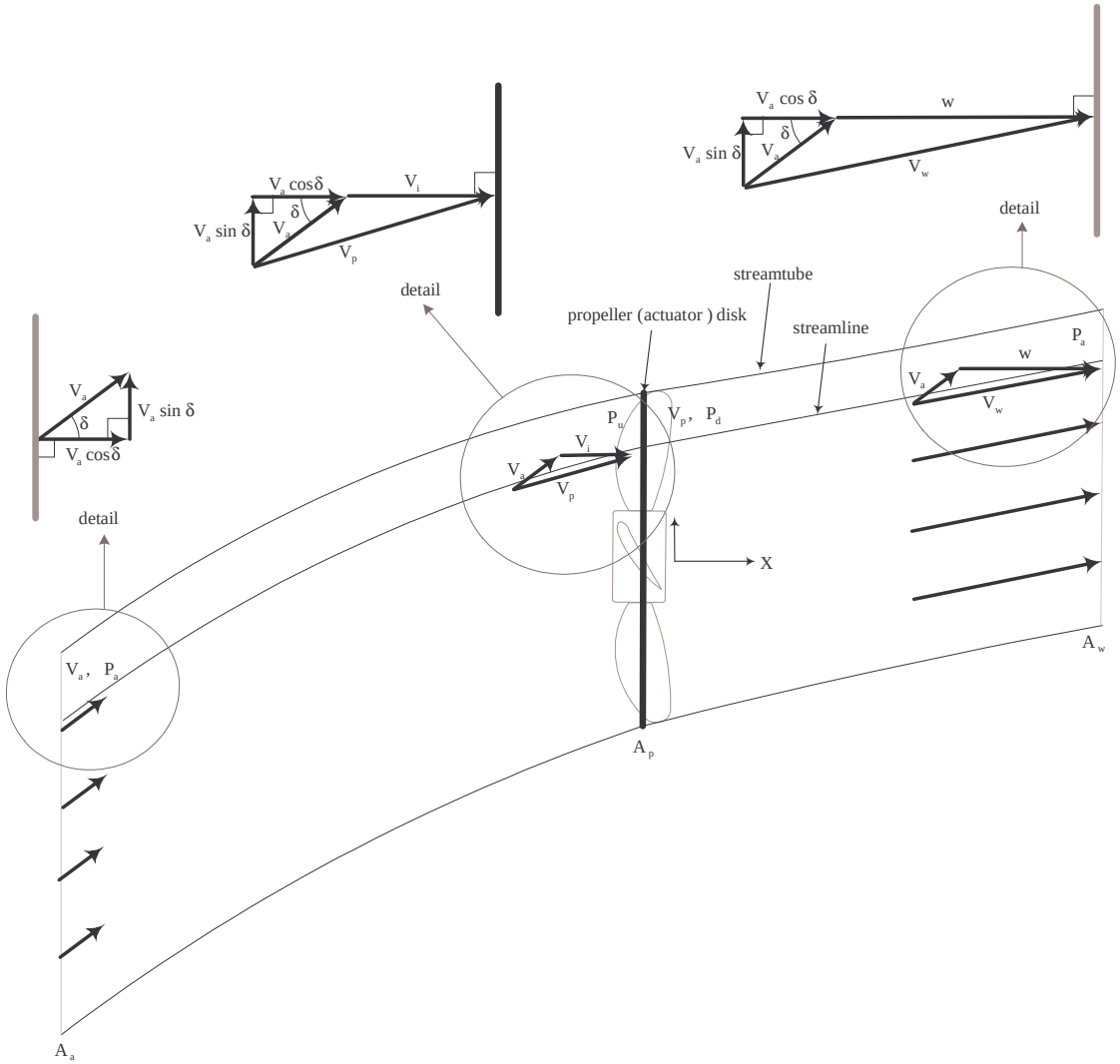

Figure 6-2: A modified momentum model for a propeller operating in oblique inflow.

6.1.3 The general momentum propeller model including angular momentum

In the classical momentum model, it was assumed that the actuator disk could only accelerate the fluid in the axial direction. Rotation of the slipstream was neglected. The general momentum theory includes accounting for rotation of the slipstream. This is sometimes referred to as the idealized form of the screw propeller [74].

In the generalized momentum model, both axial and angular velocities are assumed to be uniformly distributed over the disk. Angular velocity of the flow is assumed to be zero far upstream from the disk, equal to ω at the disk, and equal to 2ω far downstream of the disk (figure 6-3). The latter is a fundamental result which follows in a parallel fashion to the axial velocity from classical momentum, using an energy balance (see [25] or [74]). Note that the angular velocity at the disk can also be written for a radius r in terms of the tangential induced velocity as $\omega = V_{\theta i}(r)/r$. Considering a control volume that is an annular streamtube as shown in figure 6-3, the elemental torque at the disk in the annulus of radius r is equal to the angular momentum change per unit time within the entire corresponding annular streamtube

$$dQ = \dot{m}(2\omega)r^2 = \dot{m}\left(2\frac{V_{\theta i}}{r}\right)r^2 \tag{6.11}$$

where $\dot{m}$ is the mass flux through the disk annulus of radius r

$$\dot{m} = 2\pi r dr\,\rho(V_A + V_{Ai}) \tag{6.12}$$

where V_A is the axial component of inflow velocity and V_{Ai} is the axial component of the induced velocity at the disk. Thus, the elemental differential torque in the disk annulus is

$$\frac{dQ}{dr} = 4\rho\pi r^2 V_{\theta i}(V_A + V_{Ai}) \tag{6.13}$$

where V_{Ai} and $V_{\theta i}$ are the axial and tangential components of the induced velocity at the disk at radius r. The net propeller torque is the integration of the elemental differential torque in each annulus over the radius of the propeller.

6.1.4 Glauert's thrust hypothesis for helicopters in forward flight

Observing the results of classical momentum applied to oblique inflow (equations (6.10)), it is apparent that the theory implies a maximum thrust limit equal to the thrust at the bollard condition (i.e. $V_a = 0$, $J = 0$). This is clear by inspection of the "typical" propeller thrust-torque-speed characterization curves (figure 2-2), and noting that in the limit as $\delta \to 90°$ (i.e. $\cos\delta \to 0$), then the maximum thrust possible is that at the bollard condition (i.e. $T = 2\rho A_p V_i^2$). Inspection

of the experimental results shown in figures 4-10 and 4-11 (also reproduced in figure 6-6) clearly indicates that the experimental thrust of the propulsor at 90° is largely in excess of the thrust obtained at the bollard condition, the amount in excess *increasing* significantly with increase in advance velocity (or advance coefficient).

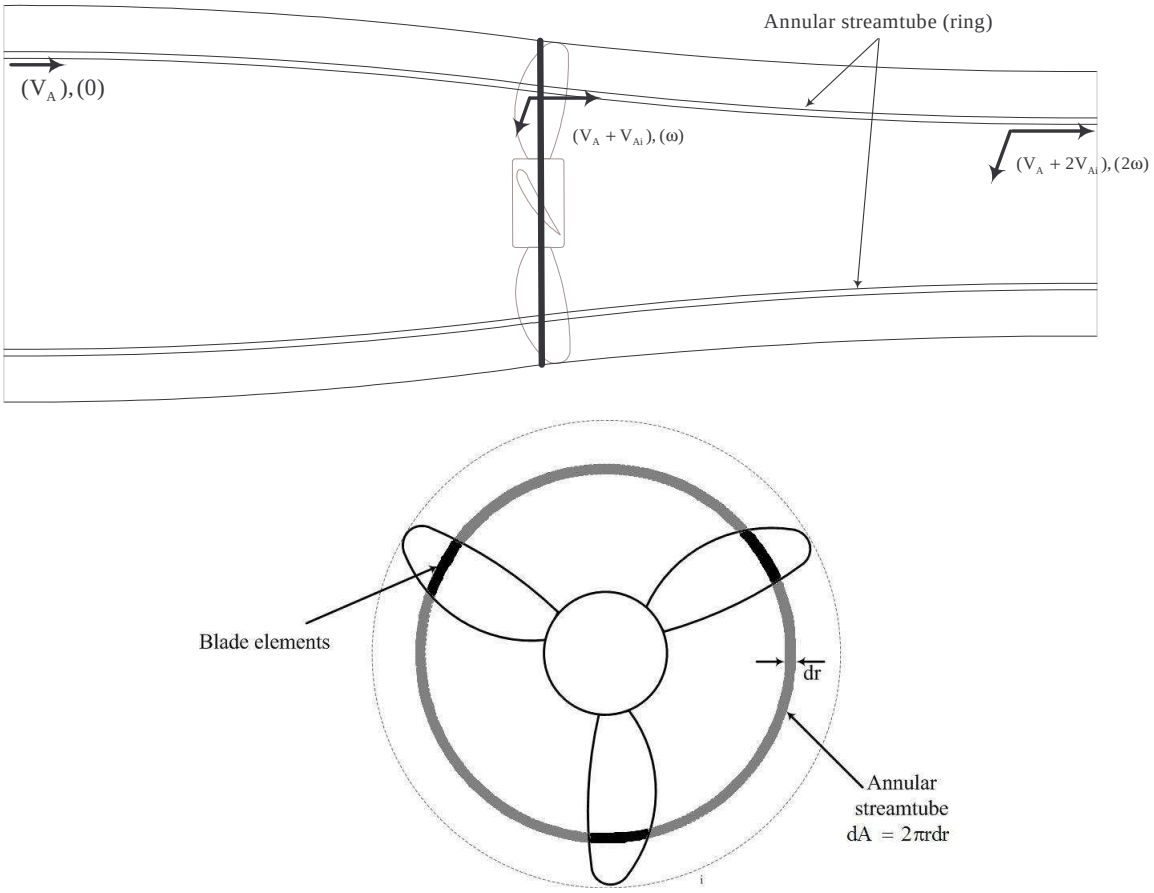

Figure 6-3: Annular streamtube concept as the basis for the general momentum theory. Axial and angular momentum are balanced within the control volume bound within the annular streamtube. This also forms the basis of the combined blade-element-momentum (BEM) method.

It was first noticed in 1897 by H.S. Maxim that translational velocity of an airscrew (i.e. an airscrew that is moved perpendicular to its axis of rotation) experiences an increased thrust for a given power input [25]. In trying to explain and predict the thrust behavior of a rotating helicopter airscrew or autogyro over the entire range of possible operating conditions (i.e. in hover, vertical flight, and forward or horizontal flight), Glauert provided a hypothesis relating the thrust of the rotor to inflow angle and velocity, which has a form markedly different that that obtained from classical momentum theory with oblique inflow (equations (6.10)).

Although not detailed in his original paper [24], Glauert hypothesized that a helicopter rotor in high-speed horizontal flight (i.e. moving at high horizontal speed, with the axis of rotation vertical, figure 6-4) was analogous to an elliptically-loaded wing. Glauert applied a basic lifting line result from vortex theory for the elliptically-loaded wing, with the result that the downwash velocity (induced velocity) is related to the lift by

$$L = \rho V_a \pi \left(\frac{b}{2}\right)^2 2v_i \tag{6.14}$$

where b is the wing span, V_a is the advance velocity (horizontal velocity) and v_i is the downwash (induced velocity). This means that the lift of an elliptically-loaded wing is equal to the product of twice the induced velocity and the mass flow rate passing through a *circular disc with diameter equal to the span of the wing*.

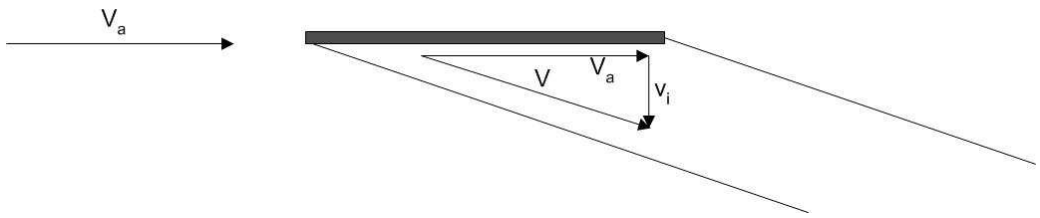

Figure 6-4: Glauert's idealization of a helicopter rotor in high-speed forward (horizontal) flight, as an elliptically-loaded wing. Adapted from [25].

Note: The basic result for an elliptically-loaded wing used by Glauert, equation (6.14), is not often given in this form. For an elliptically-loaded wing (i.e. an elliptic circulation distribution), Prandtl's lifting line theory can be used to obtain an expression for the induced downwash v_i as [41]

$$v_i = \frac{\Gamma_{max}}{2b} \tag{6.14a}$$

which is constant along the wing span. Another feature of an elliptic distribution is that the span-wise integral is simply half the area of an ellipse (with semi-axes Γ_{max} and b/2), or

$$\int_{-b/2}^{b/2} \Gamma(y)\, dy = \frac{\pi b}{4} \Gamma_{max} \tag{6.14b}$$

Consequently, the lift of the elliptically-loaded wing is

$$L = \rho V_a \int_{-b/2}^{b/2} \Gamma(y)\, dy = \frac{\pi b}{4} \rho V_a \Gamma_{max} \tag{6.14c}$$

Combining equation (6.14a) for the induced downwash with equation (6.14c) for the lift, provides equation (6.14). As a further aside: the result of Prandtl's lifting line theory for an elliptically-loaded wing is usually given in terms of a lift coefficient C_L and the induced angle of attack

$$C_L = \frac{2\pi}{1+\frac{2}{AR}}\left(\alpha - \alpha_{L_0}\right) \qquad AR = b^2/S \qquad \alpha = \tan^{-1}\left(\frac{v_i}{V_a}\right) \tag{6.14d}$$

where S is the area of the wing. This result follows in a similar manner to equation (6.14) if it is also assumed that, in addition to the elliptic load distribution, the planform (chord distribution) is also elliptic (see [41]).

Glauert applied the equation (6.14) result directly to the lift of a helicopter rotor in *high-speed* horizontal flight, with the hypothesis that the thrust and downwash (induced velocity) at the circular rotor are related by

$$T = \rho V \pi R^2 2 v_i = 2\rho A v_i V \tag{6.15}$$

with the velocity V being equal to the total vector sum of the incoming and induced velocities at the disc (i.e. $\sqrt{V_a^2 + v_i^2}$). Glauert further hypothesized that for the general case of a helicopter rotor at an arbitrary angle δ to the free-stream velocity (figure 6-5), this expression for thrust would still be valid, noting that for the general case, the total vector sum of the velocity at the disk would be

$$V = \sqrt{\left(V_a \cos\delta + v_i\right)^2 + \left(V_a \sin\delta\right)^2} = \sqrt{V_a^2 + 2 v_i V_a \cos\delta + v_i^2} \tag{6.16}$$

Although Glauert offered no specific proof of this relation for all angles δ, he pointed out that it has the correct limits. For a helicopter in high-speed horizontal flight ($V_a >> v_i$), it provides the elliptically-loaded wing result, and for a helicopter in hover or vertical flight, it provides the standard result from classical axial momentum theory. However, Stepniewski and Keys [70] point out that, although Glauert did not do so, this simple result can be and has been rigorously proven with the help of numerical methods and vortex and potential theories.

Glauert's hypothesis provides a basis for understanding the experimental "excess" thrust provided by the propeller at large angles (indeed at *all* angles between 0 and ±90° and beyond, compared to the modified momentum theory given in equations (6.10)). As can be seen in figure 6-6, where thrust at large angles with forward speed is compared to the bollard condition ($V_a = 0$), the propeller gains a "lift" as it is moved at angles relative to its inflow. This "excess" thrust or "lift" can be understood to be a result of the lift force on the propeller disk as it moves horizontal to the fluid, as an "elliptically-loaded wing," in accordance with equation (6.14), and Glauert's hypothesis. Thus, Glauert's hypothesis can be directly observed to be applicable in terms of

providing for this experimental "excess" thrust for propulsor azimuth, with the "excess" thrust coming from the lift force on the propeller disk in oblique flow.

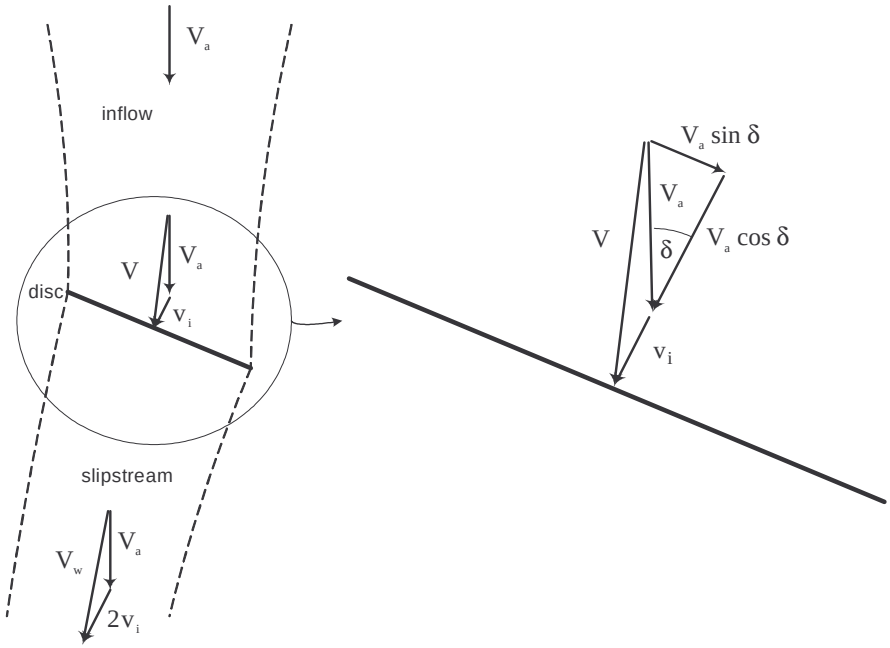

Figure 6-5: Glauert's conceptual model of a helicopter in general flight.

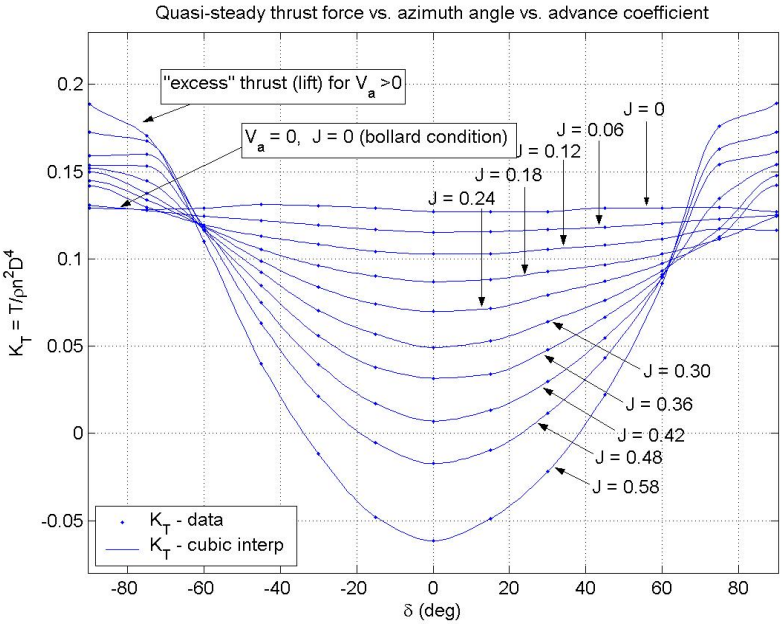

Figure 6-6: Demonstration of "excess" thrust for $V_a > 0$ compared to the bollard condition ($V_a = 0$), providing an illustration of the applicability of Glauert's basic hypothesis to an azimuthing propulsor.

6.2 A combined blade-element and momentum (BEM) model for propellers and propulsors in oblique inflow

With the help of Glauert's hypothesis, a theoretical basis can be developed which characterizes the nature of the variation of thrust force and torque with azimuth angle as illustrated in Chapter 4. However, even with the help of Glauert's hypothesis, the classical momentum theories fail to provide a theoretical basis for the existence of the in-plane propeller forces (and moments) which are a strict consequence of a propeller or propulsor operating in an oblique inflow, figure 6-7. Also, even though the classical momentum theories can be modified to include the effects of slipstream rotation, the momentum result is unable to fully characterize the variation in propeller torque, by itself.

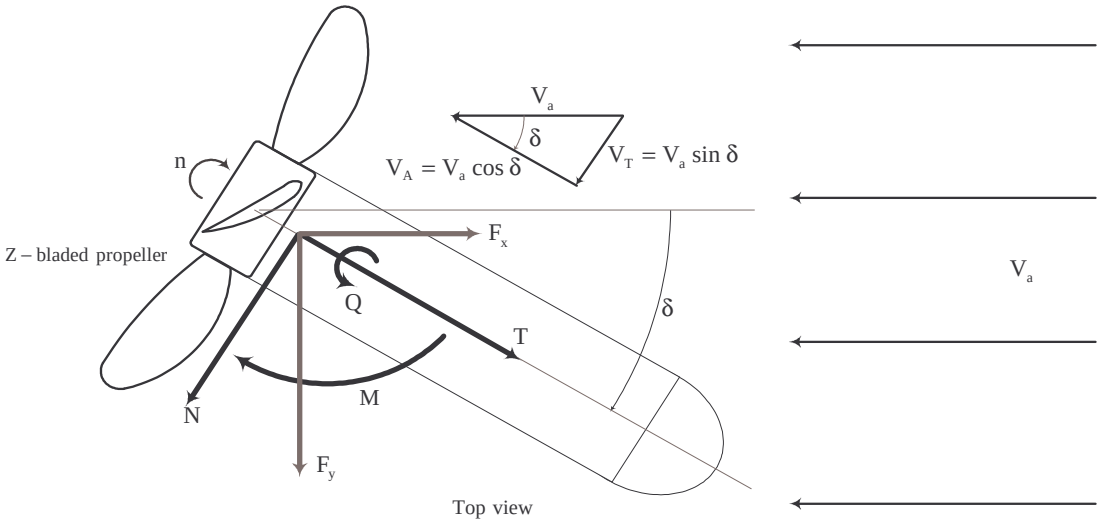

Figure 6-7: An azimuthing propulsor operating in oblique inflow.

6.2.1 A basic BEM model for propellers in oblique inflow

In order to provide a basic theoretical basis for the in-plane propeller normal force and steering moment, in addition to the modified (vectored) thrust and torque, the theory of blade-element analysis is combined with the propeller momentum theories (including slipstream rotation); an approach referred to as combined blade-element-momentum (BEM). By combining the fundamental approach of blade-element analysis with conservation of axial and angular momentum of an annular ring of the streamtube passing through the propeller disk, some of the weaknesses of either approach can be overcome. At each section or element of a blade (see

figures 6-3, 6-7, 6-8 and 6-9), a force balance is applied involving the 2-dimensional lift and drag forces with thrust and torque. At the same time, balances of axial and angular momentum are applied to the annular ring of the wake streamtube through which the blade section passes. By equating the thrust and torque determined by the blade element forces (multiplied by the Z blades of the propeller) with the thrust and torque required to balance axial and angular momentum within the annular streamtube, a pair of nonlinear equations can be obtained for each differential annular ring. The nonlinear equations can be solved for the induced velocities at the blade section using the linear and angular momentum balance equations. Thus, by iteration, the induced velocities, as well as thrust and torque of the propeller, can be calculated (the latter by integration over the propeller radius of the elemental thrust and torque values for the blades or annular rings).

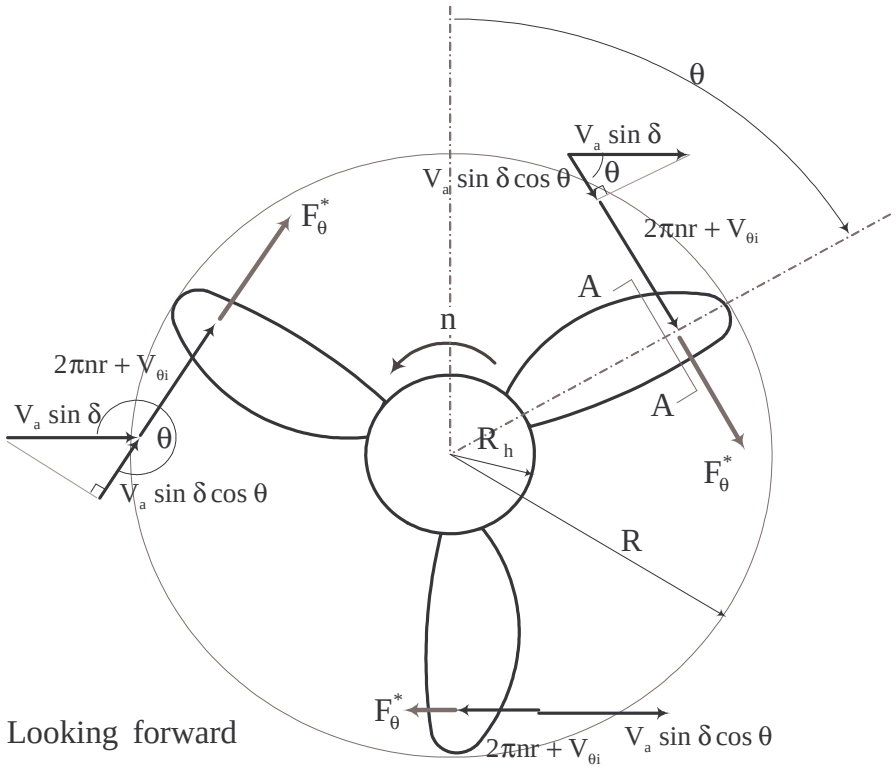

Figure 6-8: Definition of in-plane velocities and forces for a propeller operating in oblique inflow. Blade azimuthal location angle θ is defined as shown.

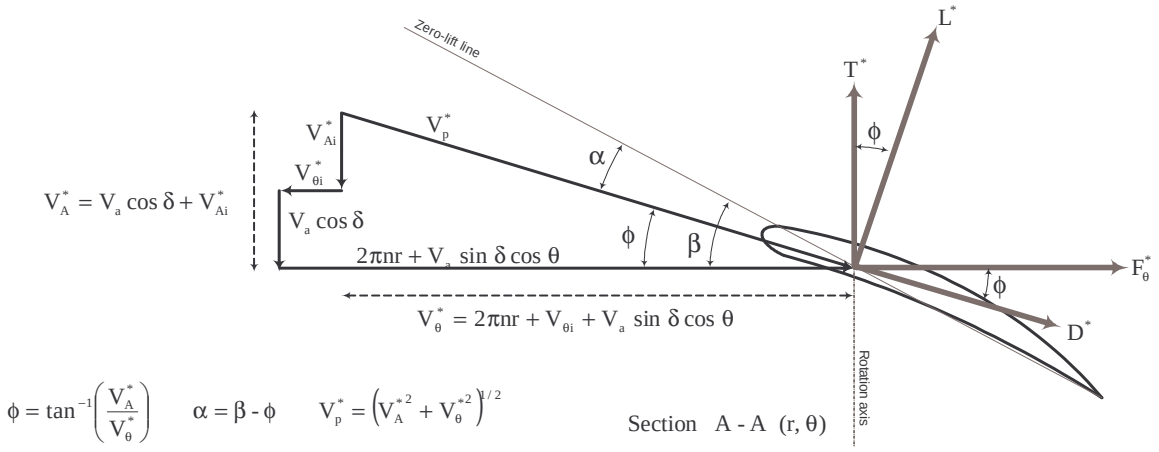

Figure 6-9: Definition of blade element (local) velocities and forces for a propeller operating in oblique inflow. Defined in the coordinate frame of the blade element.

There are a number of important assumptions inherent in the application of this type of combined approach. First, the method implies that the annular blade elements do not interact (i.e. a strip theory). This is equivalent to a simplification that the flow is locally 2-dimensional at the blade section (i.e. radial induced velocities are neglected). Other general assumptions are that the induced velocities vary only with radius (i.e. are constant around each annular ring), and that the angle of attack remains generally small [55]. The former assumption appears to invalidate the method's use for a propeller in oblique inflow (since the induced velocities (both axial and tangential) vary with azimuthal blade angle/position around the annular ring). However, if annular-averaged induced velocities, thrust and torque are obtained through spatial averaging around each annulus, then the average values can be used and the method applied (so long as the shape of the wake can still be represented reasonably well by a streamtube, which is supportable using the results of the fluorescent paint visualization given in Chapter 5, even for lightly loaded propellers at large angles). The second assumption is that lift characteristics of the foil sections that make up the blade sections remain within their linear range, below static stall, and that no dynamic stall occurs. This also can be addressed if special empirical and/or computational measures are taken to account for nonlinearities and dynamic stall (or hysteresis) with the blade lift and drag forces. Like all momentum-based theories, the BEM theory also is developed by assuming the propeller to have a large (infinite) number of blades (i.e. a disk), which results in a uniform velocity distribution within the wake. For a propeller with a finite number of blades, this can be addressed in an approximate manner by including a result from vortex wake theory developed by Prandtl [25]. The effects of wake skew (asymmetry arising from oblique inflow)

can also be addressed in an approximate manner by incorporation of a result from vortex wake theory.

The total local axial and tangential velocity at each blade element location (r,θ) can be written (see figures 6-8 and 6-9)

$$\begin{aligned} V_A^*(r,\theta) &= V_a \cos\delta + V_{Ai}(r,\theta) \\ V_\theta^*(r,\theta) &= 2\pi nr + V_{\theta i}(r,\theta) + V_a \sin\delta\cos\theta \end{aligned} \tag{6.17}$$

The total angle of attack α at each blade element location (r,θ) can be written

$$\alpha(r,\theta) = \beta(r) - \phi(r,\theta) \tag{6.18}$$

where ϕ is the inflow angle

$$\phi(r,\theta) = \tan^{-1}\left(\frac{V_A^*(r,\theta)}{V_\theta^*(r,\theta)}\right) \tag{6.19}$$

The element thrust force and in-plane tangential force can be written in terms of the element lift and drag forces

$$T^*(r,\theta) = L^*\cos\phi - D^*\sin\phi \qquad F_\theta^*(r,\theta) = L^*\sin\phi + D^*\cos\phi \tag{6.20}$$

where the element lift and drag forces can be written

$$L^*(r,\theta) = \frac{1}{2}\rho V_p^{*2} c\, C_L \qquad D^*(r,\theta) = \frac{1}{2}\rho V_p^{*2} c\, C_D \tag{6.21}$$

where C_L and C_D are the sectional lift and drag coefficients, respectively, and V_p* is the total velocity at the blade element.

The differential thrust, torque, normal force and steering moment for each annular ring at the propeller disk (radius) are calculated by integrating the blade elemental thrust force and tangential force over the annulus as follows

$$\begin{aligned} \tilde{T}(r) &= Z\frac{1}{2\pi}\int_0^{2\pi} T^*(r,\theta)\, d\theta & \tilde{Q}(r) &= Z\frac{1}{2\pi}\int_0^{2\pi} F_\theta^*(r,\theta)\, r\, d\theta \\ \tilde{N}(r) &= Z\frac{1}{2\pi}\int_0^{2\pi} F_\theta^*(r,\theta)\cos\theta\, d\theta & \tilde{M}(r) &= Z\frac{1}{2\pi}\int_0^{2\pi} -T^*(r,\theta)\, r\sin\theta\, d\theta \end{aligned} \tag{6.22}$$

By the general momentum theory discussed previously, the differential thrust and torque for each annular ring at the propeller disk calculated from the blade element theory must equal the differential thrust and torque for the corresponding annular streamtube calculated from conservation of general momentum. The thrust for each annular streamtube can be written, using Glauert's thrust hypothesis (equations (6.15) and (6.16)), in the form

$$\tilde{T}(r) = 4\rho\pi r\overline{V}_{Ai}(r)\left[\overline{V}(r)^2 + 2\overline{V}_{Ai}(r)\overline{V}_A(r) + \overline{V}_{Ai}(r)^2\right]^{1/2} \tag{6.23}$$

and the torque for each annular streamtube can be written from equation (6.13) in the form

$$\tilde{Q}(r) = 4\rho\pi r^2 \overline{V}_{\theta i}(r)\left[\overline{V}(r)^2 + 2\overline{V}_{Ai}(r)\overline{V}_A(r) + \overline{V}_{Ai}(r)^2\right]^{1/2} \tag{6.24}$$

where $\overline{V}_{Ai}(r)$ and $\overline{V}_{\theta i}(r)$ are annulus-averaged values of the induced velocities at the disk

$$\overline{V}_{Ai}(r) = \frac{1}{2\pi}\int_0^{2\pi} V_{Ai}(r,\theta)\,d\theta \qquad \overline{V}_{\theta i}(r) = \frac{1}{2\pi}\int_0^{2\pi} V_{\theta i}(r,\theta)\,d\theta$$

By equating thrust and torque from equations (6.22) with equations (6.23) and (6.24), the annulus-averaged values of the induced velocities $\overline{V}_{Ai}(r)$ and $\overline{V}_{\theta i}(r)$ can be calculated. Thus, an iterative scheme is required. Once convergence of the calculated induced velocities is obtained, the total propeller thrust, torque, normal force and steering moment can be calculated by integration of the annulus values over the propeller disk

$$T = \int_{R_h}^{R} \tilde{T}(r)\,dr \qquad N = \int_{R_h}^{R} \tilde{N}(r)\,dr \qquad Q = \int_{R_h}^{R} \tilde{Q}(r)\,dr \qquad M = \int_{R_h}^{R} \tilde{M}(r)\,dr$$

6.2.2 Extension to BEM for wake skew effects

The traditional BEM approach fundamentally assumes that the axial and tangential *induced* velocities (V_{Ai} and $V_{\theta i}$) are constant around each annulus. This does not account for the wake angle which arises as a result of the oblique inflow into the propeller, and the effect of the asymmetry of the trailing wake with respect to the propeller disk (defined as the *wake skew*). A wake skew induces velocities at the disc that favor the skew of the wake (i.e. an asymmetry of induced velocities with respect to blade azimuthal angle θ around the annular ring). One approach is to consider the results of Coleman et al. [14], who applied the Biot-Savart law to a vortex wake represented by an elliptic cylindrical shell, with a continuous distribution of vortex "rings" whose planes are parallel to the disk, figure 6-10 (the rings representing the *mean* helical surfaces of the vortex wake). The analytic result was a complex expression involving elliptic integrals for induced velocity at a general point on the rotor disk. While not a linear expression, the plotted results were nearly linear over the entire disk diameter. For purposes of simplification, a 2-term Taylor series expansion was used to derive a simple linear expression for the distributions of induced velocity, with slope equal to $\tan(\chi/2)$ across the diameter of the disk. Thus, an expression for the distribution of induced velocity for a helicopter rotor in forward flight was developed by Coleman et al. (see also [20]) as

$$V_i = V_{i0}\left(1 + \frac{r}{R}\tan\left(\frac{\chi}{2}\right)\cos\psi\right) \tag{6.25}$$

where V_{Ai0} is the mean induced velocity (i.e. at the center of the disk), r is the radial coordinate on the disk, ψ is the azimuthal angle from downstream, and χ is the wake angle (in the downstream direction). Coleman et al. also derived a related result for the mean induced velocity related to the wake angle and the advance velocity, by combining the theory with the well known Glauert thrust equation (discussed above):

$$\frac{V_{i0}}{V_a} = \frac{\cos(\chi + \alpha_D)}{2\tan\left(\frac{\chi}{2}\right)} \tag{6.26}$$

where α_D is the angle of rotor disk incidence with the incoming flow.

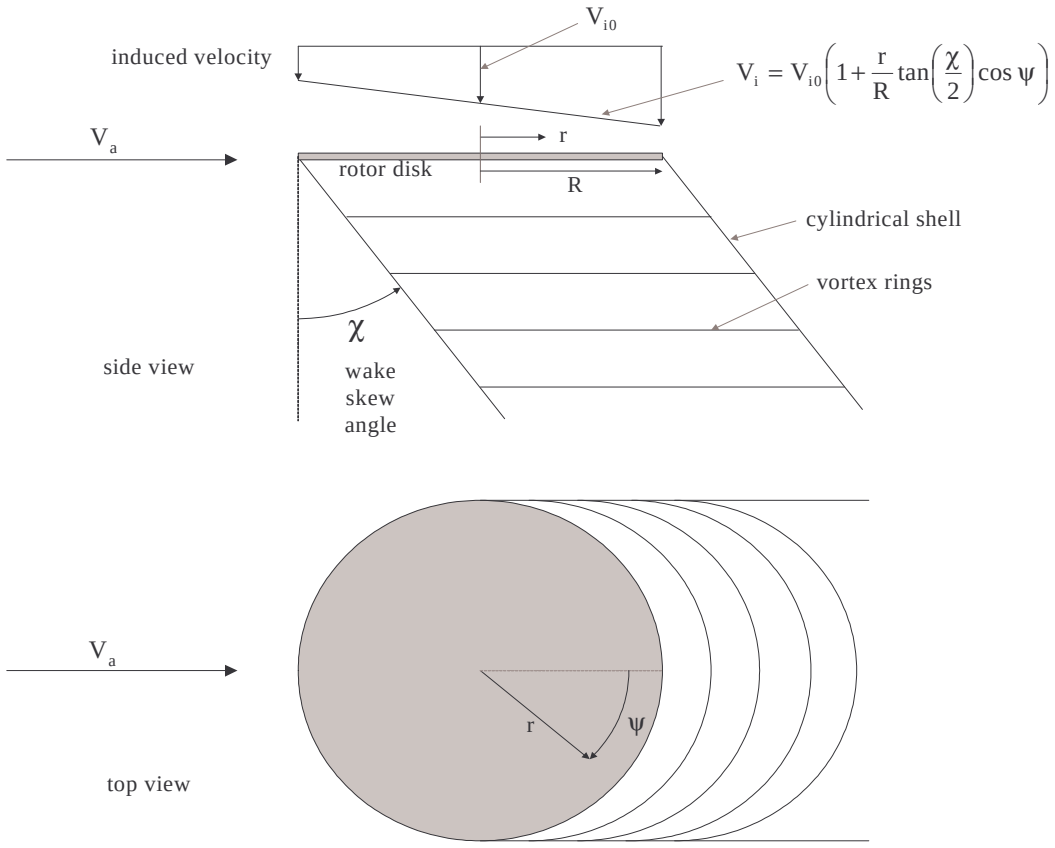

Figure 6-10: Model of the distribution of induced velocity across a rotor disk by Coleman et al., based upon a simplified vortex system of a rotor wake.

Although these results were derived for helicopters in forward flight, the mathematics (and results) are based on geometric/kinematic considerations of the helical vortex wake relative to the disk, along with application of the Biot-Savart law, with moderate assumptions, and thus are equally applicable to the current propeller problem for oblique inflow. In fact, review of the fluorescent paint flow visualization results presented in Chapter 5 would suggest that this type of

wake representation is still reasonable even for light propeller loading at large propulsor azimuth angles (see figure 5-3). Thus, for the azimuthing propulsor problem and coordinate system as defined in figures 6-7 and 6-8, the blade-azimuthal and radial distribution of axial induced velocity could be calculated using the expression

$$V_{Ai}(r,\theta) = V_{Ai0}\left(1 + \frac{r}{R}\tan\left(\frac{\chi}{2}\right)\sin\theta\right) \tag{6.27}$$

Note that, as expected, the result is a linear distribution of induced velocity across the disk (e.g. for the cross-flow across the propeller disc from $\theta = 270°$ to $\theta = 90°$):

$$\frac{V_{Ai}(r)}{V_{Ai0}} = 1 + \tan\left(\frac{\chi}{2}\right)\frac{r}{R} \tag{6.28}$$

i.e. with the slope given by $\tan(\chi/2)$.

It is also feasible to calculate the wake skew angle χ if it is considered as a constant for all radial and azimuthal positions (r,θ). This is equivalent to averaging the spatial variations of the inflow and induced velocities to obtain a single spatially-averaged wake angle. The calculations are carried out in the propulsor coordinate frame (not the blade element frame). The wake angle at the disk can be calculated as (see figure 6-11)

$$\chi = \tan^{-1}\left(\frac{V_a \sin\delta + \overline{V}_{Ti}}{V_a \cos\delta + \overline{V}_{Ai}}\right) \tag{6.29}$$

where the spatially-averaged induced velocities are calculated

$$\begin{aligned} \overline{V}_{Ti} &= \frac{1}{\pi\left(R^2 - R_h^{\,2}\right)}\int_{R_h}^{R}\int_{0}^{2\pi} V_{\theta i}(r,\theta)\cos\theta \, d\theta \, r \, dr \\ \overline{V}_{Ai} &= \frac{1}{\pi\left(R^2 - R_h^{\,2}\right)}\int_{R_h}^{R}\int_{0}^{2\pi} V_{Ai}(r,\theta) \, d\theta \, r \, dr \end{aligned} \tag{6.30}$$

Note $\overline{V}_{Ti}$ and $\overline{V}_{Ai}$ are *disk-averaged* induced velocities, with $\overline{V}_{Ti}$ the disk-averaged in-plane *transverse* induced velocity in the direction *with* the incoming oblique flow (i.e. the "cross-flow" component).

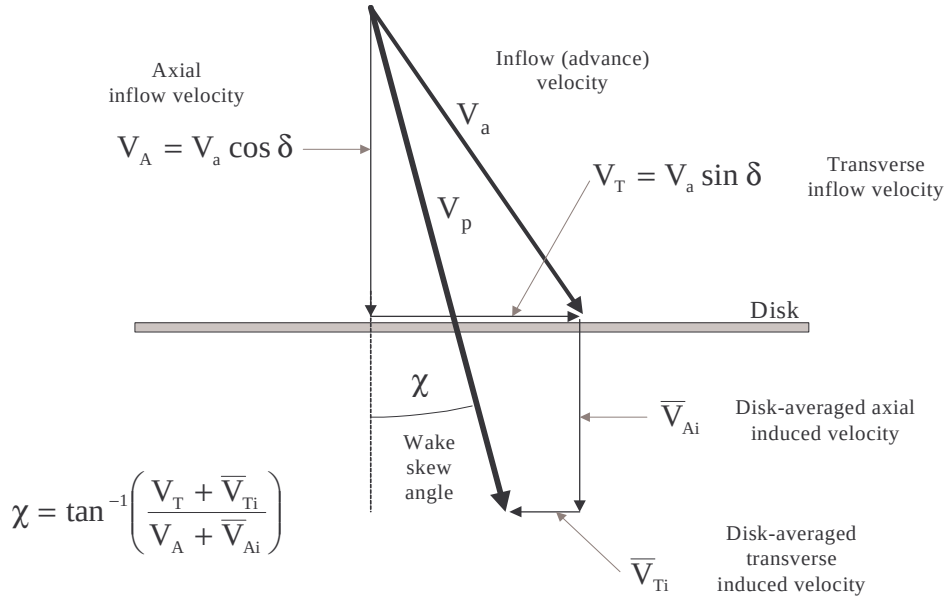

Figure 6-11: Calculation of wake skew angle from inflow and disk-averaged induced velocities.

6.2.3 Extension to BEM for finite number of blades

Application of the momentum theories implies no knowledge of the distribution of the velocities as a function of radius. However, consideration of the vortex theory requires that the trailing vortices in the wake lie on a regular screw (helical) surface, and the velocity system of the slipstream is obtained if this vortex sheet is assumed to be a rigid membrane which moves backwards with a constant velocity [25]. In the interior of the slipstream, the fluid velocity *in between* the sheets will necessarily have mainly axial and rotational components, and move with the vortex sheets. However, near the boundary of the slipstream, the fluid will tend to flow around the edges of the vortex sheets (and will acquire some radial velocity in the process), a process sometimes referred to as “leakage". Prandtl [64] developed an approximate method for estimating the effect of this radial flow. The method is presented in English by Glauert [25]. Prandtl replaced the system of vortex sheets by a series of parallel lines or plates at a regular gap, representing the vortex sheets. The flow around the edges of the vortex sheets of the slipstream was estimated by the flow around the system of straight lines or plates. Prandtl’s result is a “tip loss factor” or reduction factor which can be interpreted as expressing the fraction of the velocity of the vortex sheets which is imparted to the fluid in between the sheets (as a function of radius). In analogy to the propeller momentum theories, the “tip loss factor” is a reduction factor which must be applied to the momentum equation for flow at radius r, since it represents the fact that

only a fraction of the fluid in between the vortex sheets of the slipstream receives the full effect of the motion of the slipstream.

The Prandtl tip loss factor can be represented in one of two forms: as a momentum reduction factor F, or as an effective radius R_e [25]. The momentum reduction factor is applied directly to the momentum equations as a reduction to the calculated axial induced velocity at the disk at each radius. The effective radius is used in place of the actual radius R in integration of forces. However, the net effect is the same in either approach: to decrease the transport of momentum within the slipstream. The momentum reduction factor F can be written in the form [25]

$$F(r) = \frac{2}{\pi}\cos^{-1}\left(\exp\left[-\frac{Z}{2}\frac{(R-r)}{R}\frac{\sqrt{1+\lambda^2}}{\lambda}\right]\right) \tag{6.31}$$

where

$$\lambda \equiv \frac{(V_A + V_{Ai0})}{(2\pi nR + V_{\theta i0})} \tag{6.32}$$

is the tip speed ratio. The effective radius can be written in the form

$$R_e = R\left(1 - \frac{1.386}{Z}\frac{\lambda}{\sqrt{1+\lambda^2}}\right) \tag{6.33}$$

It is noted that, while the "tip loss factor" as derived by Prandtl was derived assuming a symmetric axial wake, its use is extended to the case of a skewed wake, with the assumption that the mean characteristics of the wake helical surface *separations* are approximately the same, as was the case for the derivation of Coleman et al. discussed above.

6.2.4 The inflow velocity deficit due to a propulsor pod wake

Application of the general BEM method assumes a uniform inflow into the propeller disk (although this assumption has been modified here by application of the oblique inflow with in-plane as well as normal velocity components to the propeller). However, as a special issue associated with a podded propulsor of the "pusher" type (i.e. where the pod body is forward of the propeller, as for the current experimental propulsor), the inflow to the propeller disk can also possess circumferential variation due to the existence of the wake of the pod when the pod is azimuthed relative to the inflow. Figure 6-12 illustrates the concept of a pod wake inflow variation.

This wake inflow variation can be described in the same basic form as the traditional nominal ship wake inflow into a traditional shafted propeller at the stern of a ship, where the inflow wake has circumferentially-varying components due to the ship's wake [74], [12], [43]. For the case of a ship's wake (and also the podded propulsor wake), since the inflow velocity is periodic in θ (figures 6-8 and 6-12), the three components of velocity (axial V_A, radial V_R, and tangential V_θ) at the propeller disk at any location (r,θ) can be written as Fourier series

$$
\begin{aligned}
V_A(r,\theta) &= A_0^A(r) + \sum_{m=1}^{\infty} A_m^A(r)\sin(m\theta) + \sum_{m=1}^{\infty} B_m^A(r)\cos(m\theta) \\
V_R(r,\theta) &= A_0^R(r) + \sum_{m=1}^{\infty} A_m^R(r)\sin(m\theta) + \sum_{m=1}^{\infty} B_m^R(r)\cos(m\theta) \\
V_\theta(r,\theta) &= A_0^\theta(r) + \sum_{m=1}^{\infty} A_m^\theta(r)\sin(m\theta) + \sum_{m=1}^{\infty} B_m^\theta(r)\cos(m\theta)
\end{aligned}
\tag{6.34}
$$

Note that the harmonic coefficients for each velocity component, A_m, B_m, are functions of radius.

In order to determine the harmonic coefficients using standard Fourier analysis techniques, the inflow velocity components (V_A, V_R, and V_θ) must be known as functions of (r,θ). Thus, either data from a detailed wake survey (for *all* of the potential pod angles and advance velocities), or numerical or analytic solution to the wake of the pod or body creating the inflow wake, must be available. For the subsequently presented BEM analyses, several generic representative pod wake field representations are assumed in order to investigate quantitatively the effect of wake variation on the propulsor maneuvering forces. These wakes are described in terms of the actual positional velocity distributions ($V_A(r,\theta)$, $V_R(r,\theta)$, and $V_\theta(r,\theta)$), rather than the Fourier series representation. However, subsequent comparative analyses utilizing the propeller analysis code MPUF-3A require the description of the inflow wake by the Fourier coefficient representation given by equations (6.34).

It should be noted that the consideration of the propulsor pod wake in this manner does *not* include any potential additional wake distribution that might be associated with the ship or vehicle's wake. Thus, the representation of the wake, either as a spatial velocity distribution (i.e. x, r, θ), or in terms of harmonic components as in equations (6.34), would need to include the ship or vehicle's wake, if necessary.

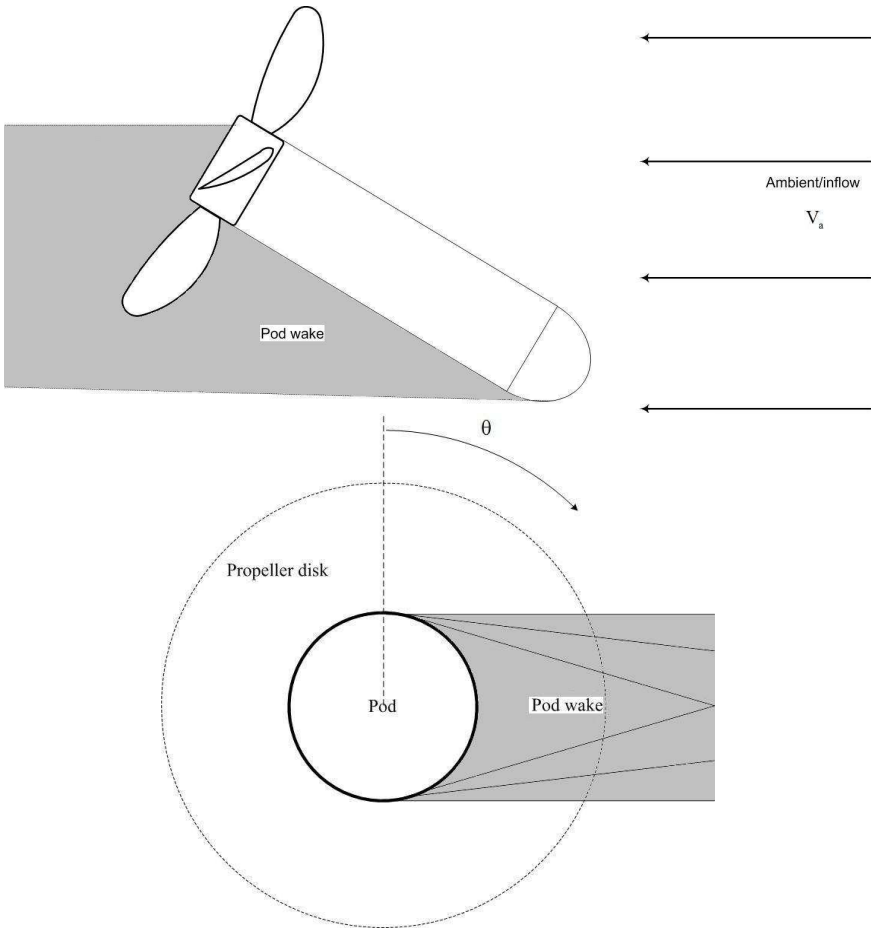

Figure 6-12: Conceptual propulsor pod wake inflow velocity variation to the propeller disk.

6.2.5 A calculation scheme for applying a modified combined BEM approach to an azimuthing podded propulsor

A summary of a scheme for calculation of the propeller forces using a modified combined BEM approach, as previously discussed, is provided in table 6-1. The detailed numerical code is executed as a Matlab® script, provided in Appendix A. The details of the propulsor and propeller geometries are provided in Chapter 3. The following additional notes are given regarding the BEM calculation scheme and subsequent calculations:

(a) The blade pitch angle distribution $\beta(r)$ for the experimental propeller is given approximately by the linear distribution

$$\beta(r) = \beta_h + \left(\frac{\beta_t - \beta_h}{R - R_h} \right)(r - R_h)$$

where subscript *h* is for hub, and *t* is for tip (the maximum propeller radius).

(b) The blade chord distribution c(r) for the experimental propeller is given approximately by the elliptic distribution

$$c(r) = c_h\left[1 - \frac{(r - R_h)^2}{(R - R_h)^2}\right]^{1/2}$$

(c) The maximum blade camber ratio at a nominal radius (0.7R) for the experimental propeller is given approximately by $\eta_0/c_0 = 0.015$ (measured).

(d) The blade element lift coefficient is given approximately by linear lifting theory for a thin foil with camber [36]

$$C_L = k_1[2\pi\alpha + 4\pi\eta_0 / c_0]$$

where the coefficient k_1 is added as an empirical factor to match experimental results at zero propulsor angle. The blade element drag coefficient is given approximately for a thin foil as a combination of a nominal (parasitic) drag and a lift-induced drag [37]

$$C_D = k_2[0.008] + 0.06C_L{}^2$$

where the coefficient k_2 is added as an empirical factor to match the parasitic drag to the experimental results at zero propulsor angle. Ultimately, the combination of coefficients k_1 and k_2 are used to match both thrust and torque for the experimental results for the zero propulsor angle case (they are found for this propeller to be $k_1 = 1.07$ and $k_2 = 1.80$).

To be more rigorous, the potential effects of an inflow velocity deficit due to the pod wake are investigated quantitatively. Because completing a detailed wake survey for all of the potential pod angles and advance velocities was impractical for this study, the BEM analyses use several generic representative pod wake field representations, assumed in order to investigate quantitatively the effect of pod wake variation on the maneuvering forces. These wake fields are described in terms of the actual positional velocity distributions ($V_A(r,\theta)$, $V_R(r,\theta)$, and $V_\theta(r,\theta)$), and are developed based upon a few fundamental assumptions regarding the pod wake as follows:

(a) The pod wake is assumed to have a general geometry as shown in figure 6-12. The wake is assumed to be of a general "rectangular" shape, with velocity distribution defined within this "rectangular" wake shape, reducing in magnitude in a linear fashion from the free-stream at the boundary of the wake to a defined minimum, a wake fraction w, at the center of the wake (at $\theta = 90°$ for positive propulsor angle δ, or $\theta = 270°$ for negative propulsor angle).

(b) For positive propulsor azimuth angle, at any radius r, the upper and lower boundaries of the "rectangular" wake are defined by

$$\theta_{min} = \cos^{-1}\left(\frac{R_p}{r}\right) \qquad \theta_{max} = \cos^{-1}\left(\frac{-R_p}{r}\right)$$

where R_p is the radius of the propulsor pod, and the middle of the wake is at $\theta_{mid} = 90°$. For negative propulsor azimuth angles, these values are increased by π radians or 180°.

(c) Implementation of a numerical scheme to define the wake magnitudes at each wake location, $V_A(r,\theta)$ and $V_\theta(r,\theta)$, is provided in the Matlab® scripts provided in Appendix A. Figure 6-13 provides an example of the inflow wake velocity components calculated for one inflow condition.

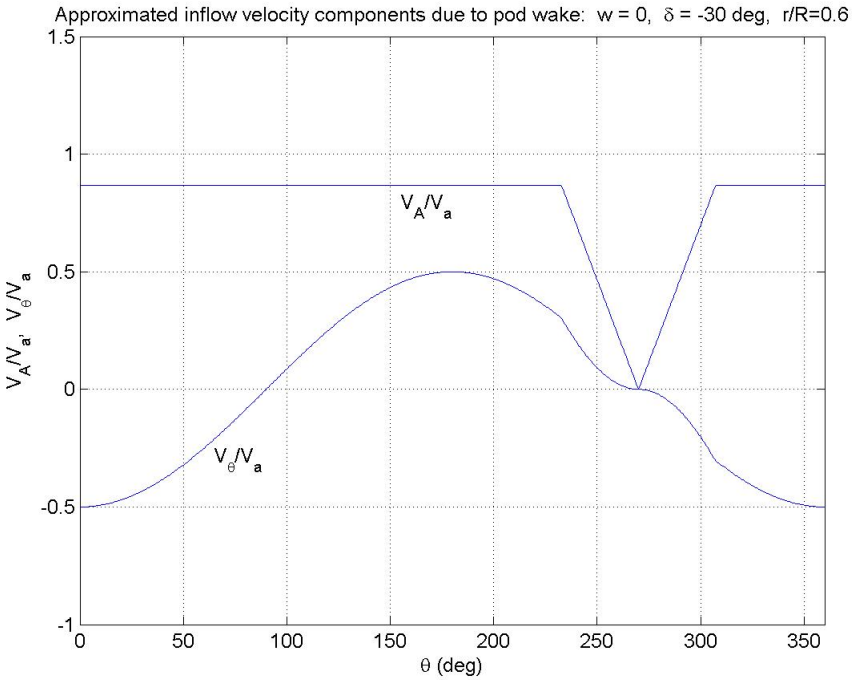

Figure 6-13: Approximated inflow velocity components due to pod wake. Assumed wake fraction w = 0, propulsor angle δ = -30°, normalized radius r/R = 0.60.

Table 6-1: A calculation scheme for a modified combined BEM approach applied to an azimuthing podded propulsor. Detailed Matlab® script is provided in Appendix A.

Guess initial disk-averaged induced velocities (axial, tangential, cross-flow)

Calculate steady axial and in-plane inflow velocity components V_A and V_T, based on V_a and δ

Step through time t (0 to t_{max})

- Iterate until change in disk-averaged induced velocities within tolerance
- Calculate wake skew angle χ based on latest iteration disk-averaged velocities
- Calculate tip speed ratio λ for Prandtl tip loss factor
- Step through radius r (R_{hub} to R)
  - Calculate blade pitch angle $\beta(r)$
  - Calculate blade chord c(r)
  - Calculate Prandtl tip loss factor F(r)
  - Step through circumference angle θ (0 to 2π)
    - Calculate element inflow velocities, modified to account for pod wake, $V_A(r,\theta)$, $V_T(r,\theta)$
    - Calculate element axial induced velocity $V_{Ai}^*(r,\theta)$ based on wake skew
    - Calculate element tangential induced velocity $V_{\theta i}^*(r,\theta)$ based on wake skew
    - Calculate element total axial velocity $V_A^*(r,\theta)$
    - Calculate element total tangential velocity $V_\theta^*(r,\theta)$
    - Calculate element total velocity $V_p^*(r,\theta)$
    - Calculate element inflow angle $\phi(r,\theta)$
    - Calculate element angle of attack $\alpha(r,\theta)$
    - Calculate element lift coefficient C_L and drag coefficient C_D
    - Calculate element thrust force $T^*(r,\theta)$ and tangential force $F_\theta^*(r,\theta)$
  - Integrate element thrust forces and tangential forces over θ to get annular dT(r), dQ(r), dN(r)
  - Integrate element induced velocities to get annular-averaged $\overline{V}_{Ai}, \overline{V}_{\theta i}$
  - Calculate *new* induced velocities, using annular momentum equations for thrust and torque
- Integrate and average old and new annular induced velocities to get disk-averaged values
- Compare old and new disk-averaged induced velocities (check for convergence)
  - If convergence *not* attained
    - Take average of old and new disk-averaged induced velocities
    - Go to next iteration
  - If convergence attained
    - Integrate annulus forces dT(r), dQ(r), dN(r) and dM(r) over r to get total T, Q, N, M
    - Go onto next time step

6.2.6 BEM calculation of propulsor forces for oblique inflow and comparison with experiment

To illustrate the use of a combined blade-element-momentum approach for the calculation of maneuvering forces for an azimuthing propulsor in oblique inflow, the above scheme is applied to the entire range of propulsor azimuth angles (±90°) for a representative advance coefficient, J = 0.304, which can be considered to be of moderate loading (zero loading occurs at approximately J = 0.43, see figure 2-2). Figure 6-14 provides the calculated net thrust and torque compared to the experimental values. Since the BEM calculations provide only the *propeller* thrust and torque, the calculated propeller thrust has been added to the pod-only axial force presented in Section 4.5. This can be seen as a major difficulty with any propeller calculation scheme used for a podded propulsor (including the more intensive computational fluid dynamics approaches discussed in the next sections). It should be clear that the inflow velocities to the propulsor (and the resulting forces) are affected by the existence of the flow past the "bluff" pod body, and, conversely, the velocities of the flow around the pod body (and the resulting forces) are affected by the additional induced velocities of the propeller. These relationships are complex, and would by themselves require extensive resources and effort to compute or determine experimentally. It has been simplified and assumed here that the two effects are decoupled and that superposition can be applied for the forces. As stated in the previous section, the sectional lift and drag coefficients have been adjusted to match the experimental results at zero propulsor azimuth angle (i.e. matching thrust and torque).

The BEM calculations have also been carried out over 3 assumed pod wake inflow velocity distributions in order to observe the sensitivity of the results to the assumed pod wake characteristics (calculated on the basis of the wake fraction w as discussed in the previous section). The effects of increase in the wake fraction are clearly greatest for moderate propulsor angles (15° - 45°). Increase in the pod wake fraction results in an increase in thrust and torque. This is as expected, since reduced inflow velocity can be seen as directly related to an increase in thrust and torque through increased blade angle of attack (figure 6-9).

The asymmetry in the experimental results due to the direction of rotation of the propeller should be obvious by inspection of the plots. This asymmetry was noted and discussed in Chapter 4 (Section 4.3) as caused by the asymmetric swirl inflow caused by blockage associated with the strut or steering shaft located atop the pod housing. Its effect is quite evident here. This asymmetric inflow swirl has not been modeled in the BEM calculations, and is therefore a source for asymmetric error in the results. It is also interesting and supportive to note that the thrust was

measured from the load cell output, while the torque was calculated from the current going to the propulsion motor (Chapters 2 and 3). Thus, the two measurements are completely uncorrelated, yet the plots of experimental force result for the two have nearly the same asymmetric form over the range ±90°.

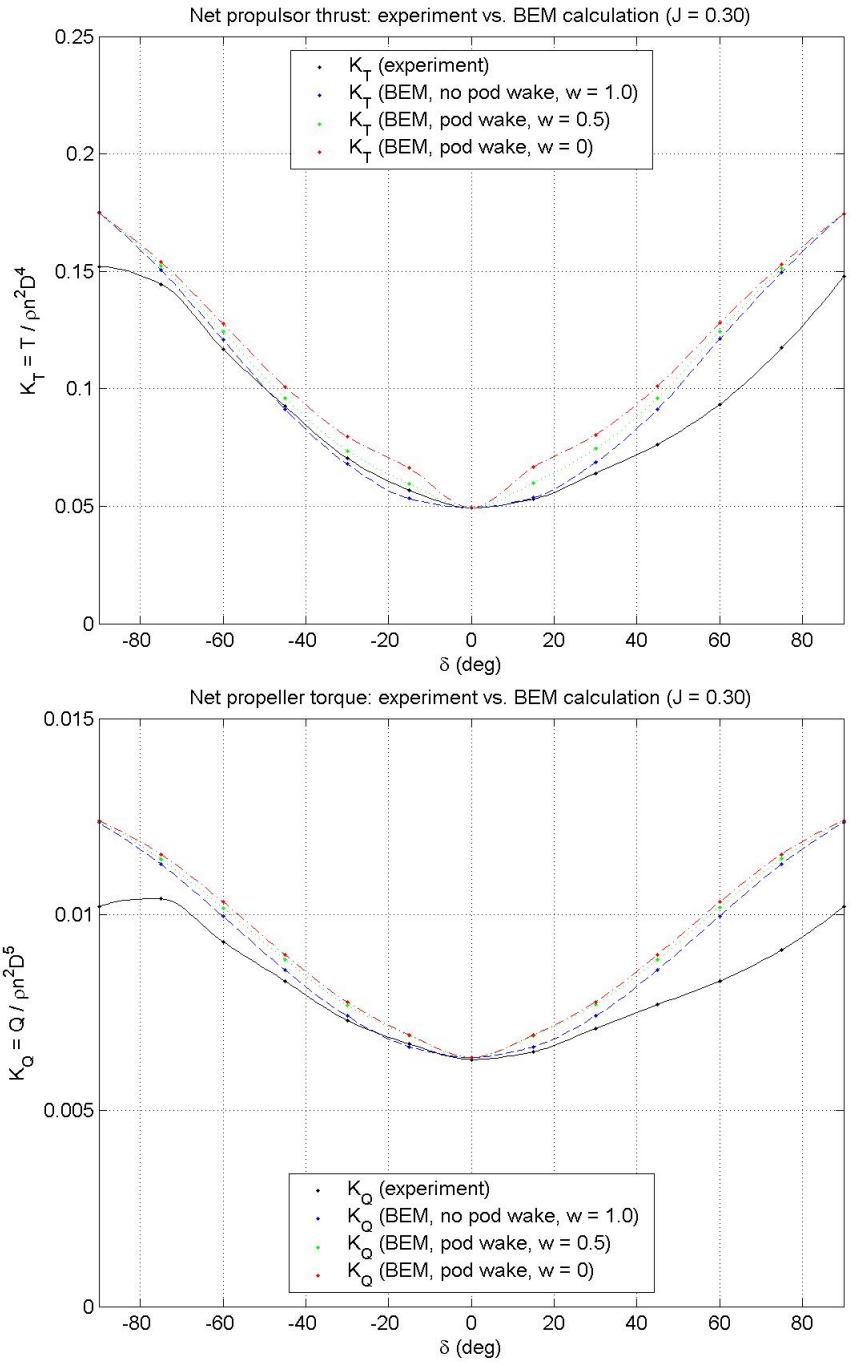

Figure 6-14: Modified combined BEM calculations vs. experiment. Top: thrust. Bottom: torque. Results are calculated propeller BEM results plus experimental pod-only forces. BEM calculations show sensitivity of results to assumed simplified inflow velocity pod wake deficit.

Despite this considerable asymmetry in experimental results, it is clear that, overall, the thrust and torque predicted by the BEM calculations exceed the experimental results over the range of propulsor azimuth angles. It is noted that the BEM method does *not* include the effects of the induced *radial* velocity as the propulsor is azimuthed to the inflow. Radial velocity at the blade elements translates to increased energy losses through the additional radial drag on the blades. Addition of these 3-dimensional frictional losses reduces the energy available to produce thrust and torque in the fluid, thus decreasing the thrust and torque over the range of propulsor azimuth angles. This is consistent with the experimental results.

Figure 6-15 provides the calculated net normal force N and steering moment M compared to the experimental values. It is interesting that the BEM calculation of normal force appears to nearly match experimental results over nearly the entire range of angles. This should actually not be surprising. As mentioned previously, the blade sectional lift and drag coefficients have been empirically adjusted so that the thrust and torque match experimental results at zero propulsor azimuth angle. Because the normal force is completely determined by the integration of the in-plane force component F_θ (equations (6.20) and (6.22)), and F_θ is determined mainly by the blade drag force D (for small inflow angles ϕ, equation (6.20)), then the normal force N is determined primarily by the drag force on the blades. Additionally, it is observed that the assumed pod wake fraction has little effect on the calculated normal force. This is also as expected, since the normal force is a function of the cosine of the circumferential angle θ (equation (6.22)), and thus is effected only minimally by the pod wake. The calculated net steering moment is seen to be highly dependent upon the pod wake fraction w. This is also as expected, since the steering moment is a function of the sine of the circumferential angle θ (equation (6.22)), and thus is effected significantly by the pod wake.

Figure 6-16 provides the calculated axial and tangential disk-averaged induced velocities, and the calculated wake skew angle χ, as they vary with propulsor azimuth angle δ. Since these are all calculated based upon the annulus-averaged and disk-averaged values of velocity (equations (6.27) and (6.29)), the overall impact of increasing the pod wake fraction w is small.

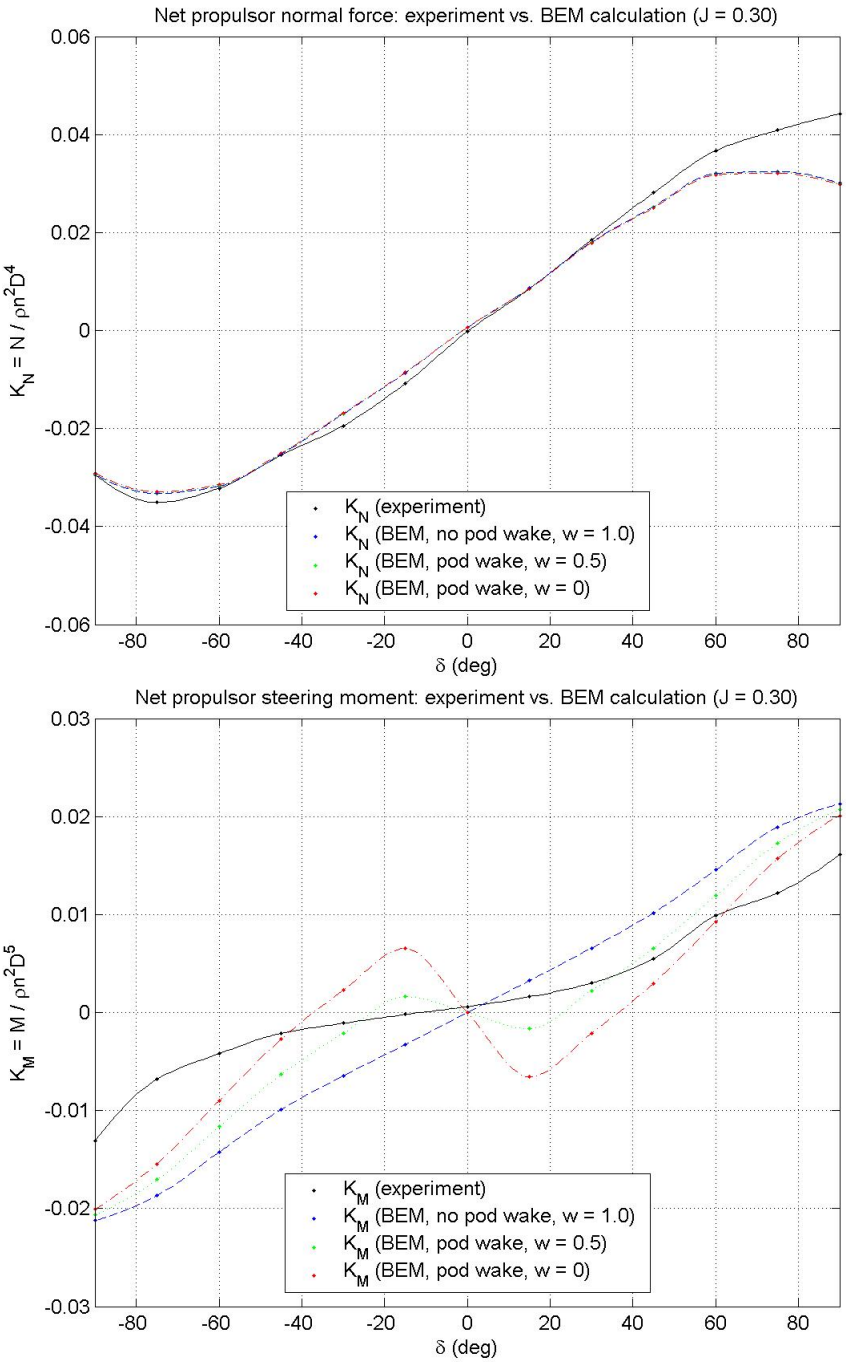

Figure 6-15: Modified combined BEM calculations vs. experiment. Top: normal force. Bottom: steering moment. Results are calculated propeller BEM results plus experimental pod-only forces. BEM calculations show sensitivity of results to assumed simplified inflow velocity pod wake deficit.

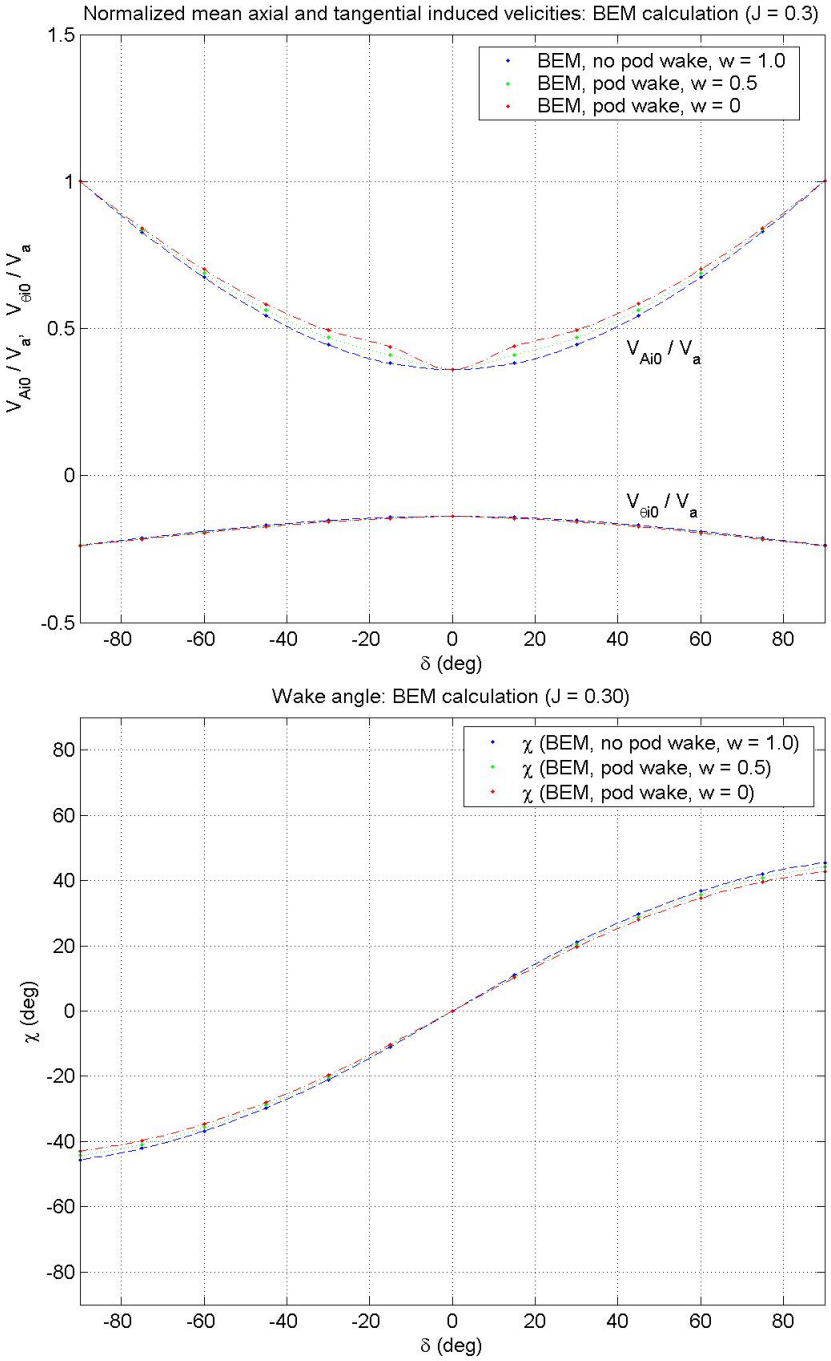

Figure 6-16: Modified combined BEM calculations. Top: disk-averaged axial and tangential induced velocities. Bottom: disk-averaged wake skew angle. BEM calculations show sensitivity of results to assumed simplified inflow velocity pod wake deficit.

6.3 Computational fluid dynamics

6.3.1 An unsteady propeller code and comparison with experiment

As a comparison with the propeller forces computed with the modified combined BEM method, and experiment, calculations have also been made using the propeller code MPUF-3A. MPUF-3A is a vortex and source lattice method originally developed at MIT in the late 1970s and 1980s [42],[44]. In the last decade, numerous additional features have been added, as summarized by Kinnas [45]. MPUF-3A now includes capabilities to perform calculations for fully-wetted as well as cavitating conditions in the presence of non-axisymmetric inflow, and also includes routines for wake alignment, inclined shaft, hub effects by imaging the vortex and source lattice with respect to the hub cylinder, plus a number of other features of importance for cavitating conditions [50]. It has been applied here only in terms of fully-wetted propeller forces.

The application of MPUF-3A to an azimuthing podded propulsor at moderate and large angles is clearly beyond the capability of the current computational routines within the program. While the program was able to compute maneuvering forces for even large propulsor angles *without* aligning the wake (i.e. assuming the wake *not* to skew relative to the disk, as discussed in Section 6.2.2), it has been found that the MPUF-3A wake alignment routines with shaft incline (i.e. for the propulsor in oblique inflow) are incapable of properly aligning the wake for more than small incline angles. However, it is noted that the experimental propulsor has a propeller with exceptionally small pitch/diameter ratio, and thus exacerbated the difficulty of the wake alignment routine.

In addition to the detailed propeller blade geometry, input to the MPUF-3A program requires description of the axisymmetric or non-axisymmetric inflow in terms of Fourier coefficients as described in Section 6.2.4. For the analyses, the same pod wake geometries and wake fraction representations used for the BEM calculations were used for the MPUF-3A calculations. Calculation of corresponding Fourier coefficients was performed as provided in Matlab® scripts in Appendix A. Figure 6-17 provides an example of the inflow velocity components required for MPUF-3A (axial, radial, tangential), and the 16-term Fourier series representation, for a specific radius and flow condition. This is the same pod wake inflow as shown in figure 6-13. Note, however, that the azimuthal angle θ is defined slightly differently here; a required transformation for input into MPUF-3A, since MPUF-3A is designed to be used for *vertical* propeller shaft incline, vice a podded propulsor with *horizontal* incline or azimuth.

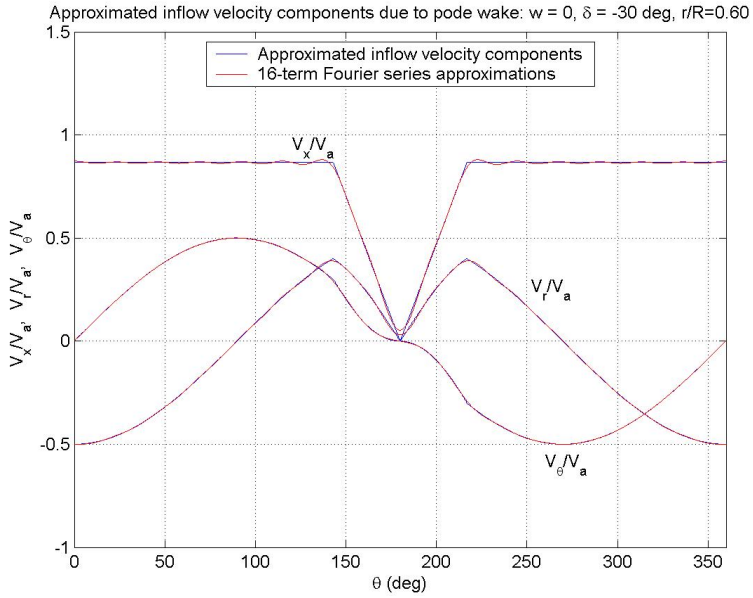

Figure 6-17: Approximated inflow velocity components due to pod wake. Assumed wake fraction w = 0, propulsor angle δ = -30°, normalized radius r/R = 0.60. Note that the origin of the azimuthal angle θ is different than figure 6-13 due to a transformation required for PUF-3A input.

Figure 6-18 shows the calculated net propulsor thrust and torque from MPUF-3A, *without* aligning the wake to the flow (i.e. the wake trails directly behind the propeller, regardless of the inflow angle), but including the vectored inflow velocity distribution as Fourier series harmonics. Note that these MPUF-3A forces are the 0^{th} harmonic force components (i.e. the steady force components), which are of primary importance to vehicle maneuvering. It is clear that, without wake alignment, MPUF-3A under-predicts thrust and torque (allowing for the experimental asymmetry as discussed in the previous section). This is as expected, since the propeller wake without alignment would induce *more* velocity at the disk than the aligned (skewed) wake. With more velocity induced at the disk, the angle of attack at the blade sections would be smaller, resulting in smaller blade thrust and torque (see figure 6-9). However, unlike the simplified BEM calculation, the vortex and source lattice wake calculation *does* include the 3-dimensional effects of the inflow (i.e. the additional *radial* inflow and induced velocity components), and thus some of the additional drag loss on the blades is accounted for. Note that the calculated net forces include the addition of the pod-only forces by superposition, as discussed in the previous section.

Figure 6-19 shows the calculated net propulsor normal force N, and steering moment M, also without wake alignment. Similar to the thrust and torque, without wake alignment to the flow, the normal force is under-predicted (since induced velocities at the disk are over-predicted without the wake skew). Similar to the BEM calculation discussed in the previous section, the

major effect on the normal force is the in-plane component of the tangential drag force. Thus, there is very little variation with the assumed inflow pod wake fraction w.

As mentioned, the wake-alignment routine in MPUF-3A was unable to properly align the wake with the flow for other than very small propulsor angles (less than 10°). This is illustrated in figure 6-20 for net propulsor thrust and torque. Figure 6-21 shows the calculated wake mappings for the unaligned and aligned calculation for the same test condition. Note the inability of the alignment routine to properly align the wake. The wake lattice of the forward blade actually passes in front of downstream blades.

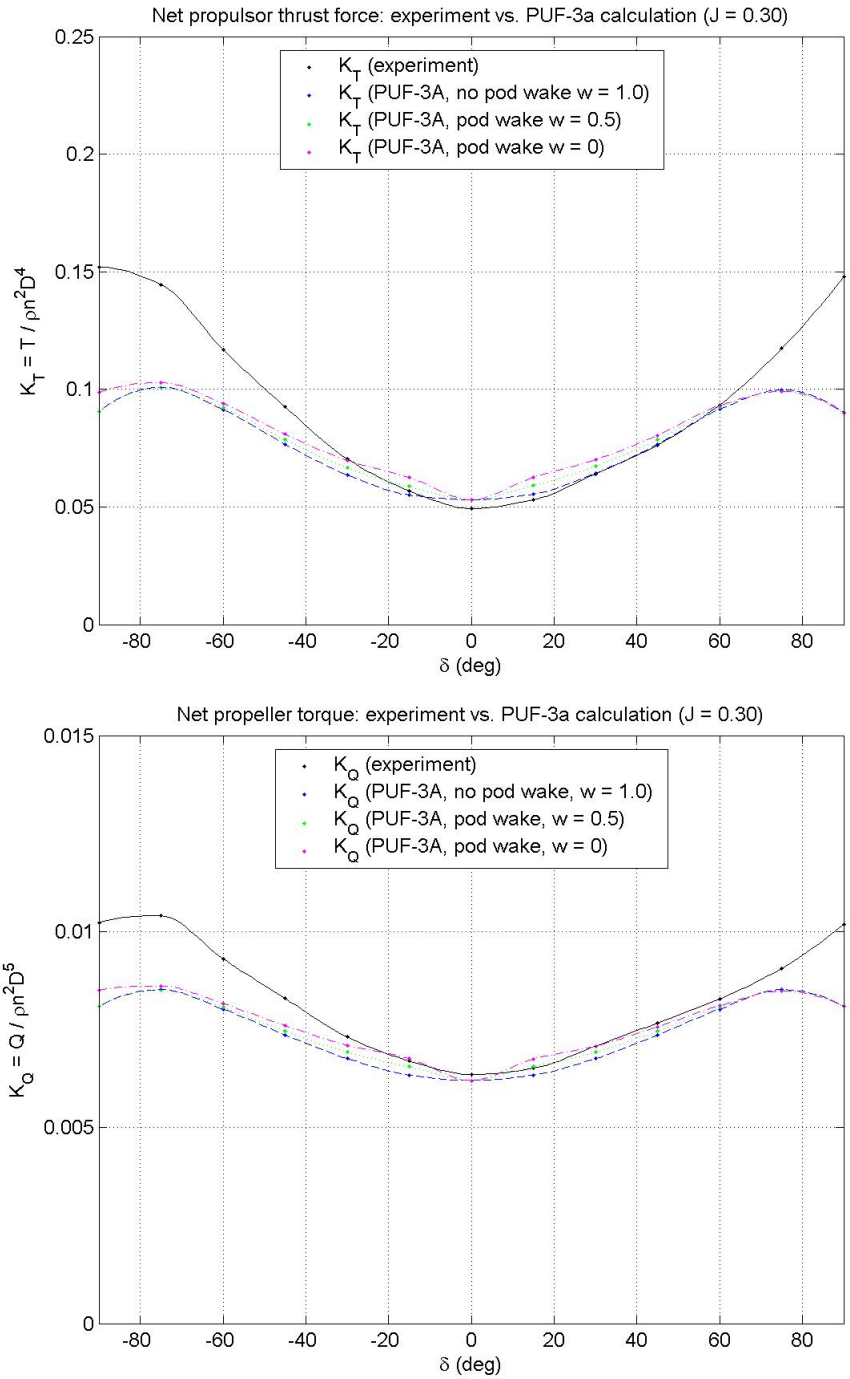

Figure 6-18: Calculations using vortex and source lattice code MPUF-3A. Wake is *not* aligned with the flow. Top: thrust. Bottom: torque. Results are calculated propeller results plus experimental pod-only forces. V_a = 2.5 ft/s, n = 10 rev/s (J = 0.304).

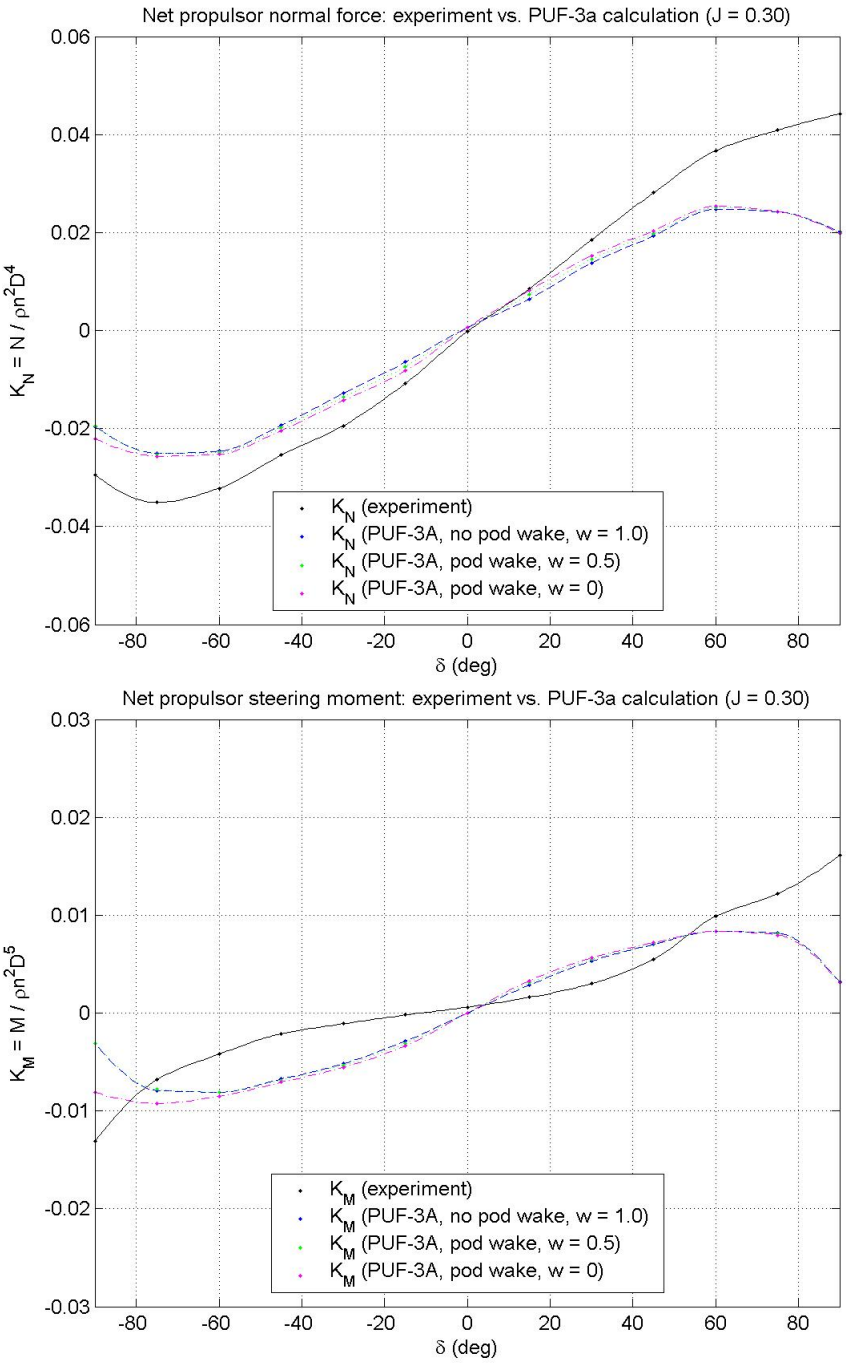

Figure 6-19: Calculations of the vortex lattice code MPUF-3A. Wake not aligned with flow. Top: Normal force. Bottom: Steering moment. Results are calculated propeller results plus experimental pod-only forces. V_a = 2.5 ft/s, n = 10 rev/s (J = 0.304).

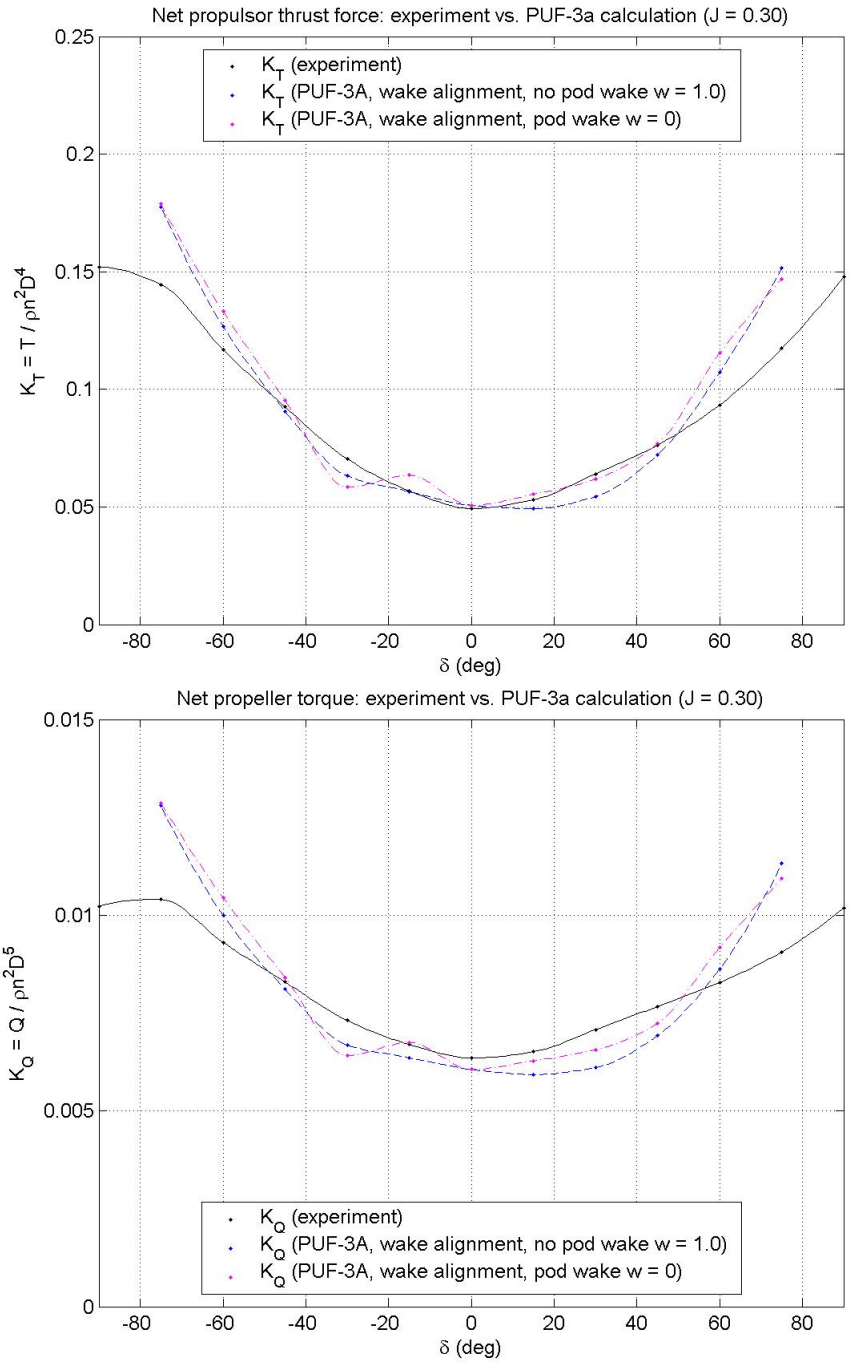

Figure 6-20: Calculations using the vortex lattice code MPUF-3A. Wake aligned with flow by MPUF-3A wake alignment method. Top: thrust. Bottom: torque. Results are calculated propeller results plus experimental pod-only forces. V_a = 2.5 ft/s, n = 10 rev/s (J = 0.304).

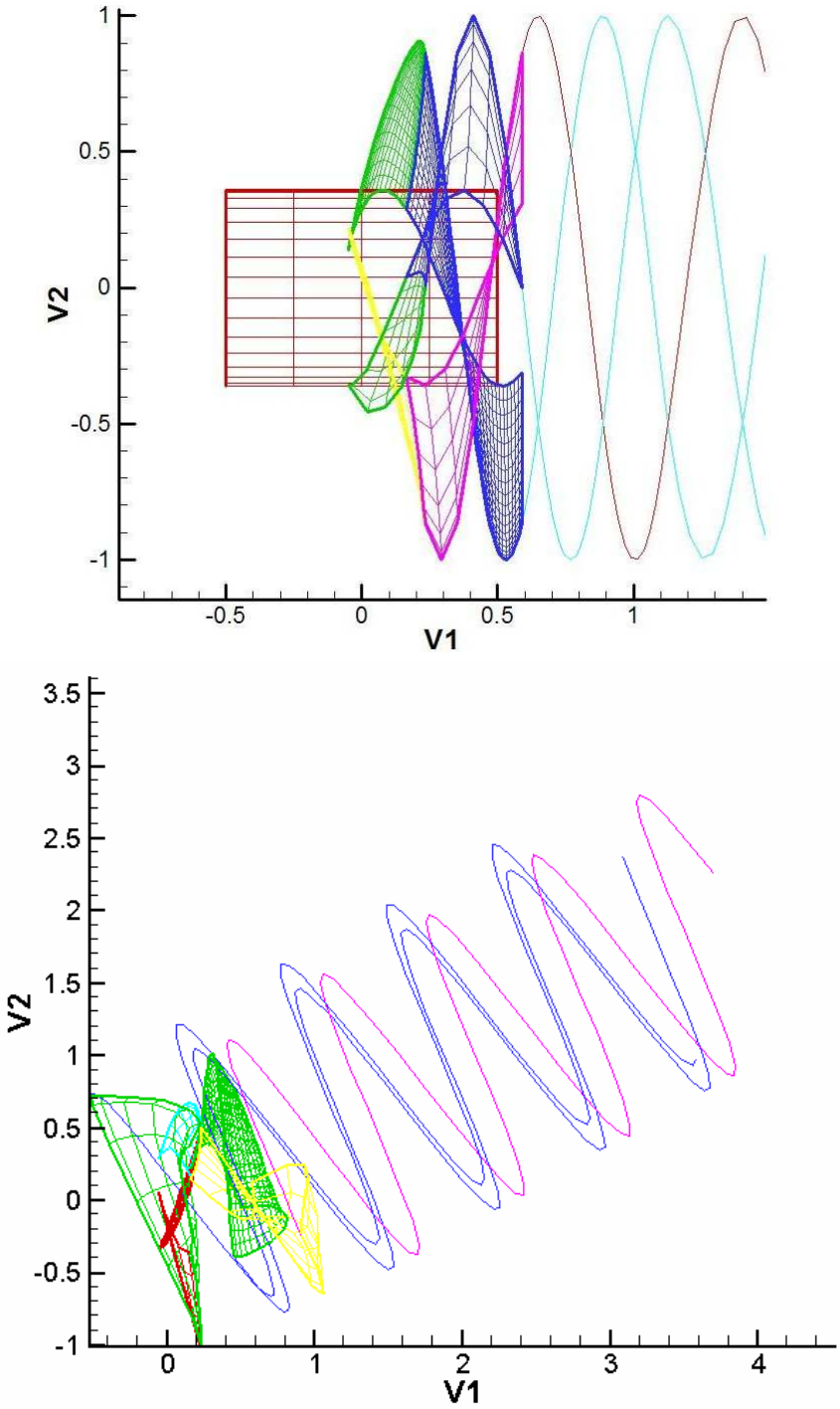

Figure 6-21: Calculations using the vortex and source lattice code MPUF-3A. Blade and wake lattice mapping. Top: Wake not aligned (trails directly behind propeller). Bottom: Wake aligned with flow. Note inability of alignment routine to properly align the wake. Wake lattice of forward blade passes in front of downstream blades. V_a = 2.5 ft/s, n = 10 rev/s (J = 0.304), propulsor azimuth $\delta = 30°$, pod wake fraction w = 0.

6.3.2 Current directions in computational fluid dynamics with azimuthing podded propulsors

As mentioned in the introduction in Chapter 1, until April 2004, there was very little available in the literature regarding ship and vehicle maneuvering and maneuvering forces associated with podded propulsors. The recent T-POD conference (see Section 1.2) has provided some initial results and experiences with computational fluid dynamics approaches being investigated for application to podded propulsors, both in terms of resistance and powering, and to a more limited extent, to maneuvering forces. However, in all cases, investigations currently underway are in the development stages, and limited to very small angle effects (i.e. small angle lift and drag forces, and steering moments).

Deniset et al. [16] provide an overview of ongoing analysis using a coupled potential flow and Reynolds-Averaged Navier Stokes (RANS) viscous flow solver for the calculation of pod lift, drag and steering moment coefficients for a tractor-type podded propulsor. The potential flow solution downstream of the propeller (velocities) is used as the inlet boundary condition within the RANS calculation, in which the pod housing and strut are explicitly modeled. Junglewitz et al. [40] use a coupled vortex lattice and RANS solver to calculate body forces on the strut and pod. The resulting velocities (wake) from the vortex lattice method are also used as input to the RANS solver. Ma et al. [54] use a vortex lattice method alone, in which propeller, pod housing and strut are all explicitly modeled, to calculate steering forces associated with the podded propulsor. In all cases, steering/maneuvering forces are currently being investigated only within the small angle or linear range.

It is apparent that the greatest difficulty inherent with the application of any of the computational fluid dynamics approaches being applied to the podded propulsion and maneuvering problem arises due to the calculation or modeling of the interaction effects between the propeller and the pod housing and strut. In either of the two primary pod configurations (i.e. pusher or tractor variants), there are unique interaction issues which must be addressed within the computational analysis scheme. For the pusher pod (i.e. propeller behind the pod), the inflow into the propeller must account for the unsteady wake of the pod and strut, which requires a viscous flow calculation to reasonably capture the large separation effects; this includes critical aspects of rotational flow variations (which are the cause of large maneuvering force asymmetries, as could be seen in the force data in Chapters 4 and 6). Conversely, the induced velocities of the propeller have a significant effect on the flow past the pods (and the resulting separation effects). For tractor pods (i.e. propeller in front of the pod), on the other hand, the inflow velocity to the propeller is relatively clean (affected only by the ship's wake field).

However, the wake of the propeller interacts strongly with the pod housing and strut, producing not only strong pressure fluctuations on the pod housing and strut, but also varying their separation characteristics. Conversely, the presence of the pod housing and strut within the slipstream of the propeller requires modification to the normally helical wake to account for the interference (especially from the large strut). Therefore, no matter what the selected pod configuration, there are significant interaction effects which must be dealt with within any computational fluid dynamics scheme, and an amount of empiricism is undoubtedly necessary to capture the relevant dynamics.

6.4 Summary

This chapter has provided a detailed discussion of a theoretical basis for the quasi-steady maneuvering dynamics associated with an azimuthing propulsor over the entire range of forward operating conditions (i.e. for propulsor azimuth to ± 90 degrees relative to the inflow). This theoretical basis has included discussion of "simple" momentum-based models for a propeller in axial and oblique inflows, and has been expanded to include a modified blade-element theory, using combined blade-element and momentum, including important wake considerations from vortex theory. Finally, a discussion of the use of computational fluid dynamics for the prediction of maneuvering forces has been presented. Results of calculations made have been provided in comparison with experimental results, with the relevance of consistencies and inconsistencies discussed in detail.

An interesting and obvious limitation on the application of a modified momentum theory to an azimuthing propulsor is the theoretical limitation of maximum thrust to that of the bollard condition ($V_a = 0$). However, force measurement results (Chapter 4) have shown that an "excess" thrust force (and torque) is seen by the propulsor over the entire range of operating angles (and is particularly obvious near $\delta = \pm 90°$). An intuitive explanation for the "excess" thrust has been offered using Glauert's hypothesis for helicopters in forward flight. Glauert's hypothesis is used to suggest that the propeller disk experiences an additional lift force when it is operating in an oblique inflow, thus providing this "excess" thrust.

The development and application of a modified combined blade-element-momentum (BEM) theory, and application of a vortex lattice computational fluid dynamics approach, have demonstrated some of the practical limitations utilizing any of the computational propeller methods in attempting to predict maneuvering forces on podded propulsors. It is apparent that the

greatest difficulty inherent with the application of any of the computational fluid dynamics approaches being applied to the podded propulsion and maneuvering problem arises due to the calculation or modeling of the interaction effects between the propeller and the pod housing and strut. In particular, for a pusher-type podded propulsor, the effect of the pod wake on the inflow is very difficult to model, even if experimental and empirical methods are applied. Conversely, the influence of the propeller flow past the pod housing and strut introduce significant uncertainty in the viscous and separation effects of the pod. Due to the close proximity and interaction of the propeller and pod housing and strut (particularly with propulsor azimuth angle or steering), complete numerical solution techniques to the podded propulsor maneuvering problem are distant.

This page left blank

Chapter 7

A theoretical basis for unsteady maneuvering dynamics

The unsteady force effects resulting from changes in propeller rate, propulsor azimuth angle, and ambient or advance velocity could be considered due to two main effects. First, there are non-stationary blade section profile dynamics related to realignment of the (2-dimensional) flow around the blade section. This flow has a flow dimension on the order of the blade chord length, and an associated time scale of the force dynamics on the order of $c/2\pi nr$ (where c is the chord length at radius r). Leishman [52] refers to this as the "inner problem" of the blade element approach. These are the "unsteady blade section dynamics" effects, which use a 2-dimensional model for the locally unsteady flow dynamics around the blade section. Analytical results for incompressible, unsteady airfoil problems (2-dimensional) have been formulated in both the frequency domain and time domain, primarily by Wagner, Theodorsen, Küssner, and vonKarman and Sears (see [9], [59] or [51]). Second, there are dynamics associated with the development of the unsteady 3-dimensional shed vortical wake (i.e. the helical wake or slipstream), and its effect on the induced velocity field in the vicinity of the propeller blades. This is the "outer problem" and can also be thought of as representing the inertia of the 3-dimensional helical wake, and therefore it has a different time scale than the non-stationary blade section profile dynamics. For helicopter rotors and wind turbines, where the rotor solidity ($\sigma = Zc/\pi R$) is very low, the time scale is on the order of D/U (where U is the inflow velocity at the disk including induced velocity) and at least an order of magnitude faster than the time scale of the non-stationary blade section profile dynamics [68]. However, for a marine propeller with higher solidity, this time scale can be somewhat faster, as will be derived and discussed in the following section. This latter wake effect, in that it considers the time variation of the velocities at the propeller (or rotor) disk, is often referred to as "dynamic inflow." Physically, of course, the two effects are intrinsically coupled. But, for both understanding and modeling purposes, they have in the past been dealt with separately [32], [33], [69], [52]. Although consideration in this chapter will focus on the "outer problem," through the development of a simple model for a "dynamic inflow" time constant τ, the "inner problem" will also be discussed.

Additionally in this chapter, the asymmetry seen in the experimental unsteady force results in Chapter 4 will be discussed in terms of additional unsteadiness in the vortical wake due to the generation of large transient vortex rings, seen in the flow visualizations in Chapter 5. The

formation of these vortex rings can be considered to occur with a given time constant (termed the "formation time"), and its "asymmetric" impact on the measured dynamic inflow time constants will be discussed.

7.1 Dynamic inflow

Unsteadiness of effective inflow and unsteadiness of induced velocities due to the time-variation of the vorticity (or inertia) in the shed wake have been studied in relation to pitch and yaw dynamics associated with helicopter maneuvering with sudden blade pitch changes, as well as in relation to unsteady blade loading on horizontal axis wind turbines in the presence of rapid blade pitch changes and sudden wind gusts. Previous approaches to modeling the unsteady 3-dimensional wake problem (i.e. the "outer problem" defined above) in helicopter and wind turbine analyses can be considered under two general headings: analytical approaches to "dynamic inflow", and numerical approaches such as "free wake" models. The latter approach is more appropriately based upon the vorticity changes in the shed helical wake, but is computationally-expensive and, for the current state, difficult to couple with desired unsteady analyses such as unsteady blade flexure dynamic and maneuvering dynamic models. The former approach is based upon the simpler analysis of the inertia of the 3-dimensional wake, and offers more suitable mathematical forms for inclusion in coupled dynamic analyses, and has been used almost exclusively for helicopter and wind-turbine blade dynamic analyses (blade flapping). However, "free wake" computational fluid dynamics have also been used to develop appropriate time constants which have subsequently been used in analytical "dynamic inflow" models [67], [68]. The general concept of the analytical approach to dynamic inflow is discussed further here as an application to gain intuition of the unsteady propulsor maneuvering dynamics.

Snel and Schepers [67], [68] have provided a thorough and interesting perspective on dynamic inflow. They use the term dynamic inflow to indicate the response of the inflow velocities in the rotor plane (helicopters or wind turbines) to changes in the load conditions on the rotor. Figure 7-1 provides a simple example, in which the blade pitch angle undergoes a rapid change from an initial value β_1 to a new value β_2. Blade-element-momentum theory (or steady vortex wake theory) gives two different equilibrium values of the induced velocities at the disk pertaining to the two pitch angles (i.e. V_{i1} and V_{i2}). In reality, there is time needed for the flow to accelerate and the 3-dimensional wake to change. If the pitch angle change is sufficiently fast, the inflow velocity will essentially still be at the initial value, and only gradually change to the

new value. The consequences of this are also shown. Instead of instantly changing the blade angle of attack from α_1 to α_2, as suggested by quasi-steady equilibrium theory, there is an important "overshoot" in the angle of attack (indicated by the heavy line). The actual "overshoot" is dependent on the time scale involved in the adjustment of the inflow (i.e. the development of the changes to the overall helical wake). Consequently to the "overshoot" of the angle of attack, the blade loads (particularly the lift force) also exhibit an "overshoot" (also compared to their equilibrium values). For an ideal step change in blade pitch angle, the induced velocity builds up more or less exponentially, with a given time constant. Conversely, the angle of attack and blade forces, following the initial overshoot transients, decay to their steady-state values, roughly with the same time constant. This time constant is referred to here as the "dynamic inflow time constant," or "wake time constant".

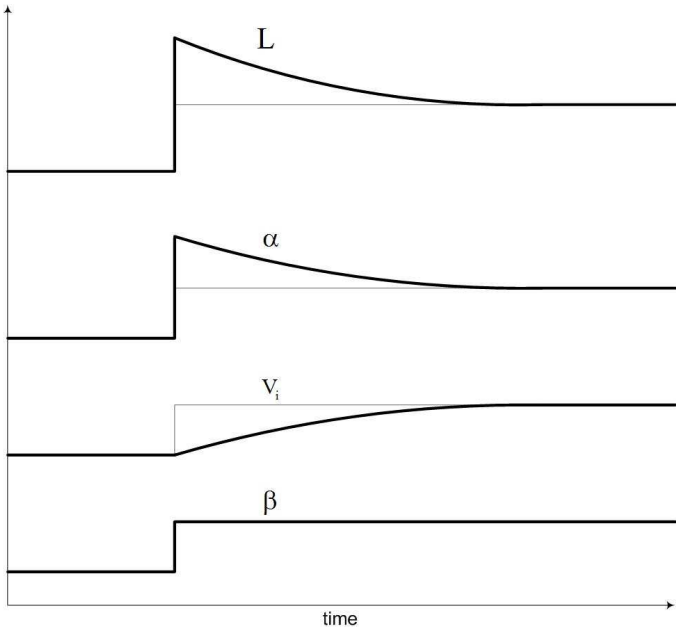

Figure 7-1: Illustration of the influence of wake inertia (dynamic inflow) on induced velocity, angle of attack, and lift force after a step change in blade pitch angle. Basic graphic adapted from [68].

The first principles of the analytical dynamic inflow approach for helicopters and wind turbines can be attributed to Carpenter and Fridovich [13], who considered the thrust dynamics associated with the unsteady aerodynamic lag of the inflow velocity development over the hovering helicopter rotor disk in response to sudden changes in blade pitch. Their approach consisted of combining an unsteady form of the combined blade-element-momentum theory,

along with simple blade flexure dynamics, to develop a set of simultaneous ordinary differential equations, with the time constant representing the dynamic lag in the build-up of the induced velocity with the changes in blade pitch angle [52]. A more recent, but more complex model for dynamic inflow, being utilized for both helicopter and wind turbine work, is that due to Pitt and Peters [63] (see also [22] and [62]), who developed a perturbation dynamic inflow velocity theory from a rigorous solution to the actuator disc theory using an unsteady potential flow method. With the added complexity of the Pitt and Peters model came a model including the range of helicopter flight conditions (hover, axial, forward flight) and the incorporation of wake skew. The Pitt and Peters model is fundamentally of the same form as earlier models for quasi-steady wake skew effects (i.e. the wake skew effects in terms of altered distribution of induced velocity across the disk, [25], [14]), with the additional incorporation of time constant(s) for the lag of induced velocities at the disk. The added functionality of the Pitt and Peters model has been utilized for unsteady blade flapping analyses of helicopter rotors and wind-turbines. However, the added complexity of the Pitt and Peters model is not considered warranted for illustration of the marine vehicle maneuvering problem considered here. Additionally, the Pitt and Peters model neglects a term that relates to the solidity of the propeller (usually very small for a helicopter rotor or wind-turbine rotor, but not necessarily for a marine propeller), and therefore would grossly over-predict the dynamic inflow time constant. As an application of a "dynamic inflow" model to the marine propeller, a model for the dynamic inflow time constant τ for a change in induced velocity with a change in propeller rate, is presented (based partially on [13] and [52]).

From momentum theory, an unsteady equation relating thrust to the induced velocity of a propeller in axial flow can be written

$$T = m_a \dot{v}_i + \rho A v_i \left(v_i + V_a \right) \tag{7.1}$$

where m_a is an apparent added mass of water influenced by the propeller disc. For the bollard condition, this is

$$T = m_a \dot{v}_i + \rho A v_i^{\,2} \tag{7.2}$$

Starting with the bollard condition, if the propeller is considered to be at a steady propeller rate n, and an instantaneous (step) change in propeller rate is applied (which is analogous to an instantaneous (step) change in pitch angle β), based on vortex theory, the induced velocity at the disc begins to build up with a certain time constant. If it is assumed that the induced velocity is of uniform distribution across the disk, then the flow field is analogous to an impervious disk being moved horizontal to the flow with velocity v_i. The added mass of an impervious circular disc being accelerated perpendicular to its face is provided by Munk [58] and is equal to

$$m_a = 0.637\left(\frac{4}{3}\right)\rho\pi R^3 \tag{7.3}$$

From blade element theory, the differential thrust force on a blade element can be written and integrated over the blade radius and summed over the Z blades

$$\begin{aligned} dT &\approx Z\frac{1}{2}\rho(2\pi n)^2 r^2 C_{l\alpha} c\left(\beta - \frac{v_i}{2\pi n r}\right)dr \\ T &\approx Z\frac{1}{2}\rho(2\pi n)^2 C_{l\alpha} c\left[\beta\int_0^R r^2 dr - \frac{v_i}{2\pi n}\int_0^R r dr\right] \approx Z\frac{1}{2}\rho c C_{l\alpha}(2\pi n)^2 R^3\left[\frac{\beta}{3} - \frac{v_i}{2(2\pi n)R}\right] \end{aligned} \tag{7.4}$$

Equating the expressions (7.2) and (7.4) for thrust

$$0.637\left(\frac{4}{3}\right)\rho\pi R^3\dot{v}_i + \rho\pi R^2 v_i^{\,2} \approx Z\frac{1}{2}\rho c C_{l\alpha}(2\pi n)^2 R^3\left[\frac{\beta}{3} - \frac{v_i}{2(2\pi n)R}\right] \tag{7.5}$$

An approximate linear dynamic inflow time constant of the buildup of induced velocity at the disk can be obtained by writing the induced velocity as a steady part plus a perturbation part

$$v_i = \bar{v}_i + v_i' \qquad \dot{v}_i = \dot{v}_i' \tag{7.6}$$

Substituting this in to equation (7.5)

$$0.637\left(\frac{4}{3}\right)\rho\pi R^3\dot{v}_i' + \rho\pi R^2\left(\bar{v}_i^{\,2} + 2\bar{v}_i v_i' + v_i'^{\,2}\right) \approx Z\frac{1}{2}\rho c C_{l\alpha}(2\pi n)^2 R^3\left[\frac{\beta}{3} - \frac{(\bar{v}_i + v_i')}{2(2\pi n)R}\right] \tag{7.7}$$

Neglecting $v_i'^2$, rearranging and dividing through, the result is a first order differential equation for the (perturbation of) induced velocity

$$\overbrace{\left(\frac{0.637(4/3)R}{2\bar{v}_i + Z(1/2)cC_{l\alpha}n}\right)}^{\tau}\dot{v}_i' + v_i' = \left(\frac{Z(2\pi)cC_{l\alpha}n^2 R\left[\frac{\beta}{3} - \frac{\bar{v}_i}{4\pi n R}\right] - \bar{v}_i^{\,2}}{2\bar{v}_i + Z(1/2)cC_{l\alpha}n}\right) \tag{7.8}$$

In this form, the coefficient of the unsteady term is the linear time constant (the large term on the right is a constant). Thus, the dynamic inflow time constant is

$$\tau = \left(\frac{0.637(4/3)R}{2\bar{v}_i + Z(1/2)cC_{l\alpha}n}\right) \tag{7.9}$$

It is noted that this time constant τ is dependent upon the propeller rate n, as well as the steady part of the induced velocity $\bar{v}_i$. It is also interesting to note that the right hand term in the denominator of equation (7.9) is neglected in the Pitt and Peters model (since the solidity of the helicopter rotor is relatively small). But, it is noted that this term is important to the marine propeller with higher solidity.

To further simplify, an expression for the steady part of the induced velocity at the bollard condition is used. For the bollard condition, the steady momentum result provides

$$T = 2\rho A_p \bar{v}_i^{\,2} \quad \rightarrow \quad \bar{v}_i = \sqrt{\frac{T}{2\rho A_p}} \tag{7.10}$$

or using the definition of thrust coefficient

$$\bar{v}_i = \sqrt{\frac{K_T \rho n^2 D^4}{2\rho\pi (D/2)^2}} = \left[\frac{2}{\pi} K_T\right]^{1/2} nD \tag{7.11}$$

Substituting equation (7.11) into the expression for the time constant and approximating the blade element lift coefficient $C_{l\alpha}$ by 2π and simplifying

$$\tau \approx \frac{(0.637)\left(\frac{1}{6}\right)D}{\left(\frac{1}{2}\right)\left(\frac{2}{\pi}\right)^{1/2} K_T^{\,1/2} Dn + \left(\frac{\pi}{4}\right) Zcn} \text{ (sec)} \tag{7.12}$$

This represents an approximate linear time constant (in *seconds*) for the development of induced velocity at the disk from a change in propeller rate, for the bollard condition. Note that this time constant is a function of the propeller rate n and the steady-state thrust coefficient at the bollard condition (J=0), as well as the propeller geometric parameters.

The time constant can also be written in non-dimensional form by using the definition of thrust coefficient and defining a non-dimensional induced velocity based upon the propeller rate and diameter (similar to the advance coefficient J)

$$\lambda_i = \frac{v_i}{nD} \quad \text{and} \quad \dot{\lambda}_i = \frac{v_i}{n^2 D} \tag{7.13}$$

and substituting into equation (7.7) or (7.8). The result is the non-dimensional time constant

$$\tau \approx \frac{(0.637)\left(\frac{1}{6}\right)D}{\left(\frac{1}{2}\right)\left(\frac{2}{\pi}\right)^{1/2} K_T^{\,1/2} D + \left(\frac{\pi}{4}\right) Zc} \text{ (rev)} \tag{7.14}$$

This represents an approximate linear time constant (non-dimensional, in propeller *revolutions*) for the development of induced velocity at the disk from a change in propeller rate, for the bollard condition.

For the experimental propeller, D = 0.8229 ft, c = 0.17 ft, Z = 3 blades, and the thrust coefficient for the bollard condition (as determined from experiment, see Chapter 4) is $K_T = 0.13$. The resulting non-dimensional time constant is

$$\tau' \approx 0.2 \text{ (rev)}$$

Using a nominal propeller rate n = 5 rev/sec = 300 RPM a nominal dimensional time constant is

$$\tau \approx 0.04 \text{ (sec)}$$

Thus, for the experimental propeller operating at a nominal 300 RPM at the bollard condition, an approximate time constant for development of induced velocity from a change in propeller rate is approximately 0.04 seconds or 0.2 propeller revolutions.

It is interesting to note the impact of the solidity of the marine propeller as mentioned above. If the solidity term (the right hand term in the denominator of equation (7.9)) were neglected as in the Pitt and Peters model, then the calculated time constant would be approximately 0.15 sec or 0.75 propeller revolutions (nearly 4 times slower).

For the non-bollard condition, the situation is a bit more complex in that there is an additional inflow velocity term V_a as in equation (7.1), and a different momentum result in place of equation (7.10)

$$T = 2\rho A_p \bar{v}_i (\bar{v}_i + V_a) \quad \rightarrow \quad \bar{v}_i^{\,2} + V_a \bar{v}_i - \left(\frac{T}{2\rho A_p} \right) = 0 \quad \rightarrow \quad \bar{v}_i = -V_a \pm \sqrt{V_a^{\,2} - 2\frac{T}{\rho A_p}}$$

However, equations (7.12) and (7.14) still approximately hold if the rotational velocity is much greater than the advance velocity (i.e. $2\pi nr >> V_a$). It is clear from inspecting equations (7.12) and (7.14) that the dominant effect for the experimental propeller is related to the propeller rate n (since in general $2\pi nr >> v_i$ and $2\pi nr >> V_a$ (Chapters 4 and 5)).

As mentioned previously, while a sudden increase in propeller rate n causes the induced velocity at the disk to build-up with first order dynamic inflow time constant τ, the local forces at the propeller blade (i.e. lift and drag, or thrust force and tangential force) see a sudden overshoot, and then *decay* approximately with time constant τ (see figures 7-1 and 7-2). With a rapid increase in propeller rate n, comes a rapid increase in the blade angle of attack α. This sudden increase in blade angle of attack directly increases lift and drag (or thrust and tangential) forces through the blade lift characteristics. The converse effects are seen with a sudden decrease in propeller rate n. Thus, the net effect is that the thrust force, torque, normal force and steering moment can be expected to be higher than their steady counterpart (at the same propeller rate or angle of attack). Thus, in terms of the response to a step current change or rapid ramp change to propeller RPM, the propeller blade forces can be considered to *"lead"* a change in propeller rate with the dynamic inflow time constant τ, as discussed in Chapter 2 (equations (2.9)).

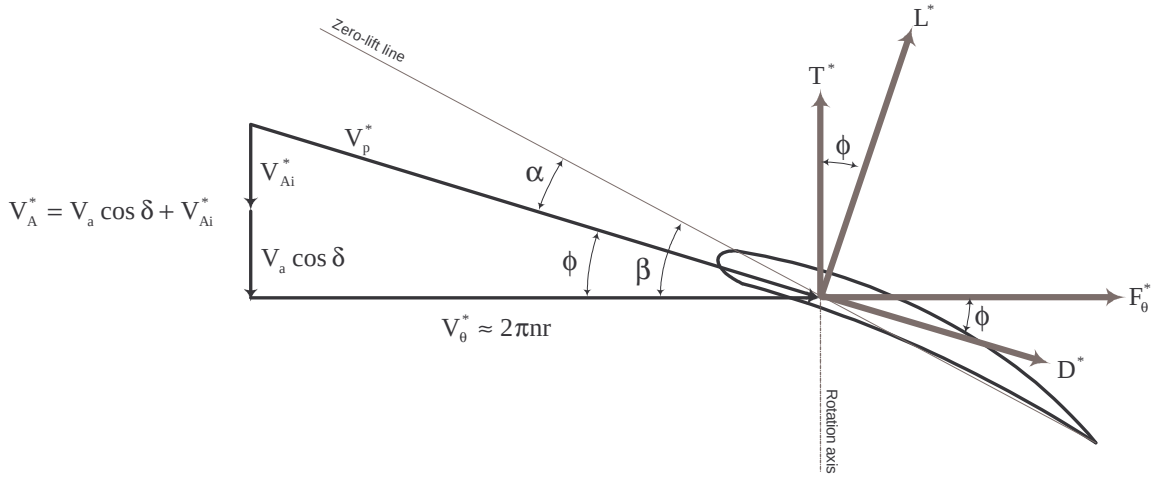

Figure 7-2: Mean blade element velocities and forces for a propeller operating in oblique inflow, neglecting slip stream rotation.

This same dynamic inflow time constant τ is also theoretically applicable for sudden changes in the other propeller states (advance velocity V_a and propulsor azimuth angle δ). Looking again at figure 7-2, it should be clear that sudden changes in either advance velocity V_a or propulsor azimuth angle δ directly effect the axial inflow velocity at the blade element V_A^*, and thus are also precisely related to a change in blade angle of attack α, and thus should theoretically have the same time constant τ for change in induced velocity at the disk or change in the blade (and propeller) forces, as discussed above. For example, a sudden *increase* in propulsor azimuth angle δ (say from zero to some moderate or large angle), *reduces* the effective inflow velocity $V_a\cos\delta$, and thus *increases* the blade angle of attack and blade forces. Thus, the blade forces should *lead* a change in azimuth angle approximately with the first order dynamic inflow time constant τ. This was shown in the experimental results in Chapters 4 and 5.

In the Pitt and Peters dynamic inflow model [63], [22], [62], an axial flow time constant as discussed above is combined with time constants for the *distributed* inflow by considering the inflow velocity as the sum of spatial harmonics around the disk

$$v_i(r,\theta) = v_o + v_s \frac{r}{R}\sin\theta + v_c \frac{r}{R}\cos\theta \qquad (7.15)$$

Thus, to model a full distribution (r,θ) of unsteady induced velocities with first order harmonics, the single time constant for the axial inflow case becomes a 3x3 matrix of time constants for the distributed inflow case. This more complex Pitt and Peters model has been used in investigation of blade flapping dynamics of helicopter and wind-turbine rotors, where those harmonic structural effects can be important.

Leishman [52] points out that one of the less satisfying aspects of the simplest analytical forms of the dynamic inflow theory is that the time constants of the dynamic inflow have been developed using the concept of an apparent mass or inertia of the flow surrounding the disk (i.e. a non-circulatory effect) as opposed to the lag in the dynamic evolution of the actual vortical wake (i.e. a circulatory effect). Additionally, the apparent mass approach assumes equivalence between the apparent force on a solid disk accelerating in a stagnant fluid and the force on a fluid accelerating through a permeable actuator disk; which of course is not a rigorous analogy. On the other hand, Snel and Schepers [67], [68] have shown that values of the dynamic inflow time constant can also be calculated based upon more rigorous "free wake" numerical methods, then used in simple dynamic equations. This process has provided excellent results compared to experiments.

Finally, a note is made regarding the local non-stationary blade section profile dynamics (or the "inner problem") mentioned in the chapter introduction. Although the dynamic inflow time constant associated with the dynamics or inertia of the wake (i.e. the "outer problem") for a helicopter or wind turbine rotor is typically an order of magnitude greater than the time constant of the blade section profile dynamics (the "inner problem"), this is not necessarily the case for a marine propeller with higher solidity. As mentioned previously, the addition of the solidity effect in the dynamic inflow model (the numerator of equation (7.9)) significantly reduces the effective dynamic inflow time constant, and could bring it into the same order as the time constant associated with the local blade section profile dynamics, which is on the order $c/2\pi nr$.

For example, a review of the solution of the "inner problem" using indicial response theory such as a Wagner function or Küssner function (see [9], [59] or [51]), indicates that the lift force *increases* toward its steady state value with a sudden change in angle of attack or inflow. The Wagner function, which is a solution for an instantaneous change in angle of attack, provides an instantaneous increase in lift to ½ its final value, then (approximately) an exponential increase to its final value. The Küssner function, which is a solution for a sharp-edged gust (i.e. an inflow change), provides an (approximately) exponential increase in lift to its final value. What is interesting is that these solutions to the "inner problem" transient solution are quite contrary to the "overshoot" seen with the "outer problem" solution due to the dynamics associated with the build up of induced velocity as the 3-dimensional wake builds (i.e. "dynamic inflow"). Thus, if the time constants of the two effects are on the same order, the two effects may *compete* in terms of the time response of the lift force on the blades.

For the experimental propeller, for the "inner problem" solution using the Wagner function, the time constant of the increase in lift force with an instantaneous change in angle of attack is

approximately $2(c(r)/2\pi nr) = c(r)/\pi nr$ (see [59] for example). This non-dimensional time constant then varies from approximately 0.4 revolutions at the hub to 0.02 revolutions near the tip (with an approximate elliptic profile for c(r)). This can be compared to the computed time constant for the dynamic inflow model of approximately 0.2 revolutions. Thus, for blade sections near the hub, the time constants of the two dynamic effects are nearly coincident. Therefore, it could be assumed that the local blade force dynamics (an exponential increase in lift force) is *competing* to some extent with the wake dynamics (an overshoot and decay in lift force). However, since the analytic dynamic inflow model gives no indication of the amount of overshoot, the magnitude and significance of this competition would be difficult to quantify. However, the results of the experiments reported in Chapter 4 provide evidence that the wake dynamics or "dynamic inflow" effect (i.e. the overshoot and decay in lift force) provides a more significant effect on the overall transient force response for this propeller.

7.2 Vortex ring formation with rapid increase in propeller rate

It was mentioned in the chapter introduction that the asymmetry seen in the experimental unsteady force results in Chapter 4 might be considered as due to unsteadiness in the vortical wake due to the generation of large transient vortex rings, seen in the flow visualizations in Chapter 5. This chapter discusses formation of vortex rings, and demonstrates that the formation of these vortex rings can be considered to occur with a given time constant (termed the "formation time"), and the "asymmetric" impact on the measured dynamic inflow time constant is discussed.

The experimental investigation of vortex rings in the laboratory has typically been conducted by the ejection of a fluid slug into a quiescent fluid by moving a piston through a tube, with a resulting vortex ring being generated at the exit of the tube. The vortex ring results from the roll up of the slug's shear layer as it is ejected from the tube. While the generation of a vortex ring associated with a rapid propeller rate increase is clearly not strictly analogous to the experimental fluid slug concept, the basic mechanisms associated with the formation of the vortex ring and the roll up of a shear layer may be considered as common (the shear layer from a propeller coming from the shedding of vorticity from the propeller blades into their respective vortical wake surfaces and tip vortices).

7.2.1 Formation time of a vortex ring for a fluid jet

General reviews of the behavior of vortex rings are given by Shariff and Leonard [66] and Lim and Nickels [53]. While experiments and computations have had varied success in identifying similarity behaviors associated with vortex rings, it is well known that the physical mechanics of the ejection process and the physical attributes of flow boundaries greatly affect the character and evolution of the vortex ring [3]. In other words, the differences in boundary conditions for the shear layer generation may play a significant role in the time for development of the vortex ring.

A widely accepted simplified model for the formation of vortex rings by the ejection of a slug of fluid by moving a piston through a tube is discussed by Glezer [26]. A vortex ring is invariably formed by a programmed discharge of fluid over a short time interval. An elementary representation of the process is the uniform cylindrical "slug" model, in which a cylindrical volume of fluid moves at a step velocity U_0 for a time T_0 through a circular tube of diameter D_0. If U_0 is not constant, then the mean velocity with respect to time can be determined

$$\overline{U}_0 = \frac{1}{T_0}\int_0^{T_0} U_0(t)\,dt \tag{7.16}$$

where, for the "slug" model, $U_0(t)$ is assumed to be uniform over the orifice or discharge area. The impulse (the momentum associated with the discharge) is

$$I = \rho A \int_0^{T_0} U_0^2(t)\,dt = \rho A\, \overline{U_0^2}\; T_0 \tag{7.17}$$

A simple expression for the initial circulation associated with the generation of the vortex ring (in a half-plane through the axis of symmetry) can be derived based upon the rate of vorticity flux from the edge of the tube or orifice, which has instantaneous magnitude of approximately $U_0^2/2$ (this is using a boundary-layer approximation for the flux of vorticity across the plane of the tube or orifice). This results in a simple expression for the development of circulation being fed to the vortex ring

$$\Gamma_0 = \int_0^{T_0} \frac{U_0^2(t)}{2}\,dt = \frac{\overline{U_0^2}\; T_0}{2} \tag{7.18}$$

Recent experiments by Gharib et al. [23] for vortex rings generated through impulsively-started jets indicate that the flow generated by large stroke ratios (i.e. large L_0/D_0) consists of a leading vortex ring, followed by a trailing jet, with the vorticity field of the leading vortex ring disconnected from the trailing jet. On the other hand, flow fields generated by small stroke ratios

show only a single vortex ring, with no trailing jet. The transition between the two phenomena occurs at a stroke ratio of approximately 4 (referred to by Gharib et al. as the "formation number"). It was shown that, in all cases, the maximum circulation that the vortex ring could attain during its formation is reached at this "formation number". Through a series of tests varying exit diameters and boundaries, as well as a variety of non-impulsive piston velocities, it was shown that the "formation number" lies in the range $3.6-4.5$ for a broad range of "slug" flow conditions. It is also noted that the "formation number" (L_0/D_0) is the same as a non-dimensional time for formation of the ring, or "formation time" (i.e. $L_0/D_0 = U_0T_0/D_0$). Gharib et al. conceived the existence of this "formation number" as a limiting value, above which vortex rings generated do not absorb more of the mass or vorticity of the discharged fluid jet, and the vortex ring is said to have "pinched-off" from the generating jet.

Following on the work of Gharib et al., Krueger et al. [48] studied the vortex ring "pinch-off" (or "formation number") in the presence of simultaneously initiated uniform background co-flow. Defining the co-flow velocity V_0 (i.e. the ambient velocity outside the jet), a ratio of co-flow to piston velocity was defined

$$R_v = \frac{V_0}{U_0} \tag{7.19}$$

The velocity ratio R_v was varied through the range 0 to 1 over a range of stroke ratios L_0/D_0. The results indicated a marked drop in "formation time" for velocity ratios greater than 0.75, implying that vortex rings reach their (reduced) peak circulation ("pinch-off") more rapidly in the presence of background (ambient) co-flow.

Making a direct computational analogy or correlation between the piston-tube "slug model" as discussed above, and the flow resulting from the rapid change in propeller rate, is probably questionable in a strict theoretical sense, since the mechanism and geometry for development of the feeding shear layer is clearly different in the two cases. However, the strong visual evidence of the generation and convection of a vortex ring with a rapid increase in propeller rate (Chapter 5) presents a compelling argument for considering the similarities in the vortex ring generation and growth process and its potential effect on induced velocities at the propeller disk. The "slug model" assumes a uniform velocity distribution across the discharge orifice, and assumes the vorticity to be generated in the boundary layer along the walls of the tube. The "slug model" then assumes this vorticity to directly "feed" the growing vortex ring as the jet exits the orifice (up to the "formation time", where the vortex ring is "pinched-off"). Since there is no "tube" with the propeller, the free vorticity that is "fed" to the growing vortex ring must come from the vorticity in the unsteady flow from the propeller blades. For the case of initial propeller motion, this

would include the startup vorticity required to meet the Kutta-Joukowsky condition at the trailing edge of the blades.

As mentioned in Chapters 4 and 5, the net effect of the abrupt shedding of vorticity into the wake and formation of the vortex ring would be in terms of the immediately altered flow around the propeller disk. For example, for a rapid increase in propeller rate, the vortex ring would tend to *increase* the axial induced velocity at the disk, and consequently *decrease* the angle of attack and blade lift (and thrust) force (see figure 7-2).

According to the results of Gharib et al. [23] and Krueger et al. [48], the non-dimensional "formation time" for the vortex ring for impulsively-started jets is on the order of 4. Initially then, making an extrapolation to the propeller and vortex ring for the bollard condition (see figure 5-6)

$$T_0 \approx \frac{4D_0}{\overline{U}_0} \approx \frac{4\,(0.80\,\text{ft})}{(1\,\text{ft/sec})} \approx 3.2\,\text{sec}$$

where the mean velocity of the "jet" is roughly estimated to be the mean axial induced velocity during the startup phase (approximately 1 ft/s). However, approximation of a "formation time" for the vortex ring of the propeller by a simple conservation of mass approach (measuring the approximate final dimensions of the vortex ring including its entrained fluid (approximated as the outside volume of a torus), calculating its final mass, and equating to an approximation for the total mass flux provided by the propeller in the bollard condition) gives

$$T_0 \approx \frac{\rho V_{torus}}{\rho A_p \overline{U}_{Ai}} \approx \frac{(0.22\,\text{ft}^3)}{(0.45\,\text{ft}^2)(1\,\text{ft/sec})} \approx 0.5\,\text{sec}$$

where V_{torus} is the outside volume of the torus that is the "final" vortex ring size (see figures 5-6 and 5-7), $\overline{U}_{Ai}$ is the mean axial induced velocity during the startup phase (approximately 1 ft/s), and A_p is the cross sectional area of the propeller disk. It is interesting to note from the image sequence shown in figures 5-6 and 5-7, that the vortex ring has reached its full size within approximately 0.5 seconds (thus, an approximate "formation time" is on the order of 0.5 seconds). Therefore, it could be deduced that the *rate* of vorticity being fed to the vortex ring by the unsteady flow from the propeller blades is significantly greater than the rate of vorticity that is fed in the "slug model" by the boundary layer of the tube in the standard experiments. This should not be surprising owing to the highly vortical nature of propeller flows in general.

7.2.2 Formation time of a vortex ring with a rapid increase in propeller rate

To develop a more appropriate expression for the non-dimensional "formation time" for a rapid increase in propeller rate, a non-dimensional time associated with the formation of the vortex ring due to a rapid increase in propeller rate can be written

$$\tau_R = \frac{U_R t}{D} \tag{7.20}$$

where U_R is the characteristic velocity of the axial flow feeding the vortex ring. If this characteristic velocity is initially represented by the velocity induced at the center of the ring by the circulation within the ring, then it can be written by simple application of the Biot-Savart Law (for a thin ring) as

$$U_R \approx U_{Ai0} \approx \frac{\Gamma_R}{2R} \tag{7.21}$$

where U_{Ai0} is the velocity induced at the center of the ring. Thus, a non-dimensional time associated with the formation of the vortex ring due to a rapid increase in propeller rate can be approximated

$$\tau_R \approx \frac{\Gamma_R t}{D^2} \tag{7.22}$$

For the propeller as the source of the circulation feeding the ring, the circulation produced by a single propeller blade can be approximated by the lift L and relative blade velocity U as

$$\Gamma \approx \frac{L}{\rho U s} \approx \frac{\frac{1}{2}\rho U^2 c\, s\, 2\pi\alpha}{\rho U s} \tag{7.23}$$

where c is the blade chord, s is the blade span and α is the angle of attack. At the standard blade radius of 0.75R

$$\Gamma \approx \frac{L}{\rho U s} \approx \frac{1}{2}\left(2\pi n\,(0.75R)\right) c_{0.75R}\, 2\pi\,\alpha_{0.75R} = 1.5R\pi^2 n\, c_{0.75R}\,\alpha_{0.75R} \tag{7.24}$$

It takes 1/n seconds for each blade to complete a revolution. Thus, the *rate* of circulation production being fed to the vortex ring (from Z propeller blades) is

$$\frac{d\Gamma}{dt} = \frac{\text{circulation}}{\text{time}} \approx Z\frac{(1.5)R\pi^2 n c_{0.75R}\,\alpha_{0.75R}}{1/n} = Z(1.5)R\pi^2 n^2 c_{0.75R}\,\alpha_{0.75R} \tag{7.25}$$

For a very approximate calculation, it is initially estimated that the blade angle of attack α is approximately constant. Then, integrating the rate of circulation production from time 0 to t gives the total circulation produced by the propeller and fed to the vortex ring up to time t

$$\Gamma_p(t) \approx Z(1.5)R\pi^2 n^2 c_{0.75R}\,\alpha_{0.75R}\, t \tag{7.26}$$

Using Kelvin's Theorem (conservation of circulation), assuming all of the vorticity shed from the propeller blades is fed into the vortex ring, then the circulation of the ring is the same as the total circulation produced by all Z propeller blades (all of which initially rolls up into the vortex ring). Thus, $\Gamma_R = \Gamma_P$, and the non-dimensional time can then be approximated

$$\tau_R \approx \frac{\Gamma_R t}{D^2} \approx \frac{Z(1.5)R\pi^2 n^2 c_{0.75R}\alpha_{0.75R}}{D^2} t^2 \approx Z(0.75)\pi^2 \frac{c_{0.75R}}{D}\alpha_{0.75R} n^2 t^2 \qquad (7.27)$$

For the experimental propeller, D = 0.80 ft, $c_{0.75R}$ = 0.17 ft, and Z = 3 blades, and the blade pitch angle at 0.75R is approximately 13 degrees. To evaluate the non-dimensional formation time for the flow visualization shown in figure 5-6, it is observed from a more detailed image sequence that the approximate formation time for the vortex ring is approximately t = 0.5 seconds. The flow visualization was executed by a step current increase, and therefore the propeller rate n and induced velocity U_{Ai} are not constant, but rather increase roughly exponentially to their steady state values. Initially, assuming a constant angle of attack α (and therefore constant propeller rate n), the time-averaged propeller rate during the period to 0.5 seconds is n = 4 rev/s. Thus, using equation (7.27), a rough estimate of the non-dimensional formation time of the vortex ring from a rapid increase in propeller rate is

$$\tau_R \approx Z(0.75)\pi^2 \frac{c_{0.75R}}{D}\alpha_{0.75R} n^2 t^2 \approx (3)(0.75)\pi^2 \frac{(0.17\,\text{ft})}{(0.8\,\text{ft})}\left(13\frac{\pi}{180}\,\text{rad}\right)(4\,\text{rev/sec})^2(0.5\,\text{sec})^2 \approx 4.3$$

which is remarkably very close to 4, which is the well-established experimental formation time for vortex rings produced by impulsively and rapidly started jets generated at the exit of a tube or orifice ($3.6 - 4.5$ over a wide range of jet velocity profiles) [23].

Now, to consider the effects of the time-varying propeller rate and axial induced velocity at the disk, consider that the blade angle of attack $\alpha(t)$ at the standard radius of 0.75R can be approximated by

$$\alpha(t) \approx \left(\beta_{0.75R} - \frac{U_{Ai}(t)}{2\pi n(t)(0.75R)}\right) \qquad (7.28)$$

where $U_{Ai}(t)$ is the time-varying axial induced velocity at the disk. Thus, the total circulation produced by the propeller and fed to the vortex ring to time t can be written by substituting equation (7.28) into equation (7.25) and integrating

$$\Gamma_p(t) \approx \int_0^t Z(1.5)R\pi^2 n(t)^2 c_{0.75R}\left(\beta_{0.75R} - \frac{U_{Ai}(t)}{2\pi n(t)(0.75R)}\right)dt \qquad (7.29)$$

Thus, the non-dimensional time associated with the formation of the vortex ring can be written

$$\tau_R \approx \frac{\Gamma_R(t)\,t}{D^2} \approx \frac{\left[\int_0^t Z(1.5)R\pi^2 n(t)^2 c_{0.75R}\left(\beta_{0.75R} - \frac{U_{Ai}(t)}{2\pi n(t)(0.75R)}\right)dt\right]t}{D^2} \tag{7.30}$$

Note that this non-dimensional time is a function of the unsteady propeller rate n(t) as well as the unsteady axial induced velocity at the propeller disk $U_{Ai}(t)$. Therefore, solution requires a priori knowledge or estimation of the axial velocity across the propeller disk as a function of time, as might be obtained through high frequency laser particle velocimetry.

As a comparison to the case above in which the angle of attack was assumed constant and the axial induced velocity was neglected, the time-varying formula of equation (7.30) is applied to calculate the non-dimensional formation time for the flow visualization shown in figure 5-6. A simple iterative scheme is applied to calculate the axial induced velocity $U_{Ai}(t)$ at each time step by iteratively solving equations (7.30) and (7.21) until convergence. The results produce a non-dimensional formation time of only 1.3 (which is significantly under the experimental range of $3.6-4.5$ for vortex rings produced by impulsively and rapidly started jets generated at the exit of a tube or orifice [23]). An explanation for this under-prediction can be provided by returning to equation (7.20) and realizing that, in reality, the characteristic velocity of the axial flow feeding the vortex ring U_R is not limited to the contribution of the ring's own induced velocity as assumed with equation (7.21) (i.e. $\Gamma_R/2R$). Rather, there is an additional inflow to the propeller disk and the ring coming from the inner area of the disk, as illustrated in figure 7-4. This additional inflow is required in order to satisfy conservation of mass, momentum, and energy (i.e. the mass, momentum, and energy flux of the "new" fluid across the propeller disk is required to "feed" the growing vortex ring). Thus, there is a complicated unknown inflow into the propeller disk (and subsequently the flow feeding the vortex ring), in addition to the ring's own self-induced velocity field. Thus, referring to figure 7-4 and equation (7.20), the non-dimensional time associated with the formation of the vortex ring would have the more complicated form

$$\tau_R = \left(\overline{U}_{AiR}(t) + \overline{U}_{AiP}(t)\right)\frac{t}{D} \tag{7.31}$$

where $\overline{U}_{AiR}(t)$ and $\overline{U}_{AiP}(t)$ are disk-averaged values of the induced velocities due to the ring and propeller, respectively.

Finally, to complicate matters more, the vortex ring translates due to its own self-induced velocity and the additional wake velocity in the forming propeller slipstream. In other words, the ring moves downstream, partially "under its own power" (its self-induced velocity) and partially due to being "pushed" by the forming propeller slipstream. This translation of the vortex ring means that the plane of the inflow velocity component required for measurement or calculation of

U_R of equation (7.20) is translating along with it, greatly complicating the hydrodynamics. These complexities associated with the variable inflow across the propeller disk and feeding the vortex ring would make this a very rich area for additional subsequent research.

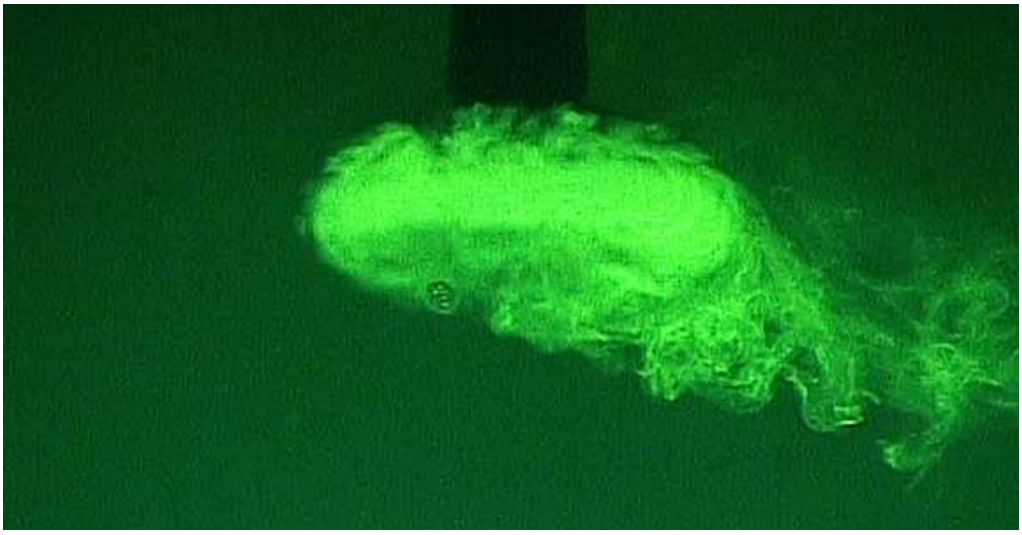

Figure 7-3: Image capture of vortex ring formation due to a rapid increase in propeller rate (here a step increase in motor current), approximately at "pinch-off" (completion of the formation). This image is the same as that at t = 0.5 seconds in figure 5-6.

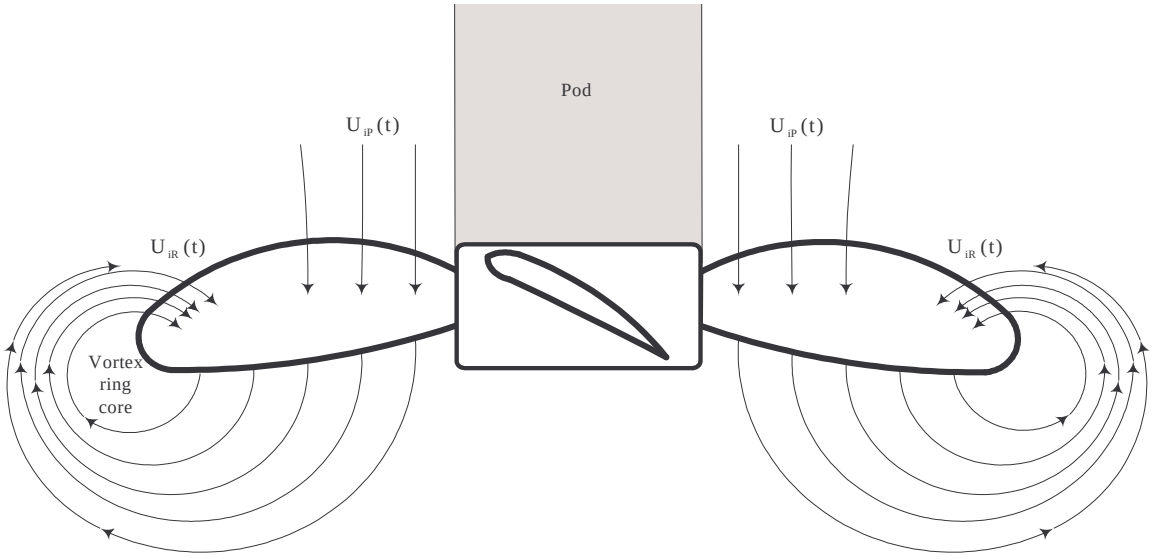

Figure 7-4: Simplified illustration of the complex propeller inflows required to "feed" the formation and growth of the vortex ring due to a rapid increase in propeller rate. The "new" fluid ($U_{AiP}(t)$) is required to satisfy conservation of mass, momentum and energy during formation and growth of the vortex ring. The "reconstituted" fluid ($U_{AiR}(t)$) is the velocity induced by the vortex ring.

7.3 Comparison with experiment

Section 7.1 provided expressions for an approximate dynamic inflow time constant based upon a dynamic inflow theory (equations (7.12) and (7.14)), and provided an approximate theoretical dynamic inflow time constant for the experimental propeller of 0.2 revolutions for the bollard condition. It was further stated that, given the dominant influence of the propeller rate on the analytical dynamic inflow time constant, this approximate dynamic inflow time constant would still approximately hold for the non-bollard condition, as long as in general the tangential velocity due to the propeller rate (relative to the blade) is much larger than the induced velocity and the advance velocity (i.e. $2\pi nr >> v_i$ and $2\pi nr >> V_a$), a condition which holds for practical operating conditions for the experimental propeller. Additionally, Section 7.2 conceptualized the influences of the vortex ring resulting from a rapid increase in propeller rate in terms of an asymmetry of dynamic propeller blade forces seen for rapid propeller rate increases and decreases, and highlighted the approximate "formation time" associated with the vortex ring.

By review of the experimental results of the current input step and rapid ramp response tests provided in Chapter 4, it can be summarized that a typical measured/calculated dynamic inflow time constant would be approximately of 0 revolutions (i.e. near zero) for rapid propeller rate increase and 0.4 revolutions for rapid propeller rate decrease. This is estimated by review of the current input step and rapid ramp results (see figures 4-18, 4-19 and 4-20). Note that this includes the asymmetry due to the vortex ring. The results of the sinusoidal tests will be addressed subsequently. This is compared to the theoretical (symmetric) dynamic inflow time constant, estimated using dynamic inflow theory, of approximately 0.2 revolutions.

Figure 4-20, which provides an example of the current saturated ramp response using input (normalized change in thrust x gain) and output (normalized change in propeller rate), provides a good example to illustrate the potential influences of dynamic inflow, and the vortex ring. Direct application of the dynamic inflow theory would imply a result that would have the output lagging behind the input by the theoretical dynamic inflow time constant, for both increase in current and decrease in current (top and bottom plots of figure 4-20). For the rapid increase in propeller rate, a vortex ring is generated which fundamentally increases induced velocities at the propeller disk, and therefore provides decreased thrust force (for the given propeller rate, as discussed previously). Thus, it would be expected that the influence of the vortex ring formation would be to reduce the input curve (change in thrust x gain) at each time. This is consistent with the general results shown in figure 4-20, as well as figures 4-18 and 4-19. Thus, it could be deduced

that the dynamic inflow theory generally under-predicts the dynamic inflow time constant by approximately 50% (i.e. 0.4 revolutions vs. 0.2 revolutions).

It should also be noted from figure 4-18 that the effect of the vortex ring on the identified dynamic inflow time constant appears to lessen with increased ambient flow (i.e. the calculated time constant for propulsor azimuth angles in the range 0 to ±45° appear to "approach" those of the rapid decrease in propeller rate as the advance velocity is increased). This is consistent with the previous discussion of the vortex ring. Specifically, the experimental results of Krueger et al. [48] indicated a marked drop in vortex ring "formation time" for velocity ratios greater than 0.75, implying that vortex rings reach their (reduced) peak circulation ("pinch-off") more rapidly in the presence of background (ambient) co-flow. This would be consistent with the apparent reduced influence of vortex ring formation on the dynamic inflow time constant measurement shown in figure 4-18.

The behavior of the dynamic inflow time constant τ, with increase in frequency in the sinusoidal current input tests discussed in Chapter 4, is also consistent with these considerations of vortex ring formation and growth. From the previous discussion of vortex ring formation and growth, the vortex ring, and its effect on the induced velocities at the propeller disk, has a characteristic "formation time" or "time constant". From the flow visualizations and the previous discussion, it is estimated that this time constant is on the order of 1/2 second for most of these test operating conditions. As the frequency of the current (and propeller rate) sinusoid is increased, the time between successive vortex rings becomes shorter, and their individual influence on the induced velocities at the propeller disk (and the corresponding blade forces) would then become less at the higher frequencies. This is consistent with the results indicated in figure 4-22 and table 4-1.

The results of the limited sinusoidal azimuth tests (only 2 frequencies at one operating condition) indicate a dynamic inflow time constant of approximately 0.7 revolutions (figure 4-23), slightly larger than the time constants determined from the unsteady propeller rate tests. One possible explanation for this discrepancy is the inherent inaccuracy of applying a sinusoidal azimuth test for this type of variation, especially for such a small amplitude variation (±15°), giving such a small variation in effective inflow velocity V_A. Another possible explanation is that this small variation in azimuth angle (±15°) is applied over a relatively long time frame (i.e. a low frequency) compared to the time constant of the wake. This latter possibility amounts to a violation of the basic assumption used in the development of the dynamic inflow theory in Section 7.1; that is that the rapid change in propeller rate or azimuth angle (or inflow velocity) is applied "instantaneously" (i.e. a step change in blade angle of attack). Clearly, the nature of the

dynamic vortical wake while the wake is undergoing a highly variable wake skew (in addition to the dynamic inflow), is not accounted for in the basic theory. This can be clearly seen in figures 5-5 or 5-17.

7.4 Summary

This chapter has provided a theoretical basis for the unsteady maneuvering dynamics of an azimuthing propulsor. The concept of "dynamic inflow" as an intuitive yet physics-based model of the inertia of the propeller wake or slipstream has been discussed. A simple analytical "dynamic inflow" model has been developed which provides an expression for an approximate dynamic inflow or wake time constant, which can be used in unsteady equations for propeller hydrodynamic forces (Chapter 2). This dynamic inflow time constant represents the lag in the build-up of induced velocity at the propeller disk due to the inertia of the propeller wake. As a result of this lag in induced velocity, the angle of attack at the blades sees a rapid overshoot, then decays to steady-state, with approximately the same time constant. Consequently, the blade forces see an overshoot and decay, with the same time constant.

Additionally, asymmetries seen in the unsteady propeller rate experimental force results (Chapter 4) have been addressed by considering the formation and growth of a vortex ring with rapid increases in propeller rate. The formation of these vortex rings was shown in flow visualizations in Chapter 5. A basic analytical model for the "formation time" of a vortex ring associated with a rapid increase in propeller rate has been developed. In previous laboratory experiments, the non-dimensional "formation time" for vortex rings resulting from the ejection of a water jet from a long tube has been shown to be approximately in the range 3.6-4.5. However, the complexity of the flows through a propeller disk make this difficult to confirm analytically for a propeller, because of the unknown velocities across the propeller disk and feeding the vortex ring. Follow-on research using a high-frequency PIV system to measure detailed velocity fields around the propeller and vortex ring may shed significant light in this area.

Chapter 8

Conclusions

8.1 Summary

This thesis research has investigated the steady and unsteady dynamic maneuvering forces associated with an azimuthing podded propulsor, and has provided supporting theoretical insight toward understanding their mechanisms and prediction. The ultimate goal of the research was to provide a sufficiently comprehensive understanding of the maneuvering forces associated with an azimuthing podded propulsor, such that future maneuvering and control applications, and computational studies in the field, could be appropriately focused.

Chapter 2 provided a brief overview of the relevant dynamics associated with maneuvering with an azimuthing propulsor, along with some intuitive understanding for their application. Basic force effects associated with propellers operating in oblique inflow were introduced, including the important concepts of vectored propeller forces leading to increased thrust and torque with propulsor azimuth. A combined dynamic maneuvering model for incorporating the fully coupled dynamics of a surface vehicle, propeller, and azimuthing propulsion motor was developed, also providing the relevant kinematics required to fully couple the dynamics. A simple model for the dynamics of an azimuthing propulsor driven by a DC motor was also presented, with nonlinear equations for the torque dynamics including important inertia and stick-slip dynamic friction effects. Finally, a new concept for unsteady propeller hydrodynamics was introduced, using a “dynamic inflow” time constant (a wake time constant) for modeling the unsteady hydrodynamic thrust, torque, normal force, and steering moment, all of importance to maneuvering of smaller vehicles. All of dynamic models are used subsequently in the further analysis of the dynamics of the azimuthing podded propulsor.

Chapter 3 provided an overview of the design and construction of an autonomous surface test vehicle, which has been used for much of the subsequent testing. Additionally, the geometric specifications of the podded propulsor and propeller are provided in standard form as might be required for subsequent computational analysis.

Chapter 4 provided an in-depth presentation of the test program conducted in quantitatively investigating maneuvering forces associated with the azimuthing propulsor, including quasi-steady effects, as well as the transient or unsteady effects of potential importance to smaller

vehicles. The experimental setups and techniques were detailed for testing conducted with the propulsor installed on a special test fixture in the MIT towing tank, and with the propulsor installed in the autonomous surface test vehicle installed on the planar motion mechanism (PMM) at the U.S. Naval Academy. The results were presented in both graphical and tabular form, with the significance of the test results to vehicle maneuvering discussed. Specifically, parametric results clearly illustrate unique characteristics of vectored-propulsion, including generation of sizeable normal force, and significant increase in vectored thrust and torque with azimuth angle. Force data has also been presented in terms of surge force (F_x) and sway force (F_y). Contour plots of F_x and F_y for moderate azimuth angles (up to ±45°) are nearly linear in the range of the typical design advance coefficient for the tested propulsor, suggesting the strong possibility of linearization, even decoupling, of the surge-sway-yaw vehicle maneuvering control problem. A thorough investigation of the unsteady propulsor hydrodynamics was also reported in Chapter 4, including identification of a characteristic "dynamic inflow" time constant, which can be used to characterize the unsteady dynamics of propeller thrust, torque, normal force and steering moment for coupled maneuvering dynamics as discussed in Chapter 2. An interesting "asymmetry" in results for rapidly changing propeller rate was observed which indicates a hydrodynamic asymmetry in the flow through the propeller disk with propeller rate increase and decrease. Identified "asymmetric" non-dimensional dynamic inflow time constants for rapid propeller rate increase are approximately zero, while those for rapid propeller rate decrease are approximately 0.4 propeller revolutions.

Chapter 5 presented and discussed results of several efforts to visualize and document the steady and unsteady/transient wake of the azimuthing propulsor. A new technique using fluorescent paint and ultraviolet black light was developed for the visualization of the vortex wake for a range of quasi-steady and unsteady/transient operating conditions. A technique using laser Particle Image Velocimetry (PIV) was also adapted to provide more precise visualization and velocity documentation of the wake for a number of quasi-steady and unsteady/transient operating conditions. Quasi-steady visualizations indicate that the helical wake pitch/diameter ratio for a given propeller rate does not appear to change with even large changes in azimuth angle. This is attributed to the fact that the pitch/diameter ratio for an azimuthing propeller depends not only on the advance ratio J and azimuth angle δ, but also on the axial induced velocity V_{Ai}, which depends on the propeller blade loading. Thus, there is an apparent cancellation effect with propulsor azimuth in terms of helical wake pitch/diameter ratio changes. Quasi-steady visualizations also provided demonstration of the wake distortion effects when the propulsor is azimuthed relative to the flow. The upstream side of the wake is stretched, while the

downstream side is compressed. The quasi-steady visualizations also demonstrate the different convection velocities for the portion of the helical wake coming from the blade, and that portion of the wake which has rolled up into the tip vortices. The tip vortices convect downstream much slower than the corresponding blade wake. Unsteady or transient visualizations provided confirmation of the "dynamic inflow" effect, in terms of a lead of propeller blade forces compared to rapid propulsor azimuth. Despite the fact that the helical wake angle lags the azimuthal position of the propulsor, the forces lead the azimuthal position. Finally, the transient visualizations provided powerful visual evidence of the formation and interaction of vortex rings with rapid increases in propeller rate. These vortex rings appear to induce significant velocity at the propeller disk, which would be consistent with the "asymmetric" results seen with rapid changes in propeller rate in Chapter 4.

Chapter 6 provided a detailed discussion of a theoretical basis for the quasi-steady maneuvering dynamics associated with an azimuthing propulsor over the entire range of forward operating conditions (i.e. for propulsor azimuth to ± 90 degrees relative to the inflow). This theoretical basis included discussion of "simple" momentum-based models for a propeller in axial and oblique inflows, and was expanded to a modified theory using combined blade-element and momentum, including important wake considerations from vortex theory. Finally, a discussion of the use of computational fluid dynamics for the prediction of maneuvering forces was presented. Results of calculations made were provided in comparison with experimental results, with the relevance of consistencies and inconsistencies discussed in detail.

An interesting and obvious limitation on the application of a modified momentum theory to an azimuthing propulsor is the theoretical limitation of maximum thrust to that of the bollard condition ($V_a = 0$). However, force measurement results (Chapter 4) showed that an "excess" thrust force (and torque) results over the entire range of azimuth angles (and is particularly obvious near $\delta = \pm 90°$). An intuitive explanation for the "excess" thrust was offered using Glauert's hypothesis for helicopters in forward flight. Glauert's hypothesis was used to suggest that the propeller disk experiences an additional lift force when it is operating in an oblique inflow, thus providing this "excess" thrust. The development and application of a modified combined blade-element-momentum (BEM) theory, and application of a vortex lattice computational fluid dynamics approach, have demonstrated some of the practical limitations utilizing any of the computational propeller methods in attempting to predict maneuvering forces of podded propulsors. It is apparent that the greatest difficulty inherent with the application of any of the computational fluid dynamics approaches being applied to the podded propulsion and maneuvering problem arises due to the calculation or modeling of the interaction effects between

the propeller and the pod housing and strut. In particular, for a pusher-type podded propulsor, the effect of the pod wake on the propeller inflow would be very difficult to model, even if experimental and empirical methods would be applied. Conversely, the influence of the propeller inflow past the pod housing and strut introduce significant uncertainty in the viscous and separation effects of the pod. Due to the close proximity and interaction of the propeller and pod housing and strut (particularly with propulsor azimuth angle or steering), numerical solution to the podded propulsor maneuvering problem are expected to remain an engineering challenge.

Finally, Chapter 7 provided a theoretical basis for the unsteady maneuvering dynamics of an azimuthing propulsor. A relatively simple analytical "dynamic inflow" model was developed which provides an expression for an approximate dynamic inflow or wake time constant, which can be used in unsteady equations for propeller hydrodynamic forces (Chapter 2). This dynamic inflow time constant represents the lag in the build-up of induced velocity at the propeller disk due to the inertia of the propeller wake. As a result of this lag in induced velocity, the angle of attack at the blade overshoots, then decays to steady-state, with approximately the same time constant. Consequently, the blade forces also overshoot and decay, with approximately the same time constant. Additionally, asymmetries seen in the unsteady propeller rate experimental force results (Chapter 4) were addressed by considering the formation and growth of a vortex ring with rapid increases in propeller rate. A basic analytical model for the "formation time" of a vortex ring associated with a rapid increase in propeller rate was developed. In previous laboratory experiments, the non-dimensional "formation time" for vortex rings resulting from the ejection of a water jet from a long tube has been shown to be approximately in the range 3.6-4.5. However, the complexity of the flows through and around a propeller disk make this difficult to confirm analytically for a propeller, because of the unknown velocities across the propeller disk and feeding the vortex ring.

8.2 Unique contributions

This research effort has provided a number of important and unique contributions to the field of naval architecture and marine engineering.

The quasi-steady propulsor force experiments provide valuable experimental data for the future validation of computational studies on podded propulsors. Specifically, fully-documented propulsor geometries, propulsor operating states, and resulting quasi-steady forces are provided

over the entire range of forward propeller operating conditions, for azimuth angles from 0 to ±180°.

The introduced fluorescent paint flow visualization technique provides a unique means for visualizing the complex helical wake of an azimuthing propulsor over a wide range of steady and unsteady operating conditions. In conjunction with the force measurement results discussed above, the visualization results also provide specific sets of wake trajectory data, including helix geometries (pitch/diameter ratios, wake angles, and wake distortions), which can be used in computational studies for wake modeling and alignment at small, moderate and large azimuth angles.

The fluorescent paint visualizations also revealed the formation of vortex rings during rapid increase in propeller rate. This provides an important rationale for the observed asymmetries in unsteady force results (i.e. dynamic inflow time constants) during rapid changes in propeller rate.

The fluorescent paint and PIV flow visualizations have also demonstrated an apparent invariance of the helical wake pitch/diameter ratio with propulsor azimuth angle, for given propeller rates and advance velocities. This apparent invariance is considered due to the relative cancellation between the decrease in effective inflow and the increase in induced velocity (i.e. loading) as the propulsor is azimuthed relative to the flow.

In addition to the fluorescent paint results, the PIV results also provide specific sets of wake trajectory data, including both helix geometries as well as wake velocities. These can likewise be used in computational studies for wake modeling and alignment at small and moderate azimuth angles, and also for validation of computed wake velocities.

The development of basic theoretical models, in conjunction with basic experimental results may provide important insights into the nature of azimuthing propulsion. For example, modification of the momentum theories using Glauert's hypothesis for helicopters in forward flight leads to an important understanding of the mechanisms associated with the "excess" thrust (and torque) seen in the quasi-steady experimental results. Specifically, it can be deduced that the propeller operating in an oblique flow produces some lift, in addition to its vectored thrust. This is particularly important when the propulsor is operating at higher velocities and at larger azimuth angles, but it is also apparent at slower velocities and smaller angles.

Investigation of maneuvering forces using modified combined blade-element-momentum (BEM) models, and using an available vortex lattice propeller design and analysis code (MPUF-3A), has led to a number of important observations regarding difficulties with analytical modeling of podded propulsors (particularly at moderate and large azimuth angles). First, wake alignment is critical to the proper calculation of propeller forces. Methods must be developed to improve

wake alignment and trajectory analysis. Additionally, there are significant pod wake and propeller inflow interaction effects that are difficult to quantify, but have a significant impact on the computational results. The induced inflow to the propeller alters the flow around and across the pod and strut, and the wake of the pod and strut significantly alter the inflow into the propeller. Further, there are significant pod/strut lift forces which must be taken into account within any computational scheme.

Application of a "dynamic inflow" model for the lag in induced velocity at the propeller disk provides a new method of modeling the unsteady propulsor force dynamics using a set of linearized dynamic equations with a single time constant (a "dynamic inflow" time constant). This has powerful implications in terms of control, in that the unsteady propeller forces can be modeled with the simple first order dynamic equations related to propeller operating states, and these equations can be incorporated readily into the combined dynamic maneuvering model.

Finally, a basic theoretical understanding of vortex ring formation and interaction with a rapid increase in propeller rate has been provided. Specifically, the analogy between "traditional" vortex rings (produced by ejection of a water jet into a quiescent fluid), was used to develop a basic understanding of the concepts and difficulties involved in modeling the formation of vortex rings from the circulation supplied by a rapidly accelerating rotating propeller.

8.3 Recommendations for further study

There are three obvious areas that are recommended for further study. First, the experimental results of force measurements should be utilized in full-vehicle simulations, which should be compared to free-running model tests of the autonomous surface test vehicle. The full set of nonlinear maneuvering coefficients for the bare hull (Chapter 2) has been identified from PMM tests, and provided in Chapter 3. The combined dynamic maneuvering model could be used as the numerical basis for simulations.

As discussed in Chapter 7, a basic analytical model for the "formation time" of a vortex ring associated with a rapid increase in propeller rate has been developed. However, the complexity of the flows through a propeller disk make this difficult to confirm analytically for a propeller, based on existing experimental flow visualizations, because of the unknown velocities across the propeller disk and feeding the vortex ring. Follow-on research using a high-frequency PIV system to measure detailed velocity fields around the propeller and vortex ring may shed significant light in this area. A high-frequency PIV system could provide a detailed velocity map

around the propeller disk, and around the forming vortex ring (see figure 7-4). These velocity maps could be used (by integration) to calculate the required fluxes for the vortex ring formation model. This would provide a means of verification of equation (7.30) for the formation of vortex rings with rapid increase in propeller rate. Subsequent investigation could lead to an improved understanding of the transient force asymmetry related to rapid propeller state changes.

Finally, and without question, investigation of azimuthing podded propulsors using computational fluid dynamics is a difficult and evolving field. Certainly, continued efforts directed toward refinement of computational procedures, especially interaction effects, is a worthy undertaking.

This page left blank

Bibliography

[1] Abkowitz, M.A., *Stability and Motion Control of Ocean Vehicles*, The M.I.T. Press, Cambridge, MA, 1969.

[2] Abkowitz, M.A., "Measurement of hydrodynamic characteristics from ship maneuvering trials by system identification," *SNAME Transactions*, Vol. 88, pp. 283-318, 1980.

[3] Allen, J.J. and Auvity, B., "Interaction of a vortex ring with a piston vortex," *Journal of Fluid Mechanics*, Vol. 465, pp. 353-378, 2002.

[4] Ayaz, Z., Turan, O., and Vassalos, D., "Maneuvering aspects of pod-driven ships," *First International Conference on Technological Advances in Podded Propulsion*, Newcastle upon Tyne, UK, pp. 135-152, April 2004.

[5] Bachmayer, R., Whitcomb, L., and Grosenbaugh, "An accurate four-quadrant nonlinear dynamical model for marine thrusters: theory and experimental validation," *IEEE Journal of Oceanic Engineering*, Vol. 25, No. 1, pp. 146-159, January 2000.

[6] Barr, R.A., "A review and comparison of ship maneuvering simulation methods," *SNAME Transactions*, Vol. 101, pp. 609-639, 1993.

[7] Beckwith, T.G., Marangoni, R.D., and Lienhard, J.H., *Mechanical Measurements*, 5th Edition, Addison-Wesley Publishing Co., Reading, MA, 1995.

[8] Bhagwat, M.J., and Leishman, J.G., "Correlation of Rotor Tip Vortex Measurements," *AIAA Journal*, Vol. 38, No. 2, pp. 301-308, February, 2000.

[9] Bisplinghoff, R.L., *Aeroelasticity*, Addison-Wesley, Cambridge, MA, 1955.

[10] Blanke, M., Lindegaard, K.P., and Fossen, T.I., "Dynamic model for thrust generation of marine propellers," *Proceedings IFAC Conference on Maneuvering of Marine Craft (MCMC2000)*, Aalborg, Denmark, pp. 23-28, August 2000.

[11] Breslin, J.P. and Anderson P., *Hydrodynamics of Ship Propellers*, Cambridge University Press, Cambridge, UK, 1994.

[12] Carlton, J.S., *Marine Propellers and Propulsion*, Butterworth-Heinemann, Oxford, 1994.

[13] Carpenter, P.J. and Fridovich, B., *Effect of a Rapid Blade-Pitch Increase on the Thrust and Induced-Velocity Response of a Full-Scale Helicopter Rotor*, NACA Technical Note 3044, National Advisory Committee for Aeronautics, 1953.

[14] Coleman, R.P., Feingold, A.M., and Stempin, C.W., *Evaluation of the Induced Velocity Field of an Idealized Helicopter Rotor*, NACA ARR No. L5E10, 1945.

[15] Crane, C.L., Eda, H., and Landsburg, A., *Principles of Naval Architecture*, Chapter IX (Controllability), Lewis, E.V. (Ed.), The Society of Naval Architects and Marine Engineers, Jersey City, New Jersey, 1988.

[16] Deniset, F., Jaouen, R., Billard, J.Y., and Laurens, J.M., "Fluctuating pressure distribution on pod," *First International Conference on Technological Advances in Podded Propulsion*, Newcastle upon Tyne, UK, pp. 237-245, April 2004.

[17] Electro-craft Corporation, *DC Motors, Speed Controls, Servo Systems: An Engineering Handbook*, prepared by Electro-craft Corporation, Pergamon Press, New York, 1977.

[18] Di Felice, F., Romano, G., and Elefante, M., "Propeller wake analysis by means of PIV," *Proceedings of the Twenty-third Symposium on Naval Hydrodynamics*, National Academy Press, Washington, DC, 2001.

[19] Doebelin, E.O., *System Dynamics: Modeling, Analysis, Simulation, Design*, Marcel Dekker, Inc., New York, 1998.

[20] Done, G. and Balmford, D., *Bramwell's Helicopter Dynamics*, 2nd Edition, American Institute of Aeronautics and Astronautics, Reston, VA, 2001.

[21] Fossen, T.I., *Guidance and Control of Ocean Vehicles*, John Wiley and Sons, New York, 1994.

[22] Gaonkar, G.H. and Peters, D.A., "Effectiveness of current dynamic-inflow models in hover and forward flight," *Journal of the American Helicopter Society*, Vol. 31, No. 2, pp. 47-57, 1986.

[23] Gharib, M., Rambod, E., and Shariff, K., "A universal time scale for vortex ring formation," *Journal of Fluid Mechanics*, Vol. 360, pp. 121-140, 1998.

[24] Glauert, H., "On the horizontal flight of a helicopter," British Aeronautical Research Council, Reports and Memorandum (ARC R&M) No. 1157, 1928.

[25] Glauert, H., "Airplane Propellers," *Aerodynamic Theory: A General Review of Progress*, Vol. IV, W.F. Durand (Ed.), Julius Springer, Berlin, 1935.

[26] Glezer, A., "The formation of vortex rings," *Physics of Fluids*, Vol. 31, No. 12, pp. 3532-3542, December 1988.

[27] Goodman, A., Gertler M., and Kohl, R., "Experimental techniques and methods of analysis used at Hydronautics for surface ship maneuvering predictions," *11th Symposium on Naval Hydrodynamics*, pp. 55-113, London, UK, 1976.

[28] Gray, R.B., "An aerodynamic analysis of a single-bladed rotor in hovering and low speed forward flight as determined from smoke studies of the vorticity distribution in the wake," *Princeton University Aeronautical Engineering Dept. Report No. 356*, 1956.

[29] Gray, R.B., "Vortex modeling for rotor aerodynamics – The 1991 Alexander A. Nikolsky lecture," *Journal of the American Helicopter Society*, Vol. 37, No. 1, January 1992.

[30] Grygorowicz, M., and Szantyr, J.A., "Open water experiments with two pod propulsor models," *First International Conference on Technological Advances in Podded Propulsion*, Newcastle upon Tyne, UK, pp. 357-370, April 2004.

[31] Gui, L., Longo, J., and Stern, F., "Towing tank PIV measurement system, data and uncertainty assessment for DTMB model 5512," *Experiments in Fluids*, 31, pp. 336-346, 2001.

[32] Hansen, A.C., *Yaw Dynamics of Horizontal Axis Wind Turbines*, Final Report to the National Renewable Energy Laboratory, NREL/TOP-442-4822, 1992.

[33] Hansen, A.C. and Butterfield, C.P., "Aerodynamics of horizontal-axis wind turbines," *Annual Review of Fluid Mechanics*, Vol. 25, pp. 115-149, 1993.

[34] Healey, A.J., Rock, S.M., Cody, S., Miles, D. and Brown, J.P., "Toward an improved understanding of thruster dynamics for underwater vehicles," *Proceedings 1994 Symposium on Autonomous Underwater Vehicle Technology*, Cambridge, MA., 1994.

[35] Heinke, H.J., "Investigations about the forces and moments at podded drives," *First International Conference on Technological Advances in Podded Propulsion*, Newcastle upon Tyne, UK, pp. 305-319, April 2004.

[36] Hoerner, S.F. and Borst H.V., *Fluid-Dynamic Lift*, L.A. Hoerner publisher, 1985.

[37] Hoerner, S.F., Fluid-Dynamic Drag, L.A. Hoerner publisher, 1992.

[38] ITTC, "The Maneuvering Committee: Final report and recommendations to the 23rd International Towing Tank Conference (ITTC)", *Proceedings of the 23rd ITTC*, Venice, IT, 2002.

[39] Jorgensen, L.H., "A method for estimating static aerodynamic characteristics for slender bodies of circular and noncircular cross section alone and with lifting surfaces at angles of attack from 0^0 to 90^0," *National Aeronautics and Space Administration (NASA) Technical Note D-7228*, 1973.

[40] Junglewitz, A., el Moctar, O., Franić, S., "Podded rudders," *First International Conference on Technological Advances in Podded Propulsion*, Newcastle upon Tyne, UK, pp. 401-418, April 2004.

[41] Katz, J., and Plotkin, A., *Low-Speed Aerodynamics*, McGraw-Hill, New York, 1991.

[42] Kerwin, J.E., and Lee, C.S., "Prediction of steady and unsteady marine propeller performance by numerical lifting surface theory," *SNAME Transactions*, Vol. 86, pp. 218-258, 1978.

[43] Kerwin, J.E., *Hydrofoils and Propellers*, Course notes for MIT course 13.04, Hydrofoils and Propellers, Department of Ocean Engineering, Massachusetts Institute of Technology, Cambridge, Massachusetts, 2001.

[44] Kerwin, J.E. *User's Manual MIT-PUF-3A*, Ocean Engineering Report 90-3, Department of Ocean Engineering, Massachusetts Institute of Technology, Cambridge, MA, 1990.

[45] Kinnas, S., Griffin, P., Choi, J.K., Kosal, E., "Automated design of propulsor blades for high-speed ocean vehicle applications," *SNAME Transactions*, Vol. 106, 1999.

[46] Kobylinski, L., "Manoeuverability tests of a vessel with pod propulsion," *First International Conference on Technological Advances in Podded Propulsion*, Newcastle upon Tyne, UK, pp. 371-381, April 2004.

[47] Kreyszig, E., *Advanced Engineering Mathematics*, 8th Edition, John Wiley and Sons, Inc., New York, 1999.

[48] Krueger, P.S., Dabiri, J.O., and Gharib, M., "Vortex ring pinch-off in the presence of simultaneously initiated uniform background co-flow," *Physics of Fluids*, Vol. 15, No. 7, pp. L49-L52, July 2003.

[49] Landgrebe, A.J., "Analytical and experimental investigation of helicopter rotor and hover performance and wake geometry characteristics," *U.S. Army Aviation and Missile Research and Development Laboratory Technical Report 71-24*, 1971.

[50] Lee, H., Gu, H., and Kinnas, S.A., *MPUF-3A (Version 2.1.1) User's Manual and Documentation*, Report No. 04-2, Ocean Engineering Group, Department of Civil Engineering, University of Texas at Austin, Austin, TX, 2004.

[51] Leishman, J.G., *Principles of Helicopter Aerodynamics*, Cambridge University Press, Cambridge, UK, 2000.

[52] Leishman, J.G., "Challenges in modeling the unsteady aerodynamics of wind turbines," *21st ASME Wind Energy Symposium and the 40th AIAA Aerospace Sciences Meeting*, Reno, Nevada, January 2002.

[53] Lim, T.T. and Nickels, T.B., "Vortex Rings," *Vortices in Fluids*, S.I. Greene (ed.), Kluwer, 1995.

[54] Ma, C., Qian, Z., Yang, C., Zhang, X., Du, D., "Research on hydrodynamic computational of pod propulsion," *First International Conference on Technological Advances in Podded Propulsion*, Newcastle upon Tyne, UK, pp. 527-547, April 2004.

[55] McCormick, B.W., *Aerodynamics of V/STOL Flight*, Academic Press, New York, 1967.

[56] McCroskey, W.J., "Unsteady airfoils," *Annual Review of Fluid Mechanics*, Vol. 14, pp. 285-311, 1982.

[57] Minsaas, K.J. and Lehn, E., *Hydrodynamical Characteristics of Rotatable Thrusters, NSFI Report R-69.78*, The Ship Research Institute of Norway, Trodheim, Norway, 1978.

[58] Munk, M.M., *Some Tables of the Factor of Apparent Additional Mass*, NACA Technical Note No. 197, National Advisory Committee for Aeronautics, 1924.

[59] Newman, J.N., *Marine Hydrodynamics*, The MIT Press, Cambridge, MA, 1977.

[60] Nienhuis, U., *Analysis of Thruster Effectivity for Dynamic Positioning and Low Speed Maneuvering*, PhD dissertation, Delft University of Technology, 1992.

[61] Norrby, R.A., and Ridley, D.E., "Notes on thrusters for ship maneuvering and dynamic positioning," *SNAME Transactions*, Vol. 88, pp. 377-402, 1980.

[62] Peters, D.A. and HaQuang, N., "Dynamic inflow for practical applications," *Journal of the American Helicopter Society*, Vol. 33, No. 4, pp. 64-68, October 1988.

[63] Pitt, D.M. and Peters, D.A., "Theoretical Prediction of Dynamic-Inflow Derivatives," *6th European Rotorcraft and Powered Lift Aircraft Forum*, Paper No. 47, Bristol, England, September 1980.

[64] Prantdl, L., Appedix to Betz, A., *Schraubenpropellers mit geringstem Energieverlust*, Gottinger Nachrichten, 1919.

[65] Rubis, C.J. and Harper, T.R., "Ship Propulsion Dynamics Simulation," *Control and Dynamic Systems*, Academic Press, Inc., 1982.

[66] Shariff, K. and Leonard, A. "Vortex Rings," *Annual Review of Fluid Mechanics*, Vol. 24, pp. 235-275, 1992.

[67] Snel, H., and Schepers, J.G., "Engineering models for dynamic inflow phenomena," *Journal of Wind Engineering and Industrial Aerodynamics*, No. 39, pp. 267-281, 1992.

[68] Snel, H., and Schepers, J.G., "Investigation and modeling of dynamic inflow effects," *European Community Wind Energy Conference*, Lubeck-Travemunde, Germany, 1993.

[69] Snel, H., "Review of the present status of rotor aerodynamics," *Wind Energy*, Vol. 1, No. 1, pp. 46-69, April 1998.

[70] Stepniewski, W.Z. and Keys, C.N., *Rotary Wing Aerodynamics*, Dover Publications, New York, 1984.

[71] Stettler, J.W., Hover, F.S., and Triantafyllou, M.S., "Preliminary results of testing on the dynamics of an azimuthing podded propulsor relating to vehicle maneuvering," *First International Conference on Technological Advances in Podded Propulsion*, Newcastle upon Tyne, UK, pp. 321-337, April 2004.

[72] Toxopeus, S., and Loeff, G., "Maneuvering aspects of fast ships with pods," *3rd International EuroConference on High Performance Marine Vehicles HIPER'02*, Bergen, pp. 392-406, September 2002.

[73] Triantafyllou, M.S., and Hover, F.S., *Maneuvering and Control of Marine Vehicles*, Course notes for MIT course 13.42, Maneuvering and Control of Marine Vehicles, Department of Ocean Engineering, Massachusetts Institute of Technology, Cambridge, Massachusetts, 2001.

[74] Van Manan, J.D. and Van Oossanen, P., *Principles of Naval Architecture*, Chapter VI (Propulsion), Lewis, E.V. (Ed.), The Society of Naval Architects and Marine Engineers, Jersey City, New Jersey, 1988.

[75] Van Terwisga, T., Quadvlieg, F., and Valkhof, H., "Steerable propulsion units: hydrodynamic issues and design consequences," Paper written on the occasion of the 80th anniversary of Schottel GmbH & Co., presented on 11 August 2001.

[76] Westerweel, J., (1997), "Fundamentals of digital particle image velocimetry," *Measurement and Science Technology*, Vol. 8, pp. 1379-1392.

[77] Whitcomb, L.L. and Yoerger, D.R., "Development, comparison, and preliminary experimental validation of nonlinear dynamic thruster models," *IEEE Journal of Oceanic Engineering*, Vol. 24, No. 4, pp. 481-494, October 1999.

[78] White, F.M., *Fluid Mechanics*, 3rd Edition, McGraw-Hill Inc., New York, 1994.

[79] Wichers, J., Bultema, S., and Matten, R., "Hydrodynamic research on and optimizing dynamic positioning system of a deep water drilling vessel," *Offshore Technology Conference OTC*, Vol. 4, No. 8854, 1998.

[80] Willert, C.E., and Gharib, M., "Digital particle image velocimetry," *Experiments in Fluids*, No. 10, pp. 181-193, 1991.

[81] Yoerger, D.R., Cooke, J.G., Slotine, J.E., "The influence of thruster dynamics on underwater vehicle behavior and their incorporation into control system design," *IEEE Journal of Oceanic Engineering*, Vol. 15, pp. 167-178, July 1990.

This page left blank

Appendix A

Example computer code

A.1 Matlab® script for modified combined blade-element-momentum (BEM) calculations with pod wake inflow calculation

```
clear all;
format short
%
%
deltai=[-90 -75 -60 -45 -30 -15 0 15 30 45 60 75 90];
for d=1:length(deltai)
   delta=deltai(d)
%
%
kl=1.0704;              % scaling factor for lift coefficient
kd=1.8040;              % scaling factor for parasitic drag coefficient
%
% Input/Parameter Entry
w=0.0;              % estimated wake fraction (for velocity inside wake)
RPM=600;            % RPM
Va=2.5;             % ambient/advance velocity (ft/s)
Vai0=1;             % initial guess for mean axial induced velocity
Vti0=-0.3;          % initial guess for mean tangential induced velocity
Vxi0=0.3;           % initial guess for mean inplane crossflow induced velocity
% delta=0;          % azimuth angle (degree)
Z=3;                % number of blades
D=0.8229;           % propeller diameter (ft)
Dh=3.5/12;          % hub diameter (ft)
Bh=22.0;            % pitch angle at hub radius (deg)
Bt=2.0;             % pitch angle at tip (deg)
Dpod=3.625/12;      % diameter of pod (ft)
ch=2.375/12;        % max chord length (at hub) (ft)
eta0=0.015;         % max camber ratio (eta0/chordlength) (parabolic assumed)
tmax=0.1;           % max time (sec)
tstep=0.1;          % step size for time (sec);
rho=1.9367;         % density (lbf-s2/ft4)
%
% Basic conversions
Rh=Dh/2;                % hub radius (ft)
R=D/2;                  % propeller radius (ft)
Rpod=Dpod/2;            % pod radius (ft)
n=RPM/60;               % convert propeller rate (rev/s)
delta=delta*pi/180;     % convert azimuth angle (rad)
t1=[0:tstep:tmax];
dtheta=(0.5)*(pi/180);  % step size of azimuthal angle (1/2 degrees) = theta differential (rad)
theta1=[0:dtheta:2*pi]; % array of azimuthal angles for calculation/integration (rad)
dr=(R-Rh)/50;
r1=[Rh:dr:R];
```

```
%
VA=Va*cos(delta);       % axial inflow velocity component
VT=Va*sin(delta);       % in-plane inflow velocity component
%
%
% Calculation of modified inflow velocities due to pod wake and strut/shaft wake VAt(j,k), VAt(j,k), (ft/s)
% modify for pod body wake
for j=1:length(r1)
   r=r1(j);
   if delta>=0
      thetamin(j)=acos(Rh/r);
      thetamax(j)=acos(-Rh/r);
   else
      thetamin(j)=acos(Rh/r)+pi;
      thetamax(j)=acos(-Rh/r)+pi;
   end
   thetamid(j)=(thetamin(j)+thetamax(j))/2;
   for k=1:length(theta1)  % theta
      theta=theta1(k);
      if (abs(delta)>(10*pi/180))
         if (theta<=thetamin(j))
            VAt(j,k)=VA;
            VTt(j,k)=VT*cos(theta);
         elseif (theta>=thetamax(j))
            VAt(j,k)=VA;
            VTt(j,k)=VT*cos(theta);
         elseif (theta>thetamin(j)) & (theta<=thetamid(j))
            VAt(j,k)=VA*(1+(w-1)/(thetamid(j)-thetamin(j))*(theta-thetamin(j)));
            VTt(j,k)=VT*cos(theta)*(1+(w-1)/(thetamid(j)-thetamin(j))*(theta-thetamin(j)));
         else
            VAt(j,k)=VA*(w+(1-w)/(thetamax(j)-thetamid(j))*(theta-thetamid(j)));
            VTt(j,k)=VT*cos(theta)*(w+(1-w)/(thetamax(j)-thetamid(j))*(theta-thetamid(j)));
         end
      else
         VAt(j,k)=VA;
         VTt(j,k)=VT*cos(theta);
      end
   end
end
%
% Modify inflow velocities for stut/shaft wake
l=4.9/12;   % distance from steering shaft to mean blade location (ft)
d1=l*tan(delta)-0.5/12;
d2=l*tan(delta)+0.5/12;
Rmin1=(Rh^2+d1^2)^0.5/12;
Rmax1=(R^2+d1^2)^0.5/12;
Rmin2=(Rh^2+d2^2)^0.5/12;
Rmax2=(R^2+d2^2)^0.5/12;
for j=1:length(r1)
   r=r1(j);
   if delta>=0
      thetamin(j)=atan(d1/r);
      thetamax(j)=atan(d2/r);
   else
      thetamin(j)=2*pi-atan(d1/r);
      thetamax(j)=2*pi-atan(d2/r);
```

```
   end
   for k=1:length(theta1)  % theta
      theta=theta1(k);
      if (theta>thetamin(j)) & (theta<thetamax(j))
         VAt(j,k)=0;
         VTt(j,k)=0;
      else
         VAt(j,k)=VAt(j,k);
         VTt(j,k)=VTt(j,k);
      end
   end
end
%
%
% Calculate disk-averaged inflow velocities (including pod wake)
for j=1:length(r1);
   for k=1:length(theta1);
      dVAm1(k)=VAt(j,k);
      dVTm1(k)=VTt(j,k);
   end
   dVAm2(j)=1/(2*pi)*sum(dVAm1*dtheta);
   dVTm2(j)=1/(2*pi)*sum(dVTm1*dtheta);
end
VAm=2/(R^2-Rh^2)*sum(dVAm2.*r1*dr);     % disk-averaged axial inflow velocity (including pod wake)
VTm=2/(R^2-Rh^2)*sum(dVTm2.*r1*dr);       % disk-averaged in-plane infow velocity (including pod
wake)
%
% BEM calculation/integration at current angle
%
for i=1:length(t1)  % time
   t(i)=t1(i);
   %
   T1=0; Q1=0; N1=0; M1=0;          % initialize total force integration at time t
   %
   finished=0;
   iter=1;
   while (finished==0)  % while loop
      X(i)=atan2((VTm+Vxi0),(VAm+Vai0));       % calculate wake skew angle (rad)
      lambda(i)=(VAm+Vai0)/(2*pi*n*R+Vti0);    % tip speed ratio for Prandtl tip loss factor calculation
      %
      for j=1:length(r1) % radius
         r=r1(j);
         Br=(Bh+((Bt-Bh)/(R-Rh))*(r-Rh))*pi/180;          % blade pitch angle at radius r (rad)
         c=ch*(1-((r-Rh)^2/(R-Rh)^2))^0.5;                % blade chord at radius r (parabolic distribution) (ft)
         F(j)=(2/pi)*acos(exp(-(Z/2)*((R-r)/R)*(1+lambda(i)^2)^0.5/lambda(i)));    % Prandtl's tip loss
               for k=1:length(theta1)  % theta
               theta=theta1(k);
               % calculation of modified inflow velocities due to pod wake VA(j,k), VT(j,k)
               VAjk=VAt(j,k); VTjk=VTt(j,k);
               Vaik(k)=Vai0*(1+(r/R)*tan(X(i)/2)*sin(theta));      % element axial induced velocity (ft/s)
               Vtik(k)=Vti0*(1+(r/R)*tan(X(i)/2)*sin(theta));      % element tangential induced velocity (ft/s)
               Vxik(k)=Vtik(k)*cos(theta);                 Vait(j,k)=Vaik(k); Vtit(j,k)=Vtik(k);
               Vas=VAjk+Vaik(k);
               Vat(j,k)=Vas;
                Vts=(2*pi*n*r+Vtik(k))+VTjk*cos(theta);
               Vps=(Vas^2+Vts^2)^0.5;
```

```
            phi=atan2(Vas,Vts);
            a=Br-phi;
            Cl=kl*(4*pi*eta0+2*pi*a);
            Cd=kd*(0.008)+(0.06*Cl^2);
            Ts=0.5*rho*Vps^2*c*(Cl*cos(phi)-Cd*sin(phi));
            Fts=0.5*rho*Vps^2*c*(Cl*sin(phi)+Cd*cos(phi));
            dTbek(k)=Ts;
            dQbek(k)=Fts*r;
            dNbek(k)=Fts*cos(theta);
            dMbek(k)=-Ts*sin(theta)*r;
            end  % theta
         dTbe(j)=Z/(2*pi)*sum(dTbek*dtheta);
         dQbe(j)=Z/(2*pi)*sum(dQbek*dtheta);
         dNbe(j)=Z/(2*pi)*sum(dNbek*dtheta);
         dMbe(j)=Z/(2*pi)*sum(dMbek*dtheta);
         Vaibar(j)=1/(2*pi)*sum(Vaik*dtheta);
         Vtibar(j)=1/(2*pi)*sum(Vtik*dtheta);
         Vxibar(j)=1/(2*pi)*sum(Vxik*dtheta);
         Vaibar1(j)=dTbe(j)/(4*rho*pi*r*(Va^2+2*Vaibar(j)*VA+Vaibar(j)^2)^0.5)*F(j);
         Vtibar1(j)=-dQbe(j)/(4*rho*pi*r^2*(Va^2+2*Vaibar(j)*VA+Vaibar(j)^2)^0.5)*F(j);
      end  % radius
      Vai0=2/(R^2-Rh^2)*sum(Vaibar.*r1*dr);
      Vti0=2/(R^2-Rh^2)*sum(Vtibar.*r1*dr);
      Vxi0=2/(R^2-Rh^2)*sum(Vxibar.*r1*dr);
      Vai01=2/(R^2-Rh^2)*sum(Vaibar1.*r1*dr);
      Vti01=2/(R^2-Rh^2)*sum(Vtibar1.*r1*dr);
      dVai=Vai0-Vai01;
      dVti=Vti0-Vti01;
      if (abs(dVai)<1.0e-5) & (abs(dVti)<1.0e-5)  % convergence check
         finished=1;
      else
         Vai0=0.5*(Vai0+Vai01);
         Vti0=0.5*(Vti0+Vti01);
         finished=0;
         iter=iter+1;
         if (iter>100)
            finished=1;
            t=t
            Vai0
            Vti0
         end
      end  % convergence check
   end  % while loop
for j=1:length(r1)
   T1=T1+dTbe(j)*dr;
   Q1=Q1+dQbe(j)*dr;
   N1=N1+dNbe(j)*dr;
   M1=M1+dMbe(j)*dr;
end
T(i)=T1;
Q(i)=Q1;
Qinlb=Q*12;
N(i)=N1;
M(i)=M1;
Minlb=M*12;
Vai0t(i)=Vai0;
```

```
   Vti0t(i)=Vti0;
end  % time
%
Tmean(d)=mean(T);
Qmeaninlb(d)=mean(Qinlb);
Nmean(d)=mean(N);
Mmeaninlb(d)=mean(Minlb);
Xm(d)=mean(X)*180/pi;
Vai0m(d)=mean(Vai0t);
Vti0m(d)=mean(Vti0t);
%
end  % deltai
format short
A=[deltai; Tmean; Nmean; Mmeaninlb; Qmeaninlb; Xm; Vai0m; Vti0m];
wk1write('RectWakeOut.wk1',A, 0, 0)
%
%
% Plot inflow velocity components vs. theta for r = 0.8*R (j=35)
%
figure(1); clf; hold on;
grid on; plot(theta1*180/pi,VAt(35,:)/Va,'b');plot(theta1*180/pi,VTt(35,:)/Va,'b');
axis([0 360 -1 1.5]);ylabel('V_A/V_a,  V_\theta/V_a');box on;
title('Approximated pod wake inflow:  w = 0  \delta = 30 deg,  r/R=0.8'); xlabel('Angle (deg)');
box on; legend('Approximate inflow velocity component',0);
text(155,0.78,'V_A/V_a');
text(155,-0.6,'V_\theta/V_a');
```

A.2 Matlab® script for calculation of pod wake inflow Fourier harmonics for MPUF-3A calculations

```
clear all;
%
delta=-30;      % Input propulsor azimuth angle (deg)
Va=2.5;         % Ambient/advance velocity (ft/s)
w=0.00;         % Input wake fraction (mean fraction of freestream velocity in wake of propulsor pod)
%
rR=[0.36 0.44 0.52 0.60 0.68 0.76 0.84 0.92 1.00];      % normalized radii
dtheta=0.001;
theta1=[0:dtheta:2*pi];
delta=delta*pi/180;
%
RhR=0.36;          % hub radius normalized to propeller radius
%
%
VA=Va*cos(delta);   % axial inflow velocity component
VT=Va*sin(delta);   % in-plane inflow velocity component
%
% Calculation of modified inflow velocities due to pod wake Vat(j,k), Vtt(j,k), Vrt(j,k) (ft/s)
for j=1:length(rR)
   % Calculate min and max angles of the wake for current radius (with theta = 0 opposite to inflow for
delta > 0:
   if delta>=0
      thetamin(j)=2*pi-asin(RhR/rR(j));
      thetamax(j)=asin(RhR/rR(j));
      thetamid(j)=0;
   else
      thetamin(j)=-asin(RhR/rR(j))+pi;
      thetamax(j)=asin(RhR/rR(j))+pi;
      thetamid(j)=pi;
   end
   for k=1:length(theta1)  % theta
   theta=theta1(k);
   if delta>(10*pi/180)
      if (theta>=thetamax(j)) & (theta<=thetamin(j))
         Vat(j,k)= VA;
         Vtt(j,k)=-VT*sin(theta);
         Vrt(j,k)= VT*cos(theta);
      elseif (theta>thetamin(j))
         Vat(j,k)= VA*(1+(w-1)/(2*pi-thetamin(j))*(theta-thetamin(j)));
         Vtt(j,k)=-VT*sin(theta)*(1+(w-1)/(2*pi-thetamin(j))*(theta-thetamin(j)));
         Vrt(j,k)= VT*cos(theta)*(1+(w-1)/(2*pi-thetamin(j))*(theta-thetamin(j)));
      else
         Vat(j,k)= VA*(w+(1-w)/thetamax(j)*(theta-thetamid(j)));
         Vtt(j,k)=-VT*sin(theta)*(w+(1-w)/thetamax(j)*(theta-thetamid(j)));
         Vrt(j,k)= VT*cos(theta)*(w+(1-w)/thetamax(j)*(theta-thetamid(j)));
      end
   elseif delta<(-10*pi/180)
      if (theta<=thetamin(j))
         Vat(j,k)= VA;
         Vtt(j,k)=-VT*sin(theta);
         Vrt(j,k)= VT*cos(theta);
```

```
        elseif (theta>=thetamax(j))
            Vat(j,k)= VA;
            Vtt(j,k)=-VT*sin(theta);
            Vrt(j,k)= VT*cos(theta);
        elseif (theta>thetamin(j)) & (theta<thetamid(j))
            Vat(j,k)= VA*(1+(w-1)/(thetamid(j)-thetamin(j))*(theta-thetamin(j)));
            Vtt(j,k)=-VT*sin(theta)*(1+(w-1)/(thetamid(j)-thetamin(j))*(theta-thetamin(j)));
            Vrt(j,k)= VT*cos(theta)*(1+(w-1)/(thetamid(j)-thetamin(j))*(theta-thetamin(j)));
        else
            Vat(j,k)= VA*(w+(1-w)/(thetamax(j)-thetamid(j))*(theta-thetamid(j)));
            Vtt(j,k)=-VT*sin(theta)*(w+(1-w)/(thetamax(j)-thetamid(j))*(theta-thetamid(j)));
            Vrt(j,k)= VT*cos(theta)*(w+(1-w)/(thetamax(j)-thetamid(j))*(theta-thetamid(j)));
        end
    else
        Vat(j,k)= VA;
        Vtt(j,k)=-VT*sin(theta);
        Vrt(j,k)= VT*cos(theta);
    end
end
end
%
% Normalize inflow velocities
Vatn=Vat/Va;
Vttn=Vtt/Va;
Vrtn=Vrt/Va;
%
% Calculate Fourier coefficients for 1st 16 harmonics (incl. 0th) for normalized inflow velocities
%
for j=1:length(rR)
    for p=1:15
        aa0=0;
        aa(p)=0;
        ba(p)=0;
        at0=0;
        at(p)=0;
        bt(p)=0;
        ar0=0;
        ar(p)=0;
        br(p)=0;
        for k=1:length(theta1)
            aa0=aa0+(1/(2*pi))*Vatn(j,k)*dtheta;
            aa(p)=aa(p)+(1/(pi))*Vatn(j,k)*cos(p*theta1(k))*dtheta;
            ba(p)=ba(p)+(1/(pi))*Vatn(j,k)*sin(p*theta1(k))*dtheta;
            at0=at0+(1/(2*pi))*Vttn(j,k)*dtheta;
            at(p)=at(p)+(1/(pi))*Vttn(j,k)*cos(p*theta1(k))*dtheta;
            bt(p)=bt(p)+(1/(pi))*Vttn(j,k)*sin(p*theta1(k))*dtheta;
            ar0=ar0+(1/(2*pi))*Vrtn(j,k)*dtheta;
            ar(p)=ar(p)+(1/(pi))*Vrtn(j,k)*cos(p*theta1(k))*dtheta;
            br(p)=br(p)+(1/(pi))*Vrtn(j,k)*sin(p*theta1(k))*dtheta;
        end
        AA0(j)=aa0;
        AA(j,p)=aa(p);
        BA(j,p)=ba(p);
        AT0(j)=at0;
        AT(j,p)=at(p);
        BT(j,p)=bt(p);
```

```
        AR0(j)=ar0;
        AR(j,p)=ar(p);
        BR(j,p)=br(p);
    end
end
%
%
% Check calculation by calculating velocities based upon truncated Fourier series and plotting
for j=1:length(rR)
    for k=1:length(theta1)
        va1(k)=AA0(j);
        vt1(k)=AT0(j);
        vr1(k)=AR0(j);
        for p=1:15
            va1(k)=va1(k)+(AA(j,p)*cos(p*theta1(k))+BA(j,p)*sin(p*theta1(k)));
            vt1(k)=vt1(k)+(AT(j,p)*cos(p*theta1(k))+BT(j,p)*sin(p*theta1(k)));
            vr1(k)=vr1(k)+(AR(j,p)*cos(p*theta1(k))+BR(j,p)*sin(p*theta1(k)));
        end
        Va1n(j,k)=va1(k);
        Vt1n(j,k)=vt1(k);
        Vr1n(j,k)=vr1(k);
    end
end
% plot to compare
% (not included)
%
%
% Output formatted Fourier coefficients to screen
format short
AA0=AA0;
AA1=AA';
BA1=BA';
AR0=AR0;
AR1=AR';
BR1=BR';
AT0=AT0;
AT1=AT';
BT1=BT';

%
format short
A=[0 0 0 0 0 0 0 0 0; AA0; AA1; BA1; AR0; AR1; BR1; AT0; AT1; BT1];
wk1write('WakeTemp.wk1',A, 0, 0)
```

This page left blank